Université de Montréal

TESS exoplanet candidate follow-up with ground- and space-based instruments

par

Christopher Mann

Département de physique
Faculté des arts et des sciences

Thèse présentée en vue de l'obtention du grade de
Philosophiæ Doctor (Ph.D.)
en Astrophysique

Aug 1, 2023

Université de Montréal

Faculté des arts et des sciences

Cette thèse intitulée

TESS exoplanet candidate follow-up with ground- and space-based instruments

présentée par

Christopher Mann

a été évaluée par un jury composé des personnes suivantes :

Laurence Perreault Levasseur
(président-rapporteur)

David Lafrenière
(directeur de recherche)

Björn Benneke
(membre du jury)

Stanimir Metchev
(examinateur externe)

(représentant du doyen de la FESP)

Résumé

La découverte d'exoplanètes a connu une croissance quasi exponentielle au cours des trois dernières décennies. Nous savons désormais que les systèmes d'exoplanètes sont la norme dans la galaxie et qu'il existe une variété d'archétypes de planètes qui ne correspondent pas à notre propre système solaire. Ces progrès rapides sont dus en grande partie aux missions spatiales qui utilisent la méthode des transits pour trouver et caractériser de nouvelles exoplanètes. Kepler et, plus récemment, le Transiting Exoplanet Survey Satellite (TESS) ont contribué à la majorité des exoplanètes confirmées ou candidates connues à ce jour. Les exoplanètes découvertes par TESS sont particulièrement prometteuses, car TESS a délibérément ciblé des étoiles hôtes brillantes pour faciliter l'analyse spectroscopique détaillée de l'atmosphère de leurs planètes. Bien que TESS soit très efficace pour identifier de nouveaux signaux de transit, un effort de suivi substantiel est nécessaire pour valider chaque nouvelle candidate et le succès global de la mission TESS dépend fortement de l'obtention de ce suivi de la part d'observatoires externes. Une attention particulière est souvent requise pour les planètes à longue période qui souffrent fortement des biais impliqués dans les recherches de transit. Si l'on peut surmonter les défis observationnels supplémentaires, ces planètes constituent des bancs d'essai rares et précieux pour étudier la physique et la chimie des atmosphères plus froides.

Dans cette thèse, j'ai collaboré avec la communauté de suivi des exoplanètes TESS sur plusieurs fronts en apportant des instruments précédemment inutilisés, en contribuant à l'effort général de vérification des candidates, ainsi qu'en menant des études de validation et de confirmation de cibles difficiles à longue période. Nous avons adapté le réseau de téléobjectifs Dragonfly (alias "Dragonfly"), conçu pour les cibles de faible luminosité de surface, à l'observation des transits d'exoplanètes. J'ai développé un nouveau mode d'observation adapté aux transits et créé des pipelines de planification, de traitement des données et d'analyse. Nous avons atteint une précision photométrique d'environ 0,5 ppt dans des intervalles de 4 à 5 minutes sur la plage $9 < m_V < 13$, compétitive avec d'autres observatoires au sol de classe 1–2 m. Nous avons également développé un vaste programme d'observation avec le satellite de surveillance des objets proches de la Terre (NEOSSat) couvrant 3 ans et 6 cycles d'observation pour observer les transits d'exoplanètes de longue durée, qui représentent un défi majeur à capturer avec des observatoires au sol. En utilisant ces deux instruments, nous avons fourni des observations pour le programme d'observation de suivi

des exoplanètes TESS (ExoFOP). Grâce à mon travail dans ExoFOP, j'ai dirigé une publication de validation pour TOI-1221 b, une planète sub-neptunienne de 2,9 $R_\oplus$ sur une orbite de 92 jours. Non seulement nous avons écarté les scénarios de faux positifs pour cette planète tempérée à longue période, mais grâce à notre analyse détaillée de 6 transits TESS et 2 détections au sol, nous avons trouvé des preuves de variations de synchronisation de transit qui pourraient indiquer une autre planète cachée dans le système. Nous avons également utilisé NEOSSat pour rechercher un deuxième transit de TOI-2010 b, qui n'en montrait qu'un seul dans les données TESS. En surveillant l'étoile hôte sur une fenêtre d'incertitude de 7 jours, nous avons capturé le transit et amélioré considérablement notre connaissance de l'éphéméride de la planète. J'ai dirigé l'article de confirmation sur cette planète semblable à Jupiter avec une orbite de 142 jours, ajoutant une cible de faible insolation à la petite collection d'exoplanètes connues avec des périodes supérieures à 100 jours et des étoiles hôtes suffisamment brillantes pour un suivi spectroscopique. En plus de diriger ces deux projets spécifiques, mes observations avec Dragonfly et NEOSSat ont jusqu'à présent contribué à 10 autres publications dont je suis co-auteur.

Mots clés: Analyse de données astronomiques — Réduction photométrique — Transits — Validation et confirmation d'exoplanètes — Exoplanètes à longue période — TESS — Dragonfly Telephoto Array — NEOSSat

Abstract

Exoplanet discovery has undergone near-exponential growth over the last three decades. We now know exoplanet systems are the norm in the Galaxy and that a variety of planet archetypes exist that do not necessarily match our own Solar System. This rapid advancement is due in large part to space-based discovery missions utilizing the transit method to find and characterize new exoplanets. Kepler, and more recently, the Transiting Exoplanet Survey Satellite (TESS) have contributed the majority of confirmed or candidate exoplanets known today. The exoplanets discovered by TESS show particular promise, as TESS has deliberately targeted bright host stars to facilitate detailed spectroscopic analysis of their planets' atmospheres. While TESS is highly efficient at identifying new transit signals, substantial follow-up effort is required to validate each new candidate and the overall success of the TESS mission heavily depends on attaining this follow-up from external observatories. Special attention is often required for long-period planets that suffer heavily from the biases involved in transit searches. If one can overcome the added observational challenges, these planets provide rare and valuable testbeds to investigate cool-atmosphere physics and chemistry.

Through this thesis, I engaged with the TESS exoplanet follow-up community on several fronts by bringing previously unused instrument options to the endeavour, contributing to the general effort of candidate verification, as well as leading validation and confirmation studies of challenging long-period targets. We adapted the Dragonfly Telephoto Array (a.k.a. "Dragonfly"), designed for low-surface brightness targets, to the observation of exoplanet transits. I developed a new transient-appropriate observing mode and created scheduling, data processing, and analysis pipelines. We achieve a photometric precision floor of ~0.5 ppt in 4–5-minute bins over the range $9 < m_V < 13$, competitive other 1–2 m class ground-based observatories. We also developed an extensive observing program with the Near-Earth Object Surveillance Satellite (NEOSSat) spanning 3 years and 6 observing cycles to observe long-duration exoplanet transits that provide a major challenge to capture with ground-based observatories. Using these two instruments, we provided follow-up observations for the TESS Exoplanet Follow-up Observing Program (ExoFOP). Through my work with ExoFOP, I led a validation publication for TOI-1221 b, a 2.9 $R_\oplus$ sub-Neptune planet on a 92-day orbit. Not only do we rule out the false-positive scenarios for this long-period temperate planet, but through our detailed analysis of 6 TESS transits and 2 ground-based detections, we find evidence of transit timing variations that may indicate an additional hidden planet in the system.

We also used NEOSSat to hunt for an elusive second transit of TOI-2010 b. By monitoring the host star over a 7-day uncertainty window, we caught the transit and vastly improved our knowledge of the planet's ephemeris. I led the confirmation paper on this temperate Jupiter-like planet with a 142-day orbit, adding a low-insolation target to the small collection of known exoplanets with periods above 100 days and host stars bright enough for spectroscopic follow-up. Beyond leading these two specific projects, my observations with Dragonfly and NEOSSat have thus far contributed to 10 other publications for which I am co-author.

Keywords : Astronomical data analysis — Photometric reduction — Transits — Exoplanet validation and confirmation — Long-period exoplanets — TESS — Dragonfly Telephoto Array — NEOSSat

Contents

List of tables

List of figures

List of Acronyms and Abbreviations

AO	Adaptive Optics
APF	Automated Planet Finder
`batman`	BAsic Transit Model cAlculatioN
BJD	Barycentric Julian Date
CHEOPS	CHaracterising ExOPlanets Satellite
CoRoT	Convection, Rotation et Transits planétaires
CSA	Canadian Space Agency
CTIO	Cerro Tololo Inter-American Observatory
CTOI	Community TESS Object of Interest
Dec	Declination
Dragonfly	Dragonfly Optical Array

DRDC	Defence Research and Development Canada
DV	Data Validation
EB	Eclipsing Binary
ELT	Extremely Large Telescope
ESM	Eclipse Spectroscopy Metric
Exo-Dragonfly	The exoplanet sub-project with Dragonfly
EOS	Equation of State
ExoFOP	Exoplanet Follow-up Observing Program. Repository for compiled exoplanet follow-up data. Contains a TESS subdivision.
FAP	False Alarm Probability
FLWO	Fred Lawrence Whipple Observatory
FPP	False Positive Probability
FWHM	Full Width at Half Maximum

GMU	George Mason University
GP	Gaussian Process
HATNet	Hungarian-made Automated Telescope Network
HIRES	High Resolution Echelle Spectrometer
JWST	James Webb Space Telescope
K2	Kepler's extended mission
KELT	Kilodegree Extremely Little Telescope
LCOGT	Las Cumbres Observatory Global Telescope
LSB	Low Surface Brightness
MAST	Mikulski Archive for Space Telescopes
MCMC	Markov Chain Monte Carlo
MIRI	Mid-Infrared Instrument
MIST	MESA Isochrones & Stellar Tracks

NASA	National Aeronautics and Space Administration
NEB	Nearby Eclipsing Binary
NEOSSat	Near-Earth Object Surveillance Satellite
NFPP	Nearby False Positive Probability
NIRISS	Near Infrared Imager and Slitless Spectrograph
NMS	New Mexico Skies telescope hosting facility
NRES	Network of Robotic Echelle Spectrographs
O-C	Observed-minus-Calculated
OGLE	Optical Gravitational Lensing Experiment
PCA	Principle Component Analysis
PDCSAP	Presearch Data Conditioning Simple Aperture Photometry
PEST	Perth Exoplanet Survey Telescope
ppm	parts per million

ppt	parts per thousand
PSF	Point-Spread Function
RA	Right Ascension
RM	Rossiter McLaughlin effect
RMS	Root-Mean-Square
RUWE	Renormalized Unit Weight Error
RV	Radial Velocity
SAAO	South African Astronomical Observatory
SAP	Simple Aperture Photometry
SBIG	Santa Barbara Imaging Group
SDSS	Sloan Digital Sky Survey
SED	Spectral Energy Distribution
SNR	Singal-to-Noise Ratio

SOAR	Southern Astrophysical Research telescope
SOPHIE	Spectrographe pour l'Observation des Phénomènes des Intérieurs stellaires et des Exoplanètes
SPOC	Science Processing Operations Center
SSO	Siding Springs Observatory
SPC	Stellar Parameter Classification
SPECULOOS	Search for habitable Planets EClipsing ULtra-cOOl Stars
Sticks	Name given to local storage on each individual camera's control computer on Dragonfly
TIC	TESS Input Catalog
TOI	TESS Object of Interest
TDV	Transit Duration Variation
TESS	Transiting Exoplanet Survey Satellite
TFOP	TESS Follow-Up Observing Program. The follow-up community aiding the TESS mission.

TMT	Thirty Meter Telescope
TRAPPIST	Transiting Planets and Planetesimals Small Telescope
TRES	Tillinghast Reflector Echelle Spectrograph
TRICERATOPS	Tool for Rating Interesting Candidate Exoplanets and Reliability Analysis of Transits Originating from Proximate Stars
TSM	Transit Spectroscopy Metric
TSTPC	TESS Single Transit Planet Candidate
TTV	Transit Timing Variation
UDG	Ultra-Diffuse Galaxy
VSG	Visual Survey Group
WASP	Wide Angle Search for Planets
XO	Prounced "exo"
XUV	X-ray and UltraViolet

To Tara, Freya & Loki;
For putting up with me and keeping my life on track.

Acknowledgements

I would like to, first and foremost, thank my Ph.D. advisor David for his endless patience, support, and dedication to all his students, myself included. David, you foster an environment where inquiry is encouraged and not knowing an answer feels like an opportunity to learn, rather than a failure to understand. Your praise feels meaningful, and your encouragement helped me through this program. Thank you so very much for everything.

Neil and Farbod (and Céline and Fatane, of course), while we may not have had much overlap in our respective research projects, your friendship and camaraderie throughout my stay in Montreal has been invaluable. Our many hours playing board games, sharing dinners, or wandering the city provided a little bubble of home for me on this side of the country.

To everyone else in iREx, thank you for simply being amazing people. I always felt welcome and my days at UdeM were never short of friendly faces. As I move along my career path, it's the people I met in Montreal that I will miss the most from my time here.

To my wife, Tara, there's not much to say that you don't already know. You picked up your life and moved 4000 km with me to take this adventure. Thank you for sticking by me, celebrating with me during the fun parts, and pulling me through the stressful ones.

To my cats, Loki and Freya, you are a boon to my mental health, even if you don't let me sleep late anymore. Few things are better after a hard day than an armful of fur and a quiet purr.

Chapter 1

Introduction

1.1. An Intro to Exoplanets

1.1.1. History and progress

The term "exoplanet" refers to an extra-solar planet, or in other words, a planet outside of our own solar system. There is no reason to believe that our own solar system is particularly unique in the Galaxy, so detecting exoplanet systems was just a matter time, technique, and instrumental acuity.

The first exoplanets to be confirmed were found in a setting vastly different than our solar system. The discovery came from studying a pulsar, a class of neutron star (ultra-dense, collapsed stellar remnants) which emit radio-band electromagnetic pulses at *extremely* regular intervals. The pulse period can be measured to such exquisite precision that minuscule deviations can be detected. Wolszczan & Frail (1992) determined that anomalies discovered in the precise timing of the millisecond-period pulsar PSR B1257+12 could be explained by the presence of two planetary-mass objects orbiting it and affecting its dynamics. It was later confirmed that a third object (Moon-mass) also orbited the pulsar (Wolszczan, 1994).

While the pulsar planets were the first to be confirmed, two other exoplanets were detected earlier but confirmed later. Campbell et al. (1988) reported subtle evidence for a planetary mass object orbiting γ Cephei A, later confirmed by Hatzes et al. (2003). Latham et al. (1989) reported a planetary companion around the F-type star HD 114762, later to be confirmed by Cochran et al. (1991). A few years after these early detections, 51 Pegasi b made a strong impression on the astronomical community as the first known exoplanet around a Sun-like star (Mayor & Queloz, 1995).

These keystone discoveries marked the beginning of the field of exoplanet observation. Since then, the field has exploded in a near-exponential fashion. At the time of writing, there are 5400+ confirmed exoplanets and many thousands more candidates. A brief examination of Figure 1.1

[1] https://exoplanetarchive.ipac.caltech.edu/index.html

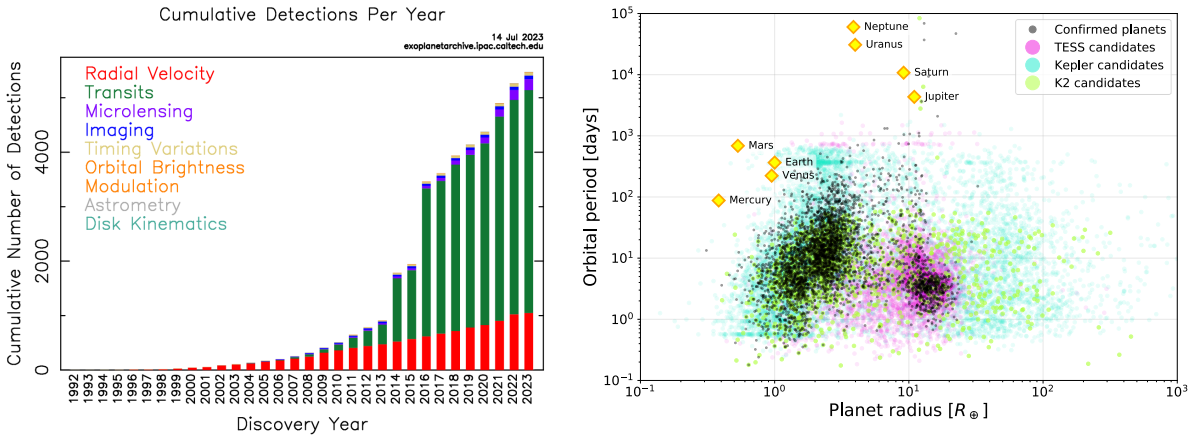

Fig. 1.1. *Left panel:* Cumulative count of confirmed exoplanets through time, colour-coded by discovery method. The two major jumps correspond to Kepler's announcements of 725 and 1285 newly discovered planets in 2014 and 2016. *Right panel:* Period–radius distribution of exoplanets. Black points show confirmed exoplanets while coloured points show unconfirmed candidates from three major survey missions. Yellow points mark our own solar system planets. Observing biases make it very challenging to detect planets with orbital periods beyond a few hundred days with the raidal velocity and transit methods. Most of the very large candidates are likely stellar object false-positives. Data from the NASA Exoplanet Archive[1].

shows that, though many detection methods exist, two in particular have discovered the vast majority of planets. The radial velocity (RV) method, discussed further in section 1.4.2, was dominant in the early days of exoplanet discovery. It involves measuring the planet-induced wobbling of a star due to their mutual gravity. The RV method has continued to produce steady discoveries over the years, but has been more recently outpaced by dedicated surveys looking for exoplanet transits. A transit is when an object passes between the host star and the observer, blocking a portion of the starlight, and causing a drop in the flux received at Earth. Entire fields of stars can be monitored simultaneously for the tell-tale dip in brightness due to an exoplanet crossing, and so searching for exoplanet transits has proven to be a hugely efficient detection method and has produced the majority of discoveries to date.

1.1.2. The current picture of exoplanets

Over the last few decades, one of the most ubiquitous and possibly surprising results of exoplanet discovery, has been variety. We have now firmly buried the old idea that exoplanet systems would generally look like variations on our own solar system. The very first known exoplanets were found in a completely alien neutron star system. We have learned that roughly 1% of stars have extremely short-orbit giant planets dubbed "hot Jupiters" orbiting them (e.g. Dawson & Johnson, 2018). We have discovered what are likely molten lava planets (e.g. CoRoT-7 b (Léger et al., 2009; Queloz et al., 2009), Kepler-10 b (Batalha et al., 2011), and Kepler-78 b (Sanchis-Ojeda et al., 2013)), as well as puffed-up giants (e.g. Kepler-51 b, c, and d (Steffen et al., 2013; Masuda, 2014), and

Kepler-87 c (Ofir & Dreizler, 2013; Ofir et al., 2014)) with bulk densities similar to cotton candy. The most prevalent planets in the entire Galaxy appear to be in the super-Earth and sub-Neptune size range (Guo et al., 2019). All of these are planet archetypes that are completely lacking in our own solar system.

In conducting exoplanet searches, we have learned that there are likely more planets than stars in the Galaxy[2], meaning planetary systems are the rule rather than the exception. Our various exoplanet survey missions have been able to map out a wide range of parameter space where exoplanets appear to exist (e.g., Figure 1.1) and we are now able to discern trends for specific sub-populations. For example, we can distinguish the statistics of planets around different types of stars. A true "Earth2.0" would be a planet with Earth-like properties orbiting a Sun-like (or G-type) star. Small planets are common around G stars, peaking around 2–4 $R_\oplus$ before dropping off at larger radii (Foreman-Mackey et al., 2014). There also seems to be a shift in orbital period statistics for different planet sizes. For instance, small planets peak at specific periods ($\sim$ 20 days for 0.5–2$R_\oplus$, and $\sim$ 70 days for 2–8$R_\oplus$), whereas the occurrence rates for large planets ($>$ 8$R_\oplus$) appears to steadily increase out to several hundred days where our statistics become much poorer (Foreman-Mackey et al., 2014).

Based on their sheer numbers in the Galaxy and properties that facilitate planet detection (discussed later in Section 1.5.1), M dwarf stars have become a promising place to look for habitable rocky planets. A recent occurrence rate inquiry on close-orbiting rocky planets around mid-to-late M dwarfs reported $0.61^{+0.24}_{-0.19}$ terrestrial planets per star with radii above 0.5 $R_\oplus$ and periods between 0.4 and 7 days (Ment & Charbonneau, 2023). Interestingly, though terrestrial planets and larger sub-Neptunes are equally prevalent around G and K stars (Fulton et al., 2017), rocky planets outnumber sub-Neptunes around M-dwarfs, possibly by a ratio as high as 14:1 (Ment & Charbonneau, 2023). This follows a general trend of more rocky planets around less massive stars (Fulton & Petigura, 2018; Wu, 2019; Cloutier & Menou, 2020). There is also a tentative suggestion that terrestrial planet occurrence drops off for radii below 0.9$R_\oplus$, indicating that large rocky bodies could be more common than small ones (Ment & Charbonneau, 2023).

Despite the successes we have enjoyed, a number of questions remain uncertain and have proven challenging to address. One major collection of ideas that has social implications beyond simple astronomical curiosity: just how unique is Earth and life? How does our solar system fit into the grander picture of planetary systems? How common are Earth-like planets with habitable conditions? What makes a planet "habitable"? Will we be able to detect signatures of life on exoplanets? These are some far-reaching questions that do not yet have solid answers.

Questions surrounding the precise mechanisms for planet formation remain unclear. Two main avenues of formation have been proposed: A low-entropy ("cold-start") mechanism where planets are built up from smaller solid constituents via core accretion before capturing gas, or a high-entropy ("hot-start") mechanism where local instabilities allow for a direct collapse of protostellar

[2]https://exoplanets.nasa.gov/keplerscience/

disk material into large gas giants (Fortney et al., 2008; Baraffe et al., 2003; Chabrier et al., 2000). While both appear possible, it is not clear if one process dominates and under what specific conditions.

There also exists a curious gap in planet sizes around 1.8 times the mass of Earth (Fulton et al., 2017), dubbed the “Fulton gap". This may indicate a demarcation between large rocky planets and small gas-rich ones, but it is unclear whether planets rarely form at this size, or if (and how) they might evolve away from it once formed (Owen & Wu, 2017; Jin & Mordasini, 2018; Rogers & Owen, 2021; Gupta & Schlichting, 2019; Lee & Chiang, 2016; Lopez & Rice, 2018). Curiously, this gap seems to mostly vanish when looking at planets around low-mass stars (Cloutier & Menou, 2020). It has also recently been found that there is space for water-rich worlds with modest hydrogen envelopes to exist in this region (e.g., Piaulet et al., 2023). Many degeneracies exist between planetary composition and bulk density (e.g., Luque & Pallé, 2022), and atmospheric characterization may be required to break them.

Mapping out the distribution of many planets according to their parameters (e.g., radius, mass, orbit size, temperature, etc.) helps to define the edges of these distributions. However, care must be taken not to confuse a lack of detections for lack of planets in regions of parameter space where observing biases are strong. It can require care, diligence, and innovation to expand the detection limits past these hard-to-observe planets. Long-period ($\gtrsim$100 days) exoplanets are currently very challenging to access, despite their scientific value as atmospheric laboratories decoupled from stellar irradiation and as comparison points to our own solar system planets. They tend to fall through the cracks in most survey sensitivities and require a lot more effort to measure than their short-period counterparts. Fortunately, the field does not lack dedicated inquirers and talented innovators. These big questions and more are being tackled from many angles and progress is inexorable, if perhaps not always as fast as one might wish.

This thesis primarily focuses on using the transit method for exoplanet characterization, and participating in planet candidate follow-up efforts. While the main thrust is exoplanet transits, we employ and discuss several related and complimentary techniques as well. However, before detailing the doctoral thesis work, we begin with some discussion about the transit method itself and its relation with some other complementary science.

1.2. Background and History of Transits

1.2.1. A basis in binary star studies

The history of transit studies begins not with planets, but with binary stars. Some stars that orbit in binary pairs may, by their random orientation, periodically pass in front of and behind one another with respect to our viewing angle. Since binary stars can have size ratios near unity,

and dramatic differences in surface brightness, the amount of light blocked by a companion and corresponding flux received at Earth may modulate substantially, even to the naked eye.

Indeed, likely the first documentation of what is now known as an eclipsing binary variable dates back over 200 years. John Goodricke described in letters to a colleague the periodic brightness changes he had observed in the star Algol (Goodricke, 1783, 1784). However, a physical interpretation of the phenomenon did not arise until nearly 100 years later when Pickering (1880) proposed that the sequential eclipsing of two round bodies in mutual orbit could explain the observed variability of Algol. We now, of course, have exquisitely detailed measurements of Algol's variability (Figure 1.2).

The study of eclipsing binaries really began to take off several years later, at which time the first mathematical framework was developed by Henry Norris Russell and Harlow Shapley to quantitatively characterize any general eclipsing system (Russell, 1912a,b; Russell & Shapley, 1912b,a). Though effective in pushing the field forward, it made some oversimplifications regarding the stellar shapes and their surface intensity profiles.

A better strategy was introduced by Kopal and Piotrowski a few decades later (Kopal, 1941, 1946, 1948; Piotrowski, 1947, 1948). Instead of solving for exact solutions, they employed an iterative series of approximations. This allowed for less simplistic and more general formulations of the stellar shape, limb darkening profile (see Section 1.3.1 and Figure 1.6) and mutual illumination

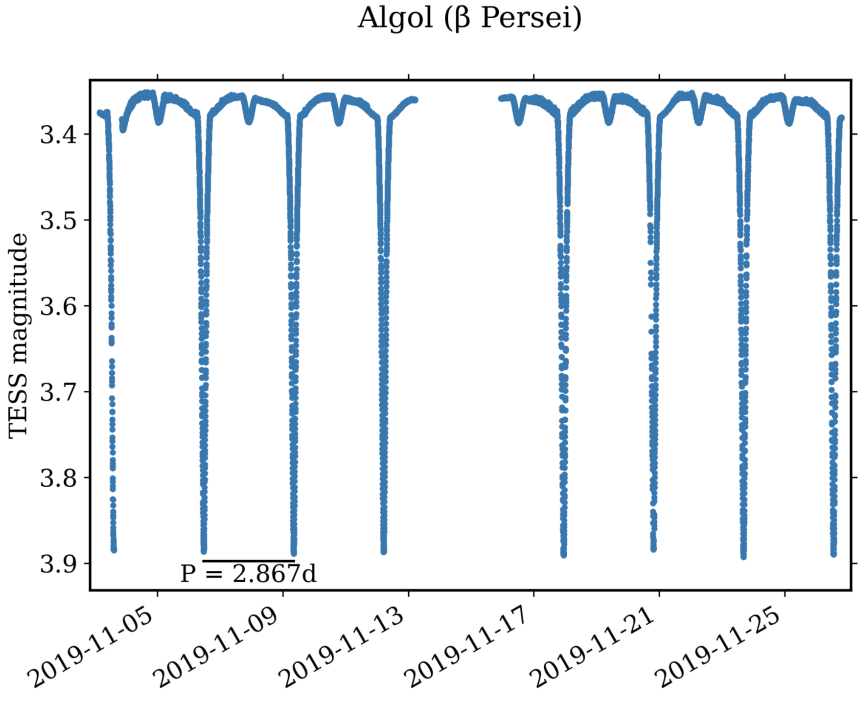

Fig. 1.2. Algol's light curve from the Transiting Exoplanet Survey Satellite mission. Deep flux drops indicate the brighter primary star being partially occulted whereas the reverse is true during the small flux drops.

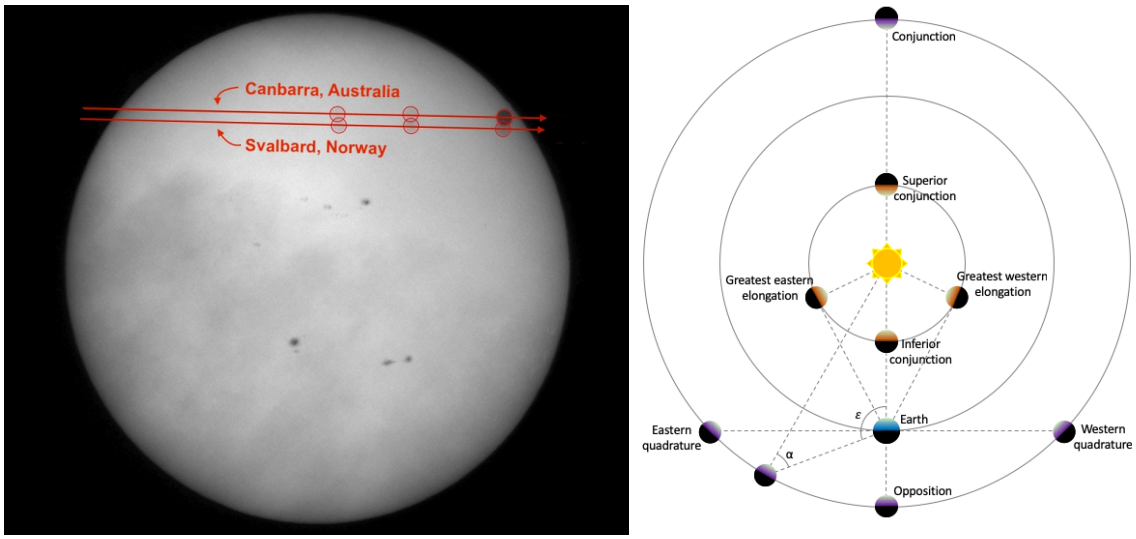

Fig. 1.3. *Left panel:* Venus' transit trajectory differs when viewed from widely separated latitudes[3]. *Right panel:* Schematic showing terms for orbital position relations. The elongation angle is ϵ and the phase angle is α.

of the stars. The iterative approach also quantified the uncertainty and stability of the solution, although the calculations involved proved to be a long and tedious process. With the advent and proliferation of "automatic computers", the calculations could be performed iteratively by a machine rather than searching for close-formed solutions (Huffer & Collins, 1962; Jurkevich, 1970; Linnell & Proctor, 1970; Budding, 1973; Soderhjelm, 1974). This set the groundwork for modern stellar eclipse codes, which themselves have since been modified to handle star–planet transits and eclipses.

1.2.2. First applications to planets

A ubiquitous difficulty encountered in astronomy is the challenge of observing objects and phenomena at extremely large distances. It should come as no surprise then, that planetary transits were first observed in our own solar system rather than in distant star systems. Mercury and Venus, having orbits interior to Earth, sometimes transit across the disk of the Sun and can be observed in great detail from Earth. These Sun-transiting events have proven very useful, not just as exoplanet transit analogues, but as astronomical events in and of themselves.

Indeed, observing the transit of Venus from different locations on Earth's surface is a relatively simple and accurate way to measure the astronomical unit. By observing the transit event from different locations, one can calculate a parallactic shift in Venus' trajectory across the solar disk. This parallax measurement provides an Earth–Venus distance at the point of inferior conjunction, i.e., when Venus is aligned directly between the Earth and the Sun. Knowing the Earth–Venus distance, and measuring Venus' angle of greatest elongation, a few steps of simple geometry and

[3] https://general-tools.cosmos.esa.int/vex/venus_transit.html

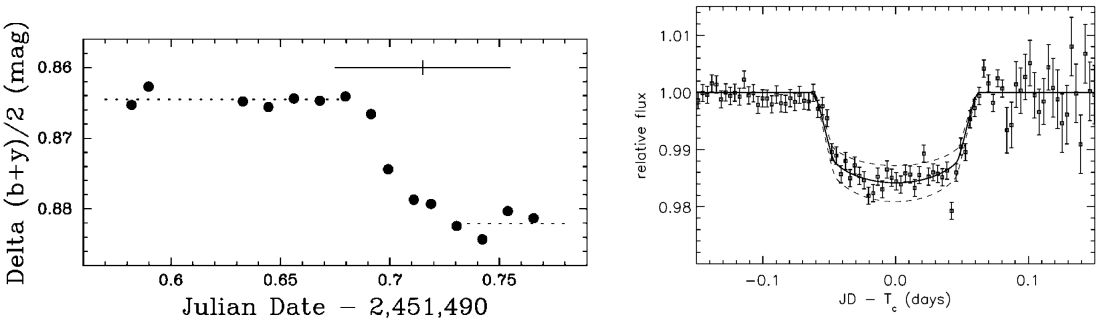

Fig. 1.4. Light curves of HD 209458 b first published by Henry et al. (2000) (left) and Charbonneau et al. (2000) (right), marking the first measured exoplanet transit.

trigonometry produce the Earth–Sun distance (~150 million kilometres). Figure 1.3 shows the parallactic shift in Venus' transit trajectory and also various definitions of planetary alignment.

Looking outside our solar system, the idea of discovering exoplanets via the transit method dates back as early as Struve (1952), and the first serious quantitative discussion of finding exoplanets this way was put forward by Rosenblatt (1971). The first true exoplanet transit measurements were of the planet HD 209458 b, with both Charbonneau et al. (2000) and Henry et al. (2000) publishing their detections in the same journal issue (Figure 1.4). This exoplanet was already known to exist as it had been previously discovered with RV measurements. The first discovery of a previously unknown exoplanet by the transit method was OGLE-TR-56 b (Udalski et al., 2002), detected by the Optical Gravitational Lensing Experiment (OGLE). Designed to look for the photometric variability of stars caused by gravitational lensing of small objects, OGLE was well suited to also detecting exoplanet transits. As detectors, telescopes, and techniques have improved we have been able to discover ever smaller exoplanets in ever larger quantities.

1.3. Geometry of Transits

1.3.1. Anatomy of a transit light curve

Unlike observing transits of our own solar system bodies, the host star is never spatially resolved when observing exoplanet systems. Instead of seeing a dark shadow move across a stellar disk, we only detect the small drop in the received starlight flux as the planet transits. Tracking this flux level over the duration of a transit produces a what is called a *transit light curve* which has several important features (see Figure 1.5).

The transit depth (ΔF) is how far the flux drops as a ratio of the unobstructed flux level. A deeper transit indicates that the relative size of the planet is larger. Typically, ΔF is on the order of $\sim 1\%$ for large exoplanets, and much lower for smaller ones. There are, in general, four particular times of interest along the light curve that are called contact points. The time of first contact (t_I) marks when the planet first encounters the stellar disk and the light curve first begins to drop. This

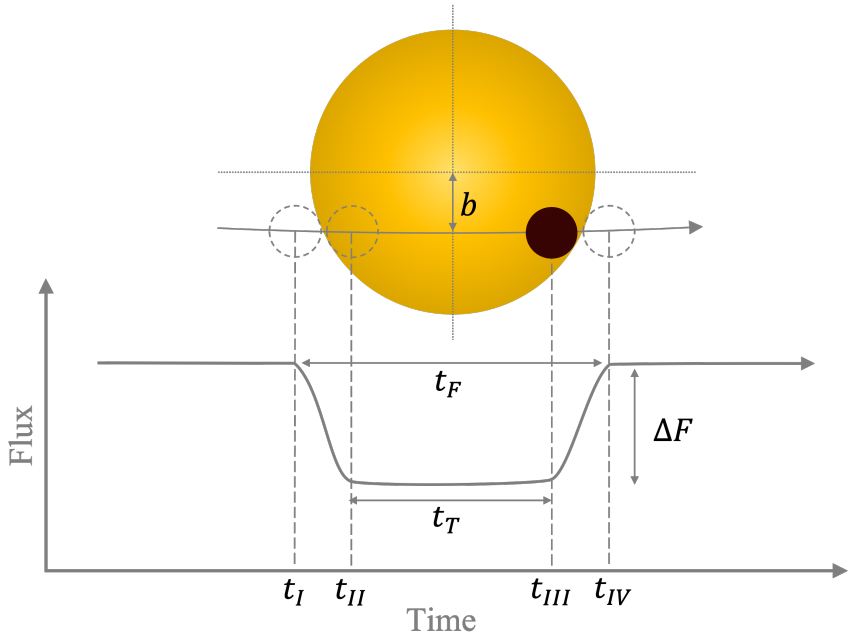

Fig. 1.5. As the planet crosses the stellar disk, the shape of the time-variable flux drop is determined by characteristics of the star, the exoplanet, and its orbit. The transit depth (ΔF) and four "contact points" (t_{I-IV}) are important values for characterizing the system.

is the beginning of the *ingress* of the planet. Second contact (t_{II}) is defined by the flattening of the curve and marks when the planet is, in projection, fully within the stellar disk. This point marks the end of the ingress period. The third and fourth contacts (t_{III}, t_{IV}) are the reverse of the first two, tracing the *egress* of the planet from the stellar disk.

The impact parameter (b) is the fractional projected distance the transit trajectory takes from the centre of the star's disk (Figure 1.6, left panel). For example, a perfectly edge-on system will have a planet pass directly through the centre of the stellar disk, giving an impact parameter of $b = 0$. Tilting the orbit away from this orientation increases b. As $b \rightarrow 1$, the planet just grazes the edge of the stellar disk. In such grazing transits there may not be distinct t_{II} and t_{III} locations on the light curve. If the planet does not fully enter the disk of the star, we observe only a smooth U-shaped dip in the flux from t_I to t_{IV}. Grazing transits are much more common in binary star systems where the relative sizes of the objects are more similar, but it can still occur in systems where the size ratio is very unbalanced.

Another factor in the shape of the light curve, is fact that the projected disk of a star may not be uniformly illuminated. For instance, the phenomenon of *limb darkening* causes the intensity of the stellar disk to drop towards its edge (or "limb") which occurs to varying degrees depending on the type of star. Limb darkening is the result of gas opacity in the outer regions of the star. If one considers the typical path length that a photon can travel in the outer layers of the star, the photons emitted towards the observer from the centre of the star originate from a deeper and hotter layer than photons emitted from the limb. Therefore the centre of the stellar disk appears somewhat brighter

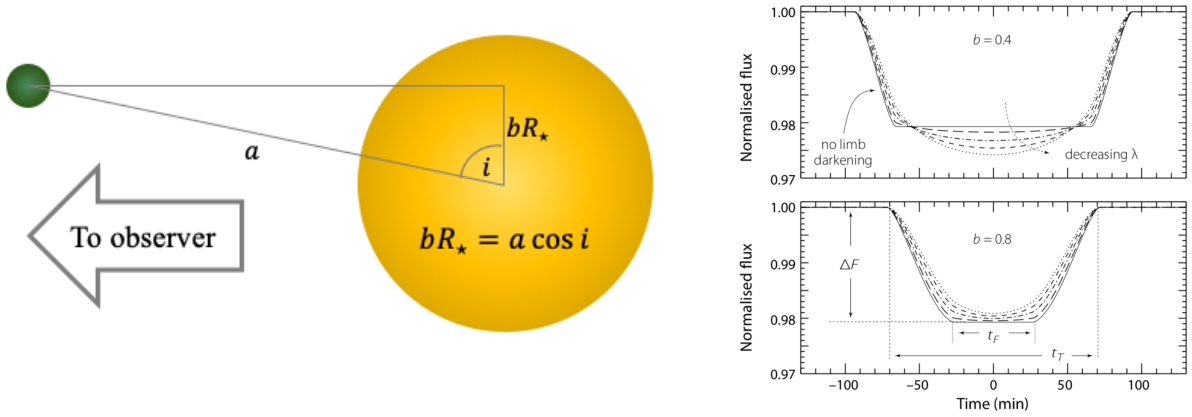

Fig. 1.6. *Left panel:* Geometric interpretation of the impact parameter, b. *Right panel:* Comparing the similar smoothing effect of impact parameter and limb darkening. Figure from Perryman (2018a), adapted from Seager & Mallén-Ornelas (2003).

and hotter. Unfortunately, the effect on the observed transit light curve is very similar to that of a large impact parameter: it rounds out the otherwise sharp corners and makes determinations of t_{I-IV} less clear (Figure 1.6, right panel).

The resulting impact parameter–limb darkening degeneracy typically requires multi-wavelength observations to break. Though strong limb darkening and a high impact parameter both work to soften the sharp edges of a transit light curve, only the effect of the impact parameter is achromatic. The optical depth through the outer gas of the star depends on wavelength, and so the limb darkening profile will as well. The impact parameter is a purely geometric effect and will remain largely unchanged at different wavelengths. This differing behaviour can be used to break the degenerate effects.

1.3.2. Transit probability

Though it has proven itself to be a powerful exoplanet detection and characterization tool, one of the major drawbacks the transit technique suffers from is the low probability that any given exoplanet system is appropriately oriented with respect to our sight line. Without an inclination (the angle between our line of sight and the exoplanet's orbital axis) sufficiently close to 90°, no transit is visible at all.

Making the assumption of a circular exoplanet orbit and a small exoplanet size, we can carry out a very simple calculation of the transit probability (see Figure 1.7). By simple geometry, the exoplanet casts a shadow in the angular region of $2\theta = 2R_\star/a$ behind it. Since this angle is constant if the orbit is circular, we simple multiply by 2π to find the band of solid angle the planet traces out during one full orbit ($4\pi R_\star/a$). Assuming a totally random inclination angle with respect to our line of sight, the probability that an observer will be able to see a transit is simply the solid angle of the transiting band divided by the solid angle of the full sky sphere (4π). The probability works

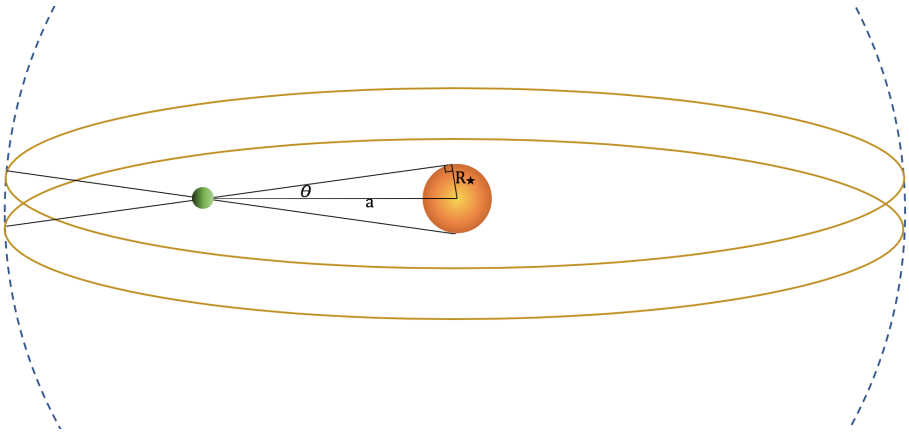

Fig. 1.7. The “shadow" cast by a planet traces out a swath of solid angle across the sky. The geometric transit probability is the fraction this band makes of the whole sky.

out to be the simple ratio of the star size and the orbit size: $P = R_\star/a$. A larger star and a tighter orbit contribute to a higher transit probability. Rewritten into more conventional units,

$$P \approx 0.005 \left(\frac{R_\star}{R_\odot}\right) \left(\frac{a}{1\text{au}}\right)^{-1}, \tag{1.3.1}$$

the probability of a transit is clearly very low for systems similar to the Earth–Sun system.

1.3.3. Realistic dependencies

In more realistic scenarios, the transit probability is less straightforward. Orbits are not perfectly circular, but belong to a family of ellipses. Fully specifying an orbiting system in space requires a set of six parameters. Two of the parameters describe the size and shape of the orbit (a, the semimajor axis and e, the eccentricity). The others describe the orientation of the system with respect to a reference direction (often our line of sight), and the location of the orbiting body along the ellipse. The inclination (i), longitude of the ascending node (Ω), argument of pericentre (ω), and true anomaly (ν) are shown in Figure 1.8.

Any eccentricity in the planet’s orbit causes the planet–star distance to change over the course of one period. Accordingly, the solid angle swath traced out by the planet’s shadow is non-uniform in angular size. The range of inclinations that a transit is observable from is greatest in the direction of the pericentre location (where the planet is at its closest approach to the host star) and is smallest in the direction of the apocentre location (where the planet is at its greatest separation from the host star). The non-uniformity of the transiting regions for an eccentric orbit is displayed in Figure 1.9

This non-uniformity means the argument of pericentre (ω, which defines the location of pericentre) plays a role in defining the transit probability for a given observing direction. If pericentre is aligned toward the observer, transit probabilities are higher than if some other phase (especially apocentre) is aligned with the observer. This will cause us to detect more systems with pericentre aligned towards us than any other direction which is not representative of a random population.

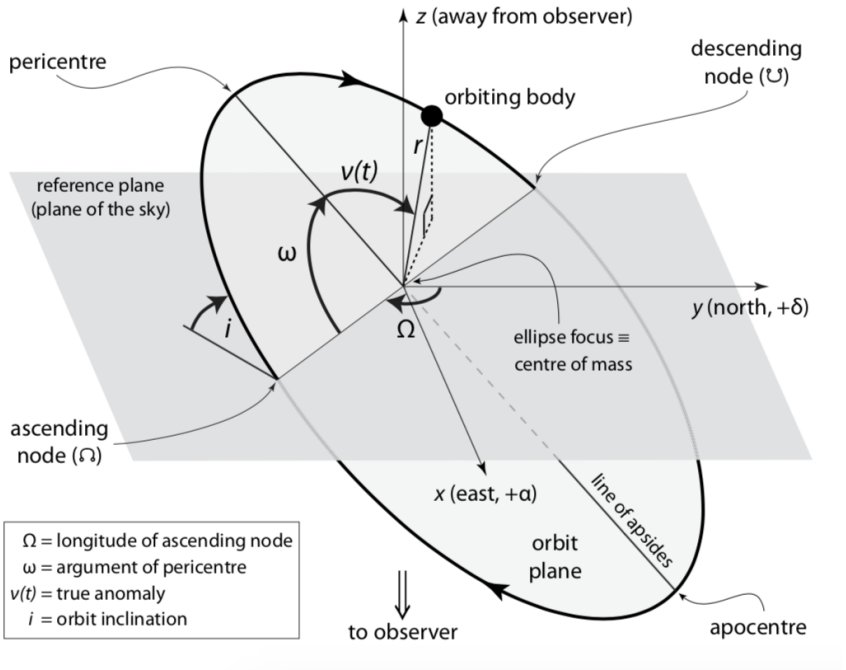

Fig. 1.8. Schematic of parameters used to fully describe an orbital system. Figure from Perryman (2018a).

To calculate the specific transit probability of an eccentric system being visible from anywhere on the sky, one must carry out a full integral over the orbit using the expression

$$r(\nu) = \frac{a(1-e^2)}{1+e\cos\nu}.$$

An additional consideration is the finite size of the planet. There are viewing angles from which the observer can only see a grazing transit. The probability of a full transit is smaller than the probability of seeing any kind of transit signal due to these grazing zones.

1.4. Information Available from a Transit Light Curve

1.4.1. Using photometry alone

Upon measuring a transit light curve, there are generally four principal observables that can be immediately extracted: the period of the orbit P, the depth of the transit ΔF, the interval between the first and fourth contacts $t_T = t_{IV} - t_I$ (i.e., the whole transit duration), and the interval between the second and third contacts $t_F = t_{III} - t_{II}$ (i.e., the duration that the transit is at its full depth). These four observables can be used to create geometrical equations that relate other features of the transiting system. The geometries and formulations are more thoroughly discussed in Seager & Mallén-Ornelas (2003) and Perryman (2018a), but a brief coverage is provided below.

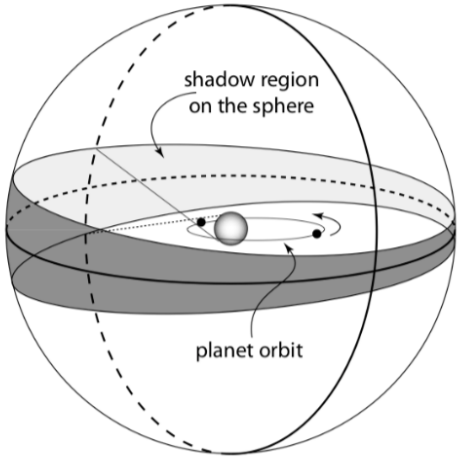

Fig. 1.9. When the planet has nonzero eccentricity, the varying distance from the host star produces a "transit shadow" that depends on orbital phase. Figure from Perryman (2018a), adapted from Barnes (2007).

First of all, P is not well-constrained by a single transit measurement, but by measuring the time separating subsequent detections. One must be careful that transits were not missed between two separated observations, otherwise various $P = P_{\rm measured}/n$ (where n is an integer) aliases remain possible.

The flux drop is simply the fraction of the cross-sectional area of the host star that is covered by the transiting body,

$$\Delta F = \left(\frac{R_p}{R_\star}\right)^2 \tag{1.4.1}$$

(Perryman, 2018a). This, of course, assumes a uniformly intensity of stellar surface, which isn't exactly true. However, it provides a reasonable approximation.

The total transit duration t_T is equal to the fraction of the orbital period where the projected distance between the planet and stellar centres are less than $R_\star + R_p$ (see Figure 1.10):

$$\sin(t_T\pi/P) = \frac{R_\star}{a}\left[\frac{[1+(R_p/R_\star)]^2 - [(a/R_\star)\cos i]^2}{1-\cos^2 i}\right]^{1/2}, \tag{1.4.2}$$

(Sackett, 1999). A similar calculation can be done for the duration of full transit, t_F, the difference being the boundaries are marked by when the separation between the planet and stellar centres are less than $R_\star - R_p$. The result simply exchanges the "+" for a "−" in the first bracketed term. It has been written in fractional form with Eq. 1.4.2 to remove some common coefficients:

$$\frac{\sin(t_F\pi/P)}{\sin(t_T\pi/P)} = \left[\frac{[1-(R_p/R_\star)]^2 - [(a/R_\star)\cos i]^2}{[1+(R_p/R_\star)]^2 - [(a/R_\star)\cos i]^2}\right]^{1/2}. \tag{1.4.3}$$

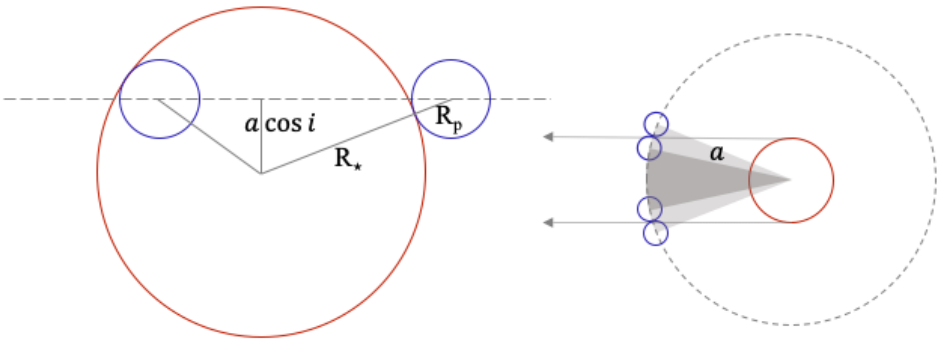

Fig. 1.10. Calculating the duration of the transit (full or partial) involves the fraction of the orbit where the projected disks of the planet fully or partially overlap. *Left panel:* Transit observer's perspective. *Right panel:* Top-down view of orbit.

In addition to these three geometric equations, two physical equations complete the set that is needed to ascertain the available parameters of the system. Kepler's third law helps by relating the period, semi-major axis, and stellar mass (using the approximation of $M_\star \gg M_p$)

$$P^2 = \frac{4\pi^2 a^3}{G(M_\star + M_p)} \approx \frac{4\pi^2 a^3}{G M_\star}, \tag{1.4.4}$$

and the final piece needed is the stellar mass–radius relationship,

$$R_\star = k M_\star^x. \tag{1.4.5}$$

Here, the coefficient k and power-law index x are dependent on the type of star (e.g. main sequence, giants, etc.).

With these five equations, the five unknown parameters ($M_\star, R_\star, a, i$, and R_p) can ultimately be found, though there are useful physical quantities that can be derived from just the first four relations (Eqs. 1.4.1–1.4.4) and the four measured quantities $P, \Delta F, t_T$, and t_F.

A trivial rearranging of Equation 1.4.1 provides the simple relation of,

$$\frac{R_p}{R_\star} = \sqrt{\Delta F}. \tag{1.4.6}$$

Recall that, strictly speaking, this requires the assumption of a uniformly illuminated stellar disk (i.e., neglecting limb darkening). The impact parameter (b) can be obtained from observed quantities by combining Equations 1.4.3 and 1.4.6,

$$b \equiv \frac{a}{R_\star}\cos i = \left[\frac{(1-\sqrt{\Delta F})^2 - [\sin^2(t_F\pi/P)/\sin^2(t_T\pi/P)](1+\sqrt{\Delta F})^2}{1 - [\sin^2(t_F\pi/P)/\sin^2(t_T\pi/P)]}\right]^{1/2}. \tag{1.4.7}$$

The orbit's semi-major axis in units of stellar radii ($a/R_\star$) can be extracted from Equations 1.4.1 and 1.4.2,

$$\frac{a}{R_\star} = \left[\frac{(1+\sqrt{\Delta F})^2 - b^2[1-\sin^2(t_T\pi/P)]}{\sin^2(t_T\pi/P)}\right]^{1/2}. \tag{1.4.8}$$

Finally, and perhaps surprisingly, the bulk density of the star can be constrained by the observables using Kepler's third law (Equation 1.4.4, assuming $M_p \ll M_\star$) and Equation 1.4.8:

$$\rho_\star \equiv \frac{M_\star}{R_\star^3} = \left(\frac{4\pi^2}{P^2 G}\right)\left[\frac{(1+\sqrt{\Delta F})^2 - b^2[1-\sin^2(t_T\pi/P)]}{\sin^2(t_T\pi/P)}\right]^{3/2}. \tag{1.4.9}$$

The equations listed above take on more simplified forms under the assumption of $R_\star \ll a$. This is equivalent to the statement $t_T\pi/P \ll 1$, in which case $\sin(t_T\pi/P) \approx t_T\pi/P$ (and similarly for t_F, which is smaller than t_T) (Seager & Mallén-Ornelas, 2003; Perryman, 2018a).

Finally, with these useful quantities calculated, we are in position to determine the five physical parameters. It is at this point where we need to invoke the stellar mass–radius relation despite its accompanying empirical uncertainty. Putting Equation 1.4.9 in solar units, $\rho_\star/\rho_\odot \equiv M_\star/M_\odot(R_\star/R_\odot)^{-3} = k^{-3}(M_\star/M_\odot)^{1-3x}$, we can determine the stellar mass,

$$\frac{M_\star}{M_\odot} = \left(k^3\frac{\rho_\star}{\rho_\odot}\right)^{1/(1-3x)}. \tag{1.4.10}$$

The stellar radius is then easily extracted via the mass–radius relation,

$$\frac{R_\star}{R_\odot} = k\left(\frac{M_\star}{M_\odot}\right)^x = \left(k^{1/x}\frac{\rho_\star}{\rho_\odot}\right)^{x/(1-3x)}. \tag{1.4.11}$$

Obtaining the orbital radius from Kepler's third law becomes trivial now that we have expressions for the stellar mass (again assuming $M_p \ll M_\star$),

$$a = \left(\frac{P^2 G M_\star}{4\pi^2}\right)^{1/3}. \tag{1.4.12}$$

The inclination is a simple rearrangement of the impact parameter equation (1.4.7) now that $R_\star/a$ and b are known,

$$i = \cos^{-1}\left(b\frac{R_\star}{a}\right), \tag{1.4.13}$$

and most importantly for many researchers of exoplanets, the planetary radius can be extracted from the definition of ΔF:

$$\frac{R_p}{R_\odot} = \frac{R_\star}{R_\odot}\sqrt{\Delta F} = \left(k^{1/x}\frac{\rho_\star}{\rho_\odot}\right)^{x/(1-3x)}\sqrt{\Delta F}. \tag{1.4.14}$$

Everything calculated up to this point has been under the assumption of a circular orbit ($e = 0$), which is not totally accurate, but the majority of confirmed exoplanets have low eccentricity[4] so

[4] https://exoplanetarchive.ipac.caltech.edu/index.html

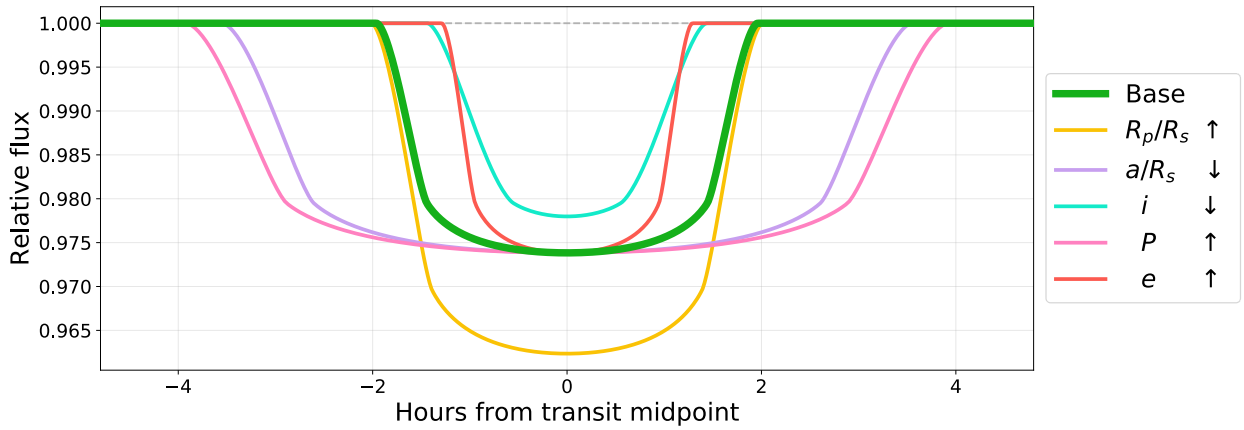

Fig. 1.11. Examples of transit light curves calculated from parameters T_0, P, $R_p/R_\star$, $a/R_\star$, e, and ω. Parameters are varied one parameter at a time compared to the base model (thick green). There is a complex interplay, not shown here, between e and ω on the transit shape. The e,ω interplay affects the velocity of the planet, and also the star–planet distance (and thus alignment) during the transit. Limb darkening has been kept constant in these examples.

the approximation can be useful. With an enormous amount of algebra, these equations can be generalized to any eccentricity (e.g. see Appendix A of Kipping, 2008).

One might note that obtaining physical units for these exoplanet and orbit quantities requires some knowledge about the stellar mass and radius. In making transit measurements, but also more generally in other areas of exoplanet research, the oft-touted aphorism of "*know thy star, know thy planet*" holds a lot of weight for the outcomes. In the formulations listed above, we use the empirical mass–radius relation (Eq. 1.4.5) for this information. On a case-by-case basis, it can often be more beneficial to use external observations to characterize the star in question. These often take the form of spectroscopic measurements and modeling to constrain stellar properties.

Nowadays, a plethora of modern software tools are available that do all of these calculations in the background while allowing a researcher to work with just the physically relevant parameters. Transit light curve models can then be generated directly from the desired physical and orbital parameters (see Figure 1.11). Some equivalent substitutions can be made in the particular basis set of parameters that uniquely describe a transit's shape, but the set of T_0 (transit midpoint), P, $R_p/R_\star$, $a/R_\star$, e, ω, and i, plus a description of the stellar limb darkening profile is perhaps the most straightforward. Other parameterizations might be used for more efficient parameter space sampling, or because a prior constraint is known on some other related quantity. Normal practice is to fit a transit model generated by these parameters directly to the acquired data. This is often carried out through statistical techniques like Markov chain Monte Carlo (MCMC) or nested sampling. These not only provide the best-fitting transit model, but map out the uncertainty and correlation of the parameters.

1.4.2. Combining transit photometry and radial velocity observations

RV measurements of an exoplanet system provide valuable data on their own, but are also extremely complementary to transit observations. The basic tenet behind RV determination is that a planet does not simply orbit a star that is fixed in place. Because the planet itself has mass, the star and planet mutually orbit a common centre of mass, or barycentre. While the reflex motion of the star due to a planet is small owing to an unbalanced mass ratio, it is often sufficient for detection by sensitive velocimeters. Such instruments measure the Doppler shift of the star's spectral lines as it wobbles toward and away from the observer over the course of the orbital period.

The following formulations are covered more fully in Perryman (2018a, Ch. 2.1) and Wright & Gaudi (2013), but we will summarize them here. Geometry defines the line of sight coordinate, z, using the time-varying barycentric distance, $r(t)$, and other angular orbital elements. It and its time derivative can be expressed as,

$$\begin{aligned} z &= r(t) \sin i \sin(\omega + \nu), \\ v_r \equiv \dot{z} &= \sin i [\dot{r} \sin(\omega + \nu) + r\dot{\nu} \cos(\omega + \nu)]. \end{aligned} \tag{1.4.15}$$

Some algebraic substitutions for r and $\dot{r}$ lead to,

$$v_r = K[\cos(\omega + \nu) + e \cos \omega], \tag{1.4.16}$$

where,

$$K \equiv \frac{2\pi}{P} \frac{a_\star \sin i}{\sqrt{1 - e^2}}, \tag{1.4.17}$$

is called the radial velocity "semi-amplitude". For circular orbits ($e = 0$), the RV signal is clearly sinusoidal with semi-amplitude K. When eccentricity is non-zero, the signal can be substantially skewed and distorted depending on the orientation of pericentre described by ω. The semi-amplitude is attenuated by any deviation from $i = 90°$, as the line-of-sight velocity component shrinks if the orbital plane is not viewed edge-on. The magnitude of K is also determined by the relative masses of the two bodies and their separation, though this is more easily seen if we expand the expression for P, as follows.

Since the RV technique aims to measure the motion of the star due to the planet, it is instructive to re-write Kepler's third law in the barycentric frame of reference. The typical $P^2 = 4\pi^2 a^3 / [G(M_\star + M_p)]$ form uses $a = a_\star + a_p$ where $a_\star$ and a_p are, respectively, the orbital sizes of the star and the planet around the barycentre. These individual semi-major axes are related to the object masses and combined semi-major axis by,

$$a_\star = \frac{M_p}{M_\star + M_p} a, \quad \text{and} \quad a_p = \frac{M_\star}{M_\star + M_p} a. \tag{1.4.18}$$

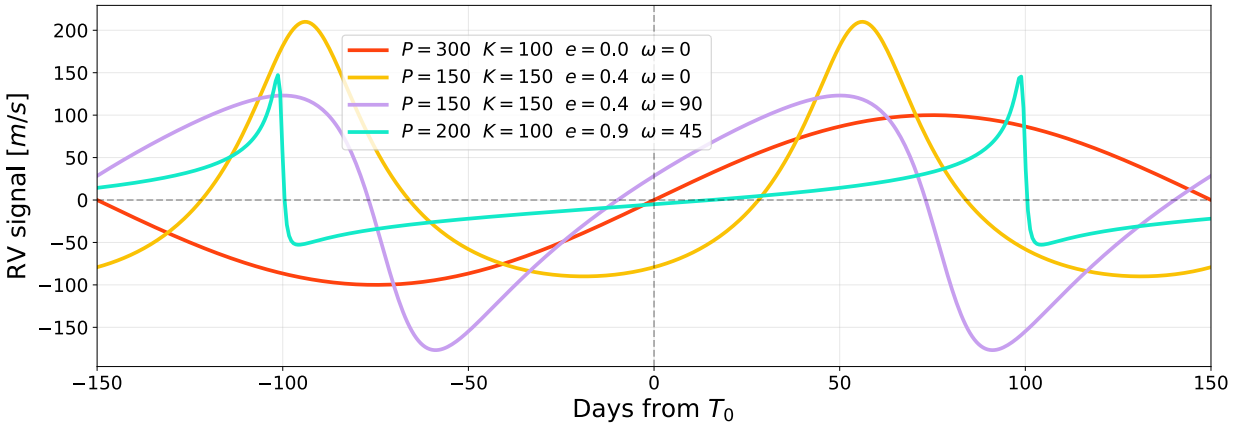

Fig. 1.12. Examples of RV curves calculated from parameters P, T_0, e, ω and K, where P is in days, ω is in degrees, and K is in m/s. Simply changing viewing angle (ω) and no other parameters can produce substantial changes in the RV curve (orange vs. purple curves). Deviations from $e = 0$ produces a non-sinusoid shape, as is evident in Equation 1.4.16.

Combining Equation 1.4.18 (for $a_\star$) and Kepler's third law with Equation 1.4.17 produces a more insightful form for the (squared) semi-amplitude,

$$K^2 = \frac{G}{(1-e^2)} \frac{1}{a_\star \sin i} \frac{M_p^3 \sin^3 i}{(M_\star + M_p)^2}. \tag{1.4.19}$$

An $a_\star \sin i$ term is kept in the denominator because neither $a_\star$ nor $\sin i$ can be uniquely determined on their own from an RV data set, but their combination can be constrained via P and e (Eq. 1.4.17). A quantity called the "mass function" ($\mathcal{M}$) is defined such that it isolates observables on one side and unknowns on the other,

$$\mathcal{M} \equiv \frac{M_p^3 \sin^3 i}{(M_\star + M_p)^2} = \frac{K^2(1-e^2)}{G}(a_\star \sin i) = \frac{PK^3(1-e^2)^{3/2}}{2\pi G}, \tag{1.4.20}$$

where the final expression comes from substituting $a_\star \sin i$ from Equation 1.4.17. The mass function is a very useful quantity for constraining the component mass ratio of the system.

On its own, an RV curve with sufficient data coverage will provide measures of P, K, e, ω, ν and $a \sin i$ based on its shape and phase (Figure 1.12). Unfortunately, without additional measurements, the absolute masses and semimajor axes of the star and planet remain confounded with one another and with the unknown inclination of the system. This is where the synergy between RV and transit studies comes into play.

Exoplanets that have been identified via transit surveys are already prime candidates for RV followup. By definition, a planet that transits has an inclination close to 90° which maximizes the RV signal and strongly constrains the $\sin i$ uncertainty. Furthermore, if an estimate of the stellar mass can be made by other means (e.g. its spectral type and luminosity class, or through transit observables and the mass–radius relation) then the RV mass function can be used to solve for

the planet mass itself. This planet mass, coupled with the planet radius obtained from the transit data together provide the bulk planet density, a glimpse into the composition of the distant planet. In fact, the only orbital parameter that is not determinable by the transit+RV combination is the longitude of the ascending node (Ω, the orientation angle on the plane of the sky). This remains unconstrained because the rotation of a system around the line of sight axis has no effect on either transit light curve or the radial velocity components. This final parameter must be obtained through other techniques such as astrometry, which involves actually seeing the motion of the star on the plane of the sky.

1.5. Pitfalls of the Transit Method

1.5.1. Intrinsic biases

We have already discussed the general low transit probability that limits the transit detection method, but there are also intrinsic biases that affect the types of exoplanet systems that are most likely to be detected. Detector precision limitations restrict how shallow of a transit can be detected in a light curve, favouring larger planets around smaller stars. In addition, not only do long-period planets have lower transit probabilities, but they are simply less likely to produce transits in a given survey's operational time interval. This leads to poorly sampled or even entirely missed long-period planets. Singular transits cannot provide a robust period estimate and require substantial follow-up effort to verify.

These two biases have led to a shift in the search for habitable worlds from Sun-like stars to small, cool red dwarfs. M-dwarfs make up the large majority of stars in the Galaxy, and their small size and mass contribute to both stronger transit and RV signals for a given orbiting planet, respectively. Because of their low luminosity, their habitable zones (where liquid water may exist) are much closer to the star, leading to short periods and increased observability. There are other unsettled questions regarding the role of M-dwarfs activity and high-energy flux on true habitability (e.g. Buccino et al., 2007; Sanz-Forcada et al., 2010; Ranjan et al., 2017; Bolmont et al., 2017; Dong et al., 2018) but from a detectability is standpoint, the best place to look for an Earth-sized habitable zone planet may be around very cool stars.

1.5.2. False positive detections

There are several types of astrophysical false positives that can mimic an exoplanet transit in an observed light curve. The light curves of grazing stellar binaries can commonly trigger a detection flag in surveys searching for exoplanet transits. Though the transiting star is much bigger than a planet, only a fraction of it actually blocks any starlight and so it may display a ΔF drop of similar magnitude as would be expected for an exoplanet. While potentially useful discoveries in their own right, grazing stellar binaries constitute a source of noise in the pipelines dedicated to exoplanet

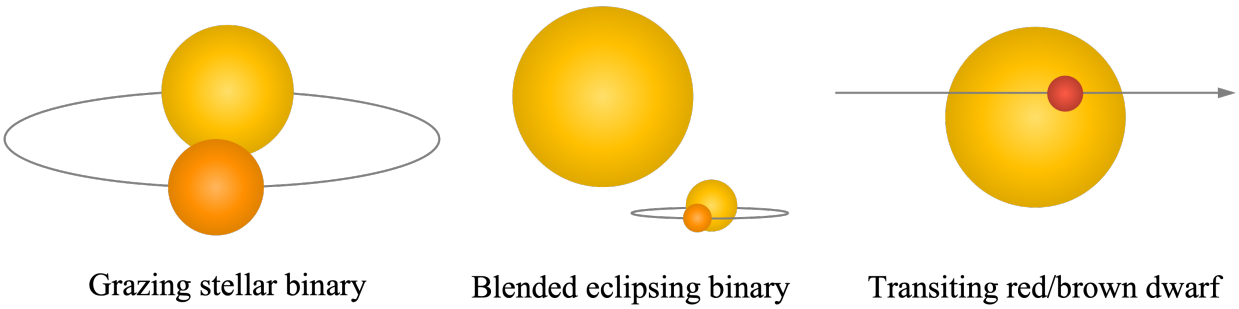

Fig. 1.13. Three potential causes of false-positive transit detections.

discovery. Fortunately, this type of false positive can often be identified by their V-shaped light curve with no clear end of ingress or beginning of egress (because contact points t_{II} and t_{III} do not exist). If one is able to constrain the limb darkening of the star via other means to be inconsistent with such a gradual flux change, this false positive could be rejected with even more confidence.

Another source that can produce exoplanet-like transit light curves are blended stellar binaries. In this case, the single source on the instrument's detector is actually composed of three unresolved stars: an eclipsing binary pair, and a solo star. These stars might either be bound together as a hierarchical triplet, or simply share a line-of sight position on the sky. The binary pair would normally show a deep ΔF if they were observed on their own, but the solo star adds its own flux to the measurement, diluting the fractional ΔF we observe to a depth consistent with an exoplanet. Unlike the grazing binary false positives discussed previously, this scenario may retain the sharp light curve contact points that mark a full ingress and egress. To combat this type of false positive, one can make a probabilistic estimate on the odds that there is a blended binary hidden in the point spread function based on stellar density and binary rates in the field, or acquire high spatial resolution images of the target's surroundings to rule out or account for optical neighbours.

Such high-contrast imaging usually takes the form of adaptive optics (AO) or speckle imaging. In AO systems, incoming light wave-fronts distorted by Earth's atmosphere are corrected in real-time using very fast feedback loops and deformable mirrors. The correction can achieve diffraction-limited imaging, even when peering through the turbulent atmosphere. Speckle imaging does not involve real-time correction, but takes images at a very rapid cadence so that the ever-changing "speckle" pattern caused by the atmosphere distortion is temporally resolved. The images can be speckle-subtracted or cross-correlated after the fact to search for sources at high spatial resolution. Use of these techniques is fairly standard practice in following-up an exoplanet candidate. They can resolve angular separations of $\sim 0\farcs1$, dramatically reducing the PSF size and limiting the area for potential blends. If no nearby source is detected, the blend probability substantially decreases given the small PSF size. If a nearby companion (bound or in projection) is detected, the additional flux dilution can be accounted for in the planetary radius estimate.

Other small objects transiting the host star can look like exoplanet transits. Low mass red and brown dwarfs are not substantially bigger than the largest exoplanets (Chabrier et al., 2009). Since transit photometry only produces the $R_p/R_\star$ ratio, one needs to characterize the host star to be able to set a physical size to the transiting body. Additional radial velocity measurements may be required to find a mass for the transiting object and determine if it is planetary in nature or not.

The three false-positive scenarios above are all the result of real transiting events, though not of exoplanets. Qualities of the star itself may provide additional false triggers if it produces some intrinsic photometric variability. Long-lived, dark star spots traverse across the disk of a rotating star and may produce a periodic flux drop (Perryman, 2018a). However, star spots are generally non-permanent and non-static features, and their projected area on the stellar disk from the observer's perspective is not constant since they are a feature of the stellar surface. This may give the "transit" a strange shape that changes between periods. Stellar activity in general can produce quasi-periodic signals that may mimic transit signals in some cases.

1.6. Transit Timing

Beyond merely measuring the photometric changes of a transiting system, the precise timing between transits can be measured once several transits have been observed. Characterizing small deviations from a constant period (transit timing variations; TTVs) or deviations in transit duration (transit duration variations; TDVs) can provide information on other dynamics that are taking place in the distant system.

The most frequently discussed causes of TTVs/TDVs are generated through direct planet-planet interactions. They can provide evidence of and information on additional unseen planets in the system that may be invisible to other detection methods. The effects can be especially large if the two planets orbit near a mean-motion resonance (Lithwick et al., 2012), i.e., when the ratio of their periods is close to a ratio of small integers. Long-term interactions between the two orbits induce transit timing and duration oscillations with characteristic timescales of tens, to hundreds, or even thousands of orbital periods. This "super-period" is dependent on the specific orbital periods involved and how close they are to resonance (Deck & Agol, 2015). Like many resonant systems, the amplitude can become very high when close to perfect resonance (Deeg & Belmonte, 2018, Ch. 37). A much shorter time scale effect also occurs due to synodic interactions every orbit. Dubbed a "chopping" signal, this effect is of much smaller amplitude than the super-period signal, but tends to act over just a couple of orbits (Figure 1.14). The full TTV and TDV model can be generated over a chosen interval of time by numerically integrating the gravitational equations of motion given some fixed parameters of the system.

Planet–planet interactions are not the only causes of TTVs/TDVs. Very large variations are seen in circumbinary exoplanets—planets orbiting a pair of binary stars. Because the binary host stars physically move about the system barycentre, sometimes the transiting planet will cross the

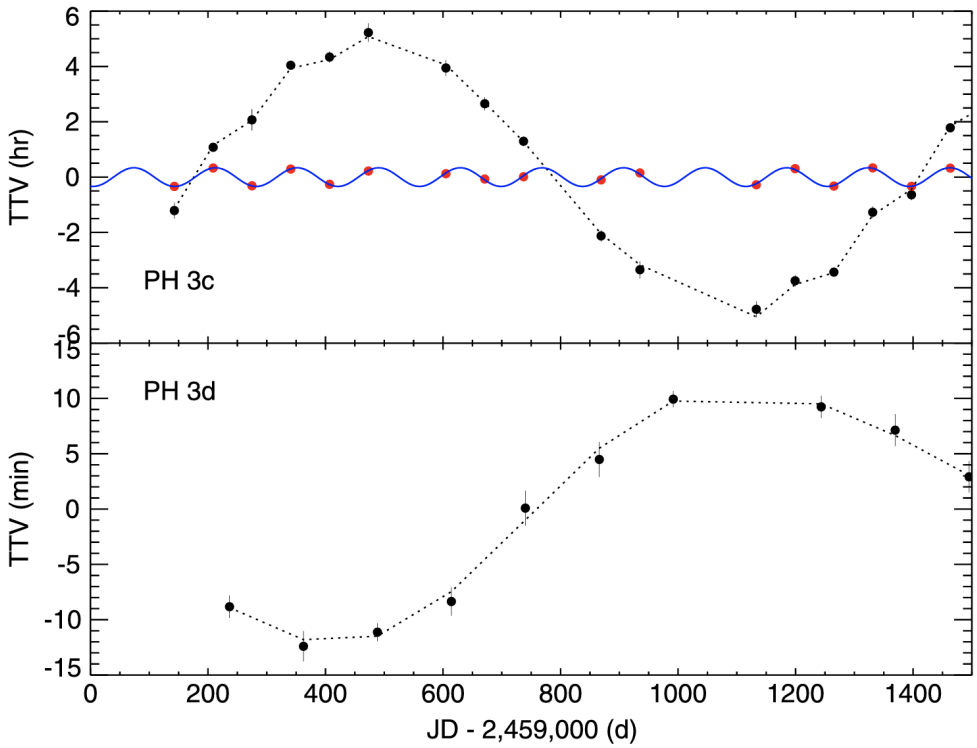

Fig. 1.14. TTV analysis of planets PH 3c and PH 3d (a.k.a Kepler-289 c and d). Transit timing measurements (black dots) trace a slow and large-amplitude super-period with a superimposed low-amplitude and high-frequency chopping signal component (shown isolated in blue and red). Original figure from Deck & Agol (2015).

stellar disk earlier or later than in other orbits (TTVs). Varying relative velocities between the planet and the host star can also change the amount of time the planet spends in transit (TDVs). The inner binary may also induce precessional effects on the transiting planets, directly altering its orbit (Armstrong et al., 2013). This concept holds for large inner planets instead of a second star as well, though with accordingly smaller amplitude.

It also stands to reason that a sizeable moon around the exoplanet (exomoon) may pull the planet off-course causing TTVs and/or TDVs. With enough photometric sensitivity in a transit observation, one may be able to see the additional ΔF added by the exomoon blocking the starlight as well. An exomoon claim of this type was put forward by Teachey & Kipping (2018), though it is has been contested (e.g. Kreidberg et al., 2019; Heller et al., 2019).

A number of additional dynamical phenomena can theoretically induce TTVs and TDVs including the oblateness of the host star, tidal forces or relativistic precession acting on close-orbiting planets, as well as eccentricity and inclination variation from secular precession (Deeg & Belmonte, 2018, Ch. 37). Indeed, even the relative motion between the Earth and the observed system can impose TTVs/TDVs. If the exoplanet system is very close to Earth and moving with a very large proper motion (i.e., tangential motion across the plane of the sky) the observer may be viewing it from a slightly different angle from one transit to the next. A similar effect can arise from the motion

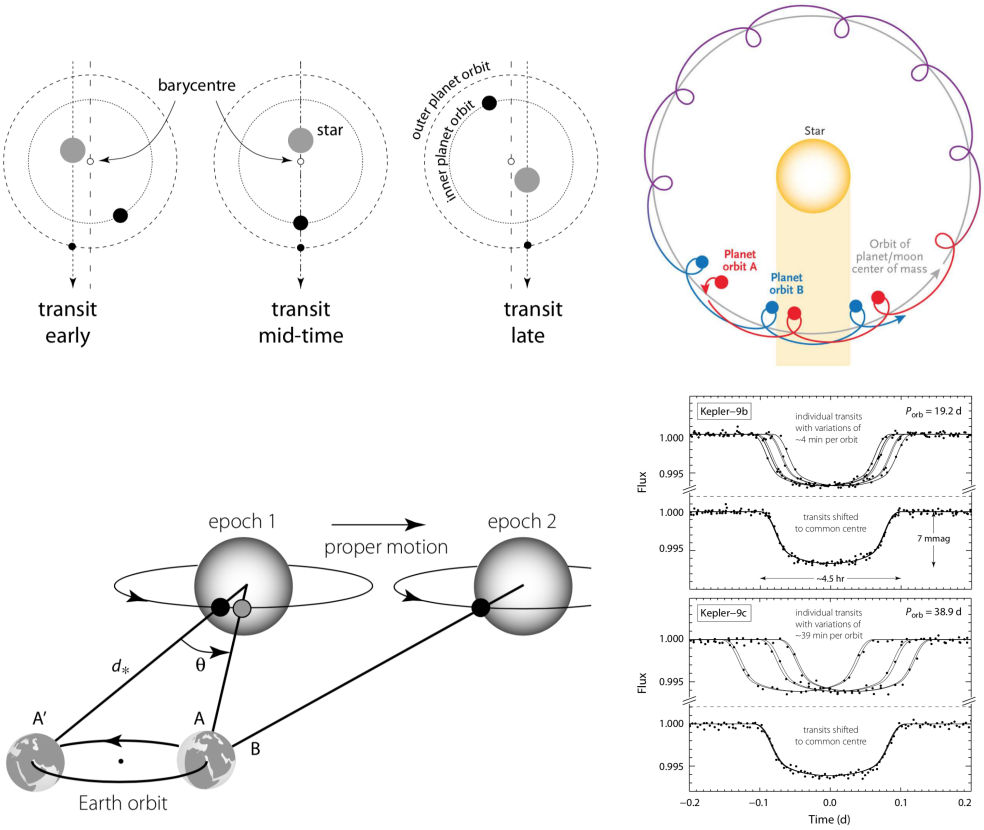

Fig. 1.15. Several situations that can cause TTVs and/or TDVs. *Top left:* Star's motion around barycentre. Figure from Perryman (2018a), adapted from Agol et al. (2005). *Top right:* Exomoon inducing additional planetary motion. Figure from Kipping et al. (2012). *Bottom left:* Geometric effects of proper motion and parallax. Figure from Perryman (2018a). *Bottom right:* Identification and realignment of TTV signals. Figure from Perryman (2018a), originally from Holman et al. (2010).

of the Earth around the Sun, however these differences are extremely small unless the system is very near Earth and/or has a very large proper motion.

1.7. Related Science

While most of this doctoral project has focused on observational transit photometry, there are a host of techniques that are related and/or complementary to the transit detection method. They frequently share some observational and scientific overlap with the topics discussed previously, but also add depth and breadth to the exoplanet inquiries that can be undertaken. A few techniques are discussed below.

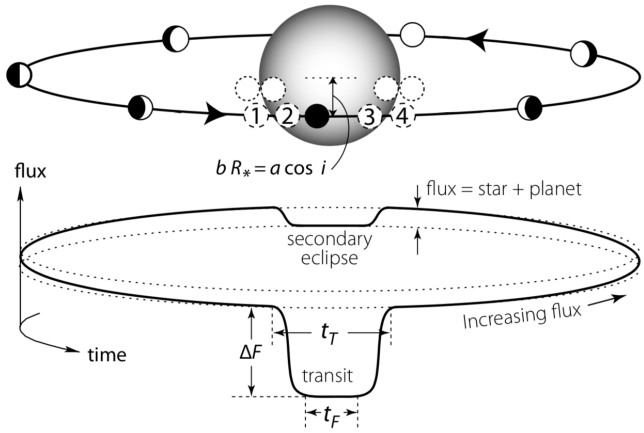

Fig. 1.16. The primary transit is only one portion of the entire phase curve, though it is the most prominent feature by far. Figure from Perryman (2018a), adapted from Winn (2009).

1.7.1. Eclipse curves and phase variation (photometric)

The photometric signal of an exoplanet around a star is not only measurable during the transit itself, but also as the planet passes behind the star and even throughout the entire orbit. These effects are of much lower amplitude than the primary transit, requiring careful selection of targets with strong signals and sensitive instrumentation to capture them.

When a planet passes behind the host star we call it an *eclipse* or *occultation* event. This is observable in a light curve because immediately prior to the occultation the observer is receiving direct light from the star as well as reflected and thermal emission from the planet's day side. As soon as the occultation begins, the received flux drops with the loss of the planetary contribution in a manner similar to the primary transit, albeit with much smaller amplitude.

Just as one can measure the sudden loss of the planet's contribution during an eclipse, it is also possible to detect the gradual change in total received flux as the planet's phase changes. Just like our own Moon's phases, the planet will display a time-varying fraction of day side versus night side throughout its orbit. This phase variation produces a sinusoidal flux signal with the deep transit drop near its minimum (when the night side is facing the observer) and a shallower eclipse dip near the maximum (when the day side is facing the observer). Figure 1.16 shows a schematic diagram of the full orbit light curve. This technique can even been used to determine if the tidally-locked face of a hot Jupiter has its hot-spot offset from the sub-stellar position (e.g. Dang et al., 2018), indicating strong longitudinal winds redistributing heat on the planet's surface.

1.7.2. Transit & eclipse spectroscopy

Spectroscopic study of exoplanets generally requires that the hugely dominant stellar light be disentangled from the planet's emitted and/or reflected light. This means that either the stellar

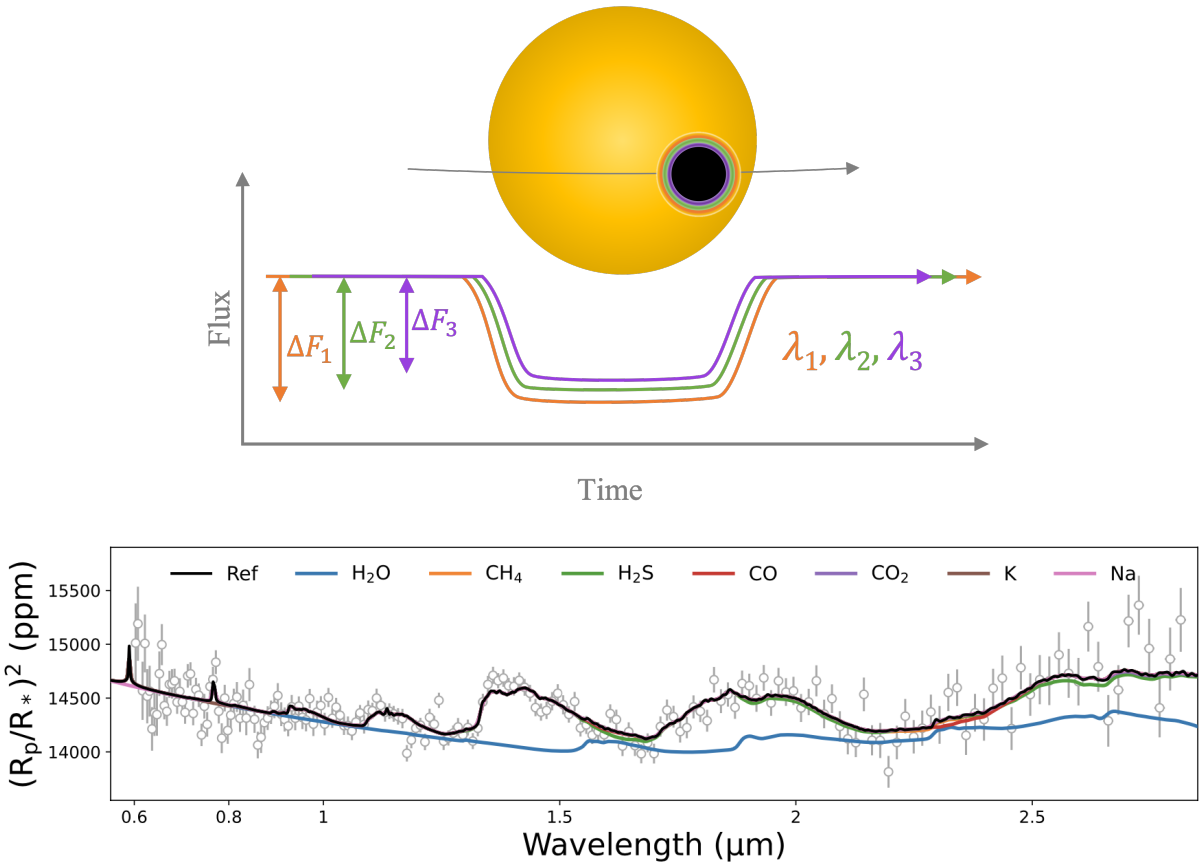

Fig. 1.17. *Top panel:* Schematic of transit spectroscopy. Planets have different effective radii at different wavelengths due to differing atmospheric opacities. By measuring the transit depth over a whole range of wavelengths, a spectrum can be built. *Bottom panel:* Transit spectroscopy of WASP-96 b, with JWST data (Radica et al., 2023). Recall from Equation 1.4.1 that $\Delta F = (R_P/R_\star)^2$. Coloured lines indicate when specific chemical components are excluded from the reference (black) model. Water is clearly the strongest feature in the spectrum, detected with high confidence.

contribution would need to be modelled out, leaving only the orders of magnitude fainter planet signal, or that the stellar light be blocked from entering the spectrograph. Blocking the starlight requires sharp spatial resolution and clever coronagraphic techniques as well as a very large planet–star separations. Direct imaging and spectroscopy of exoplanets is possible, but studies are limited to very wide-orbit planets with favourable planet–star brightness contrast ratios. Some of these challenges and limitations can be overcome by observing the planet near or during transit or eclipse phases.

Transit Spectroscopy:

The main concept behind transit spectroscopy is that the transit depth is wavelength dependent due to the presence of a planetary atmosphere. The optical depth in the atmosphere depends on its physical and chemical makeup, and can be more or less opaque at different wavelengths. An

atmosphere that blocks more light at a given wavelength has the same effect on the light curve as a larger planetary radius would. For example, if an atmosphere is mostly opaque to photons of wavelength λ_1 but fairly transparent to photons of λ_2, then the λ_1 photons will be blocked higher in the atmosphere than those of λ_2. As a result, the planet will look larger when observed at λ_1. Spectral observations reveal at which wavelengths the absorption is stronger or weaker, which can be compared to atmosphere models to determine the presence and levels of various elements or molecules. Figure 1.17 shows a schematic of a wavelength-dependent light curve, and an example of an extracted atmospheric spectrum.

This technique probes the regions of the atmosphere where the starlight passes through during transit, i.e., around the terminator and preferentially at high altitudes. Planet–star system configurations that put relatively more light through the atmosphere increase the signal strength. Hot planets and low surface gravity planets have larger/puffier atmospheres, and large planets with small stars maximize the fraction of starlight that is travelling through the planetary atmosphere.

Even with ideal circumstances, the signal strength of these effects is very low (~0.1% at best). The challenge is to obtain a high enough signal-to-noise ratio in your spectrograph so that the results can be meaningfully constraining on atmospheric models (Deeg & Belmonte, 2018, Ch. 52).

Eclipse Spectroscopy:

Eclipse (or occultation) spectroscopy measures the difference between the flux of the star alone (during eclipse) and the combined flux of the star and planet (outside eclipse), all as function of wavelength. Depending on the waveband of light being observed, this technique may be sensitive to the reflected light of the star (optical) and/or the thermal emission of the planet itself (infrared). Because occultation spectroscopy deals with light reflected or emitted from the planet surface (or opaque cloud deck), it can probe to much deeper layers of the atmosphere than transit spectroscopy does.

Carrying out occultation spectroscopy is not limited to the phase immediately outside the eclipse. If the host star is stable enough over the timescale of the exoplanet orbit, the combined planet-plus-star spectrum can be compared against the eclipse spectrum for any part of the orbit. Building a phase curve allows for longitudinal mapping of the exoplanet's atmosphere, especially if it is tidally locked to the host star so its rotation period is known (Deeg & Belmonte, 2018, Ch. 102).

The James Web Space Telescope (JWST), launched in late 2021, is an incredible instrument for these types of studies and a major upgrade from previous facilities. First of all, a space-based vantage point already provides some huge advantages over ground-based instruments in terms of schedulability and atmosphere-related systematics. But even amongst space instruments, JWST has a large aperture to provide a higher SNR, better instrumental stability and precision, and wider wavelength coverage than its predecessors. The broadband coverage gives it access to spectral regions involving more molecules and allows it to lift degeneracies between cloud cover and

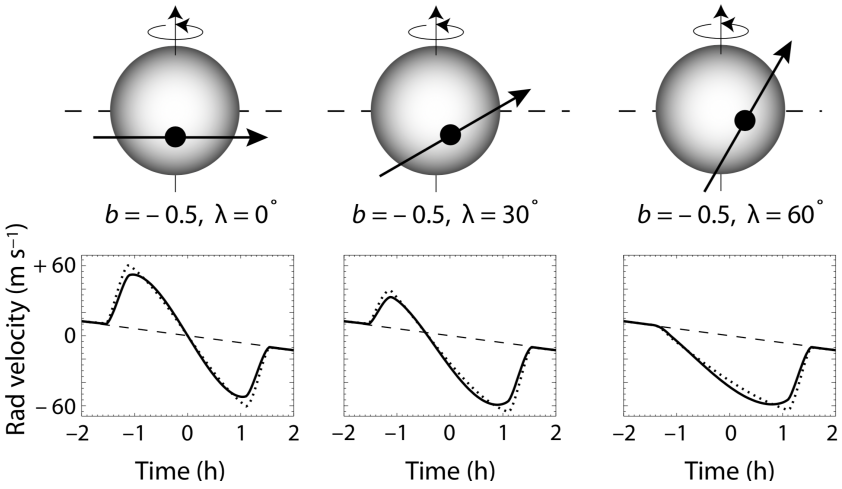

Fig. 1.18. Rossiter McLaughlin effect as a function of orbital obliquity. Figure from Perryman (2018a), adapted from Gaudi & Winn (2007).

metallicity (e.g., Constantinou et al., 2023). Despite the giant leap forward that JWST provides, these remain challenging measurements to make. Choosing optimal targets is paramount. Even doing so, it may still be a struggle to disentangle all aspects of stellar contamination, producing tenuous results in some circumstances.

1.7.3. The Rossiter-McLaughlin effect

The Rossiter-McLaughlin (RM) effect is a uniquely informative phenomenon that is intrinsically linked with the transit process. When a star has some intrinsic rotation, and is not aligned pole-on with our line of sight, one half of the stellar disk rotates towards the observer while the other half rotates away. These portions of the stellar surface that move towards or away from the observer emit Doppler-shifted light. Because the aggregate emitted light has an even mix of red- and blue-shifted light at various radial velocities, it causes an intrinsic spectral line broadening. The line broadening is symmetric, and so the net radial velocity we calculate is not shifted. However, as a transiting object traverses the stellar disk, it can preferentially block blue- or red-shifted light, resulting in a net shift in the star's measured radial velocity. The RM effect predicts a very specific departure from the Keplerian radial velocity curve during transit, according to the stellar spin and the planet's size and orbital alignment. Figure 1.18 shows how the shape of the RM signal also changes with respect to the obliquity angle, (i.e., how misaligned the planet's orbit and the star's spin axes are). It can reveal if the planet orbits in the same sense as the stellar rotation (prograde), indicated by the red-shift occurring first, or in the opposite sense as the stellar rotation (retrograde), indicated by the blue-shift occurring first. The RM signal is also affected in more subtle ways by turbulence in the stellar atmosphere, differential rotation, and convective Doppler shift of the stellar photosphere (Perryman, 2018a).

1.8. Prominent Exoplanet Transit Surveys/Missions

There have been many survey missions dedicated to the discovery of exoplanets via their transit signatures. They span a wide range of scope and sophistication, from small teams setting up a ground-based telescope to multi-national organizations constructing, launching, and operating space observatories. Each mission has its own unique capabilities and drawbacks, focusing on particular target demographics. This section briefly discusses a few of the major transit surveys and some of their more notable findings.

1.8.1. Ground-based

Ground-based telescopes suffer from the obvious disadvantages that come with being fixed to a spinning rock under a layer of atmosphere. They have to contend with the day/night cycle and the limited visibility of a given patch of sky during the year, as well as the Earth itself blocking certain latitudes from view. The atmosphere contains turbulent air and opaque clouds, and it blocks certain wavelengths from transmitting. However, the major upshot of a ground-based observatory is its substantially lower cost compared to an equivalent space-faring instrument. An Earth-bound facility is also *much* more easily maintained, repaired, operated, and upgraded. Table 1.1 provides a brief overview of some of the more prominent ground-based transit survey efforts. Most of the table's information was summarized in Deeg & Belmonte (2018) or is available on the various mission web-pages.

Mission	Hardware & Configuration	Operation	Targets	Notable Discoveries
HATNet and HATSouth (Hungarian-made Automated Telescope Network)	13×110 mm refractors. Distributed between Arizona, Hawaii, Chile, Namibia, and Australia.	1999–present. Longitudinal spacing allows for long continuous observation times (130 hrs demonstrated).	All stars of $V \lesssim 14$	• HAT-P-11 b: First transiting Neptune Fraine et al. (2014). • HAT-P-32 b & -33 b: Among the largest exoplanets ($R \sim 2R_{Jup}$) Hartman et al. (2011).
KELT (Kilodegree Extremely Little Telescope)	2×80 mm refractors. Located in Arizona and South Africa.	2005–present	Bright stars ($8 \lesssim V \lesssim 10$)	• KELT-1 b: Brightest host star with brown dwarf (BD). Became one of the best characterized BDs Siverd et al. (2012). • KELT-9 b: Giant planet around hot B/A-type star. Planet dayside temperature is 4600 K, as hot as a mid-K star Gaudi et al. (2017). • KELT-11 b: Among the most inflated planets with mass below Saturn, but radius 40% larger than Jupiter Pepper et al. (2017).
XO	3×10 cm binocular mounts. Located in Utah, Canary Islands, and Spain.	2003–present. Scans 43-degree strip of sky, continually reading CCD out.	Bright stars ($V < 11$) with period > 10 days	Found 5 hot-Jupiter planets, and a 6th object that may be a brown dwarf due to its $\sim 13 M_{Jup}$ mass Johns-Krull et al. (2008).
MEarth	16×40 cm telescopes with near-infrared detectors. Split between Arizona and Chile.	2008–present. Every telescope operates individually to track separate targets.	Nearby M-dwarfs	• Gilese 1132 b: Rocky planet 20% larger than Earth, only 12 pc away. Surface is hotter than Venus, but is an excellent atmospheric characterization candidate Berta-Thompson et al. (2015). • LHS 1140 b: Among the densest planets found with 7× Earth's mass, but only 40% bigger. It's equilibrium temp may be habitable given a sizeable greenhouse effect. Also only 12 pc away Dittmann et al. (2017).
TRAPPIST (TRAnsiting Planets and PlanetesImals Small Telescopes)	2×60 cm telescopes in Chile and Morocco.	2010–present	Solar system bodies & detectable transits	• TRAPPIST-1: System containing 7 rocky planets around an M-dwarf Gillon et al. (2017). Several of them are expected to be in the habitable zone.
SPECULOOS (Search for habitable Planets EClipsing ULtra-cOOl Stars)	4×1 m telescopes with near-infrared detectors. Split between Chile and the Canary Islands.	2017–present	M-dwarfs	• SPECULOOS-2: A system containing two super-Earths around an M-dwarf, the outer of which orbits in the habitable zone. (Delrez et al., 2022). • TOI-178: SPECULOOS provided key observations to confirm some of the resonant chain of 5 (and possibly 6) planets in this system (Leleu et al., 2021).
SuperWASP and WASP South	16×20 cm refractors. Split between the Canary Islands and South Africa.	2006–present	All stars of $7 \lesssim V \lesssim 13$	• WASP-12 b: Shows evidence of being distorted and torn apart by the stellar gravity Haswell et al. (2012). • WASP-17 b: First exoplanet shown to have a retrograde orbit Anderson et al. (2010). • WASP-18 b: Very hot super-Jupiter that orbits only 2.5 stellar radii away from its host. It is in danger of entering the roche limit and being engulfed Hellier et al. (2009). • WASP-104 b: Extremely low-albedo hot Jupiter, that would appear darker than charcoal Močnik et al. (2018).

Table 1.1. Brief summary of some prominent ground-based exoplanet transit survey missions.

1.8.2. Space-based

Space observatories have some very clear advantages over ground-based ones. They don't have to deal with weather, turbulence, or anything else related to peering through the atmosphere. With appropriate orbits and pointing, they can stare continuously at their targets without day/night cycle interruptions. However, their production costs and timelines are often prohibitive to small organizations. While there are a great many ground-based transit surveys with varying degrees of overlap in their science goals, we often see singular large space projects improve upon one another by leaps and bounds, rather than many incrementally improved-upon missions.

CoRoT:

The first space-based mission with a dedicated focus on exoplanet transits was the Convection, ROtation et Transits planétaires (CoRoT) telescope, launched late in 2006 and de-orbited in 2014. CoRoT was designed to be very sensitive to photometric variability, a capability integral to its two main science goals of measuring the vibrational modes of stars (astroseismology) and to search for exoplanet transits.

Observing star fields for up to 6 months with its 27 cm aperture, CoRoT collected light curves of ~160 000 stars. From these targets, CoRoT discovered hundreds of planet candidates, 35 of which have since been confirmed as exoplanets[5]. Notably, CoRoT discovered the first transiting rocky exoplanet CoRoT-7 b, dubbed a super-Earth (Barnes et al., 2010), as well as the first transiting brown dwarfs CoRoT-15 b and CoRoT-33 b (Bouchy et al., 2011; Csizmadia et al., 2015).

Kepler & K2:

The Kepler mission, launched in 2009, truly reshaped the exoplanet field. One only has to look at the cumulative exoplanet discoveries over time in Figure 1.1 to see Kepler's impact. The once-dominant RV discovery method (red) was rapidly overtaken by the transit method (green), mostly due to the two sharp jumps that occurred in 2014 and 2016. These spikes were the result of the Kepler mission announcing the discovery of 725, and 1285 new exoplanets, respectively. It nearly doubled the known exoplanet count with each announcement.

Kepler's mission design was to point its 0.95 m aperture telescope at a single patch of the sky (~12° diameter field of view). It would monitor this region from an Earth-trailing orbit that circles the Sun with a period of 372.5 days[6]. Kepler's goal was to monitor ~150 000 main-sequence stars in an attempt to answer the question, "Are Earth-sized planets in the habitable zone common or rare?"

[5] https://exoplanetarchive.ipac.caltech.edu/cgi-bin/TblView/nph-tblView?app=ExoTbls&config=PS

[6] https://www.nasa.gov/mission_pages/kepler/spacecraft/index.html

Kepler's success was groundbreaking. After 4 years of operation, it had produced extremely high-precision light curves of over 190 000 stars, discovering ~4600 candidate planets. These ranged from slightly larger than the moon to three times larger than Jupiter, and with orbital periods from a few hours to several years. It found 10 planets orbiting binary pairs of stars, and even several planets orbiting at extreme angles relative to their host star's rotation. And in accordance with its mission goals, Kepler found 24 Earth-size or super-Earth-size planets in the habitable zone (Deeg & Belmonte, 2018, Ch. 52).

Unfortunately, the Kepler spacecraft suffered reaction wheel failures in 2012 and 2013. These mechanical components are necessary to adjust and maintain the precise pointing of the telescope in space. The craft was launched with one redundant reaction wheel making the 2012 failure a recoverable issue, but the second failure in 2013 had no backup system to take over.

The spacecraft could not resume normal operations while short one reaction wheel, but a clever solution was devised to keep the instrument operating with an alternative observing plan. By pointing Kepler along the direction of its orbit, and balancing the subtle solar pressure on its solar panels, the spacecraft could maintain good pointing accuracy and observe 4 fields along the ecliptic each year. Adopting this strategy marked the end of the Kepler primary mission, and the transition to the K2 mission in 2014. K2 has continued to collect exoplanet data, much like it had in the Kepler phase, but its target fields were supplied by community researchers spanning a range of scientific pursuits.

The Kepler/K2 mission has earned a prominent legacy in exoplanet research due to the quality of its observations and the sheer number of exoplanets it discovered. Among the major lessons we learned from Kelper/K2 is that planets around stars are the rule rather than the exception. We learned that many exoplanet systems do not closely resemble our own solar system in their configuration or contents, and that the most common type of planet is something intermediate between Earth- and Neptune-size, a planet type we have no analogue for in our own system. Beyond exoplanets, Kepler/K2 also made numerous contributions to other fields relating to stellar variability such as supernovae, heartbeat stars, and astroseismology (Deeg & Belmonte, 2018, Ch. 52).

TESS:

Today's most current space-based transit survey mission goes by the name of TESS (Transiting Exoplanet Survey Satellite), launched in 2018. TESS's primary goal is to search nearly the entire sky for relatively bright and nearby transiting objects, and particularly looking for planets smaller than Neptune. Due to their hosts' bright nature, exoplanets found by TESS are prime candidates for detailed spectroscopic follow-up observation that can provide planet masses and atmospheric characterization.

[7] https://heasarc.gsfc.nasa.gov/docs/tess/

TESS has four cameras, each with a $24^\circ \times 24^\circ$ field of view. The four fields are linearly aligned to achieve an effective seeing area of $24^\circ \times 96^\circ$. This viewing configuration allows TESS to watch stars in a sector spanning from an ecliptic pole down to nearly the ecliptic plane in a single pointing. During TESS's primary mission, it spent nearly two years tiling of the southern and northern ecliptic hemispheres. It would spend two orbits (~27 days) pointing at each of 13 of these $24^\circ \times 96^\circ$ sectors before rotating to the next (see Figure 1.19). The sectors overlap near the ecliptic poles, meaning the observing baseline ranges from 27 to 351 days depending on the location of the star. TESS observed the southern hemisphere (Sectors 1–13) during its first year of operation, and switched to the northern hemisphere (Sectors 14–26) in July 2019. Collectively, these 26 sectors covered more than 85% of the full sky.

To manage data volume while maximizing scientific output, TESS would record full-frame images only at a slow cadence while saving small thumbnail image subsets of preselected targets at a faster cadence. For the primary mission, each sector contained ~15 000 of these preselected target stars, saved at a 2-minute cadence. The full-field images were recorded with a 30-minute cadence to facilitate additional science endeavours. The observation strategy was designed so that the regions which received nearly a year of continuous viewing by TESS (i.e., the ecliptic poles) overlap with the continuous viewing zone of JWST.

Upon completion of the primary mission in July 2020, TESS began its first extended mission. This first extension looked very similar to the primary mission, except that it included an extensive Guest Investigator Program. It allowed community members to propose specific targets for inclusion in the short-cadence list. This time around, the short-cadence could be requested at either 2-minute or 20-second rates, and the full frame images were changed to 10-minutes instead of 30. The

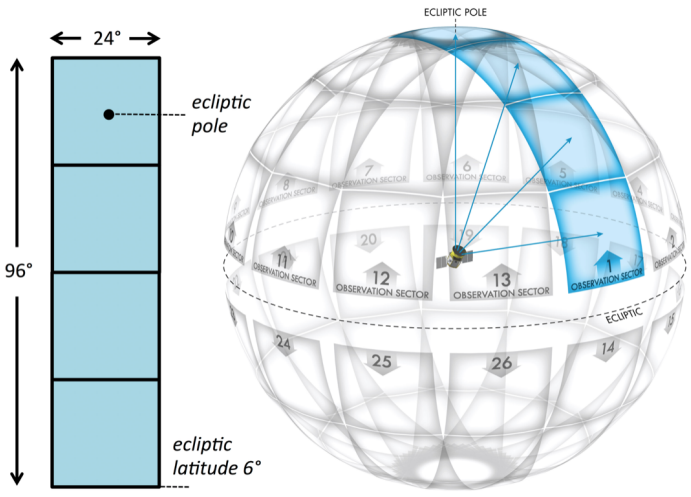

Fig. 1.19. TESS tiled nearly the entire sky over its two-year primary mission. Overlapping sectors near the ecliptic poles receive longer observing baseline which may detect longer-period transiting planets. Figure from TESS mission website[7].

southern ecliptic hemisphere pointings of this extension looked very similar to the primary mission, but the northern pointings were shuffled to include more coverage at the pole and along the ecliptic plane at the expense of some mid-latitudes. This mission extension ended in September 2022.

TESS' second extended mission followed a similar practice to the first. It is expected to operate across three years, and its pointings and targets are largely determined by the Guest Investigator Program. The major distinction between the first and second extended missions, is that the full-frame images of the second extension will be taken at a 200-second cadence instead of 10 minutes.

1.8.3. The importance of transit survey missions

In nearly all cases, the main goals of exoplanet survey missions fall into two categories: (1) Building up the exoplanet catalogues to enable population and statistical studies, or (2) discovering planets with unique or useful properties that are valuable as in-depth case studies.

Kepler and most other early missions tended to focus on the first point. When few were known, questions about exoplanets vastly outnumbered answers. It wasn't until the Kepler mission that we really understood that planets are the general rule in our Galaxy, not the exception. Any given star in the sky is likely to have at least one planet around it. By discovering multitudes of new planets, and by understanding and accounting for our observation biases, we begin to understand what our Galactic neighbourhood of exoplanets look like. With the ability to look at a collection of thousands of exoplanets, we gain the ability to discover what properties are most common, the overall span of various properties, and which types seem to be scarce or difficult to detect.

Unfortunately, the realities of successfully designing and creating a survey instrument and mission plan will always involve compromise. No mission is good at everything, and forward-thinking planners will design different missions to complement one another and overcome specific shortcomings. While Kepler provided answers to many broad questions about exoplanet populations, its static pointing at a relatively small patch of sky placed strong limits on the number of bright sources in its catalogue. The spacecraft gathered excellent long-baseline photometric information on the many stars within its field of view, but most of these targets are very faint and of limited potential for spectroscopic follow-up.

In direct answer to this, TESS was designed to survey the entire sky and focus on bright and nearby host stars. It continues the goal of building up the catalogue of known exoplanets, but does so in a way that produces targets that are also ideal candidates for detailed spectroscopic follow-up. TESS' own major shortcomings (e.g. small temporal baseline coverage and low spatial resolution), are in turn supported by a collection of ground-based observatories working together to verify TESS' targets.

The general trajectory of the exoplanet field in recent years has been less discovery for discovery's sake, and more of a focus on the ability to carry out detailed analysis with specific case studies. TESS is a stepping stone in that direction. Powerful current and future observatories

designed for detailed characterization of preselected targeted objects (e.g. JWST, TMT, ELT, etc.) require input from larger survey missions. TESS targets in particular, due to their brightness, are generally high-value options.

All this is not to say the time of the transit survey is coming to an end. As technology and techniques improve, we gain the ability to more effectively search the regions of “challenging" parameter space. Long-period exoplanets pose a difficulty for transit surveys due to their lower geometric probability and their lower sampling rate. Small rocky planets around Sun-like stars still remain largely invisible against background noise. Exploring these domains requires dedicated effort and investment.

1.9. This Doctoral Project

The primary goal that initiated and guided this doctoral thesis was the contribution to the TESS exoplanet candidate follow-up effort and involvement in related exoplanet endeavours. With this goal in mind, the next few sections describe the main elements involved in this undertaking: participation in TESS's Exoplanet Follow-up Observing Program, our adaptation of the Dragonfly Telephoto Array to the study of exoplanet transits, and our use of the Near-Earth Object Surveillance Satellite to capture challenging transit targets.

1.9.1. TESS's Follow-up Observing Program

Like Kepler before it, the TESS mission is producing so many exoplanet candidates that a specifically coordinated and concerted effort is necessary to verify their legitimacy and confirm their properties. The Exoplanet Follow-up Observing Program (ExoFOP) was created to do just that. ExoFOP provides a repository for follow-up contributions, including those by the TESS Follow-up Observing Program (TFOP). With so many targets to follow-up, the TFOP governing structure sets priorities, centralizes the observation database, minimizes redundant observations, and ensures publication credit is distributed fairly.

A subgroup within the TFOP is the TESS Single Transit Planet Candidate (TSTPC) working group. While sharing in the activities and responsibilities of the TFOP as a whole, the TSTPC group pays particular attention to the challenging targets that have very uncertain periods. Singly-transiting targets provide almost no information on their orbital periods, and transits caught in widely separated sectors may have missed intervening transit events. Such targets require significantly more time and effort to verify than those with clear-cut periods. However, chasing down these targets is a good way to find temperate long-period planets, which are underrepresented in most samples.

The overarching goal of both the TFOP and the TSTPC groups is to confirm or validate as many of the TESS candidate exoplanets as possible. In this context, we use the terms *validate* and *confirm* both to indicate the ruling-out of false positive scenarios and adequately constraining the

planet's physical and orbital parameters. However, between the two, a *confirmation* is a stronger designation as it implies the constraint of the planet's mass whereas a *validation* does not.

Members of the TFOP community submit observations of all kinds to build up the database on individual TESS targets. They may also volunteer to lead validation and confirmation publications on specific targets, making use of the collectively gathered data. These publications tend to require numerous observations of many types (e.g. additional ground-based time-series photometry, reconnaissance spectra, RVs, high-contrast imaging, etc.). The lead author spearheading the effort is in charge of organizing the observations from other contributors, or gathering them personally.

I became a member of both groups in the process of advancing this doctoral project. In this thesis-by-articles manuscript, the papers included in Chapters 2, 3, and 4 demonstrate our contributions to various aspects of the TFOP and TSTPC groups. Before presenting those papers, we would first like to introduce the two instruments that played key roles throughout the project.

1.9.2. The Dragonfly Telephoto Array

The Dragonfly Telephoto Array, hereafter simply referred to as "Dragonfly", is a small, remotely operated telescope with a unique design. Situated at a private telescope hosting facility in New Mexico, USA, Dragonfly is a composite refractor telescope consisting of 48 individual small lens/camera units working in unison. It was designed to observe and answer questions around ultra diffuse and low surface brightness targets, and it does this very well. These particular targets, however, generally require very low background light levels and cannot be observed when the Moon is in the sky. This offered an opportunity to expand upon Dragonfly's scientific purview while making use of the "bright time" to improve the instrument's on-sky efficiency. We entered an arrangement with creators and operators of Dragonfly to create a new observing mode and use the telescope's bright time to observe exoplanet transits. The goal was to produce an automated instrument that would make follow-up transit measurements of TESS targets to contribute to the TFOP.

The details of our adaptation process for Dragonfly are discussed thoroughly in Chapter 2, so we will present only a higher-level overview here. There were a few key steps that needed addressing to make the instrument a fully capable exoplanet observer. **(1) Scheduling:** We developed a semi-automated process for generating transit observation timetables. This program would query the TFOP database for suitable targets and build an observing schedule based a number of parameters and priorities, and could include specified preselected targets. **(2) Observing mode:** The observing control software itself required a new exoplanet module to execute observations in the required manner. While Dragonfly was already fully operational for the types of observations involved in low surface brightness studies, it was not immediately equipped for very time-sensitive transient events like exoplanet transits. We taught Dragonfly, in its automated operations, to pay attention to the current time and adjust its target prioritization accordingly. This ensured transit

observations only occurred during actual transits, and that the “bright time" exoplanet program did not interfere with the “dark time" low surface brightness program. We also built a new execution subroutine with improved control over imaging cadence and focus inputs. **(3) Data processing:** We developed custom image reduction and photometry extraction pipelines to handle Dragonfly's unique 48-camera design. The pipelines could be run with parallel computing to speed up the data-heavy process. The final product of these pipelines was a normalized and calibrated light curve of the target that could be submitted to the TFOP along with supporting data and analysis files.

We incrementally accomplished and fine-tuned all of these steps over the course of the project. In doing so, we successfully produced another instrument to join the exoplanet-observing roster, and we made many contributed observations ourselves. The project fostered an in-depth and hands-on understanding of how photometric data is taken, processed, and interpreted, and how to overcome challenges encountered at each step. The article included in Chapter 2 is the culmination of the exoplanet-Dragonfly project and comprised a major portion of the overall doctoral project. Publications that have made use of our Dragonfly observations are listed in Table 1.2.

1.9.3. The Near-Earth Object Surveillance Satellite

Another instrument that has played a major role in this thesis project is the Near-Earth Object Surveillance Satellite (NEOSSat). NEOSSat is a small Canadian satellite mission under collaborative operation by the Canadian Space agency (CSA) and Defence Research and Development Canada (DRDC). As its name suggests, NEOSSat was developed to monitor solar system objects (asteroids, comets, Earth-orbiting satellites, etc.) to improve our situational awareness of local space.

NEOSSat was launched in February of 2013 into a sun-synchronous polar orbit with an altitude of ~780 km (period: 100 minutes). Its onboard photometer consists of a 15 cm aperture with a clear filter (instrument effective bandpass roughly 400-900 nm). Its detector captures a $0.86^\circ \times 0.86^\circ$ degree field of view, and with 1024 pixels on a side, produces a pixel scale of $3''$ per pixel.

Since launch, the little spacecraft has experienced a fairly tumultuous and heroic history. An unfortunate hardware failure in 2016 caused a loss of attitude determination due to a malfunction and subsequent loss of the onboard magnetometer. An innovative workaround was eventually developed to use the satellite's internal dipole field with the onboard GPS to determine the spacecraft's coarse pointing. Once accomplished, the still-operational star tracker system could be engaged to achieve fine-pointing operations.

In late 2016, before the GPS solution was fully implemented, NEOSSat experienced a second major hardware failure. An unresponsive micro-controller severed access to the three torque rods used to desaturate the momentum in NEOSSat's reaction wheels. A completely novel solution was developed to use torques between Earth's magnetic field and the satellite's internal dipole

field to desaturate the built up reaction wheel momentum. The process takes a large fraction of the NEOSSat's time, but remains at <50% which still allows for science operations. Dipole desaturation is typically scheduled whenever no science operations are in progress (e.g. during Earth-eclipse, South Atlantic Anomaly crossings, etc.). After all of this, NEOSSat regained a performance essentially the same as before the hardware failures, albeit with a lower duty cycle due to increased desaturation times.

In 2019, NEOSSat was opened to general astronomy proposals for the first time, and Canadian astronomers were invited to apply with their own science cases. At this point we submitted a proposal to observe a number of long-duration transits. This Cycle 1 proposal was largely exploratory as it was not totally clear how NEOSSat would perform on this sort of task. Some rudimentary test cases had been carried out, but we needed to create a rough idea about the photometric precision that could be reached at a given magnitude.

From Cycle 1 to the current observing Cycle 6 (May–Nov., 2023) we have made 11 successful proposals as well as 10 program extensions following cycle window expansions. Over the course of our work with NEOSSat we have determined a few niche strengths of the satellite with respect to exoplanet transit observations. **(1) Very long transit durations:** A subset of transits can last for many hours. They constitute a major challenge to observe from the ground given that one typically must observe at least twice the transit duration to provide adequate calibrating baseline before and after the transit. For a 6+ hour transit, weather, airmass, and daylight become very problematic. NEOSSat's space-based vantage point circumvents all of these issues. **(2) Period aliases:** When widely spaced observations miss intervening transits, the period is known only to some integer fraction ($P_{\rm True} = P_{\rm Obs}/n$). Because the TESS mission alternated between the northern and southern hemispheres about once per year, many transits were discovered separated by ~2 years. Being able to point at a target at essentially any time, NEOSSat could check the most likely aliases easily. **(3) Single transit candidates:** When only a single transit is detected, the period is almost totally unconstrained. Only RV campaigns can provide a decent period estimate, and even those have wide uncertainties, especially for low-mass planets. If a low-precision period estimate is attained, NEOSSat is well-suited to monitor wide transit prediction windows (days/weeks long). Finding such an uncertain transit precisely determines its period and ensures future observability.

Throughout our 4 years of NEOSSat proposals, our programs have focused on a mix of these three categories. Our observations of targets with precisely known periods (or $P_{\rm Obs}/n$ aliases to check) typically span 20–40 hours each, given that we usually ask for 4× the transit duration to account for Earth-eclipse observing gaps. Window searches for our single transit targets happen less frequently, but have spanned anywhere from 1.5 to 20 days straight.

One observation stands out in particular for its success: a 7-day observation of the target TOI-2010.01. Our NEOSSat follow-up played a crucial role in precisely determining the orbital period of a very long-period single-transit exoplanet, confirming its planetary status and establishing an interesting low-insolation atmospheric test-case. Chapter 4 describes that effort in more detail.

Several other broad-window searches for long-period single-transit targets with uncertain periods are in progress under our NEOSSat program, with promising prospects.

With our NEOSSat access and long-period planet program in place, we advertised ourselves as being able to provide long-baseline observations to the TSTPC and TFOP groups. Space-based observing opportunities are not common, and we have built a reputation as someone to contact for support in this area. Before long, fellow members were reaching out to us to propose collaborations. Thus far, our NEOSSat observations have contributed to 5 publications at various levels of completion (see Table 1.2). We expect many more to arise in the near future as our general survey of long-duration transits and period alias hunt continues, as well as our concerted efforts on a few valuable long-period targets with uncertain timing.

Table 1.2. Publications contributed to by our Dragonfly and NEOSSat programs for which I am the lead or co-author.

Subject	Obs. Dates	Instrument	Lead Author	Stage	Reference
TOI-2010.01	2021-12-14	NEOSSat	**Christopher Mann**	Published	[1]
Instr. overview	2018–2022	Dragonfly	**Christopher Mann**	In preparation	–
Instr. overview + TOI-1996	2020-08-16 2021-01-25	NEOSSat NEOSSat	**Christopher Mann**	In preparation	–
TOI-1683.01	2020-11-10	Dragonfly	Michael Zhang	Published	[2]
TOI-1246.02	2021-05-27	Dragonfly	Emma Turtelboom	Published	[3]
TOI-2180.01	2020-08-27 2020-09-01	Dragonfly	Paul Dalba	Published	[4]
TOI-1694.01	2021-01-01	Dragonfly	Priyashkumar Mistry	Published	[5]
TOI-199.01	2021-03-31	NEOSSat	Melissa Hobson	Published	[6]
TOI-2134.02	2022-11-22	NEOSSat	Federica Rescigno	Published	[7]
TOI-1683.01	2020-11-10	Dragonfly	Benjamin Hord	Submitted	–
TOI-1823.01	2021-02-12 2021-03-23 2021-08-25 2021-12-19	NEOSSat NEOSSat NEOSSat Dragonfly	Hanna Kellermann	In preparation	–
TOI-1199.01	2022-02-19	Dragonfly	Ashley Chontos	In preparation	–

Note: The nature of the ExoFOP database is to slowly accumulate observations until a publication can be assembled. More observations than these have been (and will continue to be) submitted, expanding the future publication potential from our Dragonfly and NEOSSat programs.

[1] Mann et al. (2023b)

[2] Zhang et al. (2023)

[3] Turtelboom et al. (2022)

[4] Dalba et al. (2022)

[5] Mistry et al. (2023)

[6] Hobson et al. (2023)

[7] Rescigno et al. (2023)

1.9.4. Context surrounding the included articles

Paper 1: Dragonfly

The paper in Chapter 2 lays out the Exo-Dragonfly project, where we took an instrument designed for ultra-low surface brightness observations and adapted it for the study of exoplanet transits. Dragonfly on its own was the initial inspiration for this thesis project. It provided hands-on experience with the details of astronomical data taking, and it afforded an excellent way to contribute to the TESS follow-up efforts and become involved in the community and its projects. Starting in the fall of 2018 with the onset of my Ph.D. program, work with Dragonfly began slowly as I completed my required coursework. This involved mostly technical development, getting the scheduling, observing, and data processing software up and running. Observations began in earnest in the fall of 2019, continuing on to the summer of 2022. Operational stability improved and procedures were fine-tuned across much of this time span. We made hundreds of transit observations, and submitted to the TFOP repository when the performance was good and the addition would be valuable to TFOP's priorities.

The limiting factor on the productivity of the Exo-Dragonfly project was always the bottleneck arising from the flood of incoming observations and my own limited available work-hours. While I had plenty of mentorship and support, the workload of processing observations fell solely to me. We had ambitions to more fully automate the data-processing, but we never quite achieved the robustness required for intervention-free operation. As our involvement with TFOP increased, we took advantage of opportunities that arose to expand the thesis with other projects in addition to Dragonfly. These included assuming a project/publication leadership role within TFOP, and undertaking an extended observing program with another instrument.

Paper 2: TOI-1221.01

The paper comprising Chapter 3 arose from one of these TFOP-related opportunities. During the summer of 2021, I volunteered to take the lead on the publication of a target that the TFOP and TSTPC groups had been compiling observations on. I was still somewhat new to the organization and had thus far only been involved on the data submission side of things. I had been submitting Dragonfly and NEOSSat observations regularly at this point, but had not yet been personally involved in a target's validation/confirmation. This assumption of responsibility seemed like an excellent way to become more fully involved with the follow-up community, and to add breadth to the thesis project.

The target was TOI-1221.01, a shallow-transit exoplanet with a few detections by TESS. It was unlikely to be observable by Dragonfly, so none of my own data was involved. Leading the publication effort involved far more than just writing up a paper. A good amount of organization, observation, synthesis, and analysis work was required to get the paper in order. These were all things I was ultimately responsible for. The completed paper was published in May 2023. The

paper was a successful exercise in large-team organization and in understanding the standards, requirements, and processes involved in a TESS candidate validation.

Paper 3: TOI-2010.01

Chapter 4 contains a paper stemming from my involvement with the TSTPC and a particular success with our NEOSSat program. The target was TOI-2010.01 which had shown a single, deep, unambiguous transit in the TESS data, but never re-transited. This was just the kind of planet that the TSTPC was organized to follow up.

By late in 2021, a fellow TSTPC member had gathered enough RV data on the target to determine a rough period. It was at this point that he got in touch with me to try and catch the elusive transit. By then, my work with NEOSSat was known within the TSTPC and so we developed an observing proposal to monitor the uncertainty region of the transit prediction.

The observation went smoothly and we detected the transit during our 7-day window. Based on this success, I was offered the lead on the subsequent planet confirmation publication that would be prepared. With the planet's period in hand, we reached out to another research group who had also been gathering RV data. We collectively decided to pool our data sets and that they would join our publication. Like with the TOI-1221.01 paper, a number of supporting observations were available within the TFOP repository, and their contributors and analyses were also incorporated. The paper was published in November of 2023.

Chapter 2

Exo-Dragonfly: Adapting the Dragonfly Telephoto Array to the Observation of Exoplanet Transits

This manuscript is in its final phases of co-author revision before submission to the *Monthly Notices of the Royal Astronomical Society* for publication.

Christopher R. Mann [1,2], David Lafrenière [1,2], Étienne Artigau [1,2], Roberto Abraham [3], Pieter G. van Dokkum [4], Colleen Gilhuly [3], Steven R. Janssens [3], Philippe Desmarais [1,2], Pierrot Lamontaigne [1,2], Maude Larievière [1,2], and Rémi Sincennes [1,2]

[1] Département de Physique, Université de Montréal, Montréal, QC, Canada

[2] Trottier Institute for Research on Exoplanets (iREx)

[3] David A. Dunlap Department of Astronomy and Astrophysics, University of Toronto, 50 St George Street, Toronto, ON M5S 3H4, Canada

[4] Department of Astronomy, Yale University, 260 Whitney Avenue, New Haven, CT 06511, USA

Abstract. We present the process and results of the Exo-Dragonfly project, an undertaking to adapt and use the Dragonfly Telephoto Array to observe exoplanet transit light curves. The Dragonfly instrument, located in New Mexico, USA, is composed of 48 commercial 143 mm aperture telephoto lenses mounted together and simultaneously observing the same field with r and g filters. The setup has a photon collection area roughly equivalent to a 1 m diameter lens. With the driving goal of producing observations in support of the TESS follow-up efforts, we developed an automatic observation scheduling process, a new observing mode for time-sensitive time series observation, and a reduction/analysis pipeline to process data. Our results show that the Dragonfly Telephoto Array can achieve a photometric precision floor of ~ 0.5 ppt for targets in the magnitude range of $8.5 \lesssim m_V \lesssim 13$ for 4–5-minute bins. We discuss the successes and challenges encountered while using this unique multi-camera telescope as well as suggestions for improvements of this (or other similar) instruments as they pertain to exoplanet transit observations moving forward.

Keywords : Dragonfly — Instrumentation — Exoplanet transits — TESS follow-up

2.1. Introduction

The Dragonfly Telephoto Array (hereafter simply referred to as “Dragonfly") is a remotely operated telescope situated in southern New Mexico. The New Mexico Skies (NMS) telescope hosting facility, located at latitude 32°54′ N and longitude 105°32′ W, houses the instrument and provides technical on-site support. Built, maintained, and operated by a team based out of the University of Toronto and Yale University, the instrument was designed and built to address science questions involving ultra-diffuse structures and the outer regions of galaxies. Dragonfly's design consists of an array of telephoto lenses connected to individual CCDs. The cameras are split between multiple mounts and different filters are distributed in a semi-permanent configuration amongst the cameras. This setup was designed for and can produce exquisite photometric sensitivity. More details on the design philosophy and technical setup can be found in Abraham & van Dokkum (2014).

Some of the diverse research that has been done with Dragonfly to date includes: Surveys of ultra-diffuse galaxies (UDGs; Merritt et al., 2016a,b; Danieli et al., 2017; Zhang et al., 2018; Cohen et al., 2018; Danieli et al., 2020); Kinematics and dark matter constraints of UDGs (van Dokkum et al., 2019b; Wasserman et al., 2019; Keim et al., 2022); Stellar streams (van Dokkum et al., 2019a; Pasha et al., 2021); Size–luminosity relation of UDGs (Danieli & van Dokkum, 2019); Inter-galactic and interstellar medium emission (Lokhorst et al., 2019; Zhang et al., 2023); Globular clusters in UDGs (van Dokkum et al., 2017, 2016); tracing galactic outskirts (Abraham et al., 2017; Gilhuly et al., 2022); tunable ultra narrow-band filter development (Lokhorst et al., 2020); and spectral line mapping (Chen et al., 2022; Lokhorst et al., 2022).

Dragonfly's ultra-diffuse low surface brightness (LSB) studies require very low sky background levels and thus are generally only carried out during “dark time" (i.e. when the Moon is below the horizon). This represented an opportunity to expand Dragonfly's capabilities and scientific contributions to the community. Dragonfly's existing photometric precision made it a good candidate for observing exoplanet transits, an endeavor that does not suffer as strongly from brighter nighttime skies. We engaged this additional project for Dragonfly in an effort to improve its observational duty cycle, as well as bring another exoplanet-observing instrument into service. The overall goals of the “Exo-Dragonfly" project were motivated both by Dragonfly's photometric sensitivity and access to large amounts of bright time.

Dragonfly is well-suited to provide follow-up observations of transiting planet candidates discovered by the Transiting Exoplanet Survey Satellite (TESS; Ricker et al., 2015). TESS's mission has been to discover exoplanets across the full sky that orbit bright and nearby host stars. These TESS candidate exoplanets are not only amenable for follow-up from ground observatories but they generally *require* substantial follow-up effort to validate their planetary nature. In this pursuit, we became members of the TESS Follow-up Observing Program (TFOP), a community of observers created to confirm, reject, and refine TESS's discoveries in an organized and efficient manner.

This manuscript is laid out as follows. In Section 2.2 we review the physical setup of the instrument itself. Section 2.3 details the modifications to the observing practices and software that were made to accommodate exoplanet transit observations. Sections 2.4 and 2.5 describe the custom reduction and analysis pipelines, respectively, that were developed to handle the unique properties of this multi-camera telescope. In Section 2.6 we discuss the instrument's successes and challenges with regard to performance and productivity. Finally, a summary and discussion of future possibilities is provided in Section 2.7.

2.2. Instrumental Setup

2.2.1. Hardware

We present here an overview of Dragonfly's physical makeup, but for more detailed background on the specifics and motivations behind the instrument's design, as well as technical specifications, see Dragonfly's original debut paper (Abraham & van Dokkum, 2014).

Dragonfly's setup is modular in nature, allowing it to scale up over time. When the Exo-Dragonfly project began, Dragonfly's configuration consisted of 48 lens/camera units split evenly between two mounts. The lenses are commercially available Canon 400 mm $f/2.8$ IS II telephoto lenses, and make use of nano-fabricated coatings to markedly reduce internal reflections. Each lens is attached to a Santa Barbara Imaging Group (SBIG) STF-8300M camera with a Kodak KAF-8300 CCD detector. The monolithic 3326×2504 pixel detectors record images with a $2.6^\circ \times 1.9^\circ$ field of view, corresponding to a plate scale of $2\farcs8$ pixel^{-1}. Read-out time for the detectors is $\sim$15 s for the full frame. The focus is controlled using custom adaptors by Birger Engineering Inc. which interface with the internal auto-focusing motors of the lenses.

The two mounts each have 24 cameras affixed to a rigid aluminum framework by a three-point ring harness to minimize flexure. The mounts operate in sync with each other, effectively acting as a single telescope. The mounts themselves are Paramount ME II German equatorial mounts by Software Bisque Inc.

Each individual camera is outfitted with a custom Sloan Digital Sky Survey (SDSS) filter from Astrodon Imaging, Inc. Half the cameras are equipped with SDSS r and the other with SDSS g (hereafter simply referred to as r and g filters, respectively). Each 24-camera mount is evenly split between the two filters.

2.2.2. Normal operating procedure

Dragonfly is a remote-controlled telescope. Situated at the NMS telescope hosting site, its operations are aided by very prompt and capable technical support staff, but the night-to-night observing is ultimately remotely overseen by one of the Dragonfly researchers.

A typical night of observing begins before sundown with a hardware diagnostic. Using remote desktop software, the observer runs through a set of scripted routines that prepare Dragonfly for the night. The mounts, focusers, and cameras are tested for abnormal functionality. If any camera/focuser issues cannot be immediately resolved by the observer or support staff, the camera is flagged for exclusion from the night's operations.

Once the hardware is checked and ready, we initiate the observing software, a customized version of the commercially available `AstroPlanner`[1]. This software holds a table of user-defined targets and keeps a record of the accumulation of observations on each. At a predefined cadence, typically every 10 min, it also makes a decision as to what task to initiate next. It takes into consideration local weather, sky brightness, time of day, and target-related weights and priorities. During the early evening when the sky is very bright and/or the observatory domes are closed, the telescope remains inactive. During twilight hours, both dawn and dusk, a command initiating flat- and dark-field imaging routines is automatically called. When sky conditions are appropriate, the software calls an observing script to carry out an imaging routine for the chosen target. As the sky continues to brighten in the morning hours after the calibration images have been taken, it initiates an orderly shutdown and stowing of the instrument, ending the night's observing.

As the night progresses, every entry in the list of targets is assigned a frequently updated observing weight. The weight is based on many factors, but some include the current position of the target on the sky, the current altitude of the Moon, the time of the year where the target is most readily observable, and how much data have been accumulated on this target so far. These factors (and more) contribute to the decision of which target has the highest priority at the moment. When the software decides that conditions are appropriate for an observation to take place, it picks the highest weighted target and initiates the automated observing script.

The observing script reads in the information specific to the chosen target and starts the observation sequence. A focus run may be carried out if needed as well as a series of quality checks on the cameras. If all is well, a sequence of exposures are taken with a predefined exposure time.

The images taken by each camera are saved to small storage allocations on their individual local controller computers, which are termed the "Sticks". After a night's observation, data are cleared off the Sticks onto a larger consolidated storage space at NMS. The night's data can then be remotely downloaded.

2.3. Exoplanet Modifications

Before actually undertaking any transit observations, Dragonfly's observational setup needed some adaptation. Having been designed to build up many long exposures on stable, faint, galactic structures over long periods of time, Dragonfly's existing software was not immediately suited to capturing the precisely timed transient signal of an exoplanet transit.

[1] https://www.astroplanner.net/index.html

2.3.1. Observation procedures

The first major change to implement was to ensure a transiting exoplanet target receives a high weight only during the precalculated observation window. We modified the weighting system so that exoplanet targets received a large weight multiplier when the Moon is up (as opposed to the tiny multiplier the LSB targets received), and a further multiplier of zero if the current time is outside the target's precalculated transit observation window. We enriched the AstroPlanner target table with supplemental transit-specific metadata so that the software could compare the transit timings against the current time.

We also wrote an automated observing script specific to exoplanet targets. This script reads in individualized observation instructions such as the observation time window, exposure time, cadence, and intentional focus offset. This script will also make note of all the unique exoplanet exposure times that have been observed during the night. The shut-down procedure at dawn was modified to include extra dark exposures that match the unique exoplanet exposures taken during the night.

Finally, because the exoplanet and LSB data are handled and processed by separate research groups, we created an automatic "morning-clean-up" procedure to sort the night's data. It combs through the images, identifying which are exoplanet specific, and moves the appropriate files to the appropriate storage spaces. This turned out to be an important step as the Sticks have limited storage capacity and the exoplanet targets tend to have a higher data rate with their short exposures than the LSB targets with their long ones. In particular, the nights around the full Moon primarily consist of bright time and produce a large data volume. Nightly data stored on-site at NMS is remotely downloaded to permanent storage at the Université de Montréal, and eventually deleted from the NMS facilities.

2.3.2. Exoplanet observation strategy

For the duration of the Exo-Dragonfly project, exoplanet observations were undertaken any time the Moon was above the horizon. This "bright time" was unused by Dragonfly's existing LSB programs and so was devoted to the exoplanet project. To efficiently fill up the available observing time, we developed a semi-automatic scheduling process to observe transits during these times.

In this process, we define an observable span of the night between nautical dusk and dawn, and respect the "bright-sky" constraint set by the Moon's altitude. This created hard start and end points to our observing window for which we then create a list of candidate targets that are expected to transit at some point during this block of time. The list is drawn from a regularly updated master table of transiting targets observable from Dragonfly's geographic location. The table is principally composed of TESS Targets of Interest (TOIs), as well as some community-added targets (CTOIs), other known transiting planets, and supplemented by any specific priority targets of our team.

The nightly list of candidate observations gets filtered to remove targets requiring precision better than Dragonfly is likely to produce (a function of both magnitude and transit depth), and then sorted by priority. TESS TOIs have their own priority scheme determined internally by the TFOP group. Any specific targets chosen by our group are manually assigned priorities. If the full transit of a given target is visible during the night's observable span, separate ingress-only, egress-only, and full-transit observation options are all included in the candidate observation list to allow extra flexibility. Observations that include only the ingress or egress of the transit incur a penalty to their priorities, as full-transit observations are generally more useful and easier to detrend.

We then define the nominal start and end times for each candidate observation. For a full-transit observation, we extend a definable minimum baseline (plus timing uncertainty with a ceiling of 30 minutes) beyond the ingress and egress times. For ingress- or egress-only observations, a minimum observation duration around the ingress/egress time defines the observation bounds. Start times are further pushed earlier by a defined focus time buffer. This allows time for a focus run to occur if needed. Because Dragonfly's focus can slowly drift over time, it automatically refocuses between observations if the time since the last focus run exceeds a certain limit. At this point, the night's list of potential observations consists of many overlapping possibilities.

To build the final schedule, we slot observations into the available time window one by one, beginning with the most prioritized observations, until the available bright time is filled. Once the night is filled with as many observations as will fit, we expand the start and end points of each one to fill any remaining gaps in the night's bright time (again in order of priority). A schematic of a night's observing schedule is shown in Figure 2.1.

This finalized schedule for the night is added to a file containing an arbitrary number of other nights' schedules and sent to the control computer at the telescope site. The observing software monitors the current time and triggers each observation in sequence as the proper time arises.

A triggered observation begins an image-taking sequence with parameters specific to each target. Exposure time and intentional defocus are determined by the target's magnitude, and a cadence slower than the exposure time (plus readout) can be enforced if desired. The system also saves the exposure time to a nightly log so that appropriate calibration dark images can be taken.

Dragonfly automatically takes flat and dark calibration images in addition to the science images each night. The flats are twilight sky images, taken automatically around dawn and dusk at an integration time that produces optimal exposure of the CCD. Darks with exposure times matching the calibration flats are taken immediately after. We take additional dark images at dawn with exposure times matching any exoplanet science images taken during the night.

2.4. Data Reduction

Most of the available reduction software we investigated that was typically used by TFOP observers (e.g., `AstroImageJ`; Collins et al., 2017a) was not designed to efficiently handle multiple

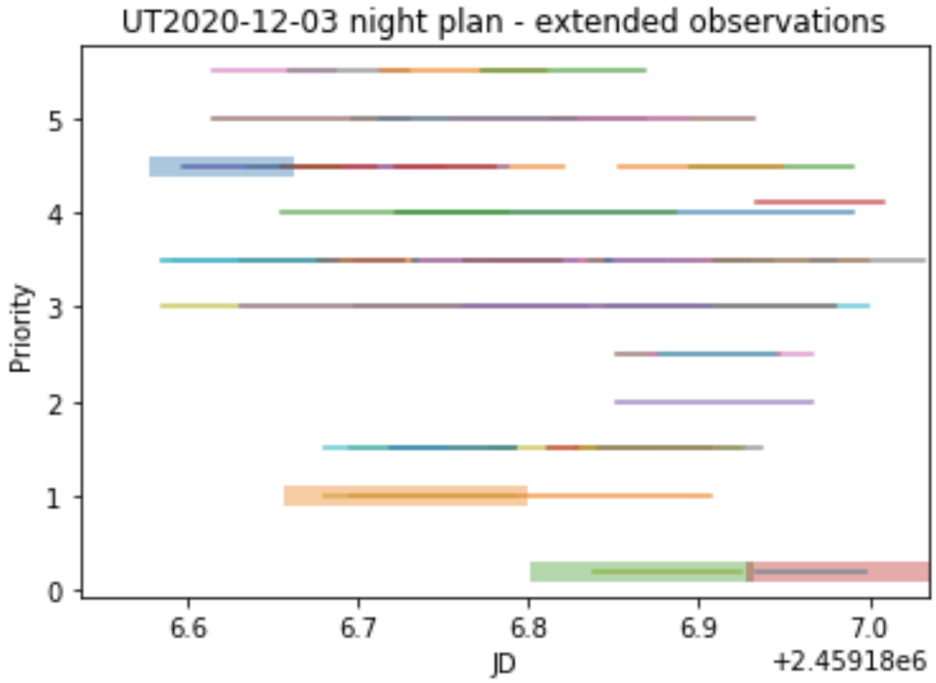

Fig. 2.1. Example of an observing night plan. Thin lines represent possible transit observations for the night. Each color is a different target/event, and overlaid thick lines represent the chosen ones. The chosen observations show the time extensions to fill gaps between observations or to extend to the edge of the Moon or twilight constraints. Observations that capture only ingress or egress are given a priority penalty to promote more full-coverage observations. Prioritized targets are lower on the y-axis (i.e., 0 is the most prioritized).

cameras with individual calibration and science images. We created our own pipeline to handle the reduction of Dragonfly's data (which could be parallelized when necessary).

In this reduction pipeline, everything occurs on a camera-by-camera basis. We first build a master flat file. This involves creating a data cube where each slice is one of the flat images taken during the night. Each slice is dark-subtracted using the dark file with the appropriate exposure time, then divided by its own median pixel value. At this point any pixels that display high variance across the data cube are flagged in a "bad pixel" map. All slices are then median-combined together, and the resulting image is again divided by its own median, producing our master flat file. By dividing the master flat by a low-pass filtered version of itself, we create a temporary "flattened" flat frame from which we can flag pixels that fall above or below limiting thresholds. The high variance and hot/cold flagged pixels together create a "bad pixel" map which is saved to file for future use.

We build a master dark file and associated bad-pixel map in essentially the same manner: creating a data cube of images with a specific exposure time, noting hot/cold pixels and large pixel variances, taking a median across images, and producing a bad-pixel map for those that show large variance or anomalously high or low pixel values.

Finally, we turn to the reduction of the science images. We begin by masking saturated pixels in the images before any calibration is applied. To reduce the science frames we cycle through them, subtracting the master dark (of matching exposure time), and dividing by the master flat. We have the option at this point of binning the pixels, and the choice of saving the image data as 16-bit integers or 64-bit floats. These measures can significantly reduce data volume. An astrometric solution to the field is added to the fits file headers using the software package from `Astrometry.net` (Lang et al., 2009).

2.5. Photometric Analysis

2.5.1. Extracting photometry

After calibration, science images are sent through our photometry extraction pipeline. Dragonfly's individual cameras do not point at exactly the same portion of the sky, nor do they behave identically when taking data. For this reason, we deal with only one camera at a time, extracting time-series photometry independently from each.

We first determine a source list for the camera. We use the `DAOStarFinder` module from Python's `photutils` package for this. We then loop through each image over the duration of the observation and remove any source that may have drifted out of the field of view due to imperfect tracking/guiding. We also cut out any sources fainter than a predefined ratio of the target's flux, leaving only sources with usefully comparable brightness. A master source file (for this particular camera) is created including the RA/Dec coordinates and relative brightness of each source.

With the source list built, we loop through each image in the observation to compute the photometry. For each image, the source coordinates are refined to account for imperfect astrometry. This refining can be done by a number of algorithms (e.g., center-of-mass or Gaussian fit) as desired. Photometry is calculated for a range of aperture sizes, and a sky annulus is defined to extend beyond them. The actual calculation is done with the `aperture_photometry` module of `photutils`. This employs a grey-pixel scheme to handle pixels on the edge of the aperture.

Finally we save the photometry to a data file. The net result for a single camera is a file for each exposure that contains the photometry measurements of each star in the source list at each aperture size.

The files also contain metadata on the timing of the observation, the airmass, aperture sizes used, measured PSF full-width-half-max (FWHM), and camera filter. These photometry files are then used in the next phase, extracting a light curve of the target star.

2.5.2. Building a light curve

To generate a light curve we choose which filter to examine, and what kind of aperture scheme to use. The seeing conditions and/or instrument focus may cause the FWHM of the stars to drift

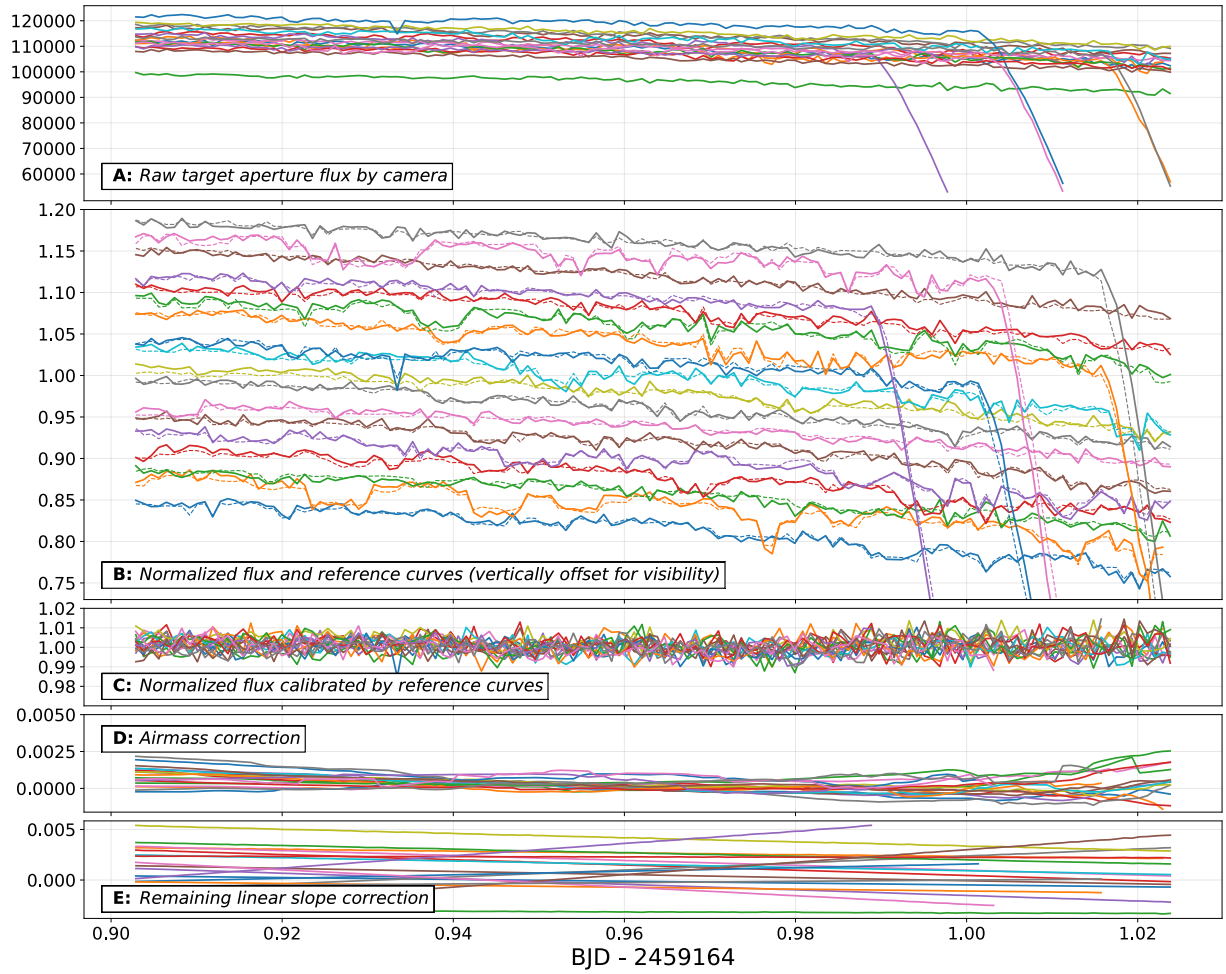

Fig. 2.2. Steps in the calibration process of the target's light curve. Individual lines show the data from individual cameras. *Panel A*: Raw flux counts from the chosen target aperture throughout the observation. *Panel B*: Solid lines indicate the normalized relative flux of the target. Dashed lines indicate the reference curve built from other stars in the field of view. Vertical offsets are applied for visibility. *Panel C*: With the reference star corrections applied, the light curve has had most of its systematic structure calibrated out. Anomalous portions of the light curve are masked at between B and C (e.g., sudden down-turns in flux due to imaging malfunctions seen in panels A and B). *Panel D*: A small airmass trend correction can be applied. *Panel E*: A small linear trend correction can be applied as well.

over time in any observation, but particularly in longer ones. To compensate for this, we often employ a variable aperture scheme. In such a case, we define the desired choice of aperture radius (r_{aper}) as a function of FWHM. Most commonly we use,

$$r_{\mathrm{aper}} = a * \mathrm{FWHM} + b, \tag{2.5.1}$$

where a is some scaling factor (typically $1 < a < 2$) and b is some offset in pixels (typically 0, ± 1, or ± 2). The final r_{aper} will actually be a ceiling function of the above calculation based on

the available $r_{\rm aper}$ increments made in the original photometry calculation (usually spanning 2–12 pixels spaced by 0.5 pixels). We typically will try several different aperture functions and settle on the one that produces the smallest RMS scatter in the final light curve. Various constant aperture options are also possible, but tracking the FWHM of the star often produces better photometric precision. Whatever aperture size scheme is used, aperture sizes are fixed across the image for a given time step for a given camera. This avoids introducing any changes in the *relative* photometry between stars in the image.

With an aperture function chosen, we have a raw flux light curve for every camera (Figure 2.2A). The next step is to choose the reference stars that will be used to build a reference light curve with which individual light curves can be normalized. We read in all the time-series photometry information (according to the chosen $r_{\rm aper}$ function) and normalize the flux of every star by dividing by its own median across time. The median for the target star is taken from points outside the expected transit region. We then cycle through each non-target reference star and divide its light curve by the median light curve across every *other* reference star. This removes instrument and environmental systematics common to all stars in the frame. Of this new collection of normalized and detrended reference stars we select the $N_{\rm ref}$ stars that show the lowest scatter in their normalized light curves. This procedure is then repeated in a second iteration, using only those $N_{\rm ref}$ "good" reference stars to calculate the median light curve with which the light curves of all sources are normalized. This avoids including the worst sources (i.e. poorest precision or stability) as reference stars.

The above process identifies the "best" reference stars in the field, in the sense that they have the lowest scatter. These $N_{\rm ref}$ stars are used to create a reference light curve with which to detrend the target. This is done by sigma-clipping the individual normalized light curves and taking their median across the stars. The reference curves (dashed lines) are displayed next to the target light curve (solid lines) in Figure 2.2B for comparison. The reference curve is divided by its own median, then the target's normalized light curve is divided by this reference, producing a calibrated light curve (Figure 2.2C).

The final detrending that we undertake is with airmass. Typically the airmass effect is very small because the cameras see very similar airmass across the $2.6^\circ \times 1.9^\circ$ field of view and the process discussed above removes trends common to all stars. However, airmass effects are somewhat SED dependent, and thus some residual trends could remain if the reference stars differ in colour from the target (or among themselves). For every star in the source list, we calibrate its light curve with the reference curve. A polynomial is fit to (X,Y) where $X \equiv$ airmass and $Y \equiv \log(\text{flux})$. The median across stars of the fitted polynomials is taken to produce a general airmass trend. The target light curve is detrended by dividing by the exponential of the median polynomial, using the target's airmass at each point. An example of the size of the airmass correction is shown in Figure 2.2D.

Sometimes a linear trend persists in a star's light curve in a given camera. To account for this, a straight line can be fit (using out-of-transit points) and removed from the light curve to remove any residual slope. An example of the scale of the linear correction is shown in Figure 2.2E.

Not every camera behaves ideally every night of operation. Focus problems or other hardware issues sometimes cause a camera to produce poor-quality images. Of the 48 cameras, it's not uncommon for a few to behave badly each night. Some of these are caught during the telescope's nightly setup and the offending camera excluded from taking data for the night, while others slip through and take exposures of varying quality. During the analysis phase, we make a visual check of the light curves from each camera and assess whether they were working properly. Cameras with very few data points (perhaps focus, saturation, or hardware issues) or cameras with highly deviant light curve shapes may be flagged and excluded from further analysis. In Figure 2.2, we see 5 cameras showing sharp drops in the target's flux. This appeared to be a hardware malfunction affecting the recorded CCD exposure that kicked in at different points for each camera. Instead of throwing out the entire light curves from these cameras, we simply mask the anomalous region (in a step between panels B and C).

Having constructed a normalized and detrended light curve for each individual camera, we combine them into a single light curve for each filter to improve the scatter (nominally by factor $\sqrt{N_{\rm cams}}$). We bin the data by any number of exposures (typically aiming for 4–5 min bins in accordance with TFOP guidelines), and combine the relative flux data within the bin by weighted mean, clipped mean, or median, as desired.

2.6. Performance

2.6.1. Example results

To showcase the details of an exoplanet observation, we present a closer inspection of two examples that demonstrate many of the strengths of the instrument and the challenges that are encountered.

TOI-1683.01:

We observed the target TOI-1683.01 on 2020-11-10, aiming to capture a predicted transit occurring that night. The host star is an $m_V = 11.0$ target and was observed with a 60-second exposure time (with a 15-second read-time producing a cadence of 75 seconds). The observation spanned a total of 2.9 hours: 53 min pre-ingress, 82 min in transit, and 38 min post-egress.

The observation had a total of 18 r-cameras and 16 g-cameras operating with acceptable performance out of an available 24 cameras per filter. As can be seen in Figure 2.3, the overall photometric precision improves with more cameras added to the analysis ($\propto \sqrt{1/N_{\rm cams}}$), as well as when creating time-bins across several exposures ($\propto \sqrt{1/N_{\rm exp}}$). We achieved a final precision of 0.7 ppt with 5 min bins (1.4 ppt unbinned) in r, and 0.8 ppt binned (1.6 ppt unbinned) in g.

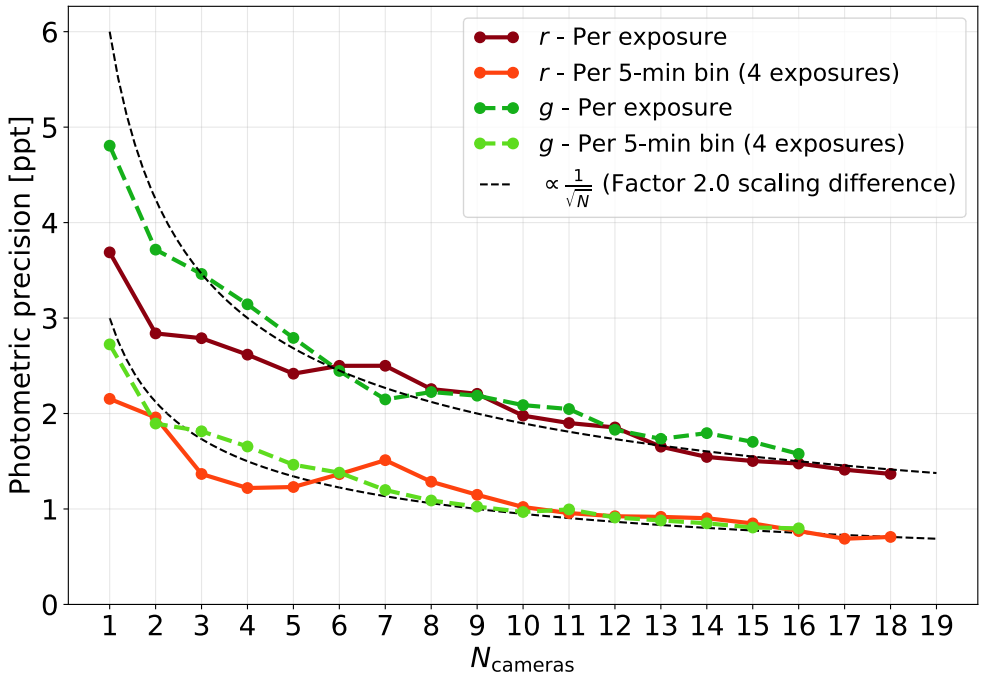

Fig. 2.3. Improvement of photometric precision as a function of the number of cameras used in the analysis. These data are from TOI-1683.01 (shown in Figure 2.4). The dashed black lines are $\propto \sqrt{1/N}$ and differ by a factor of 2 between one another, in accordance with the 4-fold binning of exposures. The stochastic nature of individual cameras plays a heavier role in the left-hand edge of the plot but quickly begins to average out with more cameras.

The observation's full camera-combined light curve is shown in panel A of Figure 2.4. Panels B–E of the figure show representative plots of how a single camera recorded various observing parameters. Panel B records the FWHM of the target throughout the observation and the accompanying choice of aperture radius. Notice the aperture size function tracks the FWHM, with a discretization of 0.5 pixels. Panel C tracks the sky background levels. In this case, things were stable until the end of the observation where dawn caused a large increase. Panel D reports the raw flux counts in the target aperture. In the current example, the slow drop in flux roughly matches the worsening airmass (also plotted on an overlaid axis). Panel E displays the target's centroid x,y pixel position on the detector. The drift seen here shows the imperfect tracking of the instrument.

In fitting a transit model using the `Juliet` python package with its built-in nested sampling fitting routine, we determine the depth of the event to be $\delta = 1.31^{+0.40}_{-0.22}$ ppt with a timing of an uncertainty of $^{+2.3}_{-4.1}$ min. As the prior timing uncertainty on this transit was 55 min, our detection produced a substantial improvement to the target's ephemeris. With a ~1 ppt transit event, this observation was among the shallowest transits we are able to confidently measure (~4σ).

In this particular case, our instrument systematics were minimal, the focusers were stable, and sky brightness conditions were steady (excepting the sharp rise near dawn). We experienced none

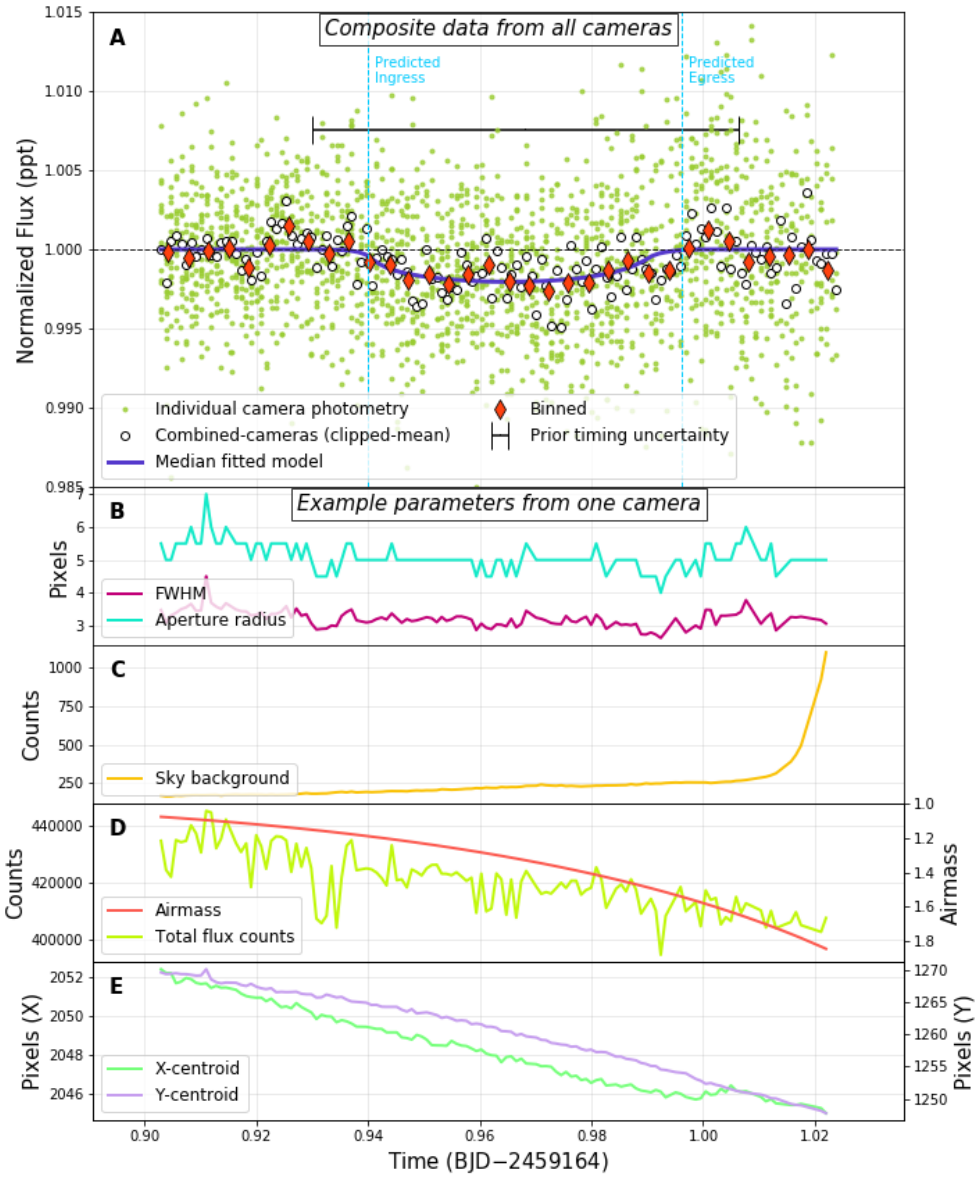

Fig. 2.4. Example observation of TOI-1683.01, a relatively problem-free transit detection. Here we see how stable conditions can lead to excellent precision (∼0.7 ppt) in ∼5 minute bins *Panel A:* The light curve from the r-filter cameras and overlaid transit model. The black horizontal error bar indicates the prior uncertainty of the predicted transit midpoint (improved from 55 min to ∼3 min). Panel A shows a combination of all cameras, whereas panels B–E show parameter histories from a single example camera. *Panel B:* Small changes in the target's FWHM over time were tracked by our aperture size choice. *Panel C:* The sky background level was stable until dawn. *Panel D:* Raw flux counts did not show dramatic variability but tracked with slowly worsening airmass throughout the observation. *Panel E:* The x,y pixel position drifts steadily due to imperfect telescope tracking.

of the time-dependent or inter-camera variances that can often lead to poor performance. As such, we achieved a 5-minute binned precision of ∼0.7 ppt.

TOI-1302.01:

As a second example, we showcase an observation that encountered more challenges. On 2021-05-23 we undertook an observation of TOI-1302.01, a large planet around an $m_V = 10.9$ host star. Using an exposure time of 22 s (we had adjusted our magnitude–exposure time function since the previous example observation) we ended up with a 36-second imaging cadence. The observation spanned 5.5 hours: 15 min pre-ingress, 221 min in transit, and 94 min post-egress. We had 21 r-cameras and 15 g-cameras in operation.

Figure 2.5 shows a summary of the TOI-1302.01 observation. The large scatter in the light curve data (panel A) makes it immediately obvious that some issues were encountered during this observation. Firstly, the focus was drifting for the first portion of the window. Panel B shows the general upward trend in the target's FWHM before being reset back to ∼4 pixels. For this observation, we were employing regularly spaced focus breaks to mitigate focus drift, as can be seen in the short data gaps. Fortunately, the drift was small and slow enough that our refocusing breaks could compensate and there was not a sizeable effect on the measured photometry.

The second and more impactful issue was the strongly variable sky brightness throughout the latter half of the observation window (panel C). This was presumably due to intermittent cloud cover. The worst segments of the light curve correspond with the spikes in sky brightness and loss of total flux counts (panel D). However, outside these segments, the precision was sufficient to clearly trace out the transit shape.

As such, we are still able to fit a transit model and constrain certain parameters. We measured the transit depth to be $9.92^{+0.54}_{-0.42}$ ppt and timing precision of $^{+1.1}_{-1.2}$ min. Our final 4.8–minute binned precision for the portion of the light curve before the sky variability kicked in came out to ∼1.5 ppt.

The clear weather at the beginning of the observation allowed for good depth and timing determination before the variable weather started. However, the precision reached before the poor weather began was still about a factor of two worse than the previously discussed TOI-1683.01 example. Choice of exposure time likely played a small role here. With a ∼15 second read-out time, TOI-1302's 22-second exposures lead to a 60% on-sky integration duty cycle, compared to TOI-1683's 80%. This may have also affected the SNR of available reference stars, compounding the issue in terms of light curve normalization. Some focus drift correction effects or smaller-scale seeing conditions may also have contributed to the poorer precision.

2.6.2. Ensemble results

The Exo-Dragonfly project has been an exercise in incremental improvement: from the data-taking procedures of the instrument itself to the analysis pipeline. Under ideal circumstances (i.e., the hardware, software, and weather are all cooperative) we can achieve better than 1 ppt precision in a single-visit observation with 4–5 minute bins. We have demonstrated this precision for target magnitudes in the range of $8.5 < m_V < 13$, however, the reliability of such precision decreases for

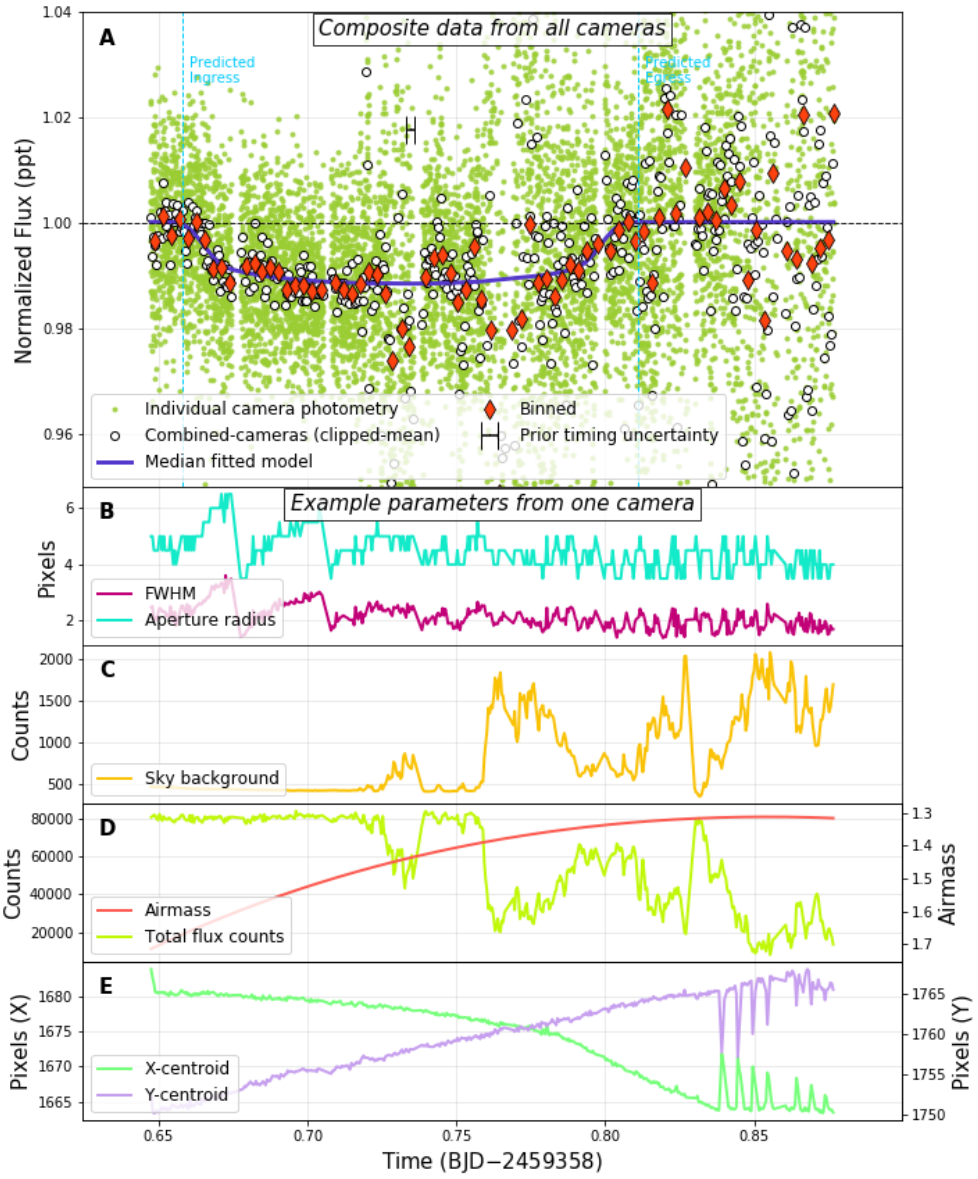

Fig. 2.5. An example observation of TOI-1302.01 shows how fluctuations in various data or observing parameters can dramatically affect performance throughout an observation. *Panel A:* The light curve from the r-filter cameras and overlaid transit model. The black horizontal error bar indicates the uncertainty on the predicted transit time. Short observing gaps indicate re-focusing breaks. Panel A shows a combination of all cameras, whereas Panels B–E show parameter histories from a single example camera. *Panel B:* Small changes in the target's FWHM over time were tracked by our aperture size choice. *Panel C:* The sky background began the night in a stable fashion but experienced dramatic shifts later on. *Panel D:* Raw flux counts showed strong variability, inversely proportionate to the sky brightness. *Panel E:* The x,y pixel position drifts due to imperfect telescope tracking.

the fainter targets. Figure 2.6 shows the achieved precision for an ensemble of 112 observations

acquired over the course of 3 years. It shows that ~0.5 ppt acts as the rough sensitivity floor of the instrument when we control for number of cameras and on-target integration time.

We make these after-the-fact corrections to the precision values plotted in Figure 2.6 to mitigate certain differing parameters between observations. A given observing night typically has several offline cameras and the number of these cameras can range from a small handful to an entire mount, depending on the technical issues at play. Thus, plotting the performance of a 15-camera observation beside a 22-camera observation is not a fair comparison. As Gaussian photometric precision improves with the square root of the cameras included (e.g., Figure 2.3) we employ a scaling of all the points in Figure 2.6 to mimic a standard 20-camera observation.

In a similar vein, differing exposure times for targets with similar magnitudes introduce another bias. Exposure times sometimes differ due to our adjusting the magnitude–exposure time function applied to the automated observation scheduling over the course of more than three years of operating. With a fixed readout time, shorter exposures experience poorer photon-collecting efficiency. We try to correct this by scaling the measured precision to a benchmark integration time (using $\sigma_{\mathrm{phot}} \propto \sqrt{1/t_{\mathrm{integration}}}$). We split the observations in Figure 2.6 into magnitude bins and find the mean integration time for observations in that bin. This integration is the number of seconds spent collecting photons within the 4–5-minute temporal bin we typically report. All observations in the magnitude bin have their precision values scaled as if they shared this mean integration time.

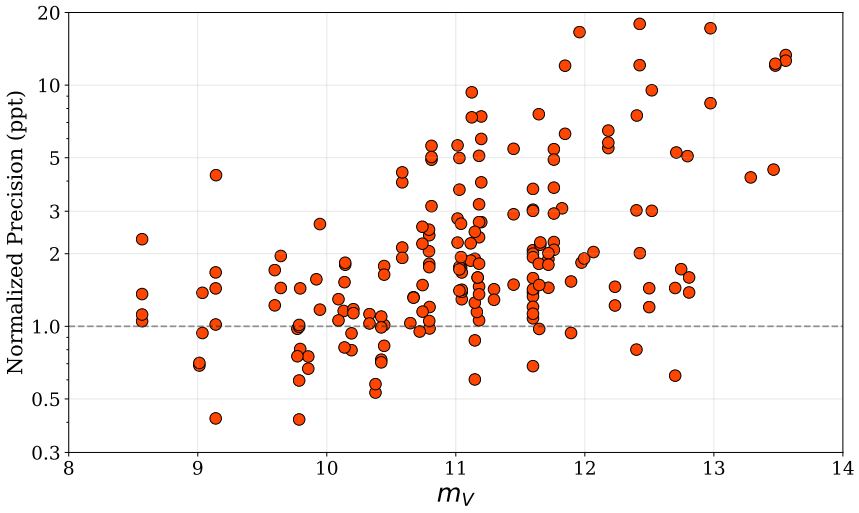

Fig. 2.6. Photometric precision reached by Dragonfly during single-visit observations using the *r* filter. Reported precision is for 4–5 minute bins and includes a normalization process to more fairly compare observations of stars with similar magnitude but that used different integration times. It also applies a compensation for variable numbers of active cameras between observations, normalizing everything to a standard of 20 cameras.

We find that Exo-Dragonfly operates best within certain target magnitude bounds. Targets with $m_V \gtrsim 13$ require very long exposure times ($\gtrsim$4 min) to build reasonable flux counts. With these faint targets, it becomes impossible to bin points and achieve temporal precision better than ~8 min. This sets Dragonfly's approximate functional magnitude limit for time-series observations of faint target transits.

We also encounter a limitation on bright targets. We rely on reference stars of comparable magnitude in the field of view to detrend our light curves. Naturally, the number of quality reference stars in a given sized patch of the sky drops rapidly for brighter targets. Using fewer and/or fainter reference stars can contribute to poorer photometric precision. To allow for longer exposures, we have experimented with applying an intentional focus offset to spread the flux over more pixels. This led to mixed success. Indeed longer exposures could allow for more flux accumulation on the target and reference stars, but the focus offset magnified existing focus-control issues leading to unreliable performance.

Most results displayed in this study are for the r-filter as it generally produced better performance. On average, the g filter had poorer precision by about 1 ppt, though this difference was magnitude-specific. Targets with $m_V \lesssim 11$ showed no systematic improvement from one filter to the other but targets with $m_V \gtrsim 11$ tended to show a comparative detriment in the g-filter of 1–2 ppt, and frequently much worse for the faintest stars ($m_V \gtrsim 12$).

2.6.3. Challenges encountered

We have seen that Dragonfly is capable of achieving very high ($\gtrsim$0.5 ppt) photometric precision in optimal cases. However, the spread in actually achieved precision for a given observation begs the question of what exactly these optimal conditions are, and what deviations are hurting the performance.

We looked into a number of potential observation metrics that might correlate with poorer precision. Some factors are straightforward to assess and account for. Others pose a challenge because the two 24-camera mounts and all 48 individual cameras do not behave identically to one another and their respective differences are not necessarily consistent night-to-night, or even within a single observation.

As discussed above, the number of cameras used in an observation has an obvious impact on achieved precision. This is well-understood and can be statistically accounted for. However, given the inter-camera variability, the applied correction will not be perfect, retaining some spread in the distribution of achieved precision.

Beyond camera counts and integration efficiencies, which can be accounted for, the factor we determined to have the strongest effect on photometric precision (besides magnitude) was related to the sky background. When the sky was generally brighter (diffuse clouds, proximity and phase of Moon, etc.), more time-variable (passing clouds), and/or more different between cameras (hardware

sensitivity, image artifacts), the precision worsened. We additionally noted that higher variability in the target's FWHM (focus control), the total raw flux counts (changing sky conditions), and/or the x,y pixel position (imperfect tracking) showed small correlations with achieved precision. A higher airmass was also found to play a minor role.

A few other factors sometimes cause outliers in the typical performance. Imperfect focus control frequently produced FWHM variability over the course of an observation. While we can take steps to accommodate the changes in flux distribution with aperture changes, some specific cases pose more serious issues. The focus may unexpectedly sharpen to the point where peak pixel values become very high. This may lead to saturation and loss of data points or more subtly, a departure into the non-linear regime of the detector. As a result, the number and quality of data points at certain points in the light curve can show deviations from expectation. On the other side of focus variability, excursions towards larger FWHM can produce an effect stronger than simply the diffusion of flux. Large aperture sizes while tracking a changing FWHM may incorporate additional flux from a close neighbor star. We have encountered cases where one portion of the light curve shows excellent precision with a low FWHM, but then deteriorates dramatically once the FWHM expands to start blending with a neighbor.

Sometimes there is no obvious cause for a disturbance during nightly operations. One such issue we periodically encountered was spurious image artifacts in the science data. Strong background gradients that overwhelm the stellar signals would sometimes appear on the images from one or a few cameras. These images typically had to be culled from the light curve or sometimes the entire camera was excluded from the analysis. The cause of these issues was not apparent.

While partial transits (i.e., ingress or egress only) can in theory provide much of the constraining power desired in a follow-up observation, we found them far more challenging to analyze than full transits. Because the SNR of individual cameras is so much lower than the combined light curve, the transit is usually lost in a single camera's noise. Also, systematics present in individual cameras can be non-negligible, only averaging out across many cameras. We found that having an anchoring baseline on either side of the transit to use in normalizing/detrending achieved far more success than when a baseline on only one side is available. Partial transits, with their shorter duration, can be useful in filling gaps in a night's observing schedule, but we focused on prioritizing full-transit observations.

2.6.4. Suitability for transit follow-up

Dragonfly has shown itself to be a useful transit observer, capable of making many of the required measurements for TESS candidate follow-up. A common false positive scenario in TESS data is due to the instrument's low spatial resolution. Large pixels allow for nearby eclipsing binary (NEB) systems to blend with the target and mimic a planetary-scale transit event through diluted flux. One of the most basic and useful ground-based follow-up contributions to the TESS mission

is spatially resolving the source of the transit signal. It is standard procedure within TFOP to check stars within a 2.′5 radius of the target for NEB signals during the expected time of transit. Detecting the transit on-target, detecting an NEB, or making significant non-detections on neighboring objects all help to properly classify a TESS candidate planet. With its 2.″8 pixel^{-1} plate scale and 5″–10″ stellar FWHM, Dragonfly is very capable of providing this service.

Another frequent follow-up requirement for a TESS candidate is to monitor transit timings. Sometimes this is due to an imprecise ephemeris and the orbital period simply needs refining (e.g., see the prior timing uncertainty in panel A of Figure 2.4). Other times, intrinsic transit timing variations (TTVs) are detected (or suspected) and can be tracked over time, revealing the gravitational effects of other objects in the system. Dragonfly can achieve a fitted timing precision on the order of ∼2 min when the transit is detected with reasonable SNR.

Refining the orbital ephemeris has broader implications than simply tightening the error bars on a cataloged value. Predictions on future transit timings have an uncertainty that scales with $\sigma_P n_{\rm epoch}$, where $n_{\rm epoch}$ is how many transits have occurred since the period uncertainty (σ_P) was last measured. Unless a target has its transits continually observed, the ability to predict future transits depreciates over time. Attaining a high-precision ephemeris ensures it will take a long time before the timing prediction deteriorates to problematic levels. Otherwise, the ephemeris precision can drift and a target can rapidly become "unschedulable" for future transits.

Another diagnostic commonly requested for false-positive rejection is a chromatic measure of transit depth. If the transit event is caused by eclipsing binary stars instead of a planet, then differing surface temperatures of the two stars (and non-negligible flux from the secondary) cause changes in transit depth across different filters. A planetary transit, which is effectively a black shadow across the stellar surface, will be achromatic (discounting the very small atmospheric effects searched for in transmission spectroscopy efforts). Dragonfly's two filters are too close together to provide much in the way of chromatic distinction, as typically one would use widely separated filters. However, the fact that Dragonfly is not a filterless white-light instrument means it could be used as a comparison point against another instrument (e.g., the Dragonfly *r* filter and another instrument's much bluer filter).

2.6.5. Contributing to TESS's Exoplanet Follow-up Observing Program

When our observations achieved suitable precision for a given target observation (i.e., a transit detection or significant non-detection) and cover an adequate time window, we submitted our findings to the TFOP repository. Our submissions have led to many ephemeris and exoplanet parameter refinements, as well as a number of false positive determinations. The submissions are listed in Table 2.1 and the data become public[2] after a 1-year probationary period. This

[2] https://exofop.ipac.caltech.edu/tess/

period allows time to accumulate observations on various targets before TFOP authors begin their publications.

The automated nature of our data acquisition has also accumulated a sizeable backlog of unprocessed observations that can greatly expand upon the existing submissions. They will be submitted as they are processed. There are roughly a half-dozen targets that are nearly ready for submission, and likely many dozens more that have yet to be reduced and investigated. The available work-hours dedicated to the observation processing within the very small Exo-Dragonfly team is the main bottleneck to submission productivity. This is something that could be improved upon in the future.

Table 2.1. TFOP Submissions

Target	Obs. Date	Submitted
TOI-573.01	2019-12-19	2020-04-24
TOI-943.01	2019-10-21	2020-04-24
TOI-1199.01	2022-02-19	2022-07-11
TOI-1246.02	2021-05-28	2021-10-28
TOI-1248.01	2021-01-04	2022-08-01
TOI-1302.01	2021-05-24	2021-08-24
TOI-1683.01	2020-11-11	2021-06-07
TOI-1694.01	2021-01-02	2021-07-23
TOI-1765.01	2020-06-29	2021-10-28
TOI-1823.01	2021-12-20	2022-07-29
TOI-1870.01	2021-05-25	2021-07-23
TOI-2180.01	2020-08-28	2020-11-23
TOI-2180.01	2020-09-02	2020-11-20
TOI-2288.01	2021-05-21	2021-10-08
TOI-2494.01	2022-03-16	2022-08-05
TOI-3808.01	2022-04-05	2022-08-16
TOI-3814.01	2022-03-12	2022-07-15
TOI-3856.01	2022-02-16	2022-07-18
TOI-4087.01	2022-04-07	2022-08-05
TOI-4436.01	2022-03-16	2022-08-01

Note: Dates are UTC.

2.7. Summary & Discussion

Dragonfly began as an ambitious project to better understand galactic structure, with no intention to pursue exoplanet science in its original mission statement. However, through this collaboration, we have been able to repurpose Dragonfly's largely unused bright time to the fruitful study of exoplanets. We have developed the infrastructure to enable Dragonfly's use for future time-series photometric studies, be it for exoplanet science or other subjects. The precision we achieve in Dragonfly's effective magnitude sensitivity range makes it competitive with other prominent, small, ground-based observatories (e.g., LCOGT (Brown et al., 2013), WASP (Pollacco et al., 2006), KELT (Pepper et al., 2007, 2012)). We have shown that an array of small, inexpensive, off-the-shelf cameras is a viable alternative to larger dish (1–2 m) telescopes for these types of transit observations.

2.7.1. Future improvements

While the Exo-Dragonfly project has seen a lot of success thus far, it is still an in-progress project and has room for improvement. There are a few areas that could benefit from additional development.

Certain technical hardware improvements would aid in the reliability of the instrument. Focus drift is generally present to varying degrees and existing focus routines can be slow and disruptive. Perhaps live-tracking with temperature or closed-loop monitoring could provide more on-the-fly focus control.

More thorough reporting of a number of internal and external observation parameters could also help with understanding and correcting departures from peak performance. By collecting more exposure-by-exposure details on things like weather, seeing conditions, and focus levels, we could more clearly identify and potentially detrend against their effects on the photometry.

During analysis, the process of selecting and utilizing reference stars could likely be refined. Currently, targets of all brightness receive the same treatment for choosing reference stars (i.e., the selection of the N_{ref} sources with the lowest photometric scatter and variability in the time series, where N_{ref} is somewhat arbitrarily chosen and common to most observations). In reality, brighter targets will have fewer comparably bright sources in the field of view. Including too many faint reference stars may actually be detrimental to the calibration of these light curves. The full impact of the N_{ref} choice (or alternatively, some quality threshold cutoff) should be investigated more thoroughly in the future.

The efficiency and scientific output of the Exo-Dragonfly program could be markedly increased with improvements to photometry and analysis automation. At present, each observation requires a certain level of hands-on processing, usually involving the troubleshooting of anomalous data and fine-tuning of a few parameters. This is generally acceptable for individual targeted observations, but impractical for larger surveys. The level of robustness in the photometry and analysis pipeline

is not yet at the level where a night's observations could be ready for presentation at the push of a button. Once this is remedied, the instrument would become vastly more productive.

2.7.2. Operational considerations

Through extensive trial and error working with and fine-tuning Exo-Dragonfly, we have discovered a few factors/practices that may be worth noting for other researchers with plans for small composite-camera telescopes.

The modular nature of the instrument (many cameras act mostly independently) certainly creates its own share of operational and data processing headaches, but it also provides a degree of redundancy. Issues with specific cameras do not cripple the entire telescope. Repairs and hardware swaps can be carried out with minimal interruption of operations. Indeed, relatively inexpensive individual replacement parts can be set aside for immediate swap-in when a component fails. The instrument design also allows for modular upgrades. New mounts with new cameras can be installed to increase the total collecting power or introduce additional filters.

A drawback of the modular structure becomes quickly apparent when considering the data output volume. Data production rate and the size of required storage quickly become formidable as the scale of the instrument increases. With an equivalent collection area to a $\sim$1 m telescope, Dragonfly produces 48 images per exposure compared to a single image from a more standard design. This might be mitigated by on-site image stacking, though the system would have to be able to robustly align images and reject poor-quality data. This is not a feature we have implemented at present.

Acknowledgements

We are extremely grateful to the entirety of the Dragonfly team, led by Bob Abraham and Pieter van Dokkum. The project would not have been possible without the team's generous sharing of bright sky time, and their willingness to broaden the scope of Dragonfly's original research plan.

Software

`numpy` (Harris et al., 2020a), `matplotlib` (Hunter, 2007a), `astropy` (Astropy Collaboration et al., 2013, 2018, 2022), `pyasl` (Czesla et al., 2019a), `AstroPlanner`[3], `photutils` (Bradley et al., 2022), `Juliet` (Espinoza et al., 2019a), `batman` (Kreidberg, 2015a), `dynesty` (Koposov et al., 2023; Speagle, 2020), `celerite` (Foreman-Mackey et al., 2017)

[3]https://www.astroplanner.net/index.html

2.8. Specific Contributions

The Exo-Dragonfly project was intended from the start to comprise the backbone of my eventual Ph.D. thesis. As such, it was almost entirely carried out by me, though with plenty of guidance and mentorship by my thesis advisor, David Lafrenière. I conducted all of the communication and coordination with the original Dragonfly team, barring initial introductions. This involved planning the instrument alterations, learning the back-end of Dragonfly's operation, writing and testing new code functionalities, and ensuring that the new exoplanet operations would not interfere with existing processes and work being done. The Dragonfly team provided ample instruction and trouble-shooting assistance, but actually making changes was my own responsibility.

I developed the semi-automated observation scheduler with some algorithmic help from David. Its interface with the TFOP target list and with the Dragonfly system were my own work. I built the reduction pipeline around a core procedure written by Étienne Artigau, who made the first exploratory test observations with Dragonfly before I even began my Ph.D. program. Étienne's contribution laid out the basic reduction groundwork (i.e., master dark and flat creation, and science image calibration). The rest of my pipeline involved detailed file handling, correcting anomalous file header info, and adding a World Coordinate System to the images. As always, David provided helpful oversight.

I also wrote the large majority of the photometry and analysis pipeline. Again, David provided helpful insight on the procedures, but it was implemented by me. This pipeline extracts photometry from the stars in the field with multiple aperture sizes, manage an ID system for stars across the time-series, and produces light curves for the target star and many others in the field, all on a camera-by-camera basis. The analysis code creates reference light curves from appropriate field stars and uses them to correct systematics in the target and other reference stars. It also carries out airmass detrending, reports on many observing parameters (e.g., airmass, FWHM, target pixel, position, etc.) and combines the individual cameras' light curves into a single output light curve. I also wrote code that can fit transit models to the data if required, using established MCMC and nested sampling packages. The final stages of the pipeline generate data files and summary figures required for TFOP submissions.

Beyond the software development, I also handled nearly all of the day-to-day work involved in running the exoplanet-related telescope operations. I would act as the "on-duty observer" for Dragonfly for the one week of the month around the full Moon. The remaining weeks were handled by a rotating roster of other Dragonfly team members. The observer was responsible for nightly setup of the instrument, involving system checks and communication with the on-site support staff when issues arose. I would also maintain a log of exoplanet-related observations and manage the exoplanet data storage and transfer. The data management turned out to be a nontrivial task as the initial site storage and transfer infrastructure were insufficient for our high data volume. A process

that began with frequent back-and-forth mailing of hard drives was eventually updated to digital transfer once the on-site internet bandwidth was upgraded.

Once the infrastructure and operational procedures were largely in place, the major ongoing task was to carry out the case-by-case analysis as observations came in. While the data-taking and reductions were largely automated, the steps involved in photometry extraction and light curve analysis often required manual intervention. As such, with the flood of incoming observations, this is where the main bottleneck occurred. Amongst numerous other priorities, I would process observations when I had available time. Occasionally, we would take on undergraduate student interns to help out with the project and give them hands-on research experience. I acted as a general mentor to the students and taught them about telescopes, photometry, exoplanets, and the like. In their short times with our team, they were able to provide assistance in the data processing or other system upgrades, though this was often somewhat offset by the learning curve involved in bringing them up to speed. I believe we provided some valuable experience in exchange for their time and assistance.

Towards the end of my doctoral program, I finalized plans for the overview paper presented in this chapter. I carried out a meta-analysis of our operations to build a sense of the overall performance of the instrument, and was aided by one of our undergraduate students who helped get this started by compiling performance results. With specific examples, as well as some general metrics, of Dragonfly's performance, I wrote the entirety of the paper included here. It is our intent to submit it for publication shortly after completion of this thesis.

Chapter 3

Validation of TOI-1221 b: A Warm Sub-Neptune Exhibiting Transit Timing Variations around a Sun-like Star

This manuscript was published in the refereed journal *The Astronomical Journal* on April 28, 2023

Christopher Mann [1,2], David Lafrenière [1,2], Diana Dragomir [3], Samuel N. Quinn [4], Thiam-Guan Tan [5], Karen A. Collins [4], Steve B. Howell [6], Carl Ziegler [7], Andrew W. Mann [8], Keivan G. Stassun [9], Martti H. Kristiansen [10], Hugh Osborn [11,12], Tabetha Boyajian [13], Nora Eisner [14], Coel Hellier [15], George R. Ricker [11], Roland Vanderspek [11], David W. Latham [4], S. Seager [11,16,17], Joshua N. Winn [18], Jon M. Jenkins [19], Jesus Noel Villaseñor [11], Brian McLean [20], Pamela Rowden [21], Guillermo Torres [4], Douglas A. Caldwell [19,22], Kevin I. Collins [23], and Richard P. Schwarz [4]

[1] Département de Physique, Université de Montréal, Montréal, QC, Canada

[2] Trottier Institute for Research on Exoplanets (iREx)

[3] Department of Physics and Astronomy, University of New Mexico, 1919 Lomas Blvd NE Albuquerque, NM, 87131, USA

[4] Center for Astrophysics | Harvard & Smithsonian, 60 Garden Street, Cambridge, MA 02138, USA

[5] Perth Exoplanet Survey Telescope, Perth, Western Australia, Australia

[6] NASA Ames Research Center, Moffett Field, CA 94035, USA

[7] Department of Physics, Engineering and Astronomy, Stephen F. Austin State University, 1936 North St, Nacogdoches, TX 75962, USA

[8] Department of Physics and Astronomy, The University of North Carolina at Chapel Hill, Chapel Hill, NC 27599-3255, USA

[9] Department of Physics and Astronomy, Vanderbilt University, Nashville, TN 37235, USA

[10] Brorfelde Observatory, Observator Gyldenkernes Vej 7, DK-4340 Tølløse, Denmark

[11] Department of Physics and Kavli Institute for Astrophysics and Space Research, Massachusetts Institute of Technology, Cambridge, MA 02139, USA

[12] Physikalisches Institut, University of Bern, Gesellsschaftstrasse 6, 3012 Bern, Switzerland
[13] Louisiana State University 202 Nicholson Hall Baton Rouge, LA 70803, USA
[14] Sub-department of Astrophysics, University of Oxford, Keble Rd, Oxford, UK
[15] Astrophysics Group, Keele University, Staffordshire ST5 5BG, UK
[16] Department of Earth, Atmospheric and Planetary Sciences, Massachusetts Institute of Technology, Cambridge, MA 02139, USA
[17] Department of Aeronautics and Astronautics, Massachusetts Institute of Technology, Cambridge, MA 02139, USA
[18] Department of Astrophysical Sciences, Princeton University, 4 Ivy Lane, Princeton, NJ 08544, USA
[19] NASA Ames Research Center, Moffett Field, CA
[20] Space Telescope Science Institute, 3700 San Martin Drive, Baltimore, MD, 21218, USA
[21] Royal Astronomical Society, Burlington House, Piccadilly, London W1J 0BQ, UK
[22] SETI Institute
[23] George Mason University, 4400 University Drive, Fairfax, VA, 22030 USA

Abstract. We present a validation of a long-period ($91.68278^{+0.00032}_{-0.00041}$ days) transiting sub-Neptune planet, TOI-1221 b (TIC 349095149.01), around a Sun-like ($m_V = 10.5$) star. This is one of the few known exoplanets with a period >50 days, and belongs to the even smaller subset of which have bright enough hosts for detailed spectroscopic follow-up. We combine Transiting Exoplanet Survey Satellite light curves and ground-based time-series photometry from the Perth Exoplanet Survey Telescope (0.3 m) and Las Cumbres Observatory global telescope network (1.0 m) to analyze the transit signals and rule out nearby stars as potential false-positive sources. High-contrast imaging from the Southern Astrophysical Research Telescope and Gemini/Zorro rule out nearby stellar contaminants. Reconnaissance spectroscopy from CHIRON sets a planetary scale upper mass limit on the transiting object (1.1 and 3.5 $M_{\rm Jup}$ at 1σ and 3σ, respectively) and shows no sign of a spectroscopic binary companion. We determine a planetary radius of $R = 2.91^{+0.13}_{-0.12} R_\oplus$, placing it in the sub-Neptune regime. With a stellar insolation of $S = 6.06^{+0.85}_{-0.77} S_\oplus$, we calculate a moderate equilibrium temperature of $T_{\rm eq} = 440$ K, assuming no albedo and perfect heat redistribution. We find a false- positive probability from the `TRICERATOPS` tool of FPP = 0.0014 ± 0.0003 as well as other qualitative and quantitative evidence to support the statistical validation of TOI-1221 b. We find significant evidence ($>5\sigma$) of oscillatory transit timing variations, likely indicative of an additional nontransiting planet.

Unified Astronomy Thesaurus concepts: Exoplanet astronomy (486); Exoplanet systems (484); Exoplanet dynamics (490)

3.1. Introduction

In July of 2018, the Transiting Exoplanet Survey Satellite (TESS) mission (Ricker et al., 2015) began its task of observing nearly the entire sky for exoplanets transiting around bright and nearby stars. Although the Kepler mission (Koch et al., 2010) revolutionized exoplanet science with its explosion of discoveries, most of the Kepler targets are quite faint. The brightness of TESS host stars allows for much more detailed follow up in terms of mass measurement and atmospheric characterization. At the time of writing, the mission has produced 6133 TESS Objects of Interest (TOIs), of which 1646 have been identified as false positives and only 282 confirmed as *bona fide* exoplanets (Guerrero, 2020). The follow-up work required to verify and confirm the still-growing list of TESS candidates is substantial, challenging, and yet absolutely essential to the overall success of the mission.

Not all exoplanet systems are equal in their ease of detection and characterization. Those with deeper transits (i.e. large planets and/or small host stars) produce strong signals in their light curves and shorter-period planets have both higher transit probabilities and more frequent transit events that require less baseline time coverage to observe. In direct contrast, long-period planets are both harder to initially detect, and allow for only infrequent follow-up opportunities. The vast majority of known exoplanets for which we have both reliable mass and radius measurements have periods $\lesssim$ 50 days (NASA Exoplanet Archive, 2022).

Despite the poorer statistics on smaller, cooler exoplanets there has arisen a clear bimodal distribution of radii split on either side of ~2 Earth radii that also has a dependence on the planet's insolation flux (Fulton et al., 2017). There are competing ideas as to why the super-Earth/sub-Neptune valley occurs (e.g. photo-evaporation: Owen & Wu (2017); Jin & Mordasini (2018); Rogers & Owen (2021); cooling-luminosity driven loss: Gupta & Schlichting (2019); and gas-poor formation: Lee & Chiang (2016); Lopez & Rice (2018)). There is still a major question of whether cool sub-Neptunes larger than 2 $R_\oplus$ are mostly rocky or have sizeable H/He atmospheres. Stellar insolation's effect on atmospheric inflation may play a prominent role in distinguishing these options. Vetting long-period exoplanet candidates provides new temperate exoplanet targets across a range of stellar insolation to help disentangle this confounding factor.

In this paper we present the validation of TOI-1221 b (TIC 349095149.01), a sub-Neptune sized exoplanet located in the southern sky (RA: $07^h11^m41^s.05$, Dec: $-65°30'31''.88$) around a Sun-like m_V=10.5 star. Having a wide 91.7 day orbit, this target is at the far edge of the known transiting long-period planet parameter space and its atmospheric properties are less likely to be strongly driven by stellar insolation than its numerous hot counterparts.

The shallow transit signal in this system was initially noticed in the TESS Sector 7 data by the Visual Survey Group (VSG; Kristiansen et al., 2022) shortly after release. Immediately checking back through previous sectors, a likely second transit was discovered in Sector 3, providing a tentative 91-day period. The candidate was also independently detected by the TESS Science

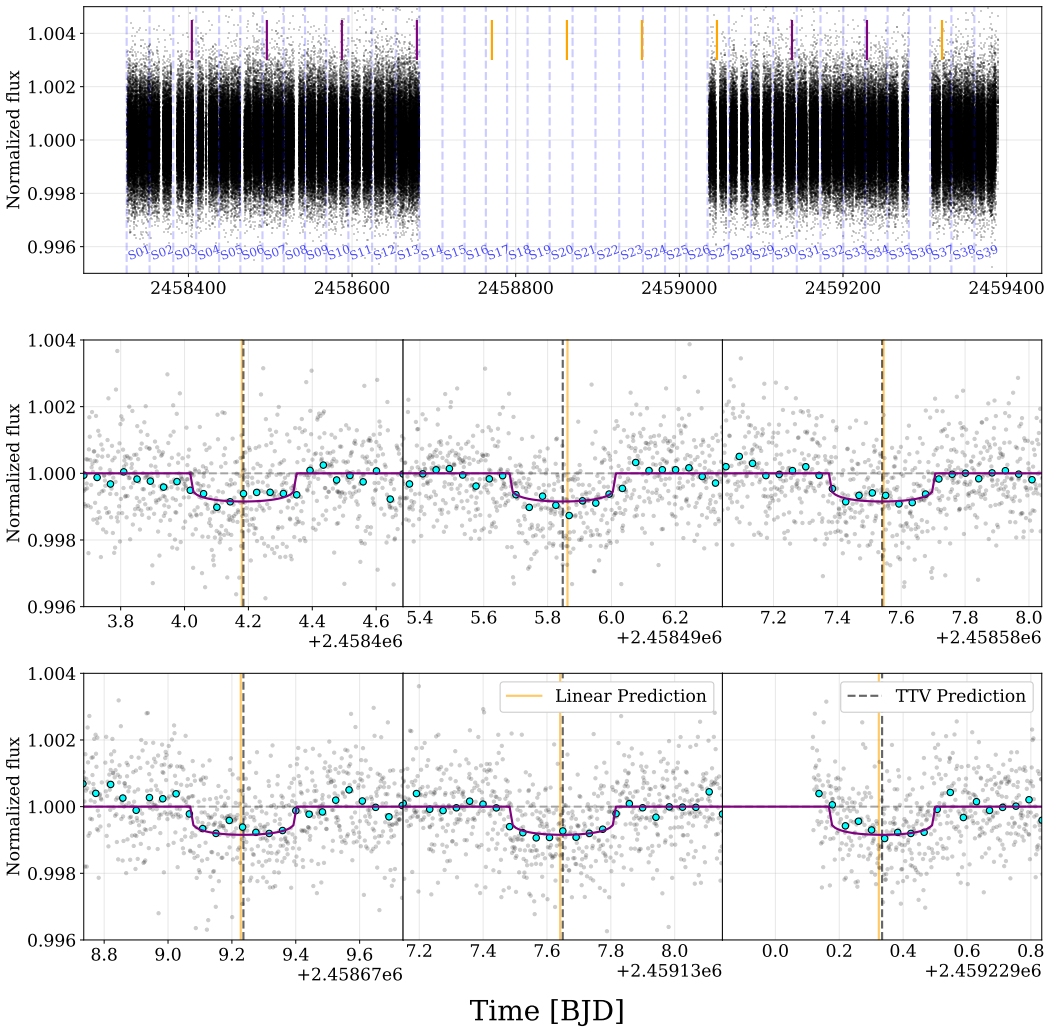

Fig. 3.1. *First row:* Sector-by-sector PDCSAP flux, normalized to within-sector median. Purple bars indicate where transits were detected, orange bars indicate where expected transits fell in observing gaps. *Rows 2 & 3:* Zoomed plot of each of the six caught transits. The TESS data were taken at a cadence of 2 minutes and are shown binned to 60-minute intervals with the cyan points. The displayed transit model is described in Sections 3.3 and 3.4. Orange vertical lines show the predicted midpoints given a fixed period ephemeris. Dashed black lines indicate the fitted midpoints, showing TTVs described in Section 3.3.4.

Processing Operations Center (SPOC; Jenkins et al., 2016) at NASA Ames Research Center when conducting a multi-sector analysis of Sectors 1-9. The periodicity was confirmed shortly thereafter with a third transit detection in Sector 10 by the VSG. A later multi-sector SPOC analysis of Sectors

1-13 discovered a fourth transit and promoted the candidate to TOI status following a positive data validation report.

Since its discovery, the TESS Follow-up Observing Program (TFOP) community has made steady efforts to contribute key observations to confirm the planet's candidacy and rule out false positive scenarios. This manuscript aims to bring together and summarize the various contributed observations in order to validate this planet's legitimacy. In Section 3.2 we provide an overview of the observations and data that contributed to the effort. Section 3.3 details the target's discovery, an assessment of false positive scenarios, and stellar characterization. It also describes the discovery of transit timing variations (TTVs) and the fitting procedures used to measure the system's parameters. Further discussion of the discovered planet properties and the implications of the TTVs occurs in Section 3.4. Finally, in Section 3.5 we summarize the results of the entire planet validation process.

3.2. Observations

In the effort to validate the target TOI-1221.01, data and observations were gathered from several teams and facilities and are summarized here.

3.2.1. TESS light curves

Due to its proximity to the southern ecliptic pole, TOI-1221 was observed by TESS over many sectors and with a very long baseline (more than 650 days of on-target coverage over 1065 days, at the time of writing). It appeared in 25 Sectors (1-13, 27-35, and 37-39). To date, six of those Sectors (3, 7, 10, 13, 30, and 34) caught a transit event allowing for a good transit fit and determination of the orbital parameters. It is scheduled to appear in 9 more sectors (61-69) in TESS's Year 5 observations (early-to-mid 2023), and sectors 64 and 67 are expected to show additional transits given the ephemeris found later in this paper.

We downloaded the Presearch Data Conditioning Simple Aperture Photometry (PDCSAP; Stumpe et al., 2012, 2014; Smith et al., 2012) light curves from the Mikulski Archive for Space Telescopes (MAST) repository (doi:10.17909/t9-nmc8-f686). These data are background subtracted and have had instrumental systematics identified and removed. The TESS data are visualized in Figure 3.1.

3.2.2. Ground-based light curves

Follow-up observations were made by members of the TFOP and are hosted on the Exoplanet Follow-up Observing Program (ExoFOP) TESS website (doi: 10.26134/ExoFOP3).

PEST:

We observed TOI-1221.01 on UTC 2021-01-14 in R_c band from the Perth Exoplanet Survey Telescope (PEST) near Perth, Australia. The ~8.1 hour observation covered pre-ingress baseline

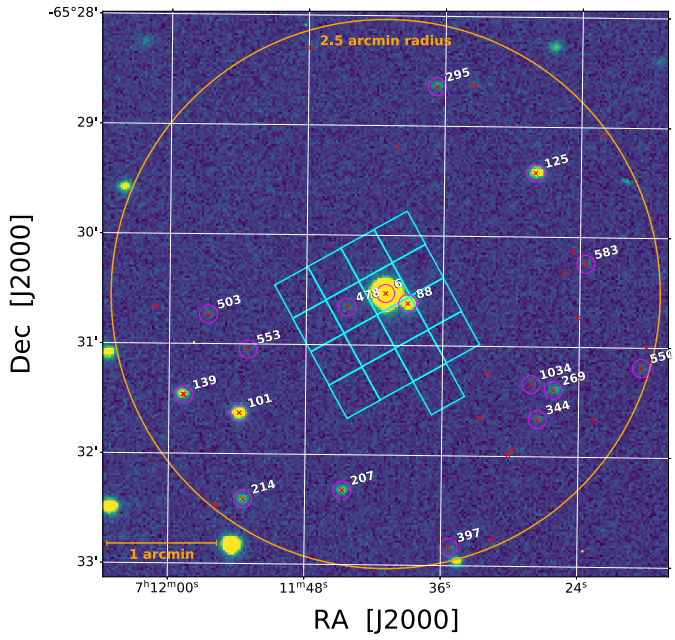

Fig. 3.2. A 5′ field of view from PEST centred on the target (centre object, ID #6). An example TESS aperture is overlaid in the same scale (cyan). Identifier numbers come from a brightness-ordered list of *Gaia* stars (red X points) in the area. Given TESS's pixel size and PSF width, it is typical to check for NEBs within 2.5′of the target (orange circle). NEB check results for detectable neighbouring stars are displayed in Table 3.1.

through about 65% of the predicted transit duration. The 0.3 m telescope is equipped with a 1530 × 1020 SBIG ST-8XME camera with an image scale of 1.″2 pixel^{-1} resulting in a 31′ × 21′ field of view. A custom pipeline based on `C-Munipack`[1] was used to calibrate the images and extract the differential photometry, using an aperture with radius 5.″0. The images have typical stellar point spread functions (PSFs) with a FWHM of ∼ 5″. The target star was intentionally saturated to check for fainter nearby eclipsing binaries (NEBs) near TOI-1221. The data rule out NEBs in stars within 2.′5 of the target star that are fainter by as much as 7.5 magnitudes in R_c band, except for the nearest neighbor (TIC 349095148) at 13.″2 separation which had a contaminated aperture. An example PEST image is shown in Figure 3.2.

LCOGT:

In order to gather additional transit detections and to clear the NEB potential of the remaining 13.2″neighbour, we obtained two observations from the Las Cumbres Observatory global telescope network (LCOGT; Brown et al. (2013)) 1.0 m telescopes using the SINISTRO instrument in the zs-band. Being distributed in various locations around the globe, LCOGT observations of TOI-1221

[1]http://c-munipack.sourceforge.net

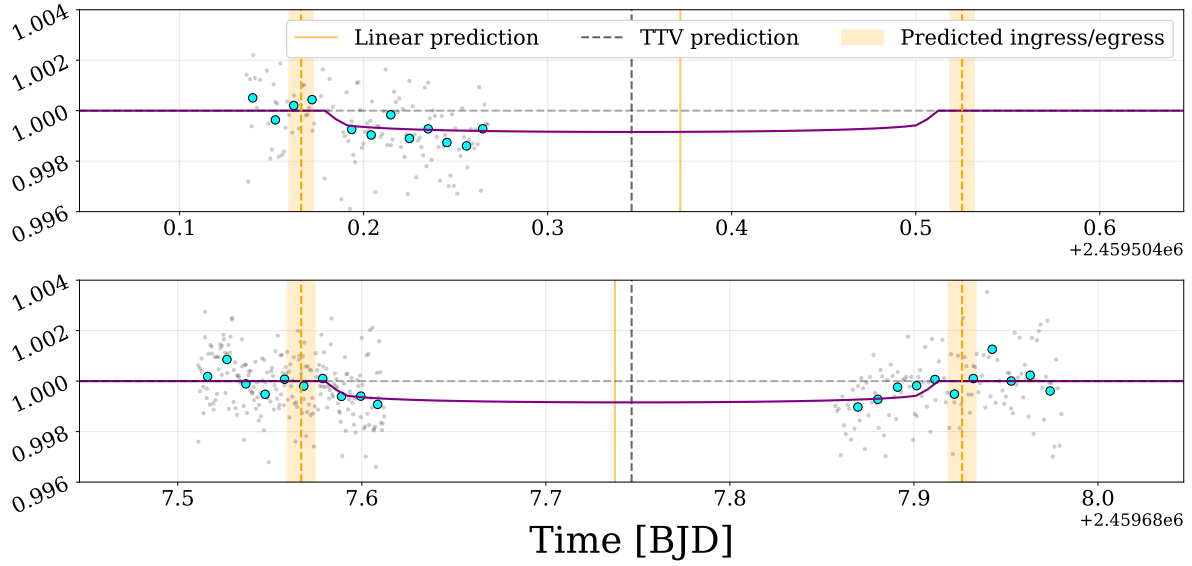

Fig. 3.3. Light curves from the two LCOGT observations. Cyan points are binned to 15-minute intervals. The predicted timings come from the fixed-period ephemeris of previous TESS data. The transit duration is long enough to require observing from two separate longitudes to detect both ingress and egress. Like in Figure 3.1, the central orange and black lines indicate the midpoint timing expected by a fixed-period model or fitted by an agnostic model allowing TTVs, respectively.

were possible at a few southern sites: the Siding Springs Observatory (SSO) in Australia, the South African Astronomical Observatory (SAAO), and the Cerro Tololo Inter-American Observatory (CTIO) in Chile. We used the `TESS Transit Finder` tool, which is a customized version of the `Tapir` software package (Jensen, 2013), to schedule these LCOGT observations.

The first observation occurred on 2021-10-16 where an ingress event was visible from the SSO site. Simultaneous observations by two on-site 1.0 m telescopes (*A* and *B*) were made, although substantial systematics on telescope *A* prompted us to exclude it from further analysis. The light curve from telescope *B* achieved photometric precision comparable to the transit depth, and so was retained. Unfortunately an attempted observation of the associated egress event at the SAAO site several hours later was thwarted by poor weather.

The second observation took place on 2022-04-17. This time the weather cooperated and we were able to capture both the ingress and egress events from the CTIO and SSO sites, respectively. The images from each observation were calibrated by the standard LCOGT `BANZAI` pipeline (McCully et al., 2018). Photometric data were extracted using `AstroImageJ` (Collins et al., 2017b) and circular photometric apertures with radii $\sim 5\farcs8$. This aperture excludes most of the flux from the nearest known *Gaia* DR3 and TIC version 8 neighbor (TIC 349095148) which is $13\farcs2$ SSW of TOI-1221. An aperture on TIC 349095148 also ruled out an NEB in this neighboring star (see section 3.3.2 and Table 3.1). LCOGT light curves are shown in Figure 3.3.

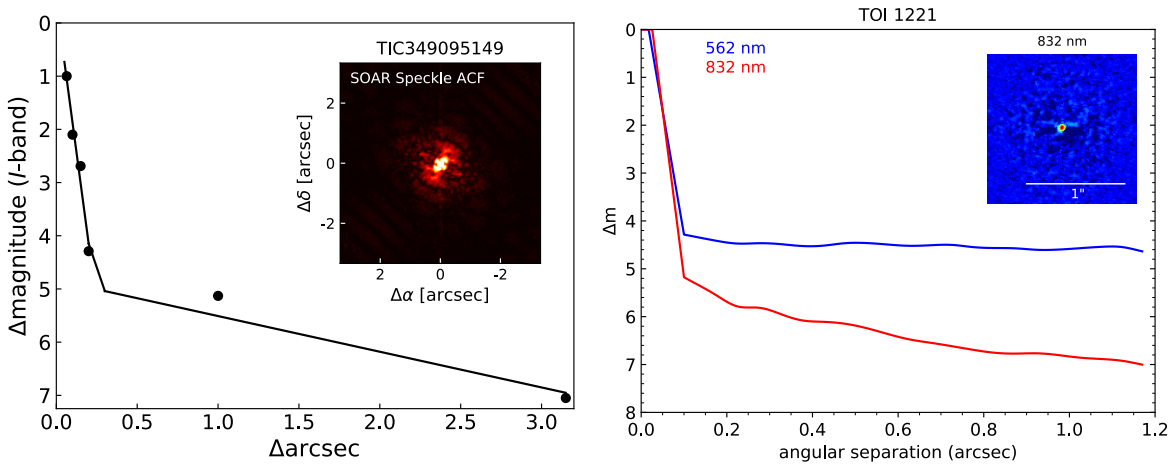

Fig. 3.4. Contrast achieved via speckle imaging from SOAR (*left*) and Gemini-S/Zorro (*right*) for TOI-1221. Neither measurement detects any neighbouring sources within the limits of their sensitivities (5σ).

3.2.3. WASP-South

Though the transit depth of TOI-1221.01 is too shallow to be detectable by this instrument, the Wide Angle Search for Planets telescope (WASP; Pollacco et al. (2006)) has archival data on this target that are useful to assess stellar activity and rotational modulation. The archive contains 23,000 photometric data points on TOI-1221 spanning 4 observing seasons (2008/09, 2009/10, 2010/11 and 2011/12). Typical cadence was 15 min with individual exposures of 30 sec and a precision of about 6 mmag.

3.2.4. High-contrast imaging

SOAR:

Initial high-contrast speckle imaging was taken on 2019-11-09 with the visiting HRCam on the Southern Astrophysical Research (SOAR) Telescope. The HRCam is a fast imager that takes rapid diffraction-limited images with a Cousins *I* filter and computes their power spectra and auto-correlation functions (ACFs). Fringes in the power spectra or symmetric peaks in the ACFs indicate the detection of a nearby neighbour (Tokovinin, 2018). The SOAR observation is shown in Figure 3.4 (top panel).

Gemini-S/Zorro:

We acquired further high-contrast speckle imaging from Gemini South with the Zorro instrument on 2021-10-19 (program ID: GN/S-2021A-LP-105) as part of the ongoing exoplanet follow-up imaging campaign of Howell et al. (2021). Zorro is able to simultaneously image in two filters, providing both 562 nm and an 832 nm measurements. Seeing conditions were variable during the

observation but remained within acceptable ranges. Images were processed using the pipeline described in Howell et al. (2011). The Gemini/Zorro observation is also shown in Figure 3.4 (bottom panel).

Table 3.1. NEB clearance by PEST and LCOGT

Parameter	Description (Units)	Values	Prior			
ID	Δmag	RMS (ppt)	$\delta_{\rm NEB}$ (ppt)	SNR	Target sep.	Instr.
101	4.03	17	20	14.6	1′43″	PEST
125	4.46	25	29	14.4	1′45″	PEST
139	4.82	30	41	17.0	2′03″	PEST
207	5.42	56	70	15.5	1′50″	PEST
214	5.43	58	71	15.2	2′16″	PEST
269	5.70	69	91	16.4	1′45″	PEST
295	5.77	76	98	16.0	1′56″	PEST
344	6.27	103	154	18.6	1′47″	PEST
397	6.34	189	165	10.8	2′23″	PEST
478	6.47	174	185	13.2	0′22″	PEST
503	7.36	331	422	15.8	1′37″	PEST
550	7.07	233	324	17.3	2′24″	PEST
553	7.16	219	350	19.8	1′22″	PEST
583	7.35	399	417	13.0	1′50″	PEST
1034	7.30	418	399	11.8	1′32″	PEST
88	3.54	8.7	13	11.9	0′13″	LCOGT

Note: The $\delta_{\rm NEB}$ quantity is a measure of how deep a transit would need to be on this particular target alone in order to cause the transit depth observed in the blended TESS aperture. Light curves for all these targets showed no indication of transit-like signals. We use the simple transit SNR calculation of Pont et al. (2006, eq.3) to justify the non-detections on each neighbour star. The aperture of the closest neighbour star (ID: 88) was contaminated by TOI-1221 in the PEST image and produced unreliable results. The subsequent higher resolution LCOGT observation was able to resolve the two stars and perform a proper NEB check on this source.

3.2.5. Reconnaissance spectroscopy

CHIRON:

We obtained three spectra of TOI-1221 between 2019-10-19 and 2021-10-04 (program IDs: BOYA-19B-0232 and QUIN-21A-3268) using the CHIRON high-resolution echelle spectrograph

on the 1.5 m SMARTS telescope at the CTIO (Tokovinin et al., 2013). In slicer mode, CHIRON uses a fiber-fed image slicer to feed the instrument and provides a resolving power of $R \sim 80{,}000$ across a broad wavelength range (4100–8700 Å). One spectrum was taken near transit, while the other two spectra were taken near opposite quadratures, providing the most radial velocity (RV) leverage. These measurements are listed in Table 3.2. The CHIRON spectra can also be used to characterize the stellar properties, place conservative mass limits on the transiting planet, search for massive outer companions, and rule out false positive scenarios that would induce large RV variations or exhibit spectral line profile variations. We use the spectra provided by the CHIRON instrument team, optimally extracted according to the procedure described in Paredes et al. (2021), which also demonstrates instrument velocity performance at the 5 m s^{-1} level for the brightest, slowly rotating, K dwarfs.

3.3. Analysis

3.3.1. Discovery

The initial Sector 7 discovery of the TOI-1221.01 transit signal by the VSG (Kristiansen et al., 2022) was made using `LcTools` (Kipping et al., 2015; Schmitt et al., 2019a) shortly after the data became available in early 2019. The search was then extended to light curves of Sectors 1-7 from the Mikulski Archive for Space Telescopes (MAST), binned at 6 points per hour in order to search for additional transits. The second transit was located in Sector 3 giving a period estimate of 91.6 days. Once the Sector 10 data were released, a third matching transit was found, confirming the periodicity.

The transiting planet signature was also independently detected by the SPOC using an adaptive wavelet-based matched filter (Jenkins, 2002; Jenkins et al., 2010, 2020) during a multi-sector search of sectors 1-9. The transit signature passed all the diagnostic tests performed by the Data Validation (DV) module (Twicken et al., 2018) which also performed an initial limb-darkened model fit (Li et al., 2019). Further, the difference image centroiding analysis performed by the DV on sectors 1-39 localized the source of the transit signature to within $7\farcs6 \pm 6\farcs8$ of TOI-1221. The TESS Science Office (TSO) promoted this candidate to TESS Object of Interest status on 2019-08-26 upon review of the DV report and other diagnostic information. No signals from additional transiting planets were discovered in this target's light curve during these searches, nor from a box least squares search including the most recent sectors.

3.3.2. False positive scenarios

The most likely false positives to mimic an exoplanet in TESS observations involve transiting objects that are non-planetary in nature. They may be physically bound to the host, or simply

situated in close sky-projected proximity. We can test for a number of typical indicators and scenarios.

Planetary nature of the 92-day signal:

We first determine that the transit event is indeed occurring on TOI-1221 and not a nearby star blended in the TESS aperture. In NEB false positive scenarios, transiting stellar companions of comparable size to their host star are prone to producing V-shaped transits or grazing geometries, both of which are argued against by the flat bottom and clear demarcations of ingress and egress seen in the light curves.

We explicitly check the surrounding sky for potential NEB sources using small ground-based telescopes to clear all reasonably bright sources in the region. In this context, clearing neighbour stars means that the unblended light curves of these stars show significant non-detections of transit-like signals at depths that would produce the observed flux drop in the blended TESS aperture. The PEST observation clears stars within Δmag $\sim$ 7.5 in a 2.′5 radius with the exception of the nearest neighbour (13.″2 away SWW) which was not cleanly resolved from the target. The subsequent LCOGT-1m observations simultaneously detected a transit on-target and was able to resolve and rule out an NEB signal on the 13.″2 neighbour. Table 3.1 shows the NEB potential for reasonably bright stars within 2.′5 ruled out by the PEST and LCOGT measurements. With these small-telescope observations, we can conclude that sources from 2.′5 out to $\sim$10″ show no indication of NEB signals.

Turning to spectroscopy, we derive RVs from the CHIRON data of TOI-1221 using fitted line profiles of each spectrum, which were extracted using least-squares deconvolution (LSD) of the observed spectrum against synthetic templates (Donati et al., 1997). The CHIRON RVs (listed in Table 3.2) show no large velocity variation across the 2-year baseline and wide phase coverage. With the relatively flat nature of the RVs gathered near pre- and post-transit quadratures, the 1σ and 3σ upper limits on the planet mass, given its period, are 1.1 M_{Jup} and 3.5 M_{Jup}, respectively. While the RV measurements are not sensitive enough to rule out massive, outer planetary companions, they do rule out stellar-mass components in the system with orbital periods similar to the observed 92-day signals. This is in line with the *Gaia* Renormalised Unit Weight Error (RUWE) measure of 1.11, which is consistent with expectations for a single star.

As a final quantitative assessment of the planet's validity we used the `TRICERATOPS` (Tool for Rating Interesting Candidate Exoplanets and Reliability Analysis of Transits Originating from Proximate Stars) statistical validation package for TESS transits (Giacalone & Dressing, 2020; Giacalone et al., 2021). `TRICERATOPS` uses a Bayesian framework developed with TESS observations in mind. It leverages the well-characterized stellar qualities in the TESS Input Catalog and specifically handles multiple blended stars in the large TESS apertures in a precise manner. It calculates false positive probabilities by leveraging known information about background star rates and bound multiplicity priors. It also applies provided contrast curves to refine its assessment.

TRICERATOPS calculates an intrinsic false positive probability (FPP) which considers scenarios only involving absent or unresolved close neighbours, as well as a nearby false positive probability (NFPP) which involves scenarios with nearby stars. Based on comparisons to externally vetted TOIs, TRICERATOPS defines a planet candidate as validated if it achieves a FPP < 0.015 and NFPP < 0.001. For our analysis at hand, we entered in the six detected TESS transits of TOI-1221.01 and the high-contrast imaging limits placed by SOAR and Zorro. We calculate the values FPP $= 0.0014 \pm 0.0003$ and NFPP $= 0.0012 \pm 0.0004$. The FPP statistic falls well below the TRICERATOPS validation threshold, and the NFPP straddles the threshold between "validated" and "likely planet" designations. It is worth noting that TRICERATOPS does not have a way to include RV constraints in its assessment, nor does it know that we have cleared the closest neighbours of NEB potential. Its findings, given these omissions, are likely very conservative.

In sections 3.3.4 and 3.4.2 we discuss the presence of transit timing variations (TTVs) in the observations. This is additional qualitative evidence against the NEB hypothesis. For the observed transits to be caused by an NEB, this NEB would have to exhibit TTVs and would therefore have to be a trinary (or more) system.

Table 3.2. CHIRON radial velocities of TOI-1221

BJD_{TDB}	RV (km s^{-1})	σ_{RV} (km s^{-1})	phase
2458775.86419	15.9562	0.0201	0.054
2459345.46777	16.0370	0.0221	0.267
2459491.84557	16.0263	0.0519	0.863

Limits on additional system companions:

We further probe tighter separations than was possible with the small ground-based telescope observations. The *Gaia* DR3 catalogue (Gaia Collaboration et al., 2016; Babusiaux et al., 2022) reports no sources within 12″, and so clears the area down to its resolving power of $\lesssim$1″ with its high completeness limits at ∼17 Gaia magnitudes[2]. For the region within 1″, we look at the acquired high contrast speckle imaging. The initial SOAR/HRCam and subsequent Gemini-S/Zorro images clear the surrounding sky of sources (at a 5σ level) down to Δmag of 5.2 at 0.″1 separation. This inner working angle corresponds to ∼13.7 au given the Gaia parallax distance of 137 pc. Out towards 3″ the contrast improves to Δmag = 7, as shown in the curves of Figure 3.4. These Δmag limits rule out the presence of anything more luminous than approximately an M4V dwarf at 0.″1 or M6V dwarf out towards 1″.

The CHIRON spectra are useful in this application as well. Blended eclipsing binaries can produce spectral line profile variations as a function of orbital phase, but we find no evidence for

[2]https://gea.esac.esa.int/archive/documentation/GEDR3/Catalogue_consolidation/chap_cu9val/sec_cu9val_introduction/ssec_cu9val_intro_completeness.html

additional stars or variable line profile shape in the spectra of TOI-1221. Additionally, while the mostly flat RVs limit anything orbiting at $P \sim 90$ days to planetary mass, a small, marginally significant RV slope exists ($0.13 \pm 0.053\,\mathrm{m\,s^{-1}\,day^{-1}}$) that could indicate an additional massive object with a wider orbit. With only 3 data points, directly fitting any kind of model is impractical. However, we can explore some limiting cases. Let us restrict ourselves to simple circular edge-on orbits that could account for the observed slope. The RVs exhibit this slope over their span of ~2 years. A $2\,M_{\mathrm{Jup}}$ object on a 3 au orbit (5.2 year period) could produce the slope, but smaller orbits would have RV variations of too high frequency. At the other end of the scale, a $0.24\,M_{\odot}$ star (~M4V) at 30 au (165 year period) could also produce the slope, but at an angular separation of 0.″2 it would be bright and separated enough to be detected in the Zorro image. Any number of mass–period combinations in between these scenarios could produce the observed slope while remaining undetected by Zorro. Photometrically, none of the objects in this range are bright enough to have a significant impact on our transit fits. Even an unresolved M4V star would only cause a minor flux dilution, affecting our radius value by <1% which is smaller than our measured uncertainties.

Of course, realistic RV curves depend strongly on orbital inclination, phase, and eccentricity which are all unknown. There is the additional possibility of the observed RV "slope" not being a true gradual slope, but undersampled aliasing of a moderate-strength signal with period shorter than the 2-year coverage. Much uncertainty remains because we have few RV measurements with poor precision.

While the 91.7-day period signal passes all planetary validation checks, the data allow for the presence of another companion in the system. The observations leave room for another body out to roughly 30 au and less than about $0.24\,M_{\odot}$. Such a companion does not pose photometric dilution issues, but may have an impact in inducing TTVs. With all these validation results taken together, we consider the practical false-positives ruled out. From this point onward, we consider the transit events to be caused by a planet and fit the light curve following that assumption. We will adopt the nomenclature of TOI-1221 b to refer to this planet moving forward.

3.3.3. Stellar characterization

We performed an analysis of the broadband spectral energy distribution (SED) of the star together with the *Gaia* EDR3 parallax (with no systematic offset applied; see, e.g., Stassun & Torres, 2021), following the procedures described in Stassun & Torres (2016); Stassun et al. (2017, 2018a). We pulled the $B_T V_T$ magnitudes from *Tycho-2*, the JHK_S magnitudes from *2MASS*, the W1–W4 magnitudes from *WISE*, the $G_{\mathrm{BP}} G_{\mathrm{RP}}$ magnitudes from *Gaia*, and the NUV magnitude from *GALEX*. Together, the available photometry spans the full stellar SED over the wavelength range 0.2–22 μm.

We performed a fit using Kurucz stellar atmosphere models, with the free parameters being the effective temperature (T_{eff}) and metallicity ([Fe/H]). The remaining free parameter is the extinction

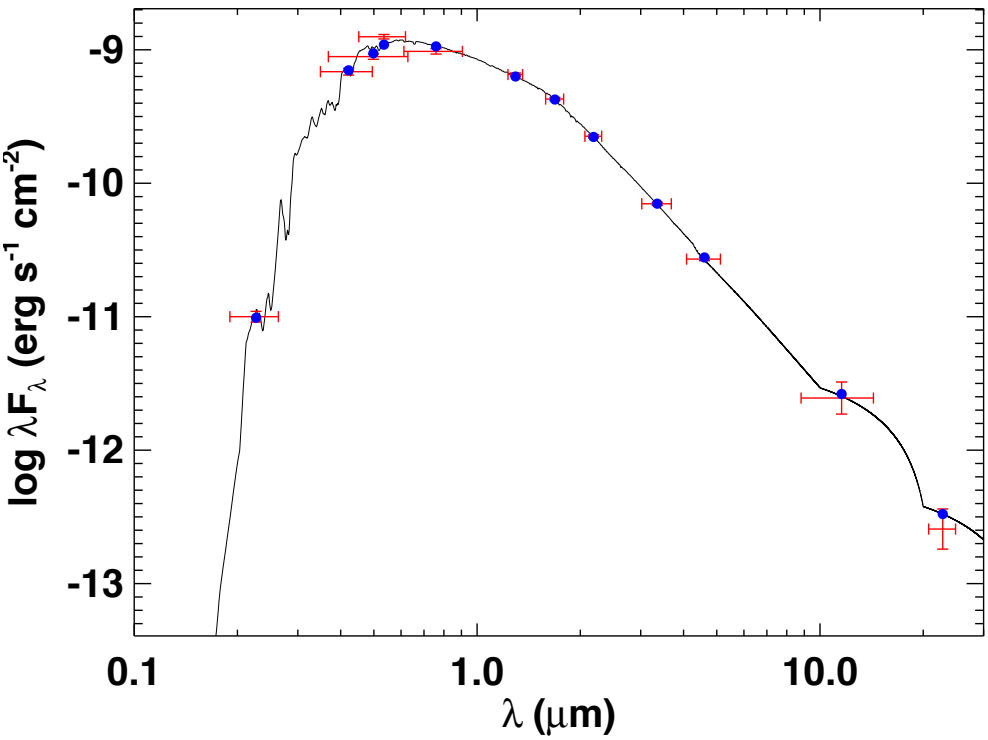

Fig. 3.5. Spectral energy distribution of TOI-1221. Red symbols represent the observed photometric measurements with the horizontal bars representing the effective width of the bandpass. Blue symbols are the model fluxes from the best-fit Kurucz atmosphere model (black).

A_V, which we limited to the maximum line-of-sight value from the Galactic dust maps of Schlegel et al. (1998a). The resulting fit (Figure 3.5) has a reduced χ^2 of 1.5, with $A_V = 0.06 \pm 0.04$, $T_{\rm eff} = 5700 \pm 100$ K, and [Fe/H] = 0.0±0.3. The departure from a smooth Rayleigh-Jeans relationship beyond 10 μm is a known artifact in the Kurucz atmosphere models. It arises from the inclusion of certain opacity sources in the mid-IR and smoothing effects. Integrating the (unreddened) model SED gives the bolometric flux at Earth, $F_{\rm bol} = 1.597 \pm 0.037 \times 10^{-9}$ erg s^{-1} cm^{-2}. Taking the $F_{\rm bol}$ and $T_{\rm eff}$ together with the *Gaia* parallax gives the stellar radius, $R_\star = 0.993 \pm 0.037$ R$_\odot$. In addition, we can estimate the stellar mass from the empirical relations of Torres et al. (2010a), giving $M_\star = 1.03 \pm 0.06$ M$_\odot$.

Finally, we can use the star's NUV flux to estimate an age via empirical activity-age relations. The observed NUV excess implies a chromospheric activity of $\log R'_{\rm HK} = -5.2 \pm 0.1$ via the empirical relations of Findeisen et al. (2011). This estimated activity implies an age of $\tau_\star = 10 \pm 2$ Gyr via the empirical relations of Mamajek & Hillenbrand (2008). This age estimate is broadly consistent with that estimated from the star's rotation via gyrochronology relations (Mamajek & Hillenbrand, 2008). From the spectroscopic $v \sin i_\star$ together with $R_\star$ we obtain a projected rotation period of $P_{\rm rot}/\sin i_\star = 25 \pm 5$ days, implying an age of $\tau_\star = 4.9^{+3.2}_{-2.5}$ Gyr.

Table 3.3. Stellar characterization by CHIRON spectroscopy and SED analysis

Parameter	CHIRON	SED	Units
$M_\star$	0.93 ± 0.22^a	1.03 ± 0.06	$M_\odot$
$R_\star$	1.031 ± 0.022^a	0.993 ± 0.037	$R_\odot$
$\rho_\star$	1580 ± 190	1190 ± 290	$\mathrm{kg\,m^{-3}}$
$T_{\rm eff}$	5592 ± 50	5700 ± 100	K
[Fe/H]	0.06 ± 0.08	0.0 ± 0.3	dex
$\log g$	4.38 ± 0.10	–	dex
$v \sin i$	2.1 ± 0.4	–	$\mathrm{km\,s^{-1}}$
$F_{\rm bol}$	–	$1.597 \pm 0.037 \times 10^{-9}$	$\mathrm{erg\,s^{-1}\,cm^{-2}}$
A_V	–	0.06 ± 0.04	–
$\log R'_{\rm HK}$	–	-5.2 ± 0.1	–
$\tau_\star^b$	–	$4.9^{+3.2}_{-2.5}$	Gyr
$\tau_\star^c$	–	10 ± 2	Gyr

[a] Derived using CHIRON values for $T_{\rm eff}$ and $\log g$ along with Gaia parallax distance (137 pc) and SED $F_{\rm bol}$.

[b] Gyrochronology.

[c] Activity.

We additionally verify the low activity of TOI-1221 with the 23,000 photometric data points from WASP-South. In searching for rotational modulations using methods described in Maxted et al. (2011), we constrain the variability to a 95% confidence upper limit of 0.7 mmag. This relative inactivity is nicely consistent with the old age estimate from the NUV.

As an independent determination of basic stellar parameters, we estimated spectroscopic stellar parameters by matching our CHIRON spectra against a library of observed spectra that have previously been classified by the Stellar Parameter Classification routines (SPC; Buchhave et al., 2012). We interpolated to the best-matched values of effective temperature, surface gravity, and metallicity using a gradient-boosting regressor implemented in the `scikit-learn` python module, and found $T_{\rm eff} = 5592 \pm 50$ K, $\log g = 4.38 \pm 0.10$, and [Fe/H] $= 0.06 \pm 0.08$. The projected rotational velocity, $v \sin i_\star$, is derived following Gray (2005) and Zhou et al. (2018), by fitting broadening kernels to the instrumental, macroturbulent, and rotational line profiles. It is measured to be 2.1 ± 0.4 km s^{-1}, but we note that this is smaller than the resolution element of the instrument and may be susceptible to systematic errors greater than the internal uncertainty quoted here.

We determine another mass and radius estimate using the CHIRON $T_{\rm eff}$ and $\log g$ values combined with the Gaia parallax distance and SED bolometric flux. The derived stellar densities ($\rho_\star$) from the CHIRON and SED analysis are in agreement with one another. They also agree with the TESS Input Catalog (TIC; Stassun et al., 2018b) value used as a prior in our model fit, discussed in the next section. The parameter values for both the CHIRON spectroscopy and SED analysis are summarized in Table 3.3.

Table 3.4. Median values and 68% confidence interval for TOI-1221 b.

Parameter	Description (Units)	Values	Prior
Target Parameters:			
P	Period[a] (days)	$91.68278^{+0.00032}_{-0.00041}$	–
T_0	Epoch reference[a] ($\mathrm{BJD_{TDB}}$)	$2458404.1791^{+0.0035}_{-0.0030}$	–
T_{14}	Transit duration (hours)	$8.12^{+1.01}_{-1.14}$	–
$R_p/R_\star$ ...	Planet radius in stellar radii	$0.02679^{+0.00067}_{-0.00056}$	$\mathcal{U}[0.0,0.05]$
R_p	Planet radius ($R_\oplus$)	$2.91^{+0.13}_{-0.12}$	–
δ	Transit depth $(R_p/R_\star)^2$	$0.00072^{+0.00004}_{-0.00003}$	–
b	Impact parameter	$0.25^{+0.22}_{-0.14}$	$\mathcal{U}[0.0,1.027]$
i	Inclination (deg)	$89.75^{+0.16}_{-0.08}$	–
$a/R_\star$ ...	Semi-major axis in stellar radii	$83.7^{+4.7}_{-4.0}$	–
a	Semi-major axis (au)	$0.387^{+0.026}_{-0.023}$	–
e	Eccentricity	< 0.21	–
ω'	Modified argument of pericentre[b] (deg)	108^{+37}_{-43}	–
$\sqrt{e}\sin\omega$ ..	e,ω parameterization	$0.00^{+0.16}_{-0.26}$	$\mathcal{U}[-1.0,1.0]$
$\sqrt{e}\cos\omega$ ..	e,ω parameterization	$0.01^{+0.40}_{-0.39}$	$\mathcal{U}[-1.0,1.0]$
ρ_p	Planet density[c] ($\mathrm{g\,cm^{-3}}$)	$2.01^{+0.71}_{-0.63}$	–
M_p	Planet mass[c] ($M_\oplus$)	$9.4^{+3.0}_{-3.7}$	–
$\log g_p$ ...	Surface Gravity[c] (g_p given in $\mathrm{cm\,s^{-2}}$) .	$3.15^{+0.19}_{-0.31}$	–
K	RV semi-amplitude[c]	$1.24^{+0.75}_{-0.91}$	–
S_p	Insolation[d] ($S_\oplus$)	$6.06^{+0.85}_{-0.77}$	–
$T_{\rm eq}$	Equilibrium temperature[e] (K)	440 ± 60	–
$\rho_\star$	Stellar density ($\mathrm{kg\,m^{-3}}$)	1320^{+220}_{-190}	$\mathcal{N}(1349, 296)$
$T_{\#0}$	Epoch 0 transit midpoint ($\mathrm{BJD_{TDB}}$)...	$2458404.1844^{+0.0060}_{-0.0051}$	$\mathcal{N}(2458404.1850, 0.02)$
$T_{\#1}$	Epoch 1 transit midpoint ($\mathrm{BJD_{TDB}}$)...	$2458495.8474^{+0.0075}_{-0.0048}$	$\mathcal{N}(2458495.8681, 0.02)$
$T_{\#2}$	Epoch 2 transit midpoint ($\mathrm{BJD_{TDB}}$)...	$2458587.5401^{+0.0061}_{-0.0087}$	$\mathcal{N}(2458587.5511, 0.02)$
$T_{\#3}$	Epoch 3 transit midpoint ($\mathrm{BJD_{TDB}}$)...	$2458679.2361^{+0.0056}_{-0.0056}$	$\mathcal{N}(2458679.2342, 0.02)$
$T_{\#8}$	Epoch 8 transit midpoint ($\mathrm{BJD_{TDB}}$)...	$2459137.6494^{+0.0043}_{-0.0061}$	$\mathcal{N}(2459137.6494, 0.02)$
$T_{\#9}$	Epoch 9 transit midpoint ($\mathrm{BJD_{TDB}}$)...	$2459229.3342^{+0.0067}_{-0.0051}$	$\mathcal{N}(2459229.3325, 0.02)$
$T_{\#12}$	Epoch 12 transit midpoint ($\mathrm{BJD_{TDB}}$)..	$2459504.3456^{+0.0054}_{-0.0047}$	$\mathcal{N}(2459504.3690, 0.02)$
$T_{\#14}$	Epoch 14 transit midpoint ($\mathrm{BJD_{TDB}}$)..	$2459687.7466^{+0.0044}_{-0.0044}$	$\mathcal{N}(2459687.7500, 0.02)$
Telescope-specific Parameters:			
$q_{1-\mathrm{TESS}}$ ..	Quadratic limb darkening coefficient[f] .	$0.26^{+0.02}_{-0.01}$	$\mathcal{N}(0.264,0.02)$
$q_{2-\mathrm{TESS}}$ ..	Quadratic limb darkening coefficient[f] .	$0.34^{+0.01}_{-0.02}$	$\mathcal{N}(0.334,0.02)$
$q_{1-\mathrm{LCOGT}}$.	Quadratic limb darkening coefficient[f] .	$0.25^{+0.02}_{-0.03}$	$\mathcal{N}(0.250,0.02)$
$q_{2-\mathrm{LCOGT}}$.	Quadratic limb darkening coefficient[f] .	$0.30^{+0.02}_{-0.02}$	$\mathcal{N}(0.301,0.02)$
$u_{1-\mathrm{TESS}}$ ..	Quadratic limb darkening coefficient[f] .	$0.35^{+0.02}_{-0.02}$	–
$u_{2-\mathrm{TESS}}$ ..	Quadratic limb darkening coefficient[f] .	$0.16^{+0.02}_{-0.01}$	–
$u_{1-\mathrm{LCOGT}}$.	Quadratic limb darkening coefficient[f] .	$0.30^{+0.02}_{-0.02}$	–
$u_{2-\mathrm{LCOGT}}$.	Quadratic limb darkening coefficient[f] .	$0.20^{+0.01}_{-0.02}$	–
μ_{TESS} ...	TESS relative flux offset	-0.00011 ± 0.00001	$\mathcal{N}(0.0,0.1)$

$\mu_{\rm LCOGT}$ ..	LCOGT relative flux offset	0.00003 ± 0.00004	$\mathcal{N}(0.0,0.1)$
$\sigma_{GP-TESS}$.	GP amplitude[g] (ppm)	< 0.132	$\mathcal{L}[10^{-6},10^{2}]$
$\rho_{GP-TESS}$.	GP time-scale of Matern part[g] (days) .	< 0.725	$\mathcal{L}[10^{-6},10^{2}]$
$\tau_{GP-TESS}$.	GP time-scale of exponential part[g] (days)	< 0.013	$\mathcal{L}[10^{-6},10^{2}]$
$\sigma_{GP-LCOGT}$	GP amplitude[g] (ppm)	< 0.175	$\mathcal{L}[10^{-6},10^{2}]$
$\rho_{GP-LCOGT}$	GP time-scale of Matern part[g] (days) .	< 0.486	$\mathcal{L}[10^{-6},10^{2}]$
$\tau_{GP-LCOGT}$	GP time-scale of exponential part[g] (days)	< 0.148	$\mathcal{L}[10^{-6},10^{2}]$

Notes: Posted uncertainties (and limits) encompass the 68% confidence interval. Directly fitted parameters include a prior description. Priors are of three varieties: Uniform over a given interval, $\mathcal{U}[a,b]$, normal with stated mean and standard deviation, $\mathcal{N}(\mu,\sigma)$, or log-uniform over a stated range, $\mathcal{L}[a,b]$. If no prior is specified, the quantity was calculated from other parameters.

[a] P and T_0 are determined as the best-fit linear ephemeris around which the individual transit timings vary.

[b] When eccentricity is low the light curve shape is insensitive to whether the transit occurs before or after pericentre passage. We define ω' as the absolute angle between the line of sight and pericentre passage. This collapses ω's strongly bimodal distribution to a unimodal posterior and is easier to present in a written table. ω has peaks at 198° and 342°.

[c] Planetary mass estimate comes from from the model uncertainty of Otegi et al. (2020). This value was used to calculate other mass-related quantities (e.g. ρ_p, $\log g_p$, and K).

[d] Insolation level assumes an orbital distance of $r = a$.

[e] Assuming no albedo and perfect thermal redistribution.

[f] Definitions and discussion of the different parameterizations $\{u_1,u_2\}$ vs. $\{q_1,q_2\}$ can be found in Kipping (2013).

[g] The reported Gaussian process posterior limits all essentially reflect the input prior.

3.3.4. Transit fitting

Fitting with `Juliet`*:*

To extract planetary parameters from the light curve, we used the `Juliet` python package (Espinoza et al., 2019b). At its core, `Juliet` generates transit models using the BAsic Transit Model cAlculatioN (`batman`; Kreidberg, 2015b) code and includes a range of MCMC and nested sampling methods to fit photometric light curves and radial velocity data sets. Among many other features, it can handle multiple planets, multiple instruments and data sets, and detrending via linear models or Gaussian processes.

The `batman` transit modelling package requires the input parameters $T_0, P, R_p/R_\star, a/R_\star, i, e, \omega$ as well as a limb darkening model and associated coefficients. However, although it can uniquely generate a transit light curve with these parameters, many of them do not facilitate efficient exploration of physically relevant parameter space. `Juliet` allows for a number of equivalent parameterizations that do a better job in this regard.

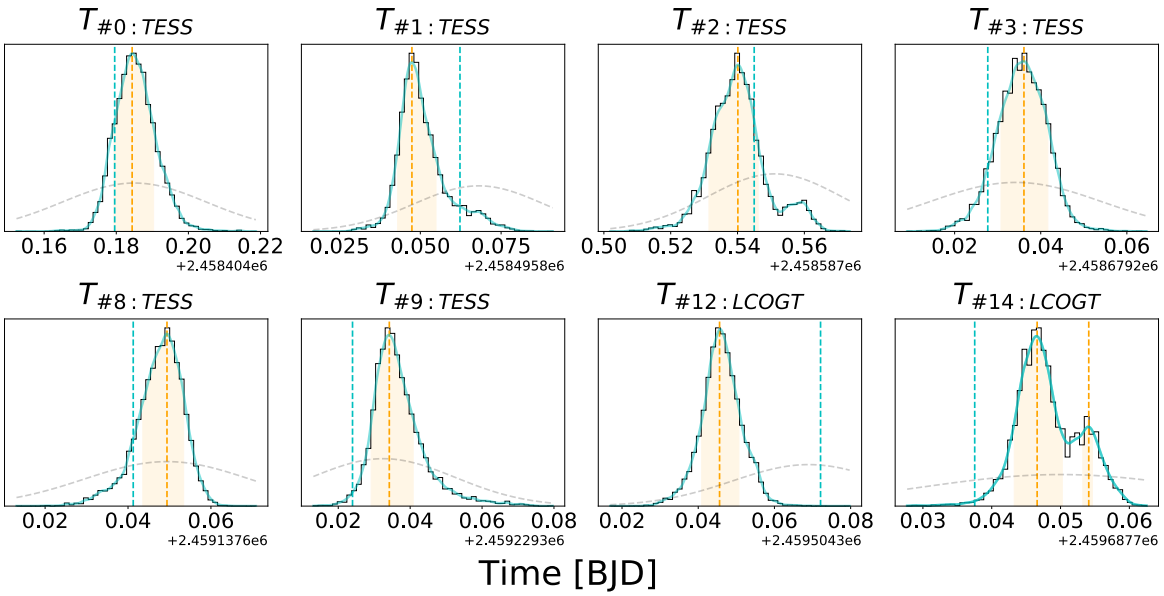

Fig. 3.6. Individual transit midpoint posteriors for each transit in our data set. In each plot, the orange region corresponds to the 68% highest-posterior density (HPD) region, and the blue line shows where the best-fitting linear ephemeris would predict the midpoint to fall. Grey dashed curves show the Gaussian prior placed on these midpoint timings.

One substitution we made was to forego directly fitting the semi-major axis ($a/R_\star$) in favour of fitting the stellar density ($\rho_\star$). For a given period, the two are directly interchangeable using Kepler's 3rd Law, and there are independent constraints already set on the stellar density to use as a prior (Stassun et al., 2018b). We also re-parameterize the eccentricity (e) and argument of periastron (ω) by instead fitting $\sqrt{e}\sin\omega$ and $\sqrt{e}\cos\omega$ for which it is easier to efficiently sample the entire parameter space. Finally, we employ a quadratic limb-darkening law and use the q_1,q_2 parameterization of Kipping (2013), corresponding to the transformations in Espinoza & Jordán (2016) for u_1,u_2. Again, this simply samples the allowable space with improved efficiency.

TTVs:

We found a few strange inconsistencies in our initial exploratory MCMC fits of the transit data. One oddity was a curious bimodal distribution in the T_0 and P posteriors. Another was the tendency for walkers in longer MCMC runs to eventually transition from a model with small impact parameter and low eccentricity (which we will label m_1) to a model with much more extreme parameters (m_2). The extreme model m_2 differed primarily in a few key parameters. The impact parameter suggested a nearly grazing transit geometry ($b_2 > 0.9$), the eccentricity was drawn to very large values ($e_2 > 0.7$), and planetary radius came out about 18% larger. Despite the wild changes in these transit parameters, m_1 and m_2 produce very similar transit shapes. The only subtle difference between the two was a slight flattening of the ingress and egress slopes of m_2 compared to m_1. Subsequent tests using nested sample routines found the same model shift even more easily,

likely because nested sample techniques tend to be less prone to getting trapped in local likelihood maxima.

The bimodal P and T_0 posteriors were are first clues that transit timing variations (TTVs) may be at play, and the specific differences in parameters between m_1 and m_2 lent credence to the idea. As described in Kipping (2014, Fig. 3), the Photo-Timing Effect produces exactly these biases when existing TTVs are unaccounted for. If one tries to fold transit observations according to a single period, which is effectively how a fixed-period fit operates, then the presence of TTVs will wash out the ingress and egress signals to a degree when they do not line up properly.

In our case at hand, the artificially flattened ingress and egress slopes mimic a high-b transit shape. A large impact parameter typically shortens the transit duration (by having a shorter chord across the stellar surface) unless another parameter can compensate. A shift of the semi-major axis ($a/R_\star$) could make up the difference, except that it is quite well-constrained by our prior knowledge of the stellar density ($\rho_\star$). The only remaining free parameter that could preserve the observed transit duration is a shift to high eccentricity (and accompanying appropriate argument of pericentre). A high-b geometry also implies the planet transits across the less bright limb of the star and possibly only grazes the stellar disk, requiring a larger planetary radius to affect the same observed flux drop. These are exactly the differences we see between m_1 and m_2 parameter sets. We take this line of reasoning as additional qualitative evidence that TTVs are truly present in this data.

We decided that the most unbiased approach was to employ a transit fitting routine that made no assumptions of fixed periodicity. `Juliet` offers just such a functionality, allowing priors to be set on individual timings for each detected transit. In this way, it is not simply the period that is fit, but the individual transit midpoints. Other parameters are constant across all transits for a given sample model, but the normally fitted timing parameter T_0 is replaced by several T_i parameters, one for each transit epoch. General P and T_0 posteriors are determined by `Juliet` , but these simply indicate the best linear ephemeris around which the TTVs oscillate.

We carried out the TTV fit on the combined set of the TESS and LCOGT observations shown in Figures 3.1 & 3.3 using `Juliet`'s built-in nested sampling routines (`dynesty`, in this case). Extreme parameter models similar to m_2 are completely absent when we make this kind of timing-agnostic fit, and only results similar to the moderate m_1 model are favoured. This leads us to believe that the m_2-like models are not physically motivated, but are the result of trying to force a fixed period model onto data with variable transit timing. The specific results of the TTV fit are addressed in Section 3.3.4.

Priors:

Specific prior distributions for fitted parameters are listed in Table 3.4. Quantities without listed priors are not directly fitted, but are calculated from other values. P and T_0 do not receive specific priors in the typical sense. Instead, each individual transit midpoint was given a wide Gaussian

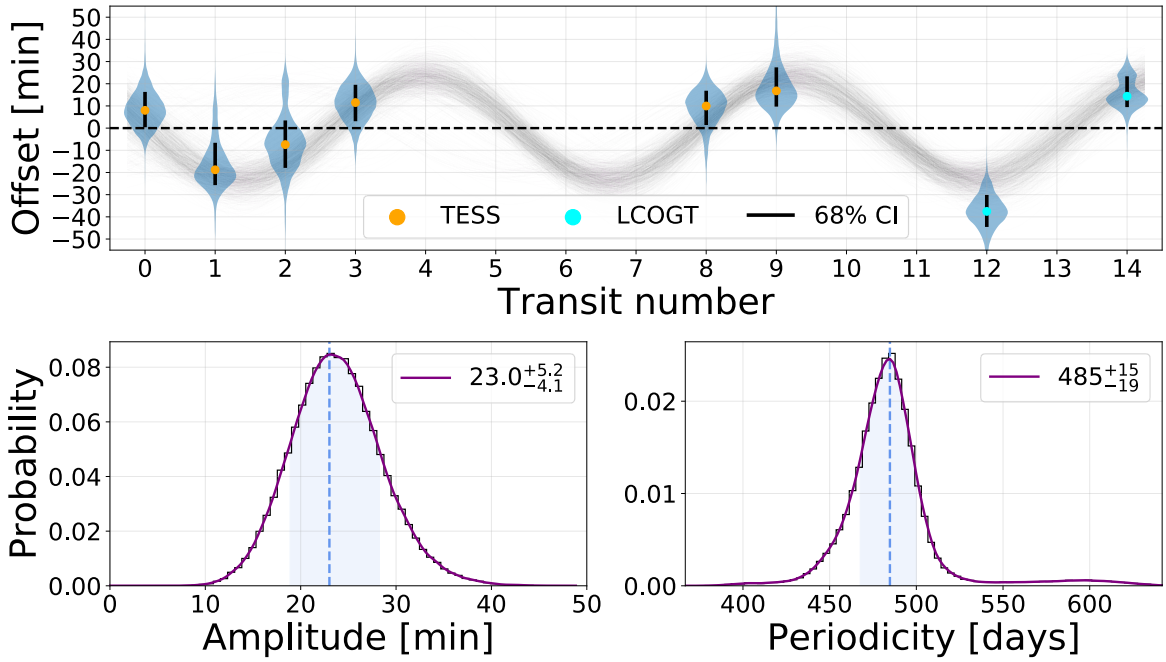

Fig. 3.7. *Top:* Midpoint timing distributions from Figure 3.6 plotted across time. Width of the blue region indicates posterior probability distribution. The purple curves show sinusoid fits to 1000 random draws of these distributions. The timings display a sinusoidal variation suggestive of systematic TTVs. *Bottom:* Distributions of the amplitude and periodicity from fitting 10^5 random draws. A zero-amplitude line (i.e. fixed-period ephemeris) is disfavoured at 5.7σ.

prior (Table 3.4 and Figure 3.6) based on timing predictions from the TESS team's original fixed-period ephemeris. The planetary radius parameter $R_p/R_\star$ receives a uniform prior over a range that comfortably encompasses the observed transit depth, including the null option of zero depth. The uniform prior for b covers the entire possible range given the expected planet size. Physically motivated limb darkening parameters q_1 and q_2 for both TESS and LCOGT were calculated using code by Espinoza & Jordán (2015) and the priors determined by the individual telescope response functions and uncertainties in stellar parameters. We used uninformative uniform priors over the whole range of the $\sqrt{e}\sin\omega$ and $\sqrt{e}\cos\omega$ parameters, and a Gaussian prior for $\rho_\star$ which comes from the TESS Input Catalog (Stassun et al., 2018b). We also include a Gaussian process in the fit. Amplitude and length-scale parameters were given very wide log-uniform priors spanning many orders of magnitude.

Fit results:

The fitted and derived parameter posterior distributions are summarized in Table 3.4. TOI-1221 b is approximately 2.9 $R_\oplus$ in size, or ~75% Neptune's radius. It orbits at ~0.4 au and, receiving about 6 times the Earth's insolation and assuming no albedo and no tidal locking, would have an equilibrium temperature (T_{eq}) of roughly 440 K.

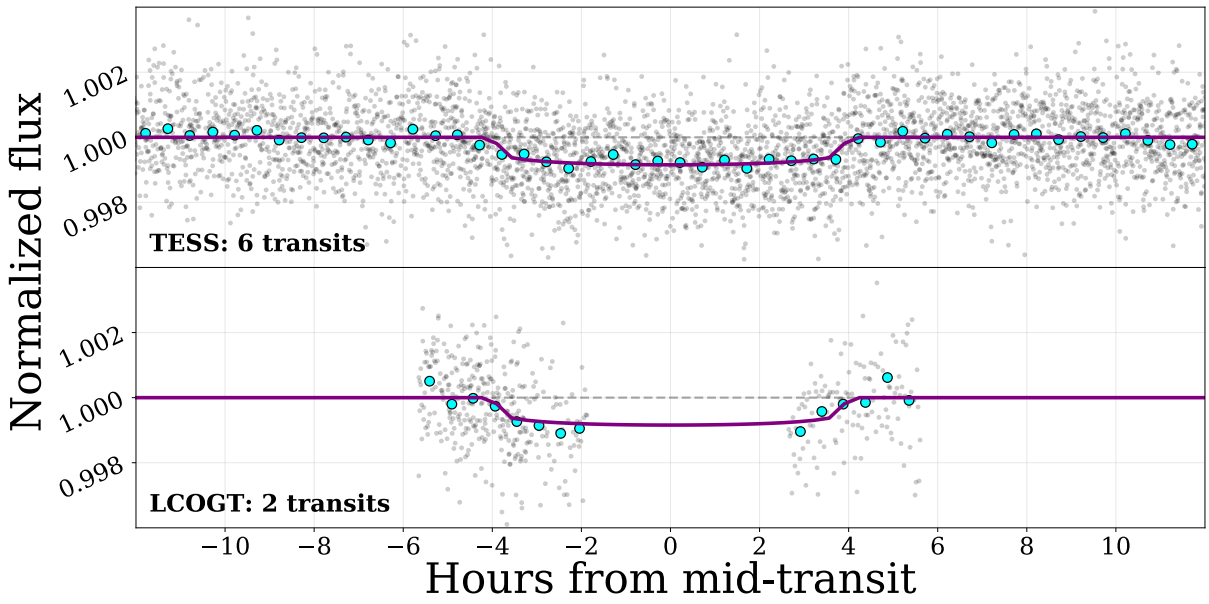

Fig. 3.8. All TESS and LCOGT transits stacked and aligned to transit midpoints with highest likelihood model overlaid. Cyan points are data binned to 30 minutes.

The timing posteriors of each of the 8 transits are also shown graphically in Figure 3.6. For most of them, the expected transit midpoints of the best-fitting fixed-period ephemeris (blue lines) fall in the wings of the distribution. Comparing the observed posteriors with the priors (grey curves) shows these features are data-driven and not strongly influenced by the prior. Plotting the observed-minus-calculated (O-C) timing differences as a function of transit epoch, we arrive at the values displayed in Figure 3.7. The timing offsets seem to preferentially follow an oscillatory pattern with amplitude $23.5^{+5.2}_{-4.1}$ minutes and periodicity of 485^{+15}_{-19} days ($5.29^{+0.17}_{-0.21}$ orbits). The amplitude distribution excludes a fixed-period ephemeris (i.e. zero amplitude) at 5.7σ. We note that the two final (LCOGT) transits appear to have large TTV offsets and might be thought to drive the sinusoidal pattern. Removing these points and running the same analysis on only the TESS transits slightly lessens the fitted amplitude by ~4 minutes and the non-fixed-period significance to 3.6σ. The fitted oscillatory TTV signal is strengthened by the two LCOGT points, but does not rely on them.

We included Gaussian process detrending parameters in our fits (trying a number of kernel models), but results consistently came back with amplitudes at least an order of magnitude smaller than the photometric scatter and transit depth. Our final fit includes an (approximate) Matern multiplied by exponential kernel, implemented via the `celerite` package (Foreman-Mackey et al., 2017). The highest log-likelihood model from the final fit is shown in Figure 3.8.

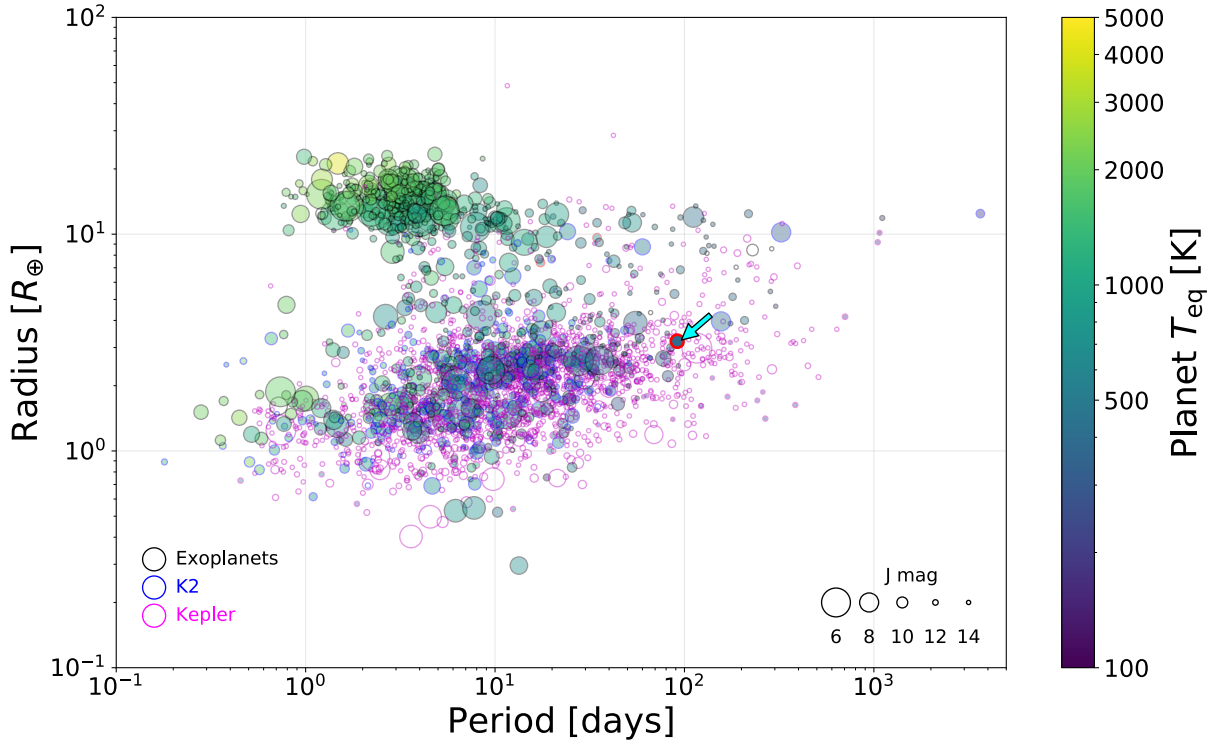

Fig. 3.9. TOI-1221 b (highlighted with a red border and marked with the cyan arrow near $P = 91$ days) placed in the context of other confirmed exoplanets with known radii. Black marker outlines denote confirmed exoplanets with mass measurements. Blue and magenta outlines are *K2* and Kepler statistically confirmed exoplanets without mass measurements, respectively.

3.4. Discussion

3.4.1. Planet properties

In one sense, given its sub-Neptune size of 2.9 $R_\oplus$, TOI-1221 b is a very typical exoplanet, as super-Earths and sub-Neptunes are the most populous exoplanet size classes (NASA Exoplanet Archive, 2022). However, it has certain other traits that place it in the outskirts. Among exoplanets that have well-constrained radii, TOI-1221 b is currently at the 97$^{\text{th}}$-percentile for orbital period, and the 10$^{\text{th}}$-percentile for T_{eq}, placing it at the edges of this parameter space (Figure 3.9; NASA Exoplanet Archive, 2022). This combination of a rare (or at least currently under-sampled) temperature regime on a common type of planet makes TOI-1221 b a valuable test-bed for understanding cooler planets.

In the course of our analysis, we experienced first-hand the importance that relatively minor TTVs can have on the outcome of a traditional transit fit. The Photo-Timing Effect (Kipping, 2014) caused dramatically different fit results, even when our TTVs are of a 20-minute scale compared

to an 8-hour transit. Allowing for some flexibility in transit timings as a test is a good practice whenever TTVs may be present.

3.4.2. Transit timing variations

When plotted against transit epoch, the TTVs (Figures 3.7 and 3.6) seem to adhere to a sinusoidal pattern. An oscillatory pattern can be indicative of gravitational perturbations of an additional unseen planet, with the strongest effects near a first-order orbital resonance (Lithwick et al., 2012). Our analysis in Section 3.3.2 of the mild RV slope and high-contrast imaging places some limits on this possible companion. The RV slope could not be produced by an object smaller than 2 $M_{\rm Jup}$ on an orbit smaller than 3,au, and the Zorro imaging would detect an object more massive than an 0.24,$M_{\odot}$ orbiting at 30 au (which could also cause the RV slope). However, objects of lower mass could potentially hide below our RV and imaging thresholds.

To explore what kind of unseen additional companion could cause the observed TTVs, we made use of the python module `TTVFast` (Deck et al., 2014). `TTVFast` accepts a list of bodies with specified masses and orbital elements, then calculates the expected transit times of each given the mutual gravitational interactions of the bodies involved.

A few findings became clear as we explored the effects of various perturbing objects on the transit timings of TOI-1221 b. Firstly, TTVs generally have multiple components to them. The major component is a long-period variation with large amplitude that typically oscillates over tens to hundreds or even thousands of transit epochs. The periodicity of this component is often referred to as the "super-period" of the system's TTVs. A secondary component caused by more frequent synodic interactions is referred to as "chopping" and has lower amplitude and higher frequency than the super-period signal. Our observed TTVs are more likely to be this short-period chopping signal, rather than the super-period of the system.

Secondly, we find that many different mass–orbit configurations of a secondary planet can faithfully reproduce the observed TTVs. These configurations can have dramatically different planet masses and orbital periods from one another, spanning all through the parameter space that remains "invisible" to our data sets. Unfortunately we also find that very small changes in the perturber's parameter space can produce wild changes in the resulting TTVs. The jagged complexity of the many-dimensional likelihood landscape means no single model gives uniquely satisfying results, no matter how closely it matches the observations.

The `TTVFast` exploration shows that it is certainly possible for another object in the system to create the TTVs we observe (particularly as a chopping signal), though they do not help very much in determining limits on the object's mass or orbit. There are many cases where TTVs can be used to estimate planet masses (e.g. Grimm et al. (2018) for TRAPPIST-1 or recently Greklek-McKeon et al. (2023) for Kepler-289), and chopping signals can even be used to break mass–eccentricity degeneracies (Deck & Agol, 2015). However, such cases generally require coverage of many more

epochs than we have for TOI-1221 b (often dozens), and have the period or even TTV measurements of the other perturbing planets. The low SNR TESS data inflating the timing uncertainties, the long 92-day period, and the lack of other detected transiting objects work against TOI-1221 b in this case. Additional transits in upcoming TESS sectors will help to extend the epoch baseline and may potentially show the beginnings of a super-period trend.

We also looked into transit duration variations (TDVs) that may accompany TTVs. `TTVFast` predicts small TDVs for most mass–orbit configurations, on the order of 1-10 minutes. Given the low SNR of single transits, individual fits of our data produce duration uncertainties on the order of ∼30 minutes. We do not achieve the timing precision necessary to draw conclusions about TDVs.

For the time being, we can only suggest that future searches of light curves or RV data sets on this target keep an eye out for additional signals, particularly near first-order interior and exterior resonances (e.g. periods of 2:1–45.84, 3:2–61.12, 4:3–68.76, 5:4–73.35, 4:5–114.60, 3:4–122.24, 2:3–137.52, and 1:2–183.36 days).

3.4.3. Future observations

A full confirmation with an RV mass measurement is the obvious next step for TOI-1221 b. With our fitted planetary radius, we can calculate the expected RV semi-amplitude signal (K) given some assumption about the planet's bulk density. With the mass estimate from Otegi et al. (2020) (displayed in Table 3.4), we expect $K \sim 1.2\,\mathrm{m\,s^{-1}}$, a challenging detection. Besides providing a mass, a precision RV campaign would also allow for a refinement of the scale height estimate and associated atmospheric signal strength. It could potentially also detect a signal from a perturbing body causing the observed TTVs.

If we assume a mean molecular weight similar to Neptune ($\mu = 2.6\,\mathrm{u}$), TOI-1221 b's atmospheric signal strength (Eq. 6.154 of Perryman (2018b)) is predicted to be around 50 ppm during transit. This small value is an expected challenge for cooler planets, but is not outside the realm of possibility with the James Webb Space Telescope (JWST), especially as the target is relatively bright (H,J,$K \sim 9$). Using the transmission spectroscopy metric (TSM) of Kempton et al. (2018, Eq. 1) we find a value of 19.4. The TSM represents the expected signal-to-noise ratio for a 10-hour JWST/NIRISS spectroscopic observation. This places TOI-1221 b slightly above the middle range of TSM values for other TOIs with reliable periods greater than 50 days (roughly 15 ± 9).

TOI-1221 b fits the TESS Mission Level One Science Requirement of measuring the mass of 50 planets with radii smaller than 4 $\mathrm{R_\oplus}$. Though the goal was officially reached in Oct 2022, this does not diminish the value of targets like TOI-1221 b. These are the kinds of planets TESS was designed to find. Longer-period and cooler planets generally require more time and effort to uncover and verify than their short-period counterparts, yet they allow us to probe very different atmospheric regimes.

While a plethora of information exists for more easily accessible short-period planets, only recently are we beginning to produce detailed examples of their longer-period brethren. We are pushing those boundaries towards the regime where we can make meaningful comparisons with our own slow and cold solar system bodies. Given TOI-1221 b's reasonable TSM value, it provides a good experimental case for the effects of low insolation on a ubiquitous planet class.

3.5. Summary & Conclusion

In the course of this paper, we have validated the exoplanet TOI-1221 b. In doing so we observed and collated a wide range of data sets. Ground-based time series photometry observations from small telescopes were able to determine that the transit signal was not caused by an eclipsing binary in any of the nearby stars. The possibility of an on-sky blend due to a background or foreground object was severely restricted by high contrast imaging by SOAR and Gemini-S/Zorro speckle images. Any very low-mass M-dwarfs that could remain undetected in our data are not sufficiently luminous to cause dilution issues with the transit fit. We further determine a low false positive probability with `TRICERATOPS`.

We characterize the stellar properties both with spectra from CHIRON and an SED analysis based on archival photometric measurements. The stellar values from these two methods are in line with one another and also with existing assessments (e.g. the TIC; Stassun et al., 2018b).

Straightforward transit fitting methods of the TESS light curves and two LCOGT transit observations were initially confounded by what appeared to be variations in the transit timings. Fitting routines that did not enforce a fixed-period on the model produced clearer results and revealed an oscillatory offset pattern in observed transit midpoints. This is potentially indicative of perturbations by an additional unseen planet in the system, likely near a first-order period resonance. Using `TTVFast` we explored the TTVs induced upon TOI-1221 b by a wide range of additional planet mass–orbit configurations. We determine that the observed TTVs are likely to be a high-frequency chopping signal, rather than the high amplitude but low frequency super-period. Unfortunately, a large number of wildly different configurations can all reproduce our observations with high accuracy. Without transit detections of the perturber, more TTVs of planet b over a much longer baseline are needed to make informative assessments of a perturber's mass and orbit.

Based on all of the work described above, we now consider TOI-1221 b to be a validated planet. All of the likely false-positive are ruled out, and the transit parameters converge to reasonable values. Moving forward, a precision RV mass measurement would solidify TOI-1221 b's planetary status, and with luck may also reveal a signal of the unseen perturber acting in the system.

The origin of the super-Earth/sub-Neptune valley remains an important question. Properly testing the various hypotheses likely requires a more thorough understanding of the effects of insolation on planetary atmospheres. Building such a robust understanding will require analysis of the hard-to-find cool planets in addition to the more easily discovered and plentiful hot ones.

Of TOIs that have strong period constraints, TOI-1221 b is the 19th-longest period TESS planet detected to date (out of 6133 TOIs) and is pushing the boundaries of our populated parameter space.

Acknowledgements

C.M. and D.L. acknowledge funding from the Trottier Family Foundation in their support of Trottier Institute for Research on Exoplanets (iREx). They also acknowledge individual funding from the Natural Sciences and Engineering Research Council (NSERC) of Canada. D. D. acknowledges support from the TESS Guest Investigator Program grants 80NSSC21K0108 and 80NSSC22K0185. S.Q. acknowledges support from the TESS GI Program under award 80NSSC21K1056. M.H.K. thanks Allan R. Schmitt for making his light curve examining software `LcTools` freely available. The work of H.P.O. has been carried out within the framework of the National Centre of Competence in Research PlanetS supported by the Swiss National Science Foundation under grants 51NF40_182901 and 51NF40_205606 for which we acknowledge the financial support of the SNSF. This paper made use of data collected by the TESS mission and are publicly available from the Mikulski Archive for Space Telescopes (MAST) operated by the Space Telescope Science Institute (STScI). Funding for the TESS mission is provided by NASA's Science Mission Directorate. We acknowledge the use of public TESS data from pipelines at the TESS Science Office and at the TESS Science Processing Operations Center. Resources supporting this work were provided by the NASA High-End Computing (HEC) Program through the NASA Advanced Supercomputing (NAS) Division at Ames Research Center for the production of the SPOC data products. This work has set the stage for a follow-up mass measurement of TOI-1221 b, a planet that matches the TESS Mission Level One Science Requirement of determining the masses of fifty (50) planets with radii less than 4 $R_{\oplus}$. This research has made use of the Exoplanet Follow-up Observation Program website, which is operated by the California Institute of Technology, under contract with the National Aeronautics and Space Administration under the Exoplanet Exploration Program. This work makes use of observations from the LCOGT network. Part of the LCOGT telescope time was granted by NOIRLab through the Mid-Scale Innovations Program (MSIP). MSIP is funded by NSF. This paper was based in part on observations obtained at the Southern Astrophysical Research (SOAR) telescope, which is a joint project of the Ministério da Ciência, Tecnologia e Inovações (MCTI/LNA) do Brasil, the US National Science Foundation's NOIRLab, the University of North Carolina at Chapel Hill (UNC), and Michigan State University (MSU). Observations in the paper (Program ID: GN/S-2021A-LP-105) made use of the High-Resolution Imaging instrument Zorro. Zorro was funded by the NASA Exoplanet Exploration Program and built at the NASA Ames Research Center by Steve B. Howell, Nic Scott, Elliott P. Horch, and Emmett Quigley. Zorro was mounted on the Gemini South telescope of the international Gemini Observatory, a program of NSF's NOIRLab, which is managed by the Association of Universities for Research in Astronomy (AURA) under a cooperative agreement with the National Science Foundation on behalf of the

Gemini Observatory partnership: the National Science Foundation (United States), National Research Council (Canada), Agencia Nacional de Investigación y Desarrollo (Chile), Ministerio de Ciencia, Tecnología e Innovación (Argentina), Ministério da Ciência, Tecnologia, Inovações e Comunicações (Brazil), and Korea Astronomy and Space Science Institute (Republic of Korea). This research has made use of the NASA Exoplanet Archive, which is operated by the California Institute of Technology, under contract with the National Aeronautics and Space Administration under the Exoplanet Exploration Program. This work has made use of data from the European Space Agency *Gaia* (`https://www.cosmos.esa.int/gaia`), processed Data Processing and Analysis Consortium (DPAC, `https://www.cosmos.esa.int/web/gaia/dpac/consortium`). Funding for the DPAC has been provided by national institutions, in particular the institutions participating in the *Gaia* Multilateral Agreement.

Data Availability

The TESS photometric light curves are freely available for download from the MAST archive (doi: 10.17909/t9-nmc8-f686).

The observations carried out by the TFOP group (PEST/ST-8XME, LCOGT/Sinistro, SMARTS/CHIRON, and Gemini-S/Zorro) have been uploaded to the group's online repository (doi: 10.26134/ExoFOP3). These data become publicly available after a 12-month proprietary period starting from the date of submission.

The *Gaia* DR3 data in the vicinity of TOI-1221 in this research is publicly available by searching the target coordinates on the online *Gaia* archive (doi: 10.5270/esa-qa4lep3).

We pulled the $B_T V_T$ magnitudes from *Tycho-2*, the JHK_S magnitudes from *2MASS*, the W1–W4 magnitudes from *WISE*, the $G_{\rm BP}G_{\rm RP}$ magnitudes from *Gaia*, and the NUV magnitude from *GALEX*.

The WASP data are not available on a public archive, but can be provided upon request by contacting Coel Hellier (c.hellier@keele.ac.uk).

Software

`Tapir` (Jensen, 2013), `BANZAI` (McCully et al., 2018; McCully et al., 2018), `AstroImageJ` (Collins et al., 2017b), `LcTools` (Schmitt et al., 2019b), `TRICERATOPS` (Giacalone & Dressing, 2020; Giacalone et al., 2021), `scikit-learn` (Pedregosa et al., 2011), `Juliet` (Espinoza et al., 2019b), `batman` (Kreidberg, 2015b), `dynesty` (Koposov et al., 2023; Speagle, 2020), `celerite` (Foreman-Mackey et al., 2017), `C-Munipack` (Motl, 2011).

3.6. Specific Contributions

This project began with my volunteering to spearhead the effort of validating this particular target. It had been flagged within the TSTPC working group as a target with nearly enough observations for publication. It was my responsibility to organize the observations involved, people who contributed, and the publication itself. Being somewhat new to the group and unpracticed in its publication procedures, I received guidance and support from Diana Dragomir, the head of the TSTPC group. I catalogued and reviewed the existing observations on the target, ensuring they were of adequate quality and useful to the project. I contacted the researchers involved with these observations and integrated them with our growing team. With Diana's help, we determined what additional observations might still be acquired to strengthen the validation.

I requested a few observations be made by collaborators with access to certain instruments. I asked Karen Collins to make the LCOGT transit observations. The first attempt captured only an ingress event due to bad weather at the second location. The second attempt caught both the ingress and egress, one from each location. The other observation I requested was the spectral measurement from CHIRON. At the time, we had one measurement close to transit, and another near quadrature. As the peaks and troughs in an RV curve occur near respective quadratures, I made a request to Samuel Quinn to acquire an additional measurement at the opposite quadrature to provide the strongest leverage on any possible mass constraints. I also personally submitted a Fast-Turnaround proposal to the Gemini-South telescope to obtain a high-contrast speckle image of the target. Though my proposal was accepted, a quirk in Gemini-South's scheduling had me team up with Steve Howell's program to make the observation. Steve carried out the actual speckle image reduction and processing.

With observations in hand, I began the task of synthesizing the results into a coherent picture. Several aspects of the collection of information came from collaborators who were more well-versed in their particular fields or with their instruments. The LCOGT final data products (i.e., light curves) came from Karen Collins. The inference about stellar activity and modulation from WASP-South was provided by Coel Hellier. Our initial high-contrast image from SOAR, and its requisite image processing came from Carl Ziegler and his team. The CHRION spectral measurements were taken by Samuel Quinn and Tabetha Boyajian, and Sam provided the RV analysis and spectral stellar characterisation. Keivan Stassun carried out the SED stellar analysis to complement our spectral results. All of the rest of the analysis and interpretation came from me. I folded the results from the various observations together to rule out false positive scenarios, and I carried out the joint TESS and LCOGT transit fit to determine the system's parameters. I also discovered the anomalous transit timing behaviour and carried out the TTV exploration.

Upon finishing the various analyses, I wrote the entirety of the paper included in this chapter. This included coordinating revisions among the 28 authors, as well as submission to the journal

and responding to the subsequent referee feedback. The final version was published in May, 2023 (Mann et al., 2023a).

Chapter 4

Giant Outer Transiting Exoplanet Mass (GOT 'EM) Survey: III. Recovery and Confirmation of a Temperate, Mildly Eccentric, Single-Transit Jupiter Orbiting TOI-2010

This manuscript is in its final stages of referee revisions before publication in the *Astronomical Journal*.

Christopher R.Mann [1,2], Paul A.Dalba [3,4], David Lafrenière [1,2], Benjamin J. Fulton [5,6], Guillaume Hébrard [7,8], Isabelle Boisse [9], Shweta Dalal [7,10], Magali Deleuil [9], Xavier Delfosse [11], Olivier Demangeon [12], Thierry Forveille [13], Neda Heidari [9], Flavien Kiefer [14], Eder Martioli [15,7], Claire Moutou [16], Michael Endl [17], William D. Cochran [17], Phillip MacQueen [19], Franck Marchis [4,9], Diana Dragomir [20], Arvind F. Gupta [21,22], Dax L. Feliz [23], Belinda A. Nicholson [24,25], Carl Ziegler [26], Steven Villanueva Jr. [27], Jason Rowe [28,2], Geert Jan Talens [29,2], Daniel Thorngren [30], Daryll LaCourse [31], Tom Jacobs [32], Andrew W. Howard [33], Allyson Bieryla [34], David W. Latham [34], Markus Rabus [35], Tara Fetherolf [36], Coel Hellier [37], Steve B. Howell [38], Peter Plavchan [39], Michael Reefe [40,39], Deven Combs [39], Michael Bowen [39], Justin Wittrock [39], George R. Ricker [41], S. Seager [41,42,43], Joshua N. Winn [29], Jon M. Jenkins [38], Thomas Barclay [44,45], David Watanabe [46], Karen A. Collins [34], Jason D. Eastman [34], and Eric B. Ting [38]

[1] Département de Physique, Université de Montréal, Montréal, QC, Canada

[2] Trottier Institute for Research on Exoplanets (iREx)

[3] Department of Astronomy and Astrophysics, University of California, Santa Cruz, CA 95064, USA

[4] SETI Institute, Carl Sagan Center, 339 Bernardo Ave, Suite 200, Mountain View, CA 94043, USA

[5] Cahill Center for Astronomy & Astrophysics, California Institute of Technology, Pasadena, CA 91125, USA

[6] IPAC-NASA Exoplanet Science Institute, Pasadena, CA 91125, USA

[7] Institut d'astrophysique de Paris, UMR7095 CNRS, Université Pierre & Marie Curie, 98bis boulevard Arago, 75014 Paris, France
[8] Observatoire de Haute-Provence, CNRS, Université d'Aix-Marseille, 04870 Saint-Michel-l'Observatoire, France
[9] Laboratoire d'Astrophysique de Marseille, Université de Provence, UMR6110 CNRS, 38 rue F. Joliot Curie, 13388 Marseille cedex 13, France
[10] Department of Astrophysics, University of Exeter, Stocker Rd, Exeter, EX4 4QL, UK
[11] Univ. Grenoble Alpes, CNRS, IPAG, 38000 Grenoble, France [12] Instituto de Astrofísica e Ciências do Espaço, Universidade do Porto, CAUP, Rua das Estrelas, 4150-762 Porto, Portugal
[13] Université Grenoble Alpes, CNRS, IPAG, 38000 Grenoble, France
[14] LESIA, Observatoire de Paris, Université PSL, CNRS, Sorbonne Université, Université de Paris, 5 place Jules Janssen, 92195 Meudon, France
[15] Laboratório Nacional de Astrofísica, Rua Estados Unidos 154, 37504-364, Itajubá - MG, Brazil
[16] Université de Toulouse, CNRS, IRAP, 14 avenue Belin, 31400 Toulouse, France
[17] McDonald Observatory and Center for Planetary Systems Habitability, The University of Texas at Austin, Austin, TX 78730, USA
[18] McDonald Observatory and Center for Planetary Systems Habitability, The University of Texas, Austin, TX, USA
[19] McDonald Observatory, The University of Texas at Austin, 2515 Speedway Blvd., Stop C1400, Austin, TX 78712, USA
[20] Department of Physics and Astronomy, University of New Mexico, 1919 Lomas Blvd NE Albuquerque, NM, 87131, USA
[21] Department of Astronomy & Astrophysics, 525 Davey Laboratory, The Pennsylvania State University, University Park, PA 16802, USA
[22] Center for Exoplanets and Habitable Worlds, 525 Davey Laboratory, The Pennsylvania State University, University Park, PA 16802, USA
[23] American Museum of Natural History, 200 Central Park West, Manhattan, NY 10024, USA
[24] Centre for Astrophysics, University of Southern Queensland, Toowoomba, Australia, 4350, Australia
[25] Sub-department of Astrophysics, University of Oxford, Keble Rd, Oxford OX13RH, UK
[26] Department of Physics, Engineering and Astronomy, Stephen F. Austin State University, 1936 North St, Nacogdoches, TX 75962, USA
[27] NASA Goddard Space Flight Center, Exoplanets and Stellar Astrophysics Laboratory (Code 667), Greenbelt, MD 20771, USA
[28] Bishops University, 2600 College St, Sherbrooke, QC J1M 1Z7, Canada
[29] Department of Astrophysical Sciences, Princeton University, 4 Ivy Lane, Princeton, NJ 08544, USA
[30] Department of Physics & Astronomy, Johns Hopkins University, Baltimore, MD 21210, USA
[31] Amateur Astronomer, 7507 52nd Pl NE, Marysville, WA 98270, USA
[32] Amateur Astronomer, 12812 SE 69th Place, Bellevue WA 98006, USA
[33] Department of Astronomy, California Institute of Technology, Pasadena, CA 91125, USA
[34] Center for Astrophysics | Harvard & Smithsonian, 60 Garden Street, Cambridge, MA 02138, USA
[35] Departamento de Matemática y Física Aplicadas, Facultad de Ingeniería, Universidad Católica de la Santísima Concepción, Alonso de Rivera 2850, Concepción, Chile
[36] Department of Earth and Planetary Sciences, University of California Riverside, 900 University Avenue, Riverside, CA 92521, USA
[37] Astrophysics Group, Keele University, Staffordshire ST5 5BG, UK
[38] NASA Ames Research Center, Moffett Field, CA 94035, USA

[39] Department of Physics & Astronomy, George Mason University, 4400 University Drive MS 3F3, Fairfax, VA 22030, USA
[40] Kavli Institute for Astrophysics and Space Research, Massachusetts Institute of Technology, 77 Massachusetts Avenue, Cambridge, MA 02139, USA
[41] Department of Physics and Kavli Institute for Astrophysics and Space Research, Massachusetts Institute of Technology, Cambridge, MA 02139, USA
[42] Department of Earth, Atmospheric and Planetary Sciences, Massachusetts Institute of Technology, Cambridge, MA 02139, USA
[43] Department of Aeronautics and Astronautics, Massachusetts Institute of Technology, Cambridge, MA 02139, USA
[44] NASA Goddard Space Flight Center, 8800 Greenbelt Road, Greenbelt, MD 20771, USA
[45] University of Maryland, Baltimore County, 1000 Hilltop Circle, Baltimore, MD 21250, USA
[46] Planetary Discoveries in Fredericksburg, VA 22405, USA

Abstract. Large-scale exoplanet surveys like the TESS mission are powerful tools for discovering large numbers of exoplanet candidates. Single-transit events are commonplace within the resulting candidate list due to the unavoidable limitation of observing baseline. These single-transit planets often remain unverified due to their unknown orbital period and consequent difficulty in scheduling follow up observations. In some cases, radial velocity (RV) follow up can constrain the period enough to enable a future targeted transit detection. We present the confirmation of one such planet: TOI-2010 b. Nearly three years of RV coverage determined the period to a level where a broad window search could be undertaken with the Near-Earth Object Surveillance Satellite (NEOSSat), detecting an additional transit. An additional detection in a much later TESS sector solidified our final parameter estimation. We find TOI-2010 b to be a Jovian planet ($M_P = 1.29\ M_{\rm Jup}$, $R_P = 1.05\ R_{\rm Jup}$) on a mildly eccentric orbit ($e = 0.21$) with a period of $P = 141.83403$ days. Assuming a simple model with no albedo and perfect heat redistribution, the equilibrium temperature ranges from about 360 K to 450 K from apoastron to periastron. Its wide orbit and bright host star ($V = 9.85$) make TOI-2010 b a valuable test-bed for future low-insolation atmospheric analysis.
Keywords : TESS — Exoplanet — Single-transit — Radial velocity — Confirmation — TOI — Long-period — Cool Jupiter

4.1. Introduction

Following its launch in 2018, the Transiting Exoplanet Survey Satellite (TESS) mission (Ricker et al., 2015) has discovered many thousands of new exoplanet candidates. As per its mission mandate, most of these targets orbit stars bright enough for detailed follow up characterization. While TESS's nearly full-sky coverage and bright object target list are undeniably valuable qualities, they do come with drawbacks. One of the most notable is its limited temporal coverage of a given patch of sky. TESS's observational strategy has been to shift its viewing angle every 25–30 days to a new sector. A portion of the sky experiences field overlap between sectors, but a large fraction (∼63%) receives only month-long baseline coverage. This is obviously detrimental for the detection of planets with orbital periods longer than ∼30 days. At best, TESS might catch one single transit in these regions before moving on to the next sector. Returning to the field in subsequent sectors can help, but does not guarantee another transit detection. Even catching a second transit detection typically leaves many possibilities for the orbital period depending on how many transits may have occurred during the unobserved time interval (Cooke et al., 2021). Without knowledge of the period, certain intrinsic system parameters remain unobtainable or strongly correlated. In particular, the semi-major axis and the period (both of which affect transit duration) are largely degenerate. As such, determination of stellar irradiation is unavailable. Attempted measurements of eccentricity and the argument of pericentre are also mostly uninformative. Lacking a clear picture of the orbital structure makes quantifying the system quite challenging. In addition, without strong constraints on the period via multiple transit detections or extensive radial velocity (RV) follow up, scheduling any sort of additional transit-based observations (e.g., transmission/emission spectroscopy, Rossiter-McLaughlin effect, etc.) becomes nearly impossible.

This is unfortunately the fate of most long-period single-transiting planet candidates in the TESS catalogue. To date, more than 98% of the 6000+ TESS Objects of Interest (TOIs) with known periods are on orbits shorter than 50 days (Exoplanet follow up Observing Program; (doi: 10.26134/ExoFOP5) and many of those that have longer reported orbits are poorly characterized and require further verification. Even if a rough period estimate can be established with RV measurements, the timing uncertainty of future transits grows with each subsequently unobserved transit ($\sigma_{T_n} \propto n\sigma_P$, where n is the number of transits since the period uncertainty, σ_P, was calculated). Generally, multiple transit observations are needed to provide tight constraints on the period and keep future timing uncertainties small.

Both transit and RV detection methods suffer observation and detection biases against long-period planets. In transit surveys, such planets require much longer baseline to capture sufficient events (Beatty & Gaudi, 2008). With finite data sets, their folded multi-transit signal-to-noise ratio (SNR) builds more slowly, making shallower transit events especially hard to detect. Their wide orbital geometries naturally lead to lower transit probabilities, reducing the number of expected

events in a given search sample. RV measurements, which are complementary to transit observations, are also hindered by wider orbits. The signal amplitude shrinks and it takes longer to cover a full orbit.

Despite and because of these challenges, there is real value in improving our catalogue of longer-period planets with their cooler equilibrium temperatures (Fortney et al., 2020). Due to these biases and accompanying investment required to study them, long-period planets tend to fall by the wayside and become underrepresented in exoplanet catalogues. Orbital periods of about 50 days mark a notable boundary in our confirmed planet databases. Given that every planet in our own solar system orbits with a period > 50 days, the restriction to our known exoplanet population is quite staggering. By confirming and cataloguing these wide-orbit planets we build up our understanding of the physical and orbital characteristics within this sparsely measured population.

Though they are few in number, our solar system giants provide detailed data on large cold planets, even allowing *in-situ* measurements (e.g. the Galileo Entry Probe; Niemann et al., 1998). Hot, giant, transiting exoplanets also comprise a high-quality data set due to their large sample size and relative ease of detection. Temperate transiting planets in between these extremes require particular effort to observe due to their adverse observational biases. However, diligent confirmation studies can still accomplish precise measurements of radius, mass, and orbital structure. These studies provide information to better understand the long-period planets as individuals, and as a population.

Another advantage of these cool giants is that they are more directly comparable to our well-studied cold solar system giants in that they do not exhibit the hot-Jupiter radius anomaly (Miller & Fortney, 2011; Thorngren et al., 2016). The relative simplicity of modeling them acts as a valuable control group for understanding hot-Jupiter inflation. Though RV surveys have measured masses for many cool/cold ($T_{\rm eq} \lesssim 500\,K$) planets, few of them exhibit transits and few of those have reasonably bright hosts, severely limiting their potential for atmospheric characterization. It is a challenge to create generalized chemical or structural atmospheric models that can span the broad temperature range of the giant planet population without having a solid testing ground in the intermediate range (Gao et al., 2021). Chasing down the longest-period targets in the TESS sample helps bridge this gap (e.g. Dalba et al., 2022). In terms of atmospheric chemistry, the cooler atmospheres may contain disequilibrium by-products that would serve as valuable probes of atmospheric physics (Fortney et al., 2020). Spectroscopic endeavours can use these lower-insolation targets to tease apart the composition transition between the very cold and very hot giant planet atmospheres.

Stellar insolation can also have many complex effects on a planet's atmosphere. The question of X-ray and ultraviolet (XUV)-driven mass loss frequently arises in the context of the super-Earth and sub-Neptune populations (Owen & Wu, 2013; Dong et al., 2017; Mordasini, 2020). Irradiation levels are also important for general structure and evolution models as well as atmospheric circulation and photochemistry in cool planets (Hörst et al., 2018). Insolation ought to push the radiative–convective boundary deeper, but also seems to drive the radius anomaly which pushes the

boundary back up along with the planet radius (Thorngren et al., 2019). Given the inverse-square law of stellar irradiation, wider-orbit planets will be significantly less affected by XUV-driven mass loss, preserving more of their primordial composition. Building a sample of planets with reduced insolation will help with the creation of more broadly applicable planetary models.

Long-period planets also provide test cases for system dynamics. Models describing the formation and migration processes thought to be responsible for the hot-Jupiter population are generally of two categories: protoplanetary disk torques (Goldreich & Tremaine, 1980; Lin & Papaloizou, 1986; Ward, 1997; Baruteau et al., 2014) or high-eccentricity migration (Rasio & Ford, 1996; Wu & Murray, 2003; Nagasawa et al., 2008; Wu & Lithwick, 2011). With the end products often being very similar, knowledge of intermediate-separation transiting planets, their companions, and their environments will help distinguish between these types of models. Transit and RV surveys are always biased against long-period planets, so filling out the eccentricity distribution of long-period giants still requires additional effort (e.g. Dalba et al., 2021). Obliquity measurements (using either the RM effect or Doppler tomography) have also been done almost exclusively on short-period giants thus far.

Table 4.1. Host Star Information

Parameter	Value	Source
TESS ID	TOI-2010	[1]
TIC ID	TIC 26547036	[1]
Gaia ID	2136815881249993600	[2]
α	$19^{h}28^{m}40.07^{s}$	[2]
δ	$+53^{d}29^{m}14.53^{s}$	[2]
m_B	10.48	[3]
m_V	9.85	[3]
m_G	9.70	[2]
m_J	8.66	[4]
m_H	8.34	[4]
m_K	8.28	[4]
Spectral type	F0	[5]
Parallax [mas]	9.2219 ± 0.0107	[2]

[1] ExoFOP; doi: 10.26134/ExoFOP5

[2] Gaia Collaboration (2020)

[3] Høg et al. (2000)

[4] Cutri et al. (2003)

[5] Simbad; doi:10.17616/R39W29

TOI-2010 (details in Table 4.1) was flagged as containing a transiting planet candidate after a single transit was detected on 2019 August 16. The transiting body, designated TOI-2010.01, did not exhibit a retransit in the remainder of TESS's primary mission. In this manuscript we confirm and characterize its planetary nature, and so we will hereafter refer to it by the designation TOI-2010 b in accordance with standard planetary nomenclature. Its initial single-transit status inspired an intensive RV campaign which constrained the period well enough to make feasible a photometric search for a second transit. While both of these efforts were successful, a much later TESS sector fortuitously revealed an additional transit during the late stages of this manuscript preparation, confirming our findings and providing even tighter parameter determination.

We present the various data and observations that contributed to this planet confirmation in Section 4.2. We then describe the various analyses carried out to characterize the star, planet, and system as a whole in Section 4.3. Sections 4.4 and 4.5 contain descriptions and discussion of our findings, respectively. Finally, a brief summary of the entire study is presented in Section 4.6.

4.2. Data and Observations

Numerous observations of this planet candidate were made by the TESS follow up Observing Program (TFOP). Some of them are overlapping in their coverage or scope, and many were intermediate steps of target validation used to green-light more intensive observations. We list all the contributions in the subsections below for completeness and recognition, but note that not every data set is included in the analysis that follows.

4.2.1. Discovery and sky-monitoring photometry

TESS:

In the early stages of the preparation of this manuscript, TOI-2010 had been observed at 2 minute cadence for Sectors 14, 15, 16, and 40 and the image data were reduced and analyzed by the Science Processing Operations Center (SPOC; Jenkins et al., 2016) at NASA Ames Research Center. A single transit was detected at the beginning of Sector 15 using an adaptive, wavelet-based matched filter (Jenkins, 2002; Jenkins et al., 2010, 2020) on 2019 September 21. The signal was also independently discovered by the Visual Survey Group (Kristiansen et al., 2022) around the same time and forwarded to the attention of the TESS Single Transit Planet Candidate (TSTPC) working group for follow up. It was alerted by the TESS Science Office as a Community TOI (CTOI) on 17 June 2020. This single transit event, though unambiguous due to its high SNR, posed a validation challenge due to its lack of period constraint.

During the late stages of manuscript preparation, TESS reobserved TOI-2010 in Sectors 54, 55, and 56 as part of its extended missions. An additional transit was detected in the Sector 56 light curve and included in our final analysis. A search by the SPOC of Sectors 14–56 reported a difference image centroiding result (Twicken et al., 2018) constraining the host star location to

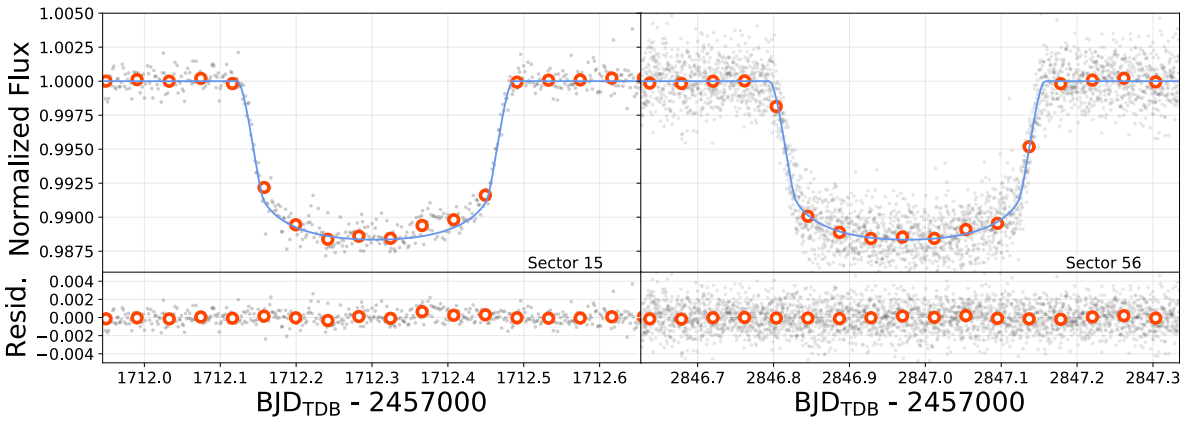

Fig. 4.1. PDCSAP data of the TESS transit detection in Sector 15 (left) and Sector 56 (right). Sector 15 was imaged with a 120 s cadence, while Sector 56 included a 20 s cadence. All bins are 60 minutes.

within $2\farcs54 \pm 2\farcs9$ of the difference image centroid. This is in agreement with the low contamination by reported nearby Gaia stars.

We acquired the Pre-search Data Conditioning Simple Aperture Photometry (PDCSAP; Stumpe et al., 2012, 2014; Smith et al., 2012) flux data from the Milkuski Archive for Space Telescopes (MAST) for the 2 minute Sector 14, 15, 16, and 40 data (doi: 10.17909/t9-nmc8-f686) and the 20 s Sector 54, 55, and 56 data (doi: 10.17909/t9-st5g-3177).

Before applying any light curve fitting, we use the `lightkurve` (Lightkurve Collaboration et al., 2018) software package's built-in `flatten` routine to remove any remaining PDCSAP variability. This applies a Savitzky–Golay filter (Savitzky & Golay, 1964) to the light curves, fitting a low-order polynomial to a rolling subset of the data to remove low-frequency trends. The transit regions were masked during this process and the subset windows were chosen to be longer than the transit duration. We apply the same `flatten` routine to the 20 s cadence Sector 56 TESS data, applying an additional rolling sigma-clip routine (3σ from the median in a window of $\pm$100 minutes) to remove outliers. The portions of the flattened light curve containing the transits and used for analysis are shown in Figure 4.1.

With the current Year 5 plan for the TESS mission, there are no scheduled visits to this region of the sky after Sector 56.

WASP:

The field containing TOI-2010 was observed by the Wide Angle Search for Planets (WASP) transit-search survey (Pollacco et al., 2006) from 2008 to 2010. In each year the observing season spanned $\sim$ 130 nights, with the SuperWASP-North camera array observing the field on clear nights with a typical 15 minute cadence. A total of 32 000 photometric data points were obtained using 200 mm, $f/1.8$ Canon lenses backed by 2k×2k CCDs. TOI-2010 is the only bright star in the 48″ extraction aperture.

The WASP data are dominated by systematics and red noise. While the transit depth is likely sufficient to show up in the WASP light curves, the survey mission relies on multiple repeated events to distinguish transits from noise. As a single-transit target at the time, WASP did not detect any events on the target. Even with the benefit of hindsight and a firm orbital ephemeris, the WASP coverage only overlaps with one predicted transit. The 4 hr span of data lies in the middle of a 8.7 hr transit, and the light curve shows no convincing transit-like features.

Table 4.2. Stellar parameters from independent spectral instruments/measurements

Parameter	HIRES	NRES	TRES	Units
$T_{\rm eff}$	5917 ± 75	5860 ± 100	5795 ± 50	K
$\log g$	$4.412^{+0.023}_{-0.026}$	4.5 ± 0.1	4.42 ± 0.10	
[Fe/H]	$0.169^{+0.055}_{-0.056}$	0.23 ± 0.06	0.22 ± 0.08	
$M_\star$	$1.107^{+0.050}_{-0.057}$	1.139 ± 0.049	–	$M_\odot$
$R_\star$	$1.084^{+0.028}_{-0.027}$	1.106 ± 0.074	–	$R_\odot$
$v \sin i_\star$	< 2.3	< 4.4	< 4.8	km s^{-1}

Note: $v \sin i_\star$ values become challenging to constrain when at the few km s^{-1} level as many line-broadening mechanisms are simultaneously at play on this scale (e.g. macroturbulence). We therefore treat spectral estimates as upper limits.

4.2.2. Candidate vetting

Once established as a TOI, a number of vetting observations were undertaken. They were used to search for false positive indications, and to assess the target's suitability for further follow up observations.

Keck/HRIES Spectra:

We obtained a spectrum of TOI-2010 with the High Resolution Echelle Spectrometer (HIRES; Vogt et al., 1994) on the Keck I telescope at W. M. Keck Observatory to explore false positive explanations for the single-transit event, to assess the quality of the host as a target for Doppler spectroscopy, and to conduct a basic spectral characterization of the host. Initial processing of the spectrum with `SpecMatch-Emp` ("Emp" indicating the "Empirical" flavour of the code; Yee et al., 2017) determined the stellar parameters. The results, along with the star's bright magnitude indicated that it would likely be a suitable target for Doppler spectroscopy.

This Keck/HIRES measurement was taken under excellent seeing conditions and produced a spectrum with SNR ~ 200. Given this data quality it was used as the template spectrum with which the Levy RV measurements were extracted (see Section 4.2.3). Similarly, we favour the Keck/HIRES extracted stellar parameters over those from LCOGT/NRES and FLWO/TRES (Section 4.2.2) due

to the quality of the spectrum, though we note the close agreement of most parameters. Table 4.2 provides a comparison of these stellar parameters.

LCOGT/NRES Spectra:

We scheduled spectroscopic observations for TOI-2010 on the Las Cumbres Observatory Global Telescope (LCOGT; Brown et al. (2013)) Network of Robotic Echelle Spectrographs (NRES; Siverd et al., 2018). NRES comprises four identical echelle spectrographs in different observatories, covering a range of longitudes in the Northern and Southern Hemispheres. The resolving power of the echelle spectrographs is $R \sim 53{,}000$ covering the wavelength range 3900–8600 Å. We obtained four good-quality (SNR 18–56) spectra with the NRES unit at the Wise Observatory between 2020 June 19 and 28. We used the `BANZAI-NRES` pipeline (McCully et al., 2022) to reduce the spectra and extract RVs, and the `SpecMatch-Synthetic` code for the stellar parameterization (Petigura, 2015; Petigura et al., 2017).

While the NRES observations provided helpful early vetting of the system, we have chosen to exclude the four RV measurements from the analysis due to their much lower precision ($>20\,\mathrm{m\,s^{-1}}$). The derived stellar parameters are generally in close agreement with the Keck/HIRES values (Table 4.2).

FLWO/TRES Spectra:

Three reconnaissance spectra of TOI-2010 were obtained on 2020 July 9, 18, and 27 with the Tillinghast Reflector Echelle Spectrograph (TRES; Fűrész, 2008). TRES is an optical (390–910 nm) spectrograph with a resolving power of $R \sim 44\,000$ mounted on the 1.5 m Tillinghast Reflector telescope at the Fred Lawrence Whipple Observatory (FLWO). The spectra, with SNR in the range of 25–35, were extracted using the TRES standard pipeline (Buchhave et al., 2010) and the stellar parameters were derived using the Stellar Parameter Classification (SPC; Buchhave et al., 2012, 2014) tool. SPC cross correlates the observed spectra against a grid of synthetic spectra based on Kurucz atmosphere models (Kurucz, 1992) deriving stellar effective temperature, surface gravity, metallicity, and rotational velocity.

In the same sense as the NRES spectra described above, these data were useful in the early classification of the star and ruling out of false positives, enabling more detailed measurements to be carried out. The FLWO/TRES stellar parameters are also generally in close agreement with the Keck/HIRES analysis (Table 4.2).

Gemini-N/'Alopeke Imaging:

Using the 'Alopeke instrument mounted on the Gemini-North telescope we acquired high-contrast imaging of TOI-2010 on 2020 June 7 (Program ID: GN-2020A-Q-132). This observation was a part of the exoplanet follow up campaign by Howell et al. (2021). With 'Alopeke's design, it can simultaneously capture imagery at both 562 nm and 832 nm. The resulting images were processed using the pipeline of Howell et al. (2011), and the resulting contrast curves are shown in

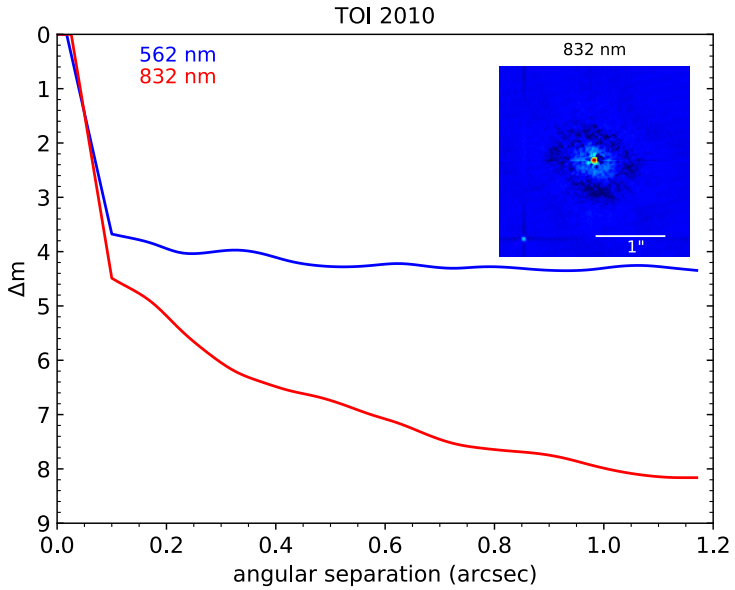

Fig. 4.2. Contrast curves from Gemini-N/'Alopeke speckle image. Curves show the 5σ contrast limit. The faint source in the lower left of the inset image is a previously unresolved neighbour star not present in the Gaia DR3 catalogue.

Figure 4.2. Due to the clearly superior performance of the 832 nm filter, we use the red contrast curve for all analyses (e.g. Section 4.3.7).

One previously unknown nearby source was detected, seen in the lower left corner of the Figure 4.2 inset. This object is separated by 1.″5 at a position angle of 138° east of north. Brightness uncertainty on this neighbour is somewhat elevated as it lies outside the speckle correlation radius of ∼1.″2. Speckle decorrelation begins to set in beyond this separation when the rays do not pass through the same atmospheric path. Our photometric estimate of the source places it at a $\Delta\text{mag} = 5 \pm 0.5$.

This source is not to be confused with the neighbouring Gaia star discussed further in Section 4.4. The Gaia source lies at a separation of 1.″9 and a position angle of 33° east of north, beyond the field of view of our 'Alopeke image. The 1.″5 source found in our 'Alopeke image does not appear in Gaia's DR2 or DR3 catalogues.

4.2.3. Radial velocities

The reconnaissance spectra from Keck/HIRES, LCOGT/NRES, and FLWO/TRES were able to place sufficient constraints on the stellar parameters to identify TOI-2010 as a suitable candidate for precise RV measurements. We collected a total of 110 RV measurements (Figure 4.3, values in the Appendix) to make up our combined RV data set. These measurements come from three separate instruments, span 992 days, and uniformly sample the phase space of the 142 day periodic signal that stands out in the data.

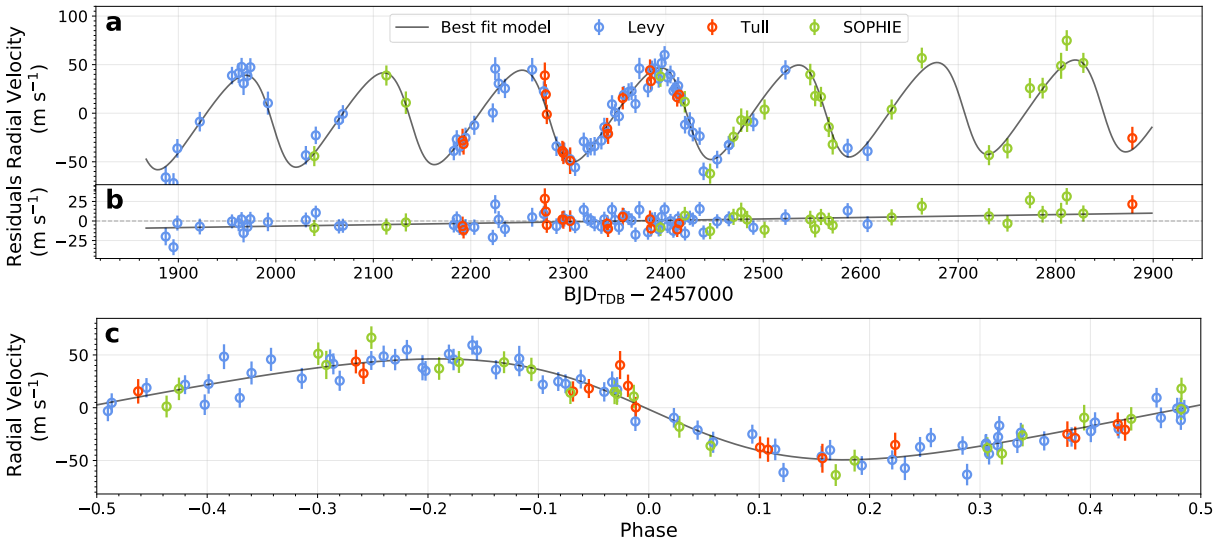

Fig. 4.3. RV coverage of 110 measurements spanning ~2.7 yr uniformly samples the full phase of the planet's orbit. A small residual acceleration remains after the removal of the planet's Keplerian signal.

Levy:

In February of 2020 (BJD 2458887), we began to gather spectra on the target for RV measurements. We started with the Levy spectrograph installed on the 2.4 m Automated Planet Finder (APF) telescope at Lick Observatory in California, acquiring 70 spectra over a 2 year period, carried out by the dynamic queue scheduler (Burt et al., 2015). The Levy spectrograph is a high-resolution ($R \sim 114\,000$) slit-fed optical echelle spectrometer (Radovan et al., 2010) that has previously been used to refine the orbital period and mass of single-transit planet candidates identified by TESS (e.g., Dalba et al., 2022). We gathered spectra with exposure times of 20–25 minutes (mostly 25), achieving signal-to-noise ratio (SNR) values of 50–100 at around 550 nm. An iodine cell in the light path allows for wavelength calibration and the forward modeling of the stellar RV for each spectrum (Butler et al., 1996; Fulton et al., 2015). This forward modeling process relies on having a high-SNR spectrum that is used as a template. The HIRES spectrum described in Section 4.2.2, which had a SNR of roughly 200, was used to create this template spectrum for the extraction of the Levy RVs which were obtained with uncertainties of 4–7 m s^{-1}.

We look for correlations in the $\log R'_{HK}$ activity index (computed from the S-index using `PyAstronomy` routines) with RVs to determine if stellar activity may be biasing the measurements. We determine a correlation coefficient of 0.10 ± 0.05 and a p-value of 0.43 ± 0.23, indicating no evidence of correlation.

Tull:

We also gathered high-precision RV observations at the McDonald Observatory using the Tull coudé spectrometer 2 (TS2) on the 2.7 m Harlan J. Smith Telescope (Tull et al., 1995). This

cross-dispersed echelle white-pupil spectrometer was used in its "TS23" mode (indicating the third focus) with an entrance slit of $1''.2 \times 8''.2$, giving a spectral resolving power of $R = 60\,000$ over most of the visible spectrum. A temperature-stabilized I_2 gas absorption cell in front of the spectrograph entrance aperture provided the velocity calibration. An exposure meter recorded the time series of flux entering the spectrograph, enabling us to compute the flux-weighted barycentric correction. A wave front sensor was used for telescope focus to optimize pupil illumination stability and throughput. We obtained the measurements with 20–30 minute exposures, achieving an SNR per pixel of 62–96 (mean $\sim$ 75). The spectra are recorded on a 2048×2048 pixel Tektronix CCD. All spectra were reduced and 1D spectra were extracted using standard `IRAF` routines (Tody, 1993, 1986). In all, a total of 16 spectra of TOI-2010 were obtained between 2020 December 8 and 2022 October 26. RVs were computed using the `AUSTRAL` code (Endl et al., 2000), resulting in uncertainties of 9–12 m s^{-1}.

We conduct a similar activity–RV correlation search as was done with the Levy, resulting in a coefficient of 0.02 ± 0.20 and a p-value of 0.59 ± 0.26 for Tull. Again, there is no indication of RV correlation.

SOPHIE:

We started observing TOI-2010 with the Spectrographe pour l'Observation des Phénomènes des Intérieurs stellaires et des Exoplanètes (SOPHIE) in July of 2020, securing 25 spectroscopic measurements up to September of 2022. SOPHIE is a stabilized échelle spectrograph dedicated to high-precision RV measurements in optical wavelengths on the 193 cm Telescope at the Observatoire de Haute-Provence, France (Perruchot et al., 2008; Bouchy et al., 2009). We used the SOPHIE high-resolution mode (resolving power $R = 75\,000$). Depending on the weather conditions, the exposure times ranged from 11 to 30 minutes (typically 18 minutes) and their SNR per pixel at 550 nm ranged from 24 to 55 (typically 46). The corresponding RVs were extracted with the standard SOPHIE pipeline using cross-correlation functions (Bouchy et al., 2009) and including CCD charge transfer inefficiency correction (Bouchy et al., 2013). Following the method described, e.g., in Pollacco et al. (2008) and Hébrard et al. (2008), we estimated and corrected for the moonlight contamination using the second SOPHIE fiber aperture, which is targeted on the sky while the first aperture points toward the star. We estimated that four of the 25 spectra were significantly polluted by moonlight; one of which was too contaminated and was excluded. The other three contaminated measurements were corrected, with corrections below 20 m s^{-1}. Thus our final SOPHIE data set included 24 measurements showing RV uncertainties ranging 3–9 m s^{-1}.

SOPHIE $\log R'_{HK}$ activity measures similarly show no correlation with RV values. We determine a correlation coefficient of 0.22 ± 0.14 and a p-value of 0.38 ± 0.27.

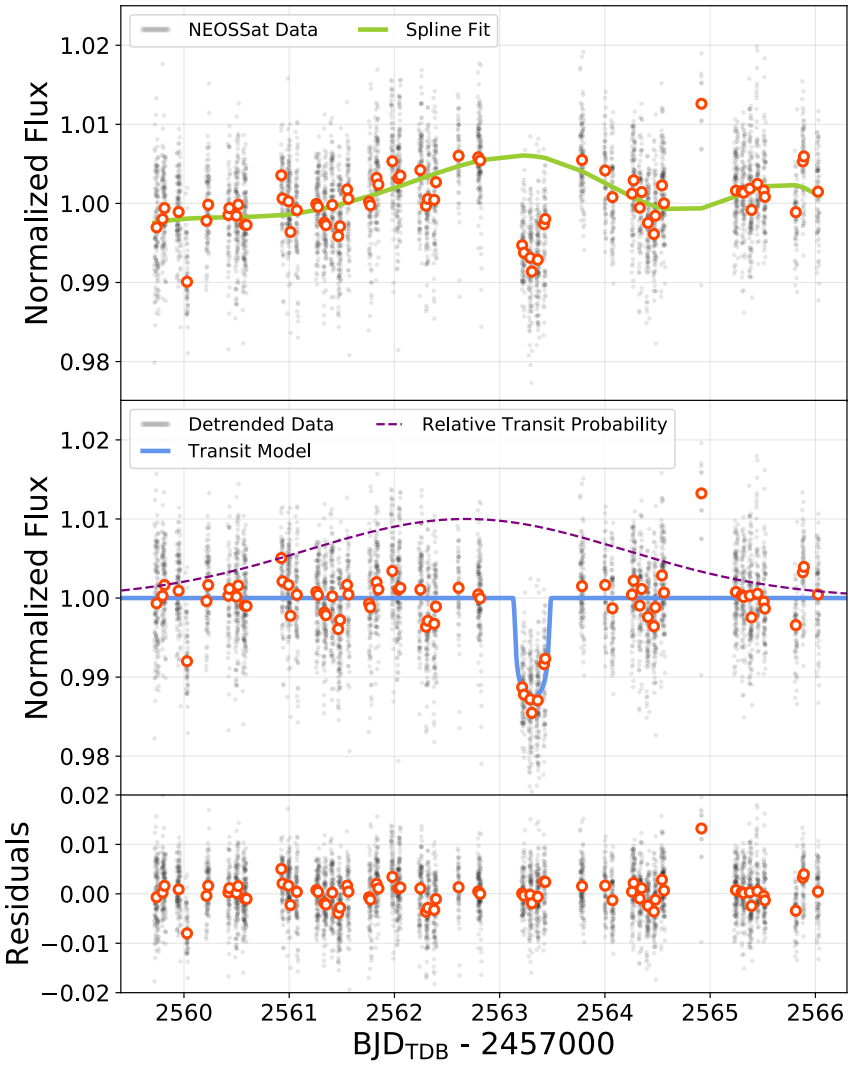

Fig. 4.4. A week-long observation by NEOSSat. Gaps in the light curve are due to Earth eclipse and other necessary telescope operations. The star was imaged with a cadence of 23 s while on target. Displayed bins are 60 minutes. *Top:* A `KEPLERSPLINE` fit to the out-of-transit region to model systematics (discussed in Section 4.3.3). *Middle:* The transit fitted to the corrected light curve. The dashed purple curve shows relative probability of the expected transit based on the RV-derived period constraints available at the time of observation. *Bottom:* Residuals of the transit fit.

4.2.4. Follow up photometry

The collective RV campaign was able to map out a clear planetary signal, but the period uncertainty was only constrained to the order of a few days. This was insufficient for reliable scheduling of transit observations, so we undertook a few efforts to catch a subsequent transit and fine-tune the period.

GMU:

We observed TOI-2010 with the George Mason University Observatory's 0.8 m Ritchey–Chretien telescope on the nights of the 2021 July 21 and 22 to capture a second transit. We imaged in R with an SBIG-16803 CCD with exposure times of 30 s repeated for a duration of ~5 and 2.5 hr each night, respectively. Both nights were impacted by intermittent clouds, and single measurement precisions of 6.5 and 7.5 ppt were obtained per 30 second exposure. Data was reduced and plate-solved using a custom python code `alnitak`[1] and aperture photometry, reference star selection, and systematic detrending were performed with `AstroImageJ` (Collins et al., 2017c).

This attempt was prompted due to a predicted transit (from preliminary RV fits) occurring very near the end of TESS Sector 40, and motivated by an absence of TESS coverage in Sector 41. Unfortunately, no transit was detected on either night. Given the broad transit timing uncertainty at the time, the narrow available observing windows, and the very long transit duration, the odds of detecting the transit here were quite low. Unbeknownst at the time, the transit occurred 1.8 days after the second observation. These data provided initial constraining power for refining the RV period, but do not benefit the global orbital model. As such, they are not included in the modeling of Section 4.3.

NEOSSat:

The Near-Earth Object Surveillance Satellite (NEOSSat) is a small spacecraft operated jointly by the Canadian Space Agency (CSA) and Defence Research and Development Canada (DRDC). It has a 15 cm telescope aperture and is capable of precision relative photometry (Abbasi et al., 2019). NEOSSat's clear-filter effective bandpass is approximately 400–900 nm.

As the RV data accumulated, preliminary joint fits (see Section 4.3 for details) of the RVs and TESS sector 15 transit revealed a roughly 142 day period, albeit with broad uncertainties. The extended transit duration (~8.7 hr), wide timing uncertainty (on the order of a week), and long period made observing a subsequent transit from the ground extremely challenging. While NEOSSat had previously proven its capability with short-period exoplanet follow up (e.g., Fox & Wiegert, 2022), TOI-2010 b marked the first attempt at using the instrument to recover a long and uncertain period. With its space-based vantage point, NEOSSat has the capability to stare continuously at a target for an extended duration, interrupted only by Earth-eclipse events and technical satellite operations. In mid-December of 2021 we employed NEOSSat to observe a ~6 day (2σ) window around the predicted transit. The telescope imaged TOI-2010 as continuously as was feasible during this time.

We reduced the raw images and extracted aperture photometry using a custom python pipeline developed for NEOSSat, available on GitHub.[2] With photometry in hand, we applied a principal component analysis (PCA) procedure to the raw photometry using other in-frame stars as reference

[1] `https://github.com/oalfaro2/alnitak`
[2] `https://github.com/jasonfrowe/neossat`

to calculate a normalized relative flux light curve of the target. The PCA process removes time-varying trends in the photometry that are common across many stars in the frame. At this point there remained some residual variability for which the PCA could not account. This low-frequency variability was removed using a spline fit (discussed in Section 4.3.3). Even against this variability the deep transit event was clearly visible roughly 15 hr after the RV-predicted midpoint (well within the 3 day, 1σ timing uncertainty).

This detection by NEOSSat provided the first precise period measurement for TOI-2010 b, and prompted the preparation of this manuscript. The much later transit detected in TESS's Sector 56 data agrees completely with the refined period. The NEOSSat light curve is displayed in Figure 4.4.

4.3. Analysis

As the RV campaign progressed, we made preliminary fits using the TESS light curve and the available RV data to place initial constraints on the orbital period. This allowed us refine the ephemeris enough to plan our follow up search for a subsequent transit event. Once they became available, the additional transit detections (NEOSSat and TESS Sector 56) allowed for much more precise period determination.

For our final global fit, we use the IDL software package `EXOFASTv2` (Eastman et al., 2019). `EXOFASTv2` provides an integrated framework to jointly analyze multiple exoplanet data sets. Drawing from the IDL astronomy library (Landsman, 1993), it simultaneously fits for wide ranges of stellar, planetary, orbital, and instrumental parameters in a self-consistent manner that leverages the rich complementarity of modern data sets.

The details listed below in Sections 4.3.1–4.3.3 pertain to the final fit, including archival SED measurements; RVs from Levy, Tull, and SOPHIE; and light curves from the initial TESS Sector 15 transit, the subsequent NEOSSat detection, and also the much later Sector 56 detection by TESS. The parameter posterior results are listed in Table 4.3. The fits converged fully by two different statistics: the Gelman–Rubin statistic, R_z, and the number of independent samples, T_z. We set very stringent thresholds of $R_z < 1.01$ and $T_z > 1000$. We provide a brief description of the steps involved, but for precise details on the internal operations of `EXOFASTv2` please consult the primary paper by Eastman et al. (2019).

Beyond `EXOFASTv2`, we conduct several other independent analyses. We model the bulk metallicity of planet b with a custom software, and we analyse the photometric modulation of TOI-2010 to assess the stellar rotation. In discovering a slight acceleration across the RV measurements, we also conduct a search of mass–orbit parameter space to determine what type of additional companion could be the cause.

4.3.1. EXOFASTv2: SED/MIST stellar modeling

EXOFASTv2 fetches archival photometry from Galaxy Evolution Explorer (GALEX; Bianchi et al., 2011), Tycho-2 (Høg et al., 2000), UCAC4 (Zacharias et al., 2012), APASS (Henden et al., 2016), the Two Micron All Sky Survey (2MASS; Cutri et al., 2003), the Wide-field Infrared Survey Explorer (WISE; Cutri et al., 2021), Gaia (Gaia Collaboration et al., 2016), the Kepler INT Survey (Greiss et al., 2012), the UBV Photoelectric Catalog (Mermilliod, 1994), and the Stroemgren–Crawford $uvby\beta$ photometry catalog (Paunzen, 2015), as well as extinctions from Schlegel et al. (1998b) and Schlafly & Finkbeiner (2011) and parallaxes from Gaia DR2 (Gaia Collaboration et al., 2018). Allowing photometric uncertainties to be inflated in case of underestimation, it then fits an SED model to this archival photometry using the parallax value and a library of stellar atmospheres. The stellar physics are constrained from either the empirical relations laid out by Torres et al. (2010b), the Yonsie Yale stellar evolutionary models Yi et al. (2001), or the MIST evolutionary models (Choi et al., 2016; Dotter, 2016), which itself is built using MESA (Paxton et al., 2011, 2013, 2015, 2018). Stellar atmospheric models from NextGen (Allard et al., 2012)), ATLAS (Kurucz, 1979), and PHOENIX (Hauschildt et al., 1997) underlie several aspects of the code.

We are able to impose Gaussian priors on the stellar effective temperature ($T_{\rm eff}$) and metallicity ([Fe/H]) in the fit, originating from the Keck/HIRES spectra (Table 4.2). The $F_{\rm bol}$ and $T_{\rm eff}$ parameters have enforced error floors representative of the systematic uncertainties between stellar evolution models to prevent unrealistic precision (2.0% and 2.4%, respectively; Tayar et al., 2022).

4.3.2. EXOFASTv2: RV modeling

The multiple instrument RV data sets are simultaneously fit to a Keplerian model, retaining separate jitter and systemic offset terms. We measured typical $\log R'_{HK}$ activity index measures of -5.1 to -4.7 that were uncorrelated with RV values. This activity level could induce stellar jitter up to $\sim 10\,{\rm m\,s^{-1}}$, but is unlikely to affect the derived parameters given such a strong planetary signal.

Within EXOFASTv2 the exoplanet mass radius relation from Chen & Kipping (2017) can be referenced to estimate the mass or radius of the exoplanet (and all relevant derived parameters) in the absence of an RV data set or transit, respectively. In this case, however, the RV data constrain the mass while the transit data constrain the radius.

A single long-term linear drift parameter is included in the model. We have excellent temporal overlap of the data across instruments, so there is no large correlation between the trend parameter and systemic RV offset parameters. The fitted RV model is shown in Figure 4.3.

4.3.3. EXOFASTv2: Transit modeling

EXOFASTv2's transit model is generated using Mandel & Agol (2002) and Agol et al. (2019) with limb-darkening parameters constrained by Claret & Bloemen (2011) and Claret (2017). We pass it the TESS coverage of the initial Sector 15-detected transit, a stretch of flat light curve from a Sector 40 that narrowly missed another transit, as well as the later detection in Sector 56. We also include the entire 6 day NEOSSat light curve with its detection. Limb-darkening parameters and transit depths are allowed to differ between instruments. Each instrument also gets its own jitter parameter and out-of-transit offset value. We impose no additional transit-specific priors for this portion of the fit. The period and other orbital element constraints arise from a simultaneous fit of the transit and RV data.

We incorporate a spline fit in the EXOFASTv2 modeling of the NEOSSat data, based on the keplerspline[3] (Vanderburg et al., 2016) designed to handle long-term variability in long Kepler light curves. We used a knot spacing of 1.1 days (roughly 3× the transit duration) to model the low-frequency variation.

4.3.4. Bulk planetary composition

To infer the bulk composition of the planet, we use the modeling and retrieval approach of Thorngren & Fortney (2019), which we will briefly summarize. Forward models parameterize the thermal state of the planet by the envelope specific entropy, which we evolve from a hot initial state using the atmosphere models of Fortney et al. (2007). This requires that we know the radius and temperature structure of the planet at a given specific entropy. We calculate this using a 1D static model of the planet which solves the equations of hydrostatic equilibrium, conservation of mass, and the equation of state (EOS). We use the H/He EOS from Chabrier et al. (2019), and a 50/50 rock/ice mixture for the metals (Thompson, 1990), combining these using the additive volumes approximation. For a given mass, metallicity, and stellar insolation, this yields evolution tracks of the radius with time. To match these models to TOI-2010 b, we use a Bayesian statistical model with the true mass, bulk metallicity, and true age as model parameters and fit them against the observed mass, radius, and age from the EXOFASTv2 fit (Table 4.3). Because TOI-2010 b is much cooler than the hot-Jupiter inflation threshold (e.g. Miller & Fortney, 2011), we do not include any additional heating in the planet.

4.3.5. TESS light curve modulation

Even in the PDCSAP TESS data, with a degree of its systematics removed, we noticed some low-level variability. As a secondary measure of stellar rotation we looked at the star's long-term light curve modulation. A simple normalization was applied in order to concatenate the TESS 2

[3] https://github.com/avanderburg/keplerspline

minute cadence SAP light curves from Sectors 14, 15, and 16. Data points that were flagged as poor quality, greater than 5σ outliers, or during the TOI-2010 b transit were removed. Stitching together multiple sectors of observations (even when observed continuously) can introduce systematics into the concatenated light curve that could produce a spurious signal in a periodogram search. Therefore, we searched for periodic photometric variability using the TESS systematics-insensitive periodogram tool, `TESS-SIP`[4] (Hedges et al., 2020), which uses PCA to account for spacecraft systematics while simultaneously performing a periodogram search. In the periodogram search from 1 day to half the baseline of the continuous TESS observations (which are ∼32 days), we identify a periodic signature in the light curve at 19.0 ± 3.0 days, albeit at a low normalized Lomb–Scargle power (<0.001). Assuming a small stellar obliquity, this 19 day signal corresponds to a $\sim$2.8 km s^{-1} stellar rotation rate, in general agreement with the spectroscopic estimates (see Table 4.2). A short-period periodogram search (0.01–13 days) was also performed separately on the PDCSAP photometry from Sectors 14, 15, and 16 following the procedure described in Fetherolf et al. (2023). A small-amplitude ($\lesssim$ 0.2 ppt), 5.7 day signal was identified in the TESS photometry but we note this is consistent with being attributed to spacecraft systematics due to its location in power–period space relative to other stars in these TESS sectors. With its low SNR and similarity to known systematics, we do not consider this signal physically relevant.

4.3.6. WASP light curve modulation

We searched each season of WASP data for a rotational modulation using methods discussed in Maxted et al. (2011). We find a significant and persistent modulation at a period of 20 ± 1 days. The modulation is weak, with an amplitude of only 1–2 mmag, but the overall false-alarm likelihood is below 1%. This closely matches the TESS photometric modulation, and also likely reflects a stellar rotation rate of ∼2.8 km s^{-1}.

4.3.7. Mass–orbit possibilities for an additional companion

A small residual acceleration is detected in the collective RV data. To constrain potential objects on very long orbits that could cause this acceleration, we adopt the process described in Bryan et al. (2016). In essence, we step through a 2D grid of semi-major axes and object masses. In each cell, we draw a set of planet b parameters from our fitted posteriors of Table 4.3, generating an RV model. This model is subtracted from the RV measurements to reveal a residual slope. A model for object 2 is created by drawing M and a values from the current cell, and i and e values from motivated distributions. In this case, i is drawn randomly from a uniform $\cos i$ distribution and e from a β distribution (eq. 3 of Bryan et al., 2016). The remaining T_0, $T_{\rm peri}$, and ω parameters are determined by fitting the drawn object 2 model to the residuals, as well as an RV offset. The offset accounts for any change to the assumed systemic velocity caused by the second object.

[4] `https://github.com/christinahedges/TESS-SIP`

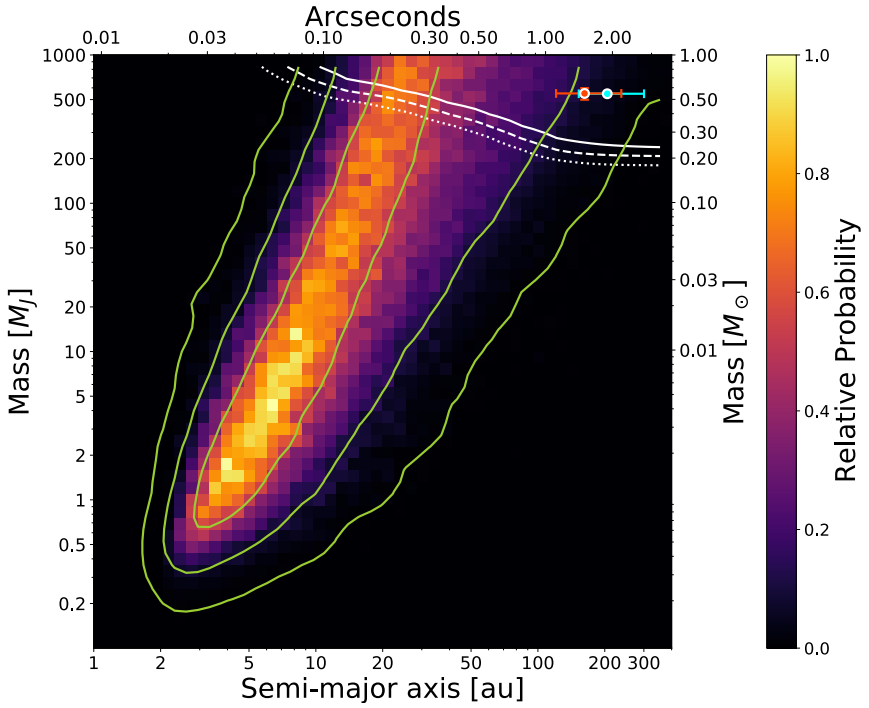

Fig. 4.5. Constraints on a potential second bound body in the system creating the observed long-term RV acceleration, assuming the objects are at the same distance as TOI-2010. Small-orbit limits are provided by the long baseline over which the gradual acceleration occurs. Green contours show the 0.607, 0.135, and 0.011 relative probability levels, corresponding to the 1, 2, and 3σ probability density values of a normal distribution. White contours show the 25%, 50%, and 75% detection probability levels (from bottom to top) set by the Gemini-N/'Alopeke contrast curve. Contours are smoothed by a Gaussian kernel with a standard deviation of one cell. Red and cyan points in the top right corner indicate the 'Alopeke-discovered (1.″5) and Gaia (1.″9) close neighbour stars.

This process is repeated 500 times per cell. For each cycle, the χ^2 is calculated and stored, as well as the probability that the object is visible. This probability is based on the inferred magnitude of the object and the fraction of its orbital period that it would spend at a detectable separation from the host, set by the Gemini-N/'Alopeke contrast curve (Figure 4.2). The data cubes are marginalized over the third axis to create a 2D probability density grid over the object's a and M. These results are displayed in Figure 4.5.

With the allowable mass–orbit space mapped out, we investigate the potential for the known nearby stars to cause the acceleration. The plotted mass uncertainties for the two nearby sources in Figure 4.5 reflect the magnitude uncertainty of the source only. They do not account for the intrinsic uncertainty of the precalculated stellar evolution grids[5] (Baraffe et al., 2015) from which they were interpolated.

To place a tentative uncertainty on the semi-major axis of the neighbouring stars (under the assumption they are bound), we follow the steps of Brandeker et al. (2006, Appendix A2) given an

[5]http://perso.ens-lyon.fr/isabelle.baraffe/BHAC15dir/

observed projected separation, unknown orbital orientation, and assumed eccentricity distribution. We do not adopt their analytic approximation (Equation (A2)) which roughly matches the numerical distribution arising from a simple $f(e) = e^2$ eccentricity distribution, but instead carry out the full Monte Carlo approach to create a nonanalytic distribution. We use $f(e) = e^{0.4}$ where $e \in [0,0.8]$ is extracted from the observation of binaries with Sun-like primaries (Moe & Di Stefano, 2017).

Table 4.3. Median values and 68% confidence interval for TOI2010, created using EXOFASTv2 commit number 96030ceb.

Parameter	Units	Values
Stellar Parameters:		
$M_\star$	Mass ($M_\odot$)	$1.112^{+0.048}_{-0.055}$
$R_\star$	Radius ($R_\odot$)	$1.079^{+0.027}_{-0.026}$
$R_{\star,SED}$ ..	Radius[1] ($R_\odot$)	$1.0753^{+0.0093}_{-0.0090}$
$L_\star$	Luminosity ($L_\odot$)	$1.299^{+0.083}_{-0.081}$
F_{Bol}	Bolometric Flux (cgs)	$0.00000000354^{+0.00000000023}_{-0.00000000022}$
$\rho_\star$	Density (cgs)	$1.243^{+0.087}_{-0.086}$
$\log g$	Surface gravity (cgs).....	$4.417^{+0.021}_{-0.025}$
$T_{\rm eff}$	Effective Temperature (K)	5929 ± 74
$T_{\rm eff,SED}$ ..	Effective Temperature[1] (K).....	5950 ± 110
[Fe/H] ..	Metallicity (dex)	0.168 ± 0.055
$[{\rm Fe/H}]_0$ ..	Initial Metallicity[2]	$0.154^{+0.054}_{-0.055}$
Age	Age (Gyr)	$1.9^{+2.2}_{-1.3}$
EEP ...	Equal Evolutionary Phase[3]	335^{+25}_{-37}
A_V	V-band extinction (mag)	$0.210^{+0.079}_{-0.085}$
σ_{SED} ...	SED photometry error scaling	$0.72^{+0.23}_{-0.15}$
ϖ	Parallax (mas).....	9.237 ± 0.017
d	Distance (pc)	108.26 ± 0.20
$\dot{\gamma}$	RV slope[4] (m/s/day).....	$0.0185^{+0.0055}_{-0.0054}$
Planetary Parameters:		b
P	Period (days)	$141.834025^{+0.000065}_{-0.000066}$
R_P	Radius ($R_{\rm J}$).....	1.054 ± 0.027
M_P	Mass ($M_{\rm J}$)	$1.286^{+0.055}_{-0.057}$
T_C	Time of conjunction[5] ($\rm BJD_{TDB}$)....	$2458712.30168^{+0.00042}_{-0.00041}$
a	Semi-major axis (AU)	$0.5516^{+0.0078}_{-0.0093}$
i	Inclination[6] (Degrees).....	$89.903^{+0.064}_{-0.059}$
e	Eccentricity	$0.212^{+0.022}_{-0.021}$
$\omega_\star$	Argument of Periastron (Degrees)...	$98.8^{+4.8}_{-4.9}$
T_{eq}	Equilibrium temperature[7] (K).....	$400.2^{+5.6}_{-5.7}$
$\tau_{\rm circ}$	Tidal circularization timescale (Gyr) .	$3980000^{+910000}_{-790000}$
K	RV semi-amplitude (m/s).....	47.8 ± 1.5

$R_P/R_\star$ ..	Radius of planet in stellar radii	$0.10035^{+0.00043}_{-0.00037}$
$a/R_\star$ ...	Semi-major axis in stellar radii	$109.8^{+2.5}_{-2.6}$
δ	$(R_P/R_\star)^2$	$0.010069^{+0.000087}_{-0.000075}$
$\delta_{\rm NEOSSat}$ ..	Transit depth in NEOSSat (fraction)..	$0.01284^{+0.00040}_{-0.00038}$
$\delta_{\rm TESS}$ ...	Transit depth in TESS (fraction) ...	0.01160 ± 0.00011
τ	Ingress/egress transit duration (days) .	$0.03363^{+0.0013}_{-0.00069}$
T_{14}	Total transit duration (days).....	$0.3617^{+0.0012}_{-0.0010}$
T_{FWHM} ..	FWHM transit duration (days)	$0.32784^{+0.00083}_{-0.00082}$
b	Transit Impact parameter	$0.147^{+0.088}_{-0.097}$
b_S	Eclipse impact parameter	$0.23^{+0.13}_{-0.15}$
τ_S	Ingress/egress eclipse duration (days) .	$0.0525^{+0.0035}_{-0.0028}$
$T_{S,14}$	Total eclipse duration (days)	$0.544^{+0.027}_{-0.025}$
$T_{S,FWHM}$.	FWHM eclipse duration (days)	0.491 ± 0.025
$\delta_{S,2.5\mu m}$ ..	Blackbody eclipse depth at 2.5μm (ppm)	$0.0094^{+0.0020}_{-0.0017}$
$\delta_{S,5.0\mu m}$ ..	Blackbody eclipse depth at 5.0μm (ppm)	$4.75^{+0.46}_{-0.43}$
$\delta_{S,7.5\mu m}$ ..	Blackbody eclipse depth at 7.5μm (ppm)	$32.1^{+2.0}_{-1.9}$
ρ_P	Density (cgs)	$1.36^{+0.11}_{-0.10}$
$logg_P$ ...	Surface gravity	$3.457^{+0.024}_{-0.026}$
Θ	Safronov Number	$1.211^{+0.049}_{-0.048}$
$\langle F \rangle$	Incident Flux (10^9 erg s^{-1} cm^{-2}) ...	$0.00557^{+0.00030}_{-0.00029}$
T_P	Time of Periastron (BJD$_{\rm TDB}$).....	2458572.7 ± 1.2
T_S	Time of eclipse (BJD$_{\rm TDB}$)	$2458780.3^{+1.7}_{-1.6}$
T_A	Time of Ascending Node (BJD$_{\rm TDB}$)..	2458685.2 ± 1.1
T_D	Time of Descending Node (BJD$_{\rm TDB}$) .	2458595.5 ± 1.1
V_c/V_e ...	.....	0.809 ± 0.018
$e \cos \omega_\star$ ..	.....	-0.032 ± 0.018
$e \sin \omega_\star$ ..	.....	$0.208^{+0.022}_{-0.021}$
$M_P \sin i$ ..	Minimum mass ($M_{\rm J}$)	$1.286^{+0.055}_{-0.057}$
$M_P/M_\star$ ..	Mass ratio	$0.001107^{+0.000039}_{-0.000038}$
$d/R_\star$ ...	Separation at mid transit	86.8 ± 4.2
P_T	A priori non-grazing transit prob ...	$0.01037^{+0.00053}_{-0.00048}$
$P_{T,G}$ ...	A priori transit prob	$0.01268^{+0.00065}_{-0.00059}$
P_S	A priori non-grazing eclipse prob ...	$0.006779^{+0.00010}_{-0.000068}$
$P_{S,G}$ ...	A priori eclipse prob	$0.008291^{+0.00013}_{-0.000085}$

Wavelength Parameters:		NEOSSat	TESS
u_1	linear limb-darkening coeff	0.442 ± 0.048	0.271 ± 0.019
u_2	quadratic limb-darkening coeff	0.301 ± 0.050	0.270 ± 0.027

Telescope Parameters:		Levy	SOPHIE	Tull
$\gamma_{\rm rel}$	Relative RV Offset[4] (m/s)	0.3 ± 1.3	$-15315.8^{+2.5}_{-2.4}$	$8778.8^{+2.9}_{-2.6}$
σ_J	RV Jitter (m/s)	$7.81^{+1.1}_{-0.97}$	$9.8^{+2.1}_{-1.7}$	$0.0^{+8.1}_{-0.00}$

σ_J^2	RV Jitter Variance	60^{+18}_{-14}	97^{+46}_{-30}	-2^{+68}_{-39}

Light Curve Parameters:

TESS UT 2019-08-16		
σ^2	Added Variance	$-0.000022669^{+0.000000031}_{-0.000000029}$
F_0	Baseline flux	$1.000132^{+0.000030}_{-0.000031}$
TESS UT 2021-07-23		
σ^2	Added Variance	$-0.000000041^{+0.000000015}_{-0.000000014}$
F_0	Baseline flux	1.000002 ± 0.000014
NEOSSat UT 2021-12-15		
σ^2	Added Variance	$0.00001984^{+0.00000059}_{-0.00000057}$
F_0	Baseline flux	$1.0003^{+0.0071}_{-0.0066}$
TESS UT 2021-09-02		
σ^2	Added Variance	$0.000000077^{+0.000000060}_{-0.000000058}$
F_0	Baseline flux	$0.999961^{+0.000033}_{-0.000034}$

Notes: See Table 3 in Eastman et al. (2019) for a detailed description of all parameters.

[1] This value ignores the systematic error and is for reference only

[2] The metallicity of the star at birth

[3] Corresponds to static points in a star's evolutionary history. See §2 in Dotter (2016).

[4] Reference epoch = 2459382.832843.

[5] Time of conjunction is commonly reported as the "transit time".

[6] Inclination symmetrically on the other side of 90° is equally valid.

[7] Assumes no albedo and perfect redistribution. Calculated at star–planet separation of a. See Table 4.4 for phase-specific values.

4.4. Results

Based on the results of the global transit, RV, and SED fit, we confirm TOI-2010 b as a temperate Jovian exoplanet around a Sun-like star. We find TOI-2010 b to have a mass of $M_P = 1.286^{+0.055}_{-0.057}\ M_{\rm J}$ and a radius of $R_P = 1.054 \pm 0.027\ R_{\rm J}$. It orbits with a period of $P = 141.834025^{+0.000065}_{-0.000066}$ days and an eccentricity of $e = 0.212^{+0.022}_{-0.021}$. A full list of the fitted and calculated parameters and their uncertainties are displayed in Table 4.3. We determine that the contribution to the uncertainty of M_P is almost evenly split between the uncertainties on K and $M_\star$, and that the uncertainties of i, e, and P have a negligible impact.

The reported $T_{\rm eq}$ of Table 4.3 comes from an assessment using a single representative star–planet distance. However, with nonnegligible eccentricity, several calculated parameters, $T_{\rm eq}$ included, are subject to variation with orbital phase. Table 4.4 displays certain of these parameters at four key points in the planet's orbit.

Table 4.4. Orbital information

Parameter	Periastron	Apoastron	Transit	Eclipse	Units
Phase	0.016	0.516	0.000	0.479	–
Orbital dist.	0.44	0.70	0.44	0.67	au
Insolation	6.9	2.9	6.8	2.9	$S_\oplus$
$T_{\rm eq}$	450	363	450	364	K

Note: $T_{\rm eq}$ calculation assumes no albedo and perfect redistribution.

TOI-2010 b's moderate eccentricity falls in the $\sim 75^{\rm th}$ percentile of giant planets with well-known masses and radii. It is distinctly above the cluster of planets with very low eccentricities, but not so high as to stand out among the population of high-eccentricity planets.

Between the SED/MIST model fitting within `EXOFASTv2` and the spectral analysis from various instruments, we determine many of TOI-2010's stellar parameters. In the global `EXOFASTv2` posteriors, we see no sign of the bimodality commonly seen between stellar mass and age. This can arise when a star is slightly evolved and the MIST stellar evolution models experience some degeneracy near the subgiant branch (e.g. Dalba et al., 2021).

From the Keck/HIRES spectral measurement, we find the stellar radius, mass, and effective temperature to be $R_\star = 1.084^{+0.028}_{-0.027}\,R_\odot$, $M_\star = 1.107^{+0.050}_{-0.057}\,M_\odot$, and $T_{\rm eff} = 5917 \pm 75\,K$, respectively. TOI-2010 has a surface gravity of $\log g = 4.412^{+0.023}_{-0.026}$ and a metallicity of $[{\rm Fe/H}] = 0.169^{+0.055}_{-0.056}$. We used these Keck/HIRES stellar values in the global fit as this spectral measurement has the highest resolution and SNR. The stellar parameters determined via spectral fitting of the Keck/HIRES, LCOGT/NRES, and FLWO/TRES data sets (Table 4.2) show close agreement in general. However, the instruments report distinct values for the stellar rotation ($v \sin i_\star$), though all indicate a slowly rotating star ($<5\,{\rm km\,s^{-1}}$). The discrepancies between the instruments may be due to differences in spectral resolution and SNR, or potentially the slow rotation of the star itself. For slowly rotating stars, the effects of rotationally induced line broadening can be of similar magnitude to other broadening mechanisms (e.g., thermal, pressure, and turbulence). Disentangling them becomes challenging, and thus $v \sin i_\star$ may be inflated if some mechanisms are not properly considered. We therefore report the spectrally derived rotation rates as rough upper limits (Table 4.2).

We note that the photometric modulations seen in the TESS and WASP light curves both suggest an equatorial rotation of $\sim 2.8\,{\rm km\,s^{-1}}$, falling in the middle of the spectral $v \sin i_\star$ values. The precise value is not central to any key findings of our study, but it does have some bearing on estimates of a potential RM signal for future endeavours. We adopt the modulation-derived value for RM calculations in Section 4.5.2 as it bypasses the line-broadening issues of a slow rotator.

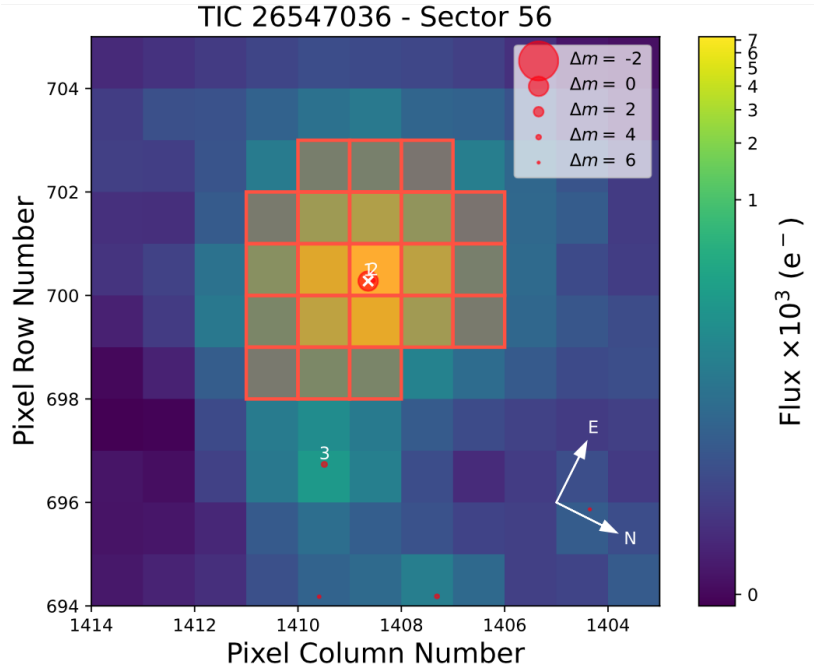

Fig. 4.6. Visual comparison of TESS photometry and nearby Gaia stars. Only one notable Gaia star contaminates the aperture (labeled "2") with a separation of 1.″9 and fainter by $\Delta m \sim 5$. The TESS PDCSAP flux values account for this very minor dilution.

Available data on the local stellar environment reveals two faint neighbours to TOI-2010. We use `tpfplotter`[6] (Aller et al., 2020) to jointly visualize the TESS aperture and Gaia positional information (Figure 4.6). The only Gaia star of note within the TESS aperture is 5 mag fainter and separated from TOI-2010 by 1.″9 at a position angle of 33° east of North (Gaia ID: 2136815881247621760). The PDCSAP flux used in our light curve analysis accounts for this minor dilution so as not to affect the radius estimate of the planet.

Though absent from the Gaia catalogue, we photometrically detect a second neighbour in the immediate vicinity of TOI-2010 using 'Alopeke high-contrast imaging. It is of similar brightness to the Gaia star (Δmag = 5 ± 0.5) and was detected at a separation of 1.″5, 138° east of North. This star does not appear in the Gaia catalogue. The flux dilution from the 'Alopeke star is small enough to cause $< 1\%$ deviation in the $R_p/R_\star$ measurement.

Spectral investigation for evidence of blended binaries also shows no indication of significant contamination. In the SOPHIE spectra, the corresponding bisectors of the cross-correlation functions do not show any significant variation nor correlation with the RV. This means there are no indications for RV variations induced by blend configurations or stellar activity. We also computed cross-correlations using masks characteristic of different spectral types: all produce similar RV variations, suggesting against the presence of a blend of stars with different spectral types. Similarly, the Keck template spectrum was run through the `ReaMatch` (Kolbl et al., 2015) software to

[6] `https://github.com/jlillo/tpfplotter`

check for blended stellar spectra. The analysis revealed no hint of any such blended components in its cross-correlation routines, and limits any unresolved sources to well below 1% of TOI-2010's flux.

With the lack of any photometric or spectroscopic evidence for significant or problematic nearby or blended stars, we conclude that the measurements of TOI-2010 are free of any significant stellar contamination. The planet radius assessment of TOI-2010 b is therefore robust.

The bulk metallicity results are shown in Figure 4.7. The bulk metal mass fraction of $Z_P = 0.11$ corresponds to 45 Earth masses of heavy elements. There appears to be a small degeneracy between age and metallicity in this analysis. This arises because leftover heat from formation in a young star (< 1 Gyr) is compensated in the model with extra metal.

In this case we used a fully mixed planet model. Using a "core+envelope" model would mean replacing compressible gas in the core with less compressible metals, requiring more metals to achieve the same radius. This model would require ~20% (or $\sim 1\sigma$) extra, according to Thorngren et al. (2016). The result is similar when using a moderate number of layers making up a semi-convective staircase "core," but when considering thousands of layers (e.g., Leconte & Chabrier, 2012) cooling slows down and even more metal is required. However, simulations suggest that small layers merge quickly as the planet evolves (Moll et al., 2017; Vazan et al., 2018), so we would not assume such an extreme case without more evidence.

The RV fit reveals a residual acceleration of $\dot{\gamma} = 0.0185 \pm 0.0055\,\mathrm{m\,s^{-1}\,day^{-1}}$. This $\sim 3\sigma$ slope detection is suggestive of some additional distant planetary or stellar companion acting on the system. In running the RV data through a generalized Lomb–Scargle periodogram (Lomb, 1976; Scargle, 1982; Zechmeister & Kürster, 2009) within the `astropy` package (Astropy Collaboration et al., 2013, 2018, 2022), the obvious 142 day signal stands out with indisputable significance. Removing the best-fit Keplerian RV model of planet b (Figure 4.3) and rerunning the periodogram on the residuals produces no peaks with false-alarm probabilities better than ~10%. These findings are shown in Figure 4.8. There appear to be no other periodic signals present in our data set for $P \lesssim 1000$ days.

We also check the TESS light curves for additional transits. Using the `astropy.stats.BoxLeastSquares` (BLS) function, we scan the available photometry for periodic transit-like signals. With two known TOI-2010 b transits in the data, the procedure flags the 1134 day separation along with accompanying aliases (including the 142 day true period). Removing the two known transits leaves a very flat light curve, and a second BLS pass detects nothing above the noise level. The BLS algorithm is sensitive only to repeated events, and so single transits (e.g., due to very long periods or transits falling in observing gaps) would not be detected here. A visual inspection of the light curve reveals no obvious transits to indicate additional bodies in the system.

To explore the possible very-long-period scenarios, we employed a 2D grid search of semi-major axis and companion mass combinations that might produce the observed RV acceleration (Bryan et al., 2016). The resulting relative probability map marks correlated boundaries on the

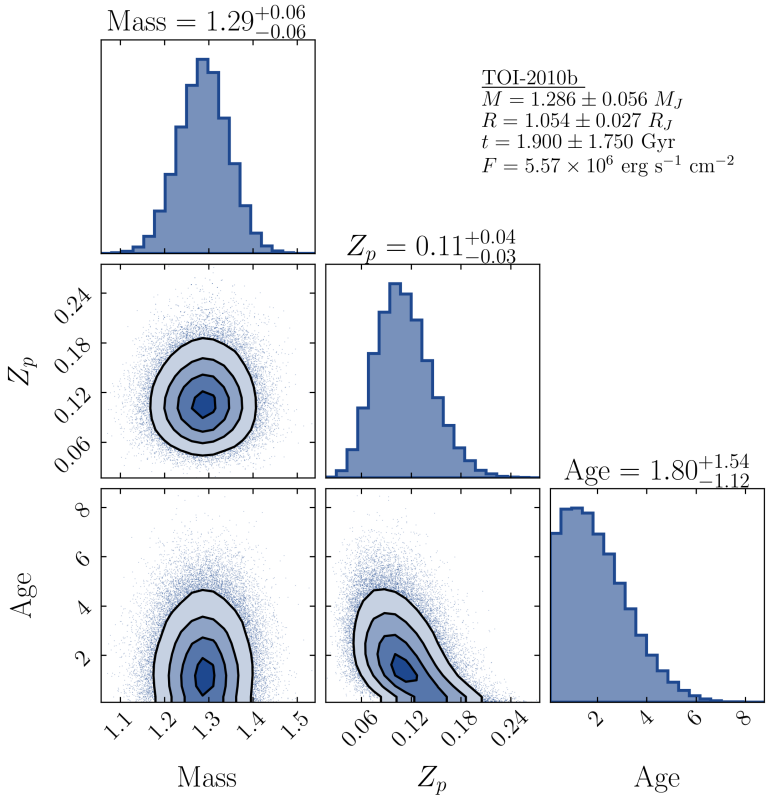

Fig. 4.7. Results of the planet's bulk metallicity analysis. Here mass is reported in Jupiter units, Z_P is the bulk metal mass fraction of the planet, and the age is given in gigayears. The small inset table shows the input priors used.

probable configurations (Figure 4.5). At the low-mass end, the system could harbour an object of 0.4 M_J orbiting at 2.6 au. Anything interior and/or less massive than that struggles to match the observed acceleration. For sources remaining below the photometric detection threshold, the most probable configuration at the high-mass end is a 475 M_J (0.46 $M_\odot$) object orbiting at ~22 au, however the allowable configuration space becomes quite broad. As we are now in the range of self-luminous low-mass main-sequence stars, the Gemini-N/'Alopeke speckle imaging would likely detect anything more massive or more separated (i.e. above the white contours).

In determining the plausibility of each close neighbour star causing the RV acceleration, we estimate some of their relevant properties. We determine the 1.″5 'Alopeke star to have a mass of $M = 0.525^{+0.045}_{-0.049}\ M_\odot$ and a semi-major axis of $a = 162.16^{+75.33}_{-41.43}$ au, while the 1.″9 Gaia star has $M = 0.5226^{+0.0001}_{-0.0001}\ M_\odot$ and $a = 205.21^{+95.33}_{-52.43}$ au. These estimates, though rough, allow us to place both stars on the Figure 4.5 grid.

If neither of these nearby stars are the cause, the most likely candidate is a yet-unseen planetary or low-mass stellar object along the high-probability region in Figure 4.5. This region through the explored parameter space roughly follows the trend of $M/[M_J] \approx 0.015\,(a/[\text{au}])^{3.2}$ where $a > 3$ au.

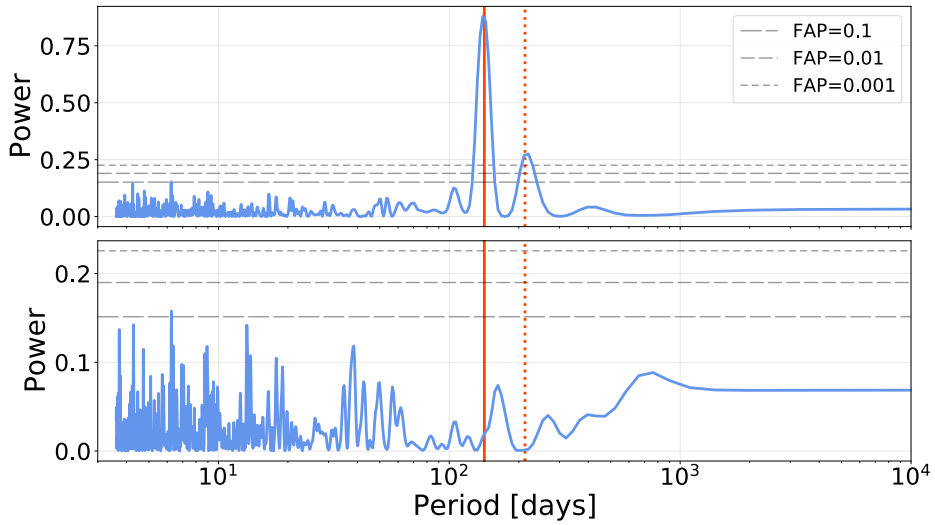

Fig. 4.8. Lomb–Scargle periodogram of RV data. False-alarm probabilities (FAPs) are shown in grey. The red solid line indicates the fitted period of TOI-2010 b, and the dotted red line is the 3/2 harmonic. The top panel periodogram shows results of the unaltered data set, whereas data used for the bottom panel has had the 141.8 day signal removed. With the removal of planet b's signal, no other significant power remains at any searchable period.

4.5. Discussion

4.5.1. TOI-2010 b in context

With physical and orbital parameters of the TOI-2010 b system properly constrained, we can place it in the context of other known exoplanets. Using planet data gathered using `ExoFile`[7] from the NASA Exoplanet Archive (2022), Figure 4.9 shows several properties for the population of confirmed giant planets ($R > 0.5\,R_J$). As can be seen in the top panel, TOI-2010 b is deep in the low-insolation wings of the population. Few other confirmed giants can boast such low stellar input, and fewer still have magnitudes bright enough to enable detailed spectroscopic follow up. TOI-2010 b stands out as valuable addition to this corner of parameter space.

The bottom panel of Figure 4.9 locates TOI-2010 b in mass and radius space. A distinction is made between strongly and weakly irradiated planets (dotted line in the top panel and marker type in the bottom panel), given that their mass–radius relationship changes. We find TOI-2010 b to be a fairly typically proportioned giant planet, akin to Jupiter though quite a bit warmer. Its moderate eccentricity may suggest a dynamic history either in its formation or due to ongoing interaction with unseen neighbours.

[7] `https://github.com/AntoineDarveau/exofile`

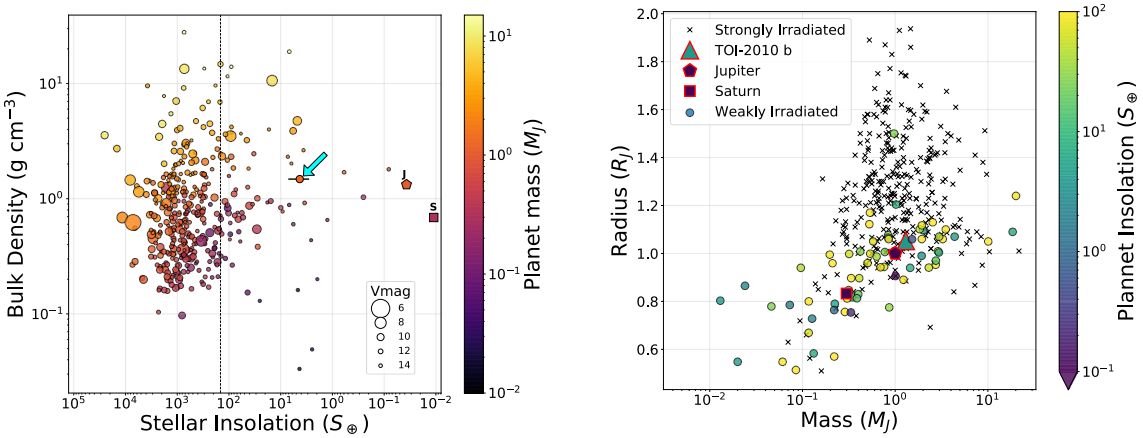

Fig. 4.9. Population of confirmed giant ($R > 0.5R_J$) transiting planets with available insolation values and better than 50% uncertainties on mass and radius. *Top:* The dotted vertical line indicates the empirical inflation boundary (Miller & Fortney, 2011; Demory & Seager, 2011) where planet radii are seen to increase with insolation. TOI-2010 b is indicated with the cyan arrow, and Jupiter and Saturn are labeled towards the right. *Bottom:* The same population of giant planets separated into strongly and weakly irradiated subgroups according to the boundary in the above plot.

4.5.2. Future observation potential

We determine the expected signal strengths for a number of potential observations that might be made on this target in the future (Figure 4.10). We calculate and report the Kempton et al. (2018) Transmission Spectroscopy Metric (TSM), though we note it was calibrated for smaller planets. The TSM nominally provides an SNR estimate for fixed-duration observations made with JWST/NIRISS. However, without the small-planet-calibrated scaling factor, the specific values of Figure 4.10a may be better interpreted by their relative strengths, rather than absolute value. We use TOI-2010 b's transit-phase equilibrium temperature (450 K) for this calculation, and in doing so we find that it has moderate transmission spectroscopy potential with TSM $\sim$ 26. As a relative measure, it lands at the $\sim$23$^{\rm rd}$ percentile for the population plotted in Figures 4.9 and 4.10.

We can also look at the Emission Spectroscopy Metric (ESM) of Kempton et al. (2018). Similarly to the TSM, the ESM estimates the SNR achieved with a mid-infrared secondary eclipse detection by JWST. We find a more promising scenario in emission than with transmission. Using the eclipse-phase equilibrium temperature (364 K), TOI-2010 b has one of the strongest predicted emission signals (ESM $\sim$ 60) among cool giants $\lesssim$ 750 K. Even against giant planets as a whole, TOI-2010 b falls near the median value. The ESM does not include an empirical calibration like the TSM, and so the values indicate the expected SNR of a JWST secondary eclipse detection with the MIRI instrument. TOI-2010 b may provide a very interesting test bed for certain atmospheric properties. The $T_{\rm eq}$ range of 360–450 K across its orbit spans a transition regime where disequilibrium chemistry may be evident. Models by Fortney et al. (2020) predict this temperature range to exhibit marked changes in CO/CH_4 and N_2/NH_3 ratios between equilibrium and disequilibrium conditions.

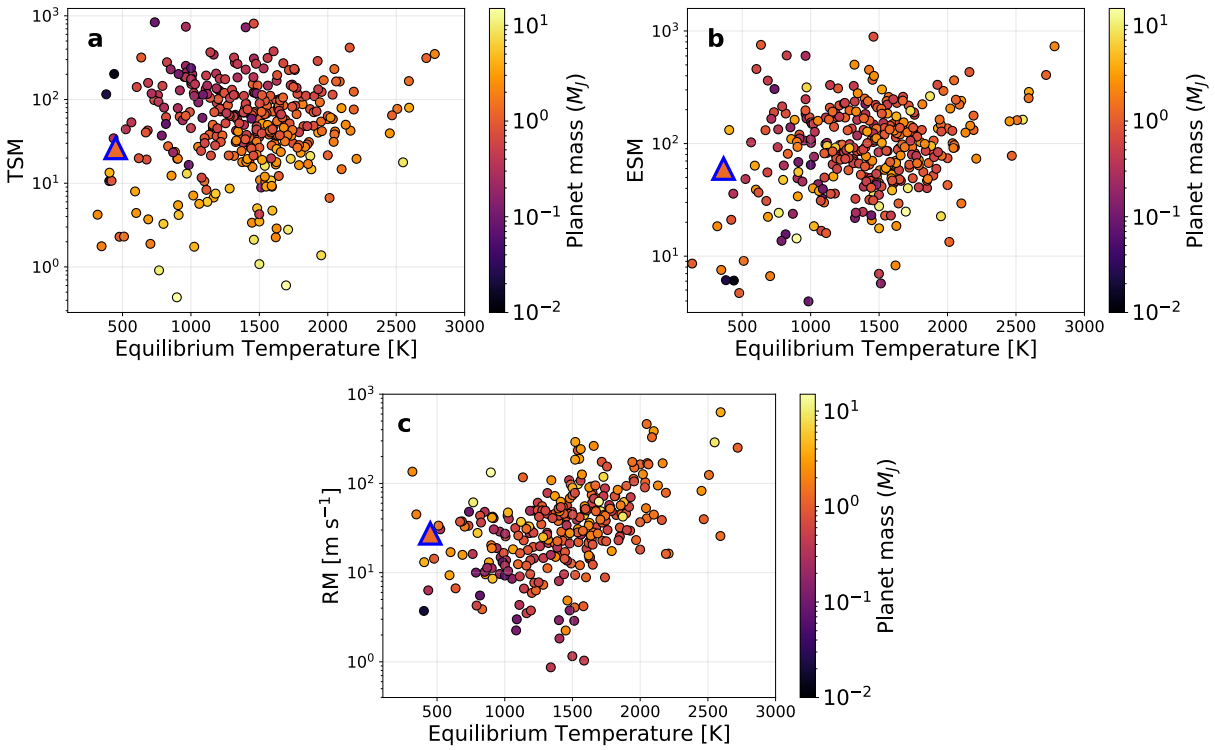

Fig. 4.10. Comparison of expected signal strengths for the same planet population shown in Figure 4.9. TOI-2010 b is indicated with the triangle marker. *Panel a:* TSM. The TSM provides an SNR estimate for a JWST/NIRISS transit observation. *Panel b:* ESM. The ESM provides an SNR estimate for a JWST/MIRI eclipse observation. *Panel c:* RM signal amplitude. The TOI-2010 b value in this plot uses $v \sin i_\star = 2.8$ km s^{-1}, derived from the TESS and WASP light curve modulations.

Such detections may go a long way toward connecting models across the Jupiter–exoplanet–brown dwarf continuum.

We also compute the potential for making an obliquity measurement using the RM effect. Winn (2010, Equation (40)) provides an approximation for calculating the ΔRV amplitude expected during transit for given planet/star size ratio, impact parameter, and projected equatorial velocity ($v \sin i_\star$) of the star. Adopting $v \sin i_\star = 2.8$ km s^{-1}, derived from the modulations observed in both the TESS and WASP light curves, we calculate an RM amplitude of 27.5 m s^{-1} (Figure 4.10(c)).

Table 4.5. Median values and 68% confidence interval for transit times, impact parameters, and depths

Transit	Planet	Epoch	T_T	b	Depth
TESS UT 2019-08-16	b	0	$2458712.30168^{+0.00042}_{-0.00041}$	$0.147^{+0.088}_{-0.097}$	0.011598 ± 0.000052
NEOSSat UT 2021-12-11	b	6	$2459563.30584^{+0.00028}_{-0.00027}$	$0.147^{+0.088}_{-0.097}$	0.01246 ± 0.00026
TESS UT 2022-09-02	b	8	2459846.97389 ± 0.00034	$0.147^{+0.088}_{-0.097}$	0.011598 ± 0.000052

4.5.3. Single-transit planets

Any transit survey mission is eventually bound to produce single-transit targets. It comes as a direct consequence of having only finite monitoring time for a particular star, and the potential for exoplanets to have very long orbits. With TESS's month-long baseline coverage for most of the sky, single-transit targets are not infrequent. Passively detected retransits in subsequent sectors can help narrow down options, but long gaps between detections leave many possible period aliases. The survey's schedule of reobserving a target is also not always compatible with the planet's orbit. For example, the second detected transit of TOI-2010 b in Sector 56 was very nearly missed. If the period had turned out even 0.6% longer (∼19 hr), the additional TESS transit would have been missed entirely.

Without substantial active follow up effort, single-transit planets often remain unviable for further study. Any phase/timing-related endeavours cannot be scheduled without a firm ephemeris, and attempting an RV study of the system requires careful vetting even before investing the sizeable observing program for the RVs themselves. Happily, the TFOP has a wide variety of researchers, infrastructure, and resources to put toward the effort. If a candidate proves suitable for RV follow up (as was the case for TOI-2010), the mass measurement and orbital refinement come packaged together. This provides a lot of value for the RV investment. That being said, RV-derived periods generally have uncertainties on the scale of hours or days for single-transit targets (which tend to have longer orbits), and the predictive timing uncertainty on future transits only grows worse as transits go undetected. This ephemeris is generally insufficiently refined to plan precisely timed observations (e.g., transits and eclipses), but it does open the door for the last step needed to constrain the system neatly.

The 3σ uncertainty window of an RV-predicted transit can easily span up to 20 days or more. Photometric instruments that are able to locate a transit within such a wide window can refine the period uncertainties to the order of minutes. The space-based vantage point provided by NEOSSat and other small space telescopes (e.g., CHEOPS; Benz et al., 2021) is ideal for this application. Such facilities can monitor this star over the whole time frame, and their detections do not even have to be of particularly high SNR. The single high-quality TESS measurement is generally sufficient to constrain the transit shape, and so a low SNR additional transit can simply supply timing information beyond the precision of the RVs. Being able to point at a target at any time also allows space-faring instruments to quickly narrow down possible period aliases if two widely spaced transits have been detected.

It is a major and ongoing challenge to carry out successful retransit searches for TESS single-transit targets. The nature of the mission's sector-by-sector and hemisphere-by-hemisphere observing strategy leaves plenty of room for longer-period planets to fall through the cracks. Small space telescopes are uniquely suited in providing support observations to pull these long-period planets back from the edge of obscurity by firmly establishing their ephemerides.

4.5.4. Cause of the RV acceleration

We inspected available kinematic Gaia data on the 1.″9 neighbouring star to determine its plausibility as a bound companion that might be causing the RV slope. This source and TOI-2010 have similar proper motions (38 and 42 milliarcseconds per year, respectively), and their trajectories differ by only 4.65°. However, their Gaia RVs differ by ∼41 km s^{-1}, significant to 5σ. This discrepancy cannot be explained by orbital motion as a circular orbital velocity at a distance of 100–200 au (see Figure 4.5) comes out as only 2–3 km s^{-1}.

Additionally, the Gaia DR3 parallax distances of TOI-2010 and this faint neighbour differ by 1.5 pc. This does place the source as a close neighbour in interstellar terms, but their respective parallax uncertainties place their distances more than 2σ discrepant. It is therefore very likely to be physically separated from TOI-2010 at the parsec scale which could not cause the observed acceleration given its low magnitude-inferred mass.

Even if we assume some bias on the parallax measure so that they are indeed at the same distance as one another, this companion does not fall in a favourable location of the Figure 4.5 plot. The source's inferred mass and orbital separation place it away from the high-probability region. The specific relative probability of its location is only ∼5% of the global peak probability, and ∼7% of the highest-probability region at its particular mass. The combination of these discussed reasons disfavour the Gaia star as the source of the acceleration.

The 1.″5 source found in the 'Alopeke image may be a slightly better candidate, though it is missing some crucial information. With a similar inferred mass but tighter separation, this source is closer to the high-likelihood region of the Figure 4.5 plot. Its particular cell is ∼12% of the peak probability for this mass. The uncertainty on its semi-major axis allows for it to intersect a bit deeper into the high-probability region. However, with an unknown parallax or proper motion, it is entirely possible that this is a background or foreground object and wholly unassociated with the system.

Based on their low-probability locations in the search grid, coupled with a parsec-scale difference in distance between the Gaia neighbour and TOI-2010 and lack of parallax information on the 'Alopeke neighbour, it appears unlikely that either star is responsible for the RV acceleration.

The presence of these two sources certainly does not rule out the additional possibility of a hidden lower-mass object. The 'Alopeke source may be approaching the right region of parameter space, but the unknown nature of its 3D position and kinematics relative to TOI-2010 precludes any certainty for now. Further characterization of the nearby sources may offer more clarity, such as refinement of the Gaia star's parallax, or a check on the 'Alopeke star's proper motion in a few years time. Additional RV coverage of TOI-2010 may even reveal some clear curvature to the residual acceleration, which would add strong constraints on the high-mass/wide-orbit end of the currently allowed parameter space.

4.6. Summary

In the course of this study, we have confirmed the planetary nature of the exoplanet TOI-2010 b. A wide range of data sets from the TESS mission and the TFOP working group were collected in this effort. Most notably, the initial single transit discovered in the TESS Sector 15 data provided strong transit morphology constraints, but no information on the period. A substantial RV campaign involving several observatories mapped the RV curve, determined a rough period, and predicted a subsequent transit to an uncertainty of a few days. Using NEOSSat, we observed a continuous week-long window and caught this transit, refining the period down to just a few minutes uncertainty. A fortuitous catch in TESS's Sector 56 light curve revealed an additional transit detection at a late stage of this manuscript's preparation.

We carried out a global model fit using `EXOFASTv2` to determine the system's physical and orbital parameters by simultaneously fitting time-series light curves, RVs, and historical photometric data. TOI-2010 b turns out to be Jupiter-like in size, about 30% more massive, and its equilibrium temperature may fluctuate between roughly 360–450 K given its moderately eccentric orbit.

Our bulk metallicity analysis also suggests a fairly Jupiter-like metal mass fraction, i.e. modestly lower than the general trend given its mass (Thorngren et al., 2016). The host star is very slightly super-solar in terms of mass, radius, luminosity, and temperature.

We find evidence of a small-amplitude residual acceleration in the RV data set once TOI-2010 b's signal has been removed, potentially indicative of an outer companion in the system. Searching a broad grid of potential mass and semi-major axis values, we determine the relative probability that such companions could cause the observed acceleration. We also determine which of these simulated systems would be visible in our high-contrast imaging. Among hidden objects (too faint and/or close to TOI-2010 to be detected), we find a correlated allowed parameter space ranging 0.4–475 $M_{\rm J}$ in mass (475 $M_{\rm J} \approx 0.45 M_{\odot}$) and 2.6–23 au in semi-major axis along its highest-probability region. Smaller masses and orbits cannot reproduce the observed RV slope, while more massive (i.e. brighter) objects on wider orbits would be observable in our Gemini-N/'Alopeke speckle imaging.

We make note of two nearby sources that could potentially be connected to the acceleration. A Gaia source, 1.″9 away, is at a similar distance to the TOI-2010 system, but perhaps not close enough to be considered a binary capable of producing the RV slope. Also, its inferred mass and semi-major axis do not fall in a likely region of the parameter space. A second source, discovered in our high-contrast imaging 1.″5 away, has an inferred mass and semi-major axis that are slightly more likely to produce the acceleration. However, with no parallax information, this source could easily be just a projected neighbour.

In refining TOI-2010 b's period, we have enabled future transit/eclipse-based research. In large part due to its cool temperature, the transmission spectroscopy potential of this target is somewhat

poor. However, its predicted signal strength is much better for emission spectroscopy and RM measurements.

TOI-2010 b turns out to be very typical member of the population of known Jovian exoplanets. However, the planet's unique value and interest stem from its observability and low insolation/effective temperature. Currently, amongst giant planets with reliable radius and mass measurements, only ~20 are at comparable or lower stellar insolation levels. Among those, only two are bright targets.

TOI-2010 b is a successful case of searching for and catching additional transits for a single-transit candidate planet. This process is often expensive and challenging, but it allows us to build up the confirmed exoplanet catalogue where it is only sparsely populated.

Acknowledgements

C.R.M. and D.L. acknowledge funding from the Trottier Family Foundation in their support of Trottier Institute for Research on Exoplanets (iREx). They also acknowledge individual funding from the Natural Sciences and Engineering Research Council (NSERC) of Canada. P.A.D. acknowledges support by a 51 Pegasi b Postdoctoral Fellowship from the Heising-Simons Foundation and by a National Science Foundation (NSF) Astronomy and Astrophysics Postdoctoral Fellowship under award AST-1903811.

S.D. is funded by the UK Science and Technology Facilities Council (grant No. ST/V004735/1).

X.D. and T.Fo. acknowledge funding from the French National Research Agency in the framework of the Investissements d Avenir program (ANR-15-IDEX-02), through the funding of the "Origin of Life" project of the Grenoble-Alpes University.

E.M. acknowledges funding from FAPEMIG under project number APQ-02493-22 and research productivity grant No. 309829/2022-4 awarded by the CNPq, Brazil.

D.D. acknowledges support from the NASA Exoplanet Research Program grant 18-2XRP18_2-0136, and from the TESS Guest Investigator Program grants 80NSSC22K1353 and 80NSSC22K0185.

T.Fe. acknowledges support from the University of California President's Postdoctoral Fellowship Program.

K.A.C. and D.W.L. acknowledge support from the TESS mission via subaward s3449 from MIT.

The authors would like to thank the on-duty telescope observers Patrick Newman, Owen Alfaro, Ben Chang, and William McLaughlin for their contribution in gathering the George Mason University Observatory data.

This paper made use of data collected by the TESS mission and are publicly available from the Mikulski Archive for Space Telescopes (MAST) operated by the Space Telescope Science Institute (STScI). Funding for the TESS mission is provided by NASA's Science Mission Directorate.

We acknowledge the use of public TESS data from pipelines at the TESS Science Office and at the TESS Science Processing Operations Center.

Resources supporting this work were provided by the NASA High-End Computing (HEC) Program through the NASA Advanced Supercomputing (NAS) Division at Ames Research Center for the production of the SPOC data products.

We would like to thank the PIs of the TESS Guest Investigator programs that put TOI-2010 on the 2 minute (Steven Villanueva – G04195, Diana Dragomir – G04231, Andrej Prsa – G04171, Andrew Mayo – G04242, and James Davenport – G04039) and 20 s (Guadalupe Tovar Mendoza – G05121, and Daniel Huber – G05144) cadence lists.

This research has made use of the Exoplanet follow up Observation Program (ExoFOP; doi: 10.26134/ExoFOP5) website, which is operated by the California Institute of Technology, under contract with the National Aeronautics and Space Administration under the Exoplanet Exploration Program.

We would like to thank and acknowledge the efforts of the TESS Single Transit Planet Candidate working group for working to keep tabs on and improving our understanding of long-period targets.

This work makes use of observations from the LCOGT network. Part of the LCOGT telescope time was granted by NOIRLab through the Mid-Scale Innovations Program (MSIP). MSIP is funded by the NSF.

Observations in the paper (Program ID: GN-2021A-LP-105) made use of the high-Resolution imaging instrument ‘Alopeke. ‘Alopeke was funded by the NASA Exoplanet Exploration Program and built at the NASA Ames Research Center by Steve B. Howell, Nic Scott, Elliott P. Horch, and Emmett Quigley. ‘Alopeke was mounted on the Gemini-North telescope of the international Gemini Observatory, a program of NSF’s NOIRLab, which is managed by the Association of Universities for Research in Astronomy (AURA) under a cooperative agreement with the National Science Foundation on behalf of the Gemini Observatory partnership: the National Science Foundation (United States), National Research Council (Canada), Agencia Nacional de Investigación y Desarrollo (Chile), Ministerio de Ciencia, Tecnología e Innovación (Argentina), Ministério da Ciência, Tecnologia, Inovações e Comunicações (Brazil), and Korea Astronomy and Space Science Institute (Republic of Korea).

This work is based on observations collected with the SOPHIE spectrograph on the 1.93 m telescope at the Observatoire de Haute-Provence (CNRS), France. We thank the staff of the Observatoire de Haute-Provence for their support at the 1.93 m telescope and on SOPHIE. We also thankfully acknowledge grants from CNES and the CNRS “Programme National de Planétologie."

This research has made use of the NASA Exoplanet Archive, which is operated by the California Institute of Technology, under contract with the National Aeronautics and Space Administration under the Exoplanet Exploration Program.

This work has made use of data from the European Space Agency Gaia (`https://www.cosmos.esa.int/gaia`), processed Data Processing and Analysis Consortium (DPAC; `https:`

//www.cosmos.esa.int/web/gaia/dpac/consortium). Funding for the DPAC has been provided by national institutions, in particular the institutions participating in the Gaia Multilateral Agreement.

Software

lightkurve (Lightkurve Collaboration et al., 2018), EXOFASTv2 (Eastman et al., 2019), ReaMatch (Kolbl et al., 2015), astropy (Astropy Collaboration et al., 2013, 2018, 2022), matplotlib (Hunter, 2007b), Numpy (van der Walt et al., 2011; Harris et al., 2020b) tpfplotter[8], ExoFile[9], KeplerSpline (Vanderburg et al., 2016), TESS-SIP (Hedges et al., 2020), SpeckMatch (Petigura, 2015; Petigura et al., 2017; Yee et al., 2017), AstroImageJ (Collins et al., 2017c), alnitak[10], AUSTRAL (Endl et al., 2000), BANZAI-NRES (McCully et al., 2022), PyAstronomy[11] (Czesla et al., 2019b).

Appendix

The RV data used in the global fit are displayed in Table 4.6. The data span three instruments and include their individual RV offsets.

Table 4.6. RV Measurements of TOI-2010

BJD_{TDB}	RV (m s^{-1})	σ_{RV} (m s^{-1})	Inst.
2458887.037868	−65.7	8.1	Levy
2458895.027687	−71.6	6.5	Levy
2458899.012701	−35.9	5.6	Levy
2458922.023014	−8.4	6.4	Levy
2458955.028682	39.1	4.4	Levy
2458961.908021	41.6	6.6	Levy
2458964.893612	48.0	5.0	Levy
2458966.898471	31.0	9.0	Levy
2458970.887634	38.8	6.5	Levy
2458973.892349	47.6	5.1	Levy
2458991.906717	10.7	8.9	Levy
2459030.819021	−42.9	5.4	Levy
2459040.997378	−22.5	4.5	Levy
2459064.767218	−6.9	4.7	Levy
2459068.806213	−0.4	4.4	Levy

[8]https://github.com/jlillo/tpfplotter
[9]https://github.com/AntoineDarveau/exofile
[10]https://github.com/oalfaro2/alnitak
[11]https://github.com/sczesla/PyAstronomy

Table 4.6 continued from previous page

BJD_{TDB}	RV (m s^{-1})	σ_{RV} (m s^{-1})	Inst.
2459182.597717	−38.5	5.6	Levy
2459185.604636	−26.5	5.0	Levy
2459188.603420	−34.3	4.6	Levy
2459194.590484	−25.0	6.9	Levy
2459203.597023	−12.1	5.9	Levy
2459222.590712	0.7	5.9	Levy
2459225.067097	46.2	8.8	Levy
2459228.601064	30.8	7.6	Levy
2459235.060004	25.8	6.1	Levy
2459262.996513	45.1	9.2	Levy
2459274.930264	22.9	6.7	Levy
2459287.907247	−33.7	6.3	Levy
2459295.883380	−40.4	6.7	Levy
2459301.842307	−47.0	6.3	Levy
2459307.004259	−55.4	4.3	Levy
2459315.878742	−28.7	4.7	Levy
2459319.949170	−36.2	4.0	Levy
2459322.978069	−34.2	4.4	Levy
2459326.986152	−33.7	5.4	Levy
2459333.953995	−27.9	4.7	Levy
2459336.970295	−14.1	5.7	Levy
2459339.999687	−20.1	4.5	Levy
2459344.872338	9.5	5.1	Levy
2459347.947959	0.7	4.3	Levy
2459351.983896	−3.0	5.6	Levy
2459356.940402	19.2	4.8	Levy
2459361.893688	22.2	4.4	Levy
2459364.922348	23.0	4.9	Levy
2459368.925800	9.8	5.0	Levy
2459372.940835	46.4	7.7	Levy
2459381.765521	26.3	5.5	Levy
2459385.822790	45.6	4.4	Levy
2459388.885495	46.5	6.5	Levy
2459392.788945	35.9	5.0	Levy
2459395.795554	51.9	4.3	Levy

Table 4.6 continued from previous page

BJD_{TDB}	RV (m s^{-1})	σ_{RV} (m s^{-1})	Inst.
2459398.811073	60.4	4.5	Levy
2459401.841438	37.1	4.6	Levy
2459404.841232	40.2	4.8	Levy
2459407.851764	23.1	4.1	Levy
2459409.840484	26.1	4.3	Levy
2459410.773285	24.0	4.4	Levy
2459412.737338	28.5	4.4	Levy
2459415.750915	16.4	4.8	Levy
2459419.751557	−11.5	4.6	Levy
2459424.700659	−8.0	5.0	Levy
2459427.744671	−19.6	4.7	Levy
2459434.772695	−23.3	4.4	Levy
2459438.778047	−59.5	4.6	Levy
2459452.747840	−47.4	4.5	Levy
2459464.768780	−32.5	5.1	Levy
2459464.768780	−32.5	5.1	Levy
2459489.826089	−9.1	4.8	Levy
2459522.781338	44.9	6.1	Levy
2459586.597180	−35.6	5.6	Levy
2459607.020932	−38.8	6.4	Levy
2459039.471600	−15360.0	3.0	SOPHIE
2459113.414800	−15277.0	3.0	SOPHIE
2459133.408700	−15305.0	6.0	SOPHIE
2459394.536800	−15278.0	4.0	SOPHIE
2459419.545000	−15304.0	5.0	SOPHIE
2459445.490100	−15378.0	3.0	SOPHIE
2459469.491100	−15340.0	3.0	SOPHIE
2459477.404500	−15323.0	7.0	SOPHIE
2459483.448000	−15324.0	5.0	SOPHIE
2459501.357500	−15312.0	3.0	SOPHIE
2459548.222100	−15276.0	5.0	SOPHIE
2459553.237600	−15298.0	4.0	SOPHIE
2459559.223100	−15299.0	3.0	SOPHIE
2459567.230500	−15330.0	3.0	SOPHIE
2459571.238700	−15348.0	3.0	SOPHIE

Table 4.6 continued from previous page

BJD_{TDB}	RV (m s^{-1})	σ_{RV} (m s^{-1})	Inst.
2459631.705700	−15312.0	3.0	SOPHIE
2459662.675900	−15259.0	4.0	SOPHIE
2459731.582800	−15359.0	3.0	SOPHIE
2459750.512000	−15352.0	3.0	SOPHIE
2459773.575100	−15290.0	3.0	SOPHIE
2459786.614400	−15290.0	4.0	SOPHIE
2459805.542600	−15267.0	9.0	SOPHIE
2459811.333900	−15241.0	4.0	SOPHIE
2459828.379100	−15264.0	3.0	SOPHIE
2459191.579631	8750.7	12.1	Tull
2459192.588106	8747.0	10.8	Tull
2459275.950854	8817.7	13.3	Tull
2459276.970138	8798.1	10.6	Tull
2459277.969833	8777.6	10.0	Tull
2459293.930022	8740.0	10.4	Tull
2459294.957330	8737.9	11.5	Tull
2459301.941670	8729.9	13.7	Tull
2459339.884675	8763.0	11.0	Tull
2459340.824938	8757.6	10.4	Tull
2459355.874441	8794.3	11.6	Tull
2459383.844963	8823.0	11.2	Tull
2459384.820734	8811.8	10.0	Tull
2459411.737865	8795.2	9.6	Tull
2459413.773637	8798.0	9.0	Tull
2459878.627818	8753.2	11.6	Tull

4.7. Specific Contributions

As was briefly discussed at the end of Chapter 1, the TOI-2010.01 project began with my collaborator Paul Dalba searching for an additional transit of the single-transit target. Responding to my open offer within the TSTPC group to aid ongoing projects with NEOSSat, Paul approached me to try and catch an upcoming transit. With Paul's input, I put together a dedicated proposal for a 7-day search for this transit. It merited an individualized proposal as it represented a significant time investment and this type of observation had not been carried out with NEOSSat previously. The proposal was accepted with high priority ranking, and I orchestrated the subsequent observation with the NEOSSat staff. I carried out the data reduction and photometry extraction using software developed by Jason Rowe, but including a few of my own small modifications. I normalized and detrended the light curve using a PCA code developed by Geert Jan Talens. With a calibrated light curve in hand, the transit was immediately apparent several hours ($<1\sigma$) from the predicted time.

Based on our successful NEOSSat detection, I was offered lead position on the planet's confirmation paper. Most of the duties and responsibilities mirrored those I described for the TOI-1221.01 paper (Chapter 3), with one main addition. In this particular case I liaised with another RV research team who had also been collecting data on the target. Given our recent transit detection, we collectively decided it was best that they join our publication. Beyond that, I carried out the organizational tasks of cataloguing, gathering, and inviting collaborators and data contributors to the project. We ended up with an author list of 51 people.

Various data sets and interpretive insights were provided by different collaborators. The investigation of out-of-transit TESS light curve modulation was conducted by Tara Fetherolf. A similar endeavour looking into the stellar modulation via WASP data was done by Coel Hellier. Andrew Howard was responsible for the Keck/HIRES spectrum. Marcus Rabus handled the LCOGT/NRES spectra and analysis, while Allyson Bieryla and David Latham provided the same for FLWO/TRES. The Gemini-North/'Alopeke speckle image was obtained and processed by Steve Howell. RV measurements came from three sources: Paul Dalba and Benjamin Fulton provided the APF data, Michael Endel and team provided the McDonald Observatory data, and Guillaume Hébrard and team provided the SOPHIE measurements. The bulk metallicity analysis was carried out by Daniel Thorngren. Some photometric follow-up was provided by Peter Plavchan and team from GMU. Finally, the NEOSSat observation, as described above, was my own contribution.

With data collected, Paul Dalba conducted the `EXOFASTv2` transit + RV + MIST/SED joint fitting. It was then my task to combine all the individual findings into a single cohesive picture of the TOI-2010 system. I summarized the various contributions, addressing each in the paper in a logical progression. I also provided descriptions of the procedures we collectively undertook in the data analysis, and reported on the outcomes and their implications. The sections containing the after-the-fact search for additional planets hidden in the system (i.e., periodogram, RV residual acceleration, nearby star analysis) was my own work. I also conducted the comparative work that

quantified the target's future observability with various methods, and placed it in context amongst other known exoplanets.

With all of the tasks and steps listed above accomplished, it was my responsibility to write the actual paper. I carried out internal revisions within our extended author list, then submitted it for publication. The submission was met with minor referee suggestions that I addressed, and was published in the Astronomical Journal in December, 2023.

Chapter 5

Conclusion

The field of exoplanet research has recently exploded. This is clearly evident by the discovery of over 4000 new exoplanets in the last 10 years, and only 1000 in the preceding two decades. And this is only counting the confirmed exoplanets, not the many thousands of pending candidates. We now know that planets outnumber stars in our Galaxy, and that many planets, including the most plentiful size class, have no direct analogue in our solar system. Abundance and variety are the names of the exoplanet game. This progress rides on the heels of ambitious and dedicated exoplanet discovery missions, the most efficient of which search via the transit method. In looking for exoplanet transits, we can simultaneously monitor thousands of stars for the tell-tale signal, and provide detailed measurements of the planet's orbit and radius when they are found. Once implemented, transit detections rapidly overtook RV measurements as the primary discovery method for exoplanets. With the planetary mass provided by RVs combined with the radius from a transit, the density of exoplanets now became accessible, shedding light on composition and atmospheric structures.

Even with a detailed map of the distribution of exoplanet properties, this map has edges. Biases intrinsic to the transit method and imposed by programmatic and technical decisions of each survey mission set limits on the populations that can be effectively explored. The most prominent bias facing transit surveys is against wider-orbiting systems. Lower transit probabilities and the long observational timescales involve mean that many of these planets get missed, are stuck as single-transit detections, or generate repeated observations too slowly to keep pace with their easier to study short-period counterparts. There are no quick solutions to overcoming these challenges. It generally takes dedicated case-by-case effort to verify the few long-period candidates available, often requiring substantial additional time and observational investment.

This thesis project addressed these challenges on a number of fronts. To contribute to the general TESS exoplanet candidate follow-up effort (a distributed, yet monumental task given the thousands of candidates), we brought "new" instruments to join the effort that were previously engaged in unrelated science. Dragonfly can now observe exoplanet transits in a largely autonomous fashion,

and is able to achieve photometric precision competitive with other major ground-based 1–2 m class observatories. Beyond providing basic transit shape measurements, Dragonfly is useful in refining orbital ephemerides, checking false positive scenarios, and tracking timing variations. With NEOSSat we developed an extended program to follow-up exoplanets with challenging observing parameters (i.e., long duration transits and/or long periods). The space-based vantage point provides huge advantages over ground-based observatories for these targets. Using these instruments and others, we have contributed observations and analysis to further the collective exoplanet follow-up effort. Certain of our endeavours have focused on targets in more challenging parameter space. For example: TOI-1221 b with its low SNR transits and a 92-day period, TOI-2010 b with only a single-transit TESS detection and 142-day period, as well as others still in progress but not included as part of this thesis.

As a result of our efforts with Dragonfly and NEOSSat, and our engagement with the TFOP, we accomplished a number of contributions to the exoplanet community. Our submissions of Dragonfly and NEOSSat data to the TFOP have resulted in several unpublished confirmations/rejections of false-positives and period aliases. These data help facilitate future observations and improve the veracity of the TFOP database. With NEOSSat, we found niche use-cases where we could provide an observational service that was lacking within the TSTPC. As described in Chapters 3 and 4, we verified two high-quality and uniquely situated targets for future atmospheric characterization. TOI-1221 b and TOI-2010 b both have moderate equilibrium temperatures due to their relatively wide orbits. They provide rare test-beds for measuring cool atmospheres, disentangled from stellar irradiation, and bridging the gap between well-studied hot Jupiters and our own cold solar system giants. NEOSSat's and Dragonfly's observational contributions are both projects that need not cease with the completion of this thesis. Efforts led by myself or others can continue, improve upon, and expand their scope into the future. This presented thesis illustrates how quality exoplanet observations can come from unlikely instruments, and how making concerted efforts on verifying long-period exoplanet candidates can push the boundaries of the types of planets we study.

References

Abbasi, V., Thorsteinson, S., Balam, D., et al. 2019, in 1st NEO and Debris Detection Conference, Vol. 22

Abraham, R., Merritt, A., Zhang, J., et al. 2017, in IAU Symposium, Vol. 321, Formation and Evolution of Galaxy Outskirts, ed. A. Gil de Paz, J. H. Knapen, & J. C. Lee, 137–146

Abraham, R. G., & van Dokkum, P. G. 2014, PASP, 126, 55

Agol, E., Luger, R., & Foreman-Mackey, D. 2019, rodluger/Limbdark.jl: Version published in AJ, Zenodo

Agol, E., Steffen, J., Sari, R., & Clarkson, W. 2005, Monthly Notices of the Royal Astronomical Society, 359, 567

Allard, F., Homeier, D., & Freytag, B. 2012, Philosophical Transactions of the Royal Society of London Series A, 370, 2765

Aller, A., Lillo-Box, J., Jones, D., Miranda, L. F., & Barceló Forteza, S. 2020, A&A, 635, A128

Anderson, D. R., Hellier, C., Gillon, M., et al. 2010, Astrophysical Journal, 709, 159

Armstrong, D., Martin, D. V., Brown, G., et al. 2013, Monthly Notices of the Royal Astronomical Society, 434, 3047

Astropy Collaboration, Robitaille, T. P., Tollerud, E. J., et al. 2013, A&A, 558, A33

Astropy Collaboration, Price-Whelan, A. M., Sipőcz, B. M., et al. 2018, AJ, 156, 123

Astropy Collaboration, Price-Whelan, A. M., Lim, P. L., et al. 2022, apj, 935, 167

Babusiaux, C., Fabricius, C., Khanna, S., et al. 2022, arXiv e-prints, arXiv:2206.05989

Baraffe, I., Chabrier, G., Barman, T. S., Allard, F., & Hauschildt, P. H. 2003, A&A, 402, 701

Baraffe, I., Homeier, D., Allard, F., & Chabrier, G. 2015, A&A, 577, A42

Barnes, J. W. 2007, The Publications of the Astronomical Society of the Pacific, 119, 986

Barnes, R., Raymond, S. N., Greenberg, R., Jackson, B., & Kaib, N. A. 2010, Astrophysical Journal, 709, L95

Baruteau, C., Crida, A., Paardekooper, S. J., et al. 2014, in Protostars and Planets VI, ed. H. Beuther, R. S. Klessen, C. P. Dullemond, & T. Henning, 667–689

Batalha, N. M., Borucki, W. J., Bryson, S. T., et al. 2011, ApJ, 729, 27

Beatty, T. G., & Gaudi, B. S. 2008, ApJ, 686, 1302

Benz, W., Broeg, C., Fortier, A., et al. 2021, Experimental Astronomy, 51, 109

Berta-Thompson, Z. K., Irwin, J., Charbonneau, D., et al. 2015, Nature, 527, 204
Bianchi, L., Herald, J., Efremova, B., et al. 2011, Ap&SS, 335, 161
Bolmont, E., Selsis, F., Owen, J. E., et al. 2017, MNRAS, 464, 3728
Bouchy, F., Díaz, R. F., Hébrard, G., et al. 2013, A&A, 549, A49
Bouchy, F., Hébrard, G., Udry, S., et al. 2009, A&A, 505, 853
Bouchy, F., Deleuil, M., Guillot, T., et al. 2011, Astronomy and Astrophysics, 525, A68
Bradley, L., Sipőcz, B., Robitaille, T., et al. 2022, astropy/photutils: 1.5.0
Brandeker, A., Jayawardhana, R., Khavari, P., Haisch, Karl E., J., & Mardones, D. 2006, ApJ, 652, 1572
Brown, T. M., Baliber, N., Bianco, F. B., et al. 2013, PASP, 125, 1031
Bryan, M. L., Knutson, H. A., Howard, A. W., et al. 2016, ApJ, 821, 89
Buccino, A. P., Lemarchand, G. A., & Mauas, P. J. D. 2007, Icarus, 192, 582
Buchhave, L. A., Bakos, G. Á., Hartman, J. D., et al. 2010, ApJ, 720, 1118
Buchhave, L. A., Latham, D. W., Johansen, A., et al. 2012, Nature, 486, 375
Buchhave, L. A., Bizzarro, M., Latham, D. W., et al. 2014, Nature, 509, 593
Budding, E. 1973, Astrophysics and Space Science, 22, 87
Burt, J., Holden, B., Hanson, R., et al. 2015, Journal of Astronomical Telescopes, Instruments, and Systems, 1, 044003
Butler, R. P., Marcy, G. W., Williams, E., et al. 1996, PASP, 108, 500
Campbell, B., Walker, G. A. H., & Yang, S. 1988, Astrophysical Journal, 331, 902
Chabrier, G., Baraffe, I., Allard, F., & Hauschildt, P. 2000, ApJ, 542, 464
Chabrier, G., Baraffe, I., Leconte, J., Gallardo, J., & Barman, T. 2009, in American Institute of Physics Conference Series, Vol. 1094, 15th Cambridge Workshop on Cool Stars, Stellar Systems, and the Sun, ed. E. Stempels, 102–111
Chabrier, G., Mazevet, S., & Soubiran, F. 2019, ApJ, 872, 51
Charbonneau, D., Brown, T. M., Latham, D. W., & Mayor, M. 2000, Astrophysical Journal Letters, 529, L45
Chen, J., & Kipping, D. 2017, ApJ, 834, 17
Chen, S., Lokhorst, D. M., Shen, J., et al. 2022, in Society of Photo-Optical Instrumentation Engineers (SPIE) Conference Series, Vol. 12182, Ground-based and Airborne Telescopes IX, ed. H. K. Marshall, J. Spyromilio, & T. Usuda, 121824E
Choi, J., Dotter, A., Conroy, C., et al. 2016, ApJ, 823, 102
Claret, A. 2017, A&A, 600, A30
Claret, A., & Bloemen, S. 2011, A&A, 529, A75
Cloutier, R., & Menou, K. 2020, AJ, 159, 211
Cochran, W. D., Hatzes, A. P., & Hancock, T. J. 1991, Astrophysical Journal Letters, 380, L35
Cohen, Y., van Dokkum, P., Danieli, S., et al. 2018, Astrophysical Journal, 868, 96
Collins, K. A., Kielkopf, J. F., Stassun, K. G., & Hessman, F. V. 2017a, AJ, 153, 77

—. 2017b, AJ, 153, 77
—. 2017c, AJ, 153, 77
Constantinou, S., Madhusudhan, N., & Gandhi, S. 2023, ApJ, 943, L10
Cooke, B. F., Pollacco, D., Anderson, D. R., et al. 2021, MNRAS, 500, 5088
Csizmadia, S., Hatzes, A., Gandolfi, D., et al. 2015, Astronomy and Astrophysics, 584, A13
Cutri, R. M., Skrutskie, M. F., van Dyk, S., et al. 2003, VizieR Online Data Catalog, II/246
Cutri, R. M., Wright, E. L., Conrow, T., et al. 2021, VizieR Online Data Catalog, II/328
Czesla, S., Schröter, S., Schneider, C. P., et al. 2019a, PyA: Python astronomy-related packages
—. 2019b, PyA: Python astronomy-related packages
Dalba, P. A., Kane, S. R., Li, Z., et al. 2021, AJ, 162, 154
Dalba, P. A., Kane, S. R., Dragomir, D., et al. 2022, AJ, 163, 61
Dang, L., Cowan, N. B., Schwartz, J. C., et al. 2018, Nature Astronomy, 2, 220
Danieli, S., & van Dokkum, P. 2019, Astrophysical Journal, 875, 155
Danieli, S., van Dokkum, P., Merritt, A., et al. 2017, Astrophysical Journal, 837, 136
Danieli, S., Lokhorst, D., Zhang, J., et al. 2020, ApJ, 894, 119
Dawson, R. I., & Johnson, J. A. 2018, Annual Review of Astronomy and Astrophysics, 56, 175
Deck, K. M., & Agol, E. 2015, The Astrophysical Journal, 802, 116
Deck, K. M., & Agol, E. 2015, ApJ, 802, 116
Deck, K. M., Agol, E., Holman, M. J., & Nesvorný, D. 2014, ApJ, 787, 132
Deeg, H. J., & Belmonte, J. A. 2018, Handbook of Exoplanets
Delrez, L., Murray, C. A., Pozuelos, F. J., et al. 2022, A&A, 667, A59
Demory, B.-O., & Seager, S. 2011, ApJS, 197, 12
Dittmann, J. A., Irwin, J. M., Charbonneau, D., et al. 2017, Nature, 544, 333
Donati, J.-F., Semel, M., Carter, B. D., Rees, D. E., & Collier Cameron, A. 1997, MNRAS, 291, 658
Dong, C., Jin, M., Lingam, M., et al. 2018, Proceedings of the National Academy of Science, 115, 260
Dong, C., Lingam, M., Ma, Y., & Cohen, O. 2017, ApJ, 837, L26
Dotter, A. 2016, ApJS, 222, 8
Eastman, J. D., Rodriguez, J. E., Agol, E., et al. 2019, arXiv e-prints, arXiv:1907.09480
Endl, M., Kürster, M., & Els, S. 2000, A&A, 362, 585
Espinoza, N., & Jordán, A. 2015, MNRAS, 450, 1879
—. 2016, MNRAS, 457, 3573
Espinoza, N., Kossakowski, D., & Brahm, R. 2019a, MNRAS, 490, 2262
—. 2019b, MNRAS, 490, 2262
Fetherolf, T., Pepper, J., Simpson, E., et al. 2023, ApJS, 268, 4
Fűrész, G. 2008, PhD thesis, University of Szeged, Hungary
Findeisen, K., Hillenbrand, L., & Soderblom, D. 2011, AJ, 142, 23

Foreman-Mackey, D., Agol, E., Ambikasaran, S., & Angus, R. 2017, AJ, 154, 220
Foreman-Mackey, D., Hogg, D. W., & Morton, T. D. 2014, ApJ, 795, 64
Fortney, J. J., Marley, M. S., & Barnes, J. W. 2007, ApJ, 659, 1661
Fortney, J. J., Marley, M. S., Saumon, D., & Lodders, K. 2008, ApJ, 683, 1104
Fortney, J. J., Visscher, C., Marley, M. S., et al. 2020, AJ, 160, 288
Fox, C., & Wiegert, P. 2022, MNRAS, 516, 4684
Fraine, J., Deming, D., Benneke, B., et al. 2014, Nature, 513, 526
Fulton, B. J., & Petigura, E. A. 2018, AJ, 156, 264
Fulton, B. J., Weiss, L. M., Sinukoff, E., et al. 2015, ApJ, 805, 175
Fulton, B. J., Petigura, E. A., Howard, A. W., et al. 2017, AJ, 154, 109
Gaia Collaboration. 2020, VizieR Online Data Catalog, I/350
Gaia Collaboration, Prusti, T., de Bruijne, J. H. J., et al. 2016, A&A, 595, A1
Gaia Collaboration, Brown, A. G. A., Vallenari, A., et al. 2018, A&A, 616, A1
Gao, P., Wakeford, H. R., Moran, S. E., & Parmentier, V. 2021, Journal of Geophysical Research (Planets), 126, e06655
Gaudi, B. S., & Winn, J. N. 2007, Astrophysical Journal, 655, 550
Gaudi, B. S., Stassun, K. G., Collins, K. A., et al. 2017, Nature, 546, 514
Giacalone, S., & Dressing, C. D. 2020, triceratops: Candidate exoplanet rating tool
Giacalone, S., Dressing, C. D., Jensen, E. L. N., et al. 2021, AJ, 161, 24
Gilhuly, C., Merritt, A., Abraham, R., et al. 2022, ApJ, 932, 44
Gillon, M., Triaud, A. H. M. J., Demory, B.-O., et al. 2017, Nature, 542, 456
Goldreich, P., & Tremaine, S. 1980, ApJ, 241, 425
Goodricke, J. 1783, Philosophical Transactions of the Royal Society of London Series I, 73, 474
—. 1784, Philosophical Transactions of the Royal Society of London Series I, 74, 287
Gray, D. F. 2005, The Observation and Analysis of Stellar Photospheres (Cambridge University Press)
Greiss, S., Steeghs, D., Gänsicke, B. T., et al. 2012, AJ, 144, 24
Greklek-McKeon, M., Knutson, H. A., Vissapragada, S., et al. 2023, AJ, 165, 48
Grimm, S. L., Demory, B.-O., Gillon, M., et al. 2018, A&A, 613, A68
Guerrero, N. 2020, TESS - Transiting Exoplanet Survey Satellite
Guo, X., Ballard, S., Dragomir, D., et al. 2019, Astrophysical Journal, 880, 64
Gupta, A., & Schlichting, H. E. 2019, MNRAS, 487, 24
Harris, C. R., Millman, K. J., van der Walt, S. J., et al. 2020a, Nature, 585, 357
—. 2020b, Nature, 585, 357
Hartman, J. D., Bakos, G. Á., Torres, G., et al. 2011, Astrophysical Journal, 742, 59
Haswell, C. A., Fossati, L., Ayres, T., et al. 2012, Astrophysical Journal, 760, 79
Hatzes, A. P., Cochran, W. D., Endl, M., et al. 2003, Astrophysical Journal, 599, 1383
Hauschildt, P. H., Baron, E., & Allard, F. 1997, The Astrophysical Journal, 483, 390

Hébrard, G., Bouchy, F., Pont, F., et al. 2008, A&A, 488, 763
Hedges, C., Angus, R., Barentsen, G., et al. 2020, Research Notes of the American Astronomical Society, 4, 220
Heller, R., Rodenbeck, K., & Bruno, G. 2019, Astronomy & Astrophysics, 624, A95
Hellier, C., Anderson, D. R., Collier Cameron, A., et al. 2009, Nature, 460, 1098
Henden, A. A., Templeton, M., Terrell, D., et al. 2016, VizieR Online Data Catalog, II/336
Henry, G. W., Marcy, G. W., Butler, R. P., & Vogt, S. S. 2000, Astrophysical Journal Letters, 529, L41
Hobson, M. J., Trifonov, T., Henning, T., et al. 2023, AJ, 166, 201
Høg, E., Fabricius, C., Makarov, V. V., et al. 2000, A&A, 355, L27
Holman, M. J., Fabrycky, D. C., Ragozzine, D., et al. 2010, Science, 330, 51
Hörst, S. M., He, C., Lewis, N. K., et al. 2018, Nature Astronomy, 2, 303
Howell, S. B., Everett, M. E., Sherry, W., Horch, E., & Ciardi, D. R. 2011, AJ, 142, 19
Howell, S. B., Scott, N. J., Matson, R. A., et al. 2021, Frontiers in Astronomy and Space Sciences, 8, 10
Huffer, C. M., & Collins, George W., I. 1962, Astrophysical Journal, Supplement, 7, 351
Hunter, J. D. 2007a, Computing In Science & Engineering, 9, 90
—. 2007b, Computing in Science & Engineering, 9, 90
Jenkins, J. M. 2002, ApJ, 575, 493
Jenkins, J. M., Tenenbaum, P., Seader, S., et al. 2020, Kepler Data Processing Handbook: Transiting Planet Search, Kepler Science Document KSCI-19081-003
Jenkins, J. M., Chandrasekaran, H., McCauliff, S. D., et al. 2010, in Society of Photo-Optical Instrumentation Engineers (SPIE) Conference Series, Vol. 7740, Software and Cyberinfrastructure for Astronomy, ed. N. M. Radziwill & A. Bridger, 77400D
Jenkins, J. M., Twicken, J. D., McCauliff, S., et al. 2016, in Proc. SPIE, Vol. 9913, Software and Cyberinfrastructure for Astronomy IV, 99133E
Jensen, E. 2013, Tapir: A web interface for transit/eclipse observability, Astrophysics Source Code Library
Jin, S., & Mordasini, C. 2018, ApJ, 853, 163
Johns-Krull, C. M., McCullough, P. R., Burke, C. J., et al. 2008, Astrophysical Journal, 677, 657
Jurkevich, I. 1970, Vistas in Astronomy, 12, 63
Keim, M. A., van Dokkum, P., Danieli, S., et al. 2022, ApJ, 935, 160
Kempton, E. M. R., Bean, J. L., Louie, D. R., et al. 2018, PASP, 130, 114401
Kipping, D. M. 2008, Monthly Notices of the Royal Astronomical Society, 389, 1383
—. 2013, MNRAS, 435, 2152
—. 2014, MNRAS, 440, 2164
Kipping, D. M., Bakos, G. Á., Buchhave, L., Nesvorný, D., & Schmitt, A. 2012, The Astrophysical Journal, 750, 115

Kipping, D. M., Schmitt, A. R., Huang, X., et al. 2015, ApJ, 813, 14
Koch, D. G., Borucki, W. J., Basri, G., et al. 2010, ApJ, 713, L79
Kolbl, R., Marcy, G. W., Isaacson, H., & Howard, A. W. 2015, AJ, 149, 18
Kopal, Z. 1941, Astrophysical Journal, 94, 145
—. 1946, An introduction to the study of eclipsing variables, Vol. 6, 1
—. 1948, Astrophysical Journal, 108, 46
Koposov, S., Speagle, J., Barbary, K., et al. 2023, joshspeagle/dynesty: v2.1.0
Kreidberg, L. 2015a, PASP, 127, 1161
—. 2015b, PASP, 127, 1161
Kreidberg, L., Luger, R., & Bedell, M. 2019, Astrophysical Journal Letters, 877, L15
Kristiansen, M. H. K., Rappaport, S. A., Vanderburg, A. M., et al. 2022, Publications of the Astronomical Society of the Pacific, 134, 074401
Kurucz, R. L. 1979, ApJS, 40, 1
Kurucz, R. L. 1992, in The Stellar Populations of Galaxies, ed. B. Barbuy & A. Renzini, Vol. 149, 225
Landsman, W. B. 1993, in Astronomical Society of the Pacific Conference Series, Vol. 52, Astronomical Data Analysis Software and Systems II, ed. R. J. Hanisch, R. J. V. Brissenden, & J. Barnes, 246
Lang, D., Hogg, D., Mierle, K., Blanton, M., & Roweis, S. 2009, Astronomical Journal, 139
Latham, D. W., Mazeh, T., Stefanik, R. P., Mayor, M., & Burki, G. 1989, Nature, 339, 38
Leconte, J., & Chabrier, G. 2012, A&A, 540, A20
Lee, E. J., & Chiang, E. 2016, ApJ, 817, 90
Léger, A., Rouan, D., Schneider, J., et al. 2009, A&A, 506, 287
Leleu, A., Alibert, Y., Hara, N. C., et al. 2021, A&A, 649, A26
Li, J., Tenenbaum, P., Twicken, J. D., et al. 2019, PASP, 131, 024506
Lightkurve Collaboration, Cardoso, J. V. d. M., Hedges, C., et al. 2018, Lightkurve: Kepler and TESS time series analysis in Python, Astrophysics Source Code Library, record ascl:1812.013
Lin, D. N. C., & Papaloizou, J. 1986, ApJ, 309, 846
Linnell, A. P., & Proctor, D. D. 1970, Astrophysical Journal, 161, 1043
Lithwick, Y., Xie, J., & Wu, Y. 2012, ApJ, 761, 122
Lokhorst, D., Abraham, R., van Dokkum, P., Wijers, N., & Schaye, J. 2019, Astrophysical Journal, 877, 4
Lokhorst, D., Abraham, R., Pasha, I., et al. 2022, ApJ, 927, 136
Lokhorst, D. M., Abraham, R. G., van Dokkum, P., & Chen, S. 2020, arXiv e-prints, arXiv:2010.00686
Lomb, N. R. 1976, Ap&SS, 39, 447
Lopez, E. D., & Rice, K. 2018, MNRAS, 479, 5303
Luque, R., & Pallé, E. 2022, Science, 377, 1211

Mamajek, E. E., & Hillenbrand, L. A. 2008, ApJ, 687, 1264
Mandel, K., & Agol, E. 2002, ApJ, 580, L171
Mann, C., Lafreniére, D., Dragomir, D., et al. 2023a, AJ, 165, 217
Mann, C. R., Dalba, P. A., Lafrenière, D., et al. 2023b, AJ, 166, 239
Masuda, K. 2014, ApJ, 783, 53
Maxted, P. F. L., Anderson, D. R., Collier Cameron, A., et al. 2011, PASP, 123, 547
Mayor, M., & Queloz, D. 1995, Nature, 378, 355
McCully, C., Daily, M., Brandt, G. M., et al. 2022, BANZAI-NRES: BANZAI data reduction pipeline for NRES, Astrophysics Source Code Library, record ascl:2212.012
McCully, C., Volgenau, N. H., Harbeck, D.-R., et al. 2018, in Society of Photo-Optical Instrumentation Engineers (SPIE) Conference Series, Vol. 10707, Software and Cyberinfrastructure for Astronomy V, ed. J. C. Guzman & J. Ibsen, 107070K
McCully, C., Turner, M., Volgenau, N., et al. 2018, LCOGT/banzai: Initial Release
Ment, K., & Charbonneau, D. 2023, AJ, 165, 265
Mermilliod, J. C. 1994, VizieR Online Data Catalog, II/193
Merritt, A., van Dokkum, P., Abraham, R., & Zhang, J. 2016a, Astrophysical Journal, 830, 62
Merritt, A., van Dokkum, P., Danieli, S., et al. 2016b, Astrophysical Journal, 833, 168
Miller, N., & Fortney, J. J. 2011, ApJ, 736, L29
Mistry, P., Pathak, K., Prasad, A., et al. 2023, AJ, 166, 9
Moe, M., & Di Stefano, R. 2017, ApJS, 230, 15
Moll, R., Garaud, P., Mankovich, C., & Fortney, J. J. 2017, ApJ, 849, 24
Mordasini, C. 2020, A&A, 638, A52
Motl, D. 2011, C-Munipack
Močnik, T., Hellier, C., & Southworth, J. 2018, Astrophysical Journal, 156, 44
Nagasawa, M., Ida, S., & Bessho, T. 2008, ApJ, 678, 498
NASA Exoplanet Archive. 2022, Planetary Systems
Niemann, H. B., Atreya, S. K., Carignan, G. R., et al. 1998, J. Geophys. Res., 103, 22831
Ofir, A., & Dreizler, S. 2013, A&A, 555, A58
Ofir, A., Dreizler, S., Zechmeister, M., & Husser, T.-O. 2014, A&A, 561, A103
Otegi, J. F., Bouchy, F., & Helled, R. 2020, A&A, 634, A43
Owen, J. E., & Wu, Y. 2013, ApJ, 775, 105
—. 2017, ApJ, 847, 29
Paredes, L. A., Henry, T. J., Quinn, S. N., et al. 2021, AJ, 162, 176
Pasha, I., Lokhorst, D., van Dokkum, P. G., et al. 2021, ApJ, 923, L21
Paunzen, E. 2015, A&A, 580, A23
Paxton, B., Bildsten, L., Dotter, A., et al. 2011, ApJS, 192, 3
Paxton, B., Cantiello, M., Arras, P., et al. 2013, ApJS, 208, 4
Paxton, B., Marchant, P., Schwab, J., et al. 2015, ApJS, 220, 15

Paxton, B., Schwab, J., Bauer, E. B., et al. 2018, ApJS, 234, 34
Pedregosa, F., Varoquaux, G., Gramfort, A., et al. 2011, Journal of Machine Learning Research, 12, 2825
Pepper, J., Kuhn, R. B., Siverd, R., James, D., & Stassun, K. 2012, Publications of the Astronomical Society of the Pacific, 124, 230
Pepper, J., Pogge, R. W., DePoy, D. L., et al. 2007, Publications of the Astronomical Society of the Pacific, 119, 923
Pepper, J., Rodriguez, J. E., Collins, K. A., et al. 2017, Astronomical Journal, 153, 215
Perruchot, S., Kohler, D., Bouchy, F., et al. 2008, in Ground-based and Airborne Instrumentation for Astronomy II, ed. I. S. McLean & M. M. Casali, Vol. 7014, International Society for Optics and Photonics (SPIE), 70140J
Perryman, M. 2018a, The Exoplanet Handbook
—. 2018b, The Exoplanet Handbook
Petigura, E. A. 2015, PhD thesis, University of California, Berkeley
Petigura, E. A., Howard, A. W., Marcy, G. W., et al. 2017, AJ, 154, 107
Piaulet, C., Benneke, B., Almenara, J. M., et al. 2023, Nature Astronomy, 7, 206
Pickering, E. C. 1880, Proc. Am. Acad. Sci., 16, 257
Piotrowski, S. L. 1947, Astrophysical Journal, 106, 472
—. 1948, Astrophysical Journal, 108, 36
Pollacco, D., Skillen, I., Collier Cameron, A., et al. 2008, Monthly Notices of the Royal Astronomical Society, 385, 1576
Pollacco, D. L., Skillen, I., Collier Cameron, A., et al. 2006, PASP, 118, 1407
Pont, F., Zucker, S., & Queloz, D. 2006, MNRAS, 373, 231
Queloz, D., Bouchy, F., Moutou, C., et al. 2009, A&A, 506, 303
Radica, M., Welbanks, L., Espinoza, N., et al. 2023, Monthly Notices of the Royal Astronomical Society, 524, 835
Radovan, M. V., Cabak, G. F., Laiterman, L. H., Lockwood, C. T., & Vogt, S. S. 2010, in Society of Photo-Optical Instrumentation Engineers (SPIE) Conference Series, Vol. 7735, Ground-based and Airborne Instrumentation for Astronomy III, ed. I. S. McLean, S. K. Ramsay, & H. Takami, 77354K
Ranjan, S., Wordsworth, R., & Sasselov, D. D. 2017, ApJ, 843, 110
Rasio, F. A., & Ford, E. B. 1996, Science, 274, 954
Rescigno, F., Hébrard, G., Vanderburg, A., et al. 2023, MNRAS
Ricker, G. R., Winn, J. N., Vanderspek, R., et al. 2015, Journal of Astronomical Telescopes, Instruments, and Systems, 1, 014003
Rogers, J. G., & Owen, J. E. 2021, MNRAS, 503, 1526
Rosenblatt, F. 1971, Icarus, 14, 71
Russell, H. N. 1912a, Astrophysical Journal, 35, 315

—. 1912b, Astrophysical Journal, 36, 54
Russell, H. N., & Shapley, H. 1912a, Astrophysical Journal, 36, 385
Russell, I. H. N., & Shapley, H. 1912b, Astrophysical Journal, 36, 239
Sackett, P. D. 1999, in NATO Advanced Science Institutes (ASI) Series C, Vol. 532, NATO Advanced Science Institutes (ASI) Series C, ed. J. M. Mariotti & D. Alloin, 189
Sanchis-Ojeda, R., Rappaport, S., Winn, J. N., et al. 2013, ApJ, 774, 54
Sanz-Forcada, J., Ribas, I., Micela, G., et al. 2010, Astronomy & Astrophysics, 511, L8
Savitzky, A., & Golay, M. J. E. 1964, Analytical Chemistry, 36, 1627
Scargle, J. D. 1982, ApJ, 263, 835
Schlafly, E. F., & Finkbeiner, D. P. 2011, ApJ, 737, 103
Schlegel, D. J., Finkbeiner, D. P., & Davis, M. 1998a, ApJ, 500, 525
—. 1998b, ApJ, 500, 525
Schmitt, A. R., Hartman, J. D., & Kipping, D. M. 2019a, arXiv e-prints, arXiv:1910.08034
—. 2019b, arXiv e-prints, arXiv:1910.08034
Seager, S., & Mallén-Ornelas, G. 2003, Astrophysical Journal, 585, 1038
Siverd, R. J., Beatty, T. G., Pepper, J., et al. 2012, Astrophysical Journal, 761, 123
Siverd, R. J., Brown, T. M., Barnes, S., et al. 2018, in Society of Photo-Optical Instrumentation Engineers (SPIE) Conference Series, Vol. 10702, Ground-based and Airborne Instrumentation for Astronomy VII, ed. C. J. Evans, L. Simard, & H. Takami, 107026C
Smith, J. C., Stumpe, M. C., Van Cleve, J. E., et al. 2012, PASP, 124, 1000
Soderhjelm, S. 1974, Astronomy and Astrophysics, 34, 59
Speagle, J. S. 2020, MNRAS, 493, 3132
Stassun, K. G., Collins, K. A., & Gaudi, B. S. 2017, AJ, 153, 136
Stassun, K. G., Corsaro, E., Pepper, J. A., & Gaudi, B. S. 2018a, AJ, 155, 22
Stassun, K. G., & Torres, G. 2016, AJ, 152, 180
—. 2021, ApJ, 907, L33
Stassun, K. G., Oelkers, R. J., Pepper, J., et al. 2018b, AJ, 156, 102
Steffen, J. H., Fabrycky, D. C., Agol, E., et al. 2013, MNRAS, 428, 1077
Struve, O. 1952, The Observatory, 72, 199
Stumpe, M. C., Smith, J. C., Catanzarite, J. H., et al. 2014, PASP, 126, 100
Stumpe, M. C., Smith, J. C., Van Cleve, J. E., et al. 2012, PASP, 124, 985
Tayar, J., Claytor, Z. R., Huber, D., & van Saders, J. 2022, ApJ, 927, 31
Teachey, A., & Kipping, D. M. 2018, Science Advances, 4, eaav1784
Thompson, S. L. 1990, ANEOS Analytic Equations of State for Shock Physics Codes Input Manual, Tech. Rep. SAND-89-2951, 6939284, Sandia National Laboratory
Thorngren, D., & Fortney, J. J. 2019, ApJ, 874, L31
Thorngren, D., Gao, P., & Fortney, J. J. 2019, ApJ, 884, L6
Thorngren, D. P., Fortney, J. J., Murray-Clay, R. A., & Lopez, E. D. 2016, ApJ, 831, 64

Tody, D. 1986, in Society of Photo-Optical Instrumentation Engineers (SPIE) Conference Series, Vol. 627, Instrumentation in astronomy VI, ed. D. L. Crawford, 733
Tody, D. 1993, in Astronomical Society of the Pacific Conference Series, Vol. 52, Astronomical Data Analysis Software and Systems II, ed. R. J. Hanisch, R. J. V. Brissenden, & J. Barnes, 173
Tokovinin, A. 2018, Speckle Interferometry at SOAR
Tokovinin, A., Fischer, D. A., Bonati, M., et al. 2013, PASP, 125, 1336
Torres, G., Andersen, J., & Giménez, A. 2010a, A&A Rev., 18, 67
—. 2010b, A&A Rev., 18, 67
Tull, R. G., MacQueen, P. J., Sneden, C., & Lambert, D. L. 1995, PASP, 107, 251
Turtelboom, E. V., Weiss, L. M., Dressing, C. D., et al. 2022, AJ, 163, 293
Twicken, J. D., Catanzarite, J. H., Clarke, B. D., et al. 2018, PASP, 130, 064502
Udalski, A., Zebrun, K., Szymanski, M., et al. 2002, Acta Astronomica, 52, 115
van der Walt, S., Colbert, S. C., & Varoquaux, G. 2011, Computing in Science and Engineering, 13, 22
van Dokkum, P., Abraham, R., Brodie, J., et al. 2016, Astrophysical Journal Letters, 828, L6
van Dokkum, P., Abraham, R., Romanowsky, A. J., et al. 2017, Astrophysical Journal Letters, 844, L11
van Dokkum, P., Gilhuly, C., Bonaca, A., et al. 2019a, arXiv e-prints, arXiv:1906.11260
van Dokkum, P., Wasserman, A., Danieli, S., et al. 2019b, Astrophysical Journal, 880, 91
Vanderburg, A., Latham, D. W., Buchhave, L. A., et al. 2016, ApJS, 222, 14
Vazan, A., Helled, R., & Guillot, T. 2018, A&A, 610, L14
Vogt, S. S., Allen, S. L., Bigelow, B. C., et al. 1994, in Society of Photo-Optical Instrumentation Engineers (SPIE) Conference Series, Vol. 2198, Instrumentation in Astronomy VIII, ed. D. L. Crawford & E. R. Craine, 362
Ward, W. R. 1997, Icarus, 126, 261
Wasserman, A., van Dokkum, P., Romanowsky, A. J., et al. 2019, arXiv e-prints, arXiv:1905.10373
Winn, J. N. 2009, in IAU Symposium, Vol. 253, Transiting Planets, ed. F. Pont, D. Sasselov, & M. J. Holman, 99–109
Winn, J. N. 2010, arXiv e-prints, arXiv:1001.2010
Wolszczan, A. 1994, Science, 264, 538
Wolszczan, A., & Frail, D. A. 1992, Nature, 355, 145
Wright, J. T., & Gaudi, B. S. 2013, Exoplanet Detection Methods, ed. T. D. Oswalt, L. M. French, & P. Kalas, 489
Wu, Y. 2019, ApJ, 874, 91
Wu, Y., & Lithwick, Y. 2011, ApJ, 735, 109
Wu, Y., & Murray, N. 2003, ApJ, 589, 605
Yee, S. W., Petigura, E. A., & von Braun, K. 2017, ApJ, 836, 77

Yi, S., Demarque, P., Kim, Y.-C., et al. 2001, The Astrophysical Journal Supplement Series, 136, 417

Zacharias, N., Finch, C. T., Girard, T. M., et al. 2012, VizieR Online Data Catalog, I/322A

Zechmeister, M., & Kürster, M. 2009, A&A, 496, 577

Zhang, J., Abraham, R., van Dokkum, P., Merritt, A., & Janssens, S. 2018, Astrophysical Journal, 855, 78

Zhang, M., Knutson, H. A., Dai, F., et al. 2023, AJ, 165, 62

Zhou, G., Rodriguez, J. E., Vanderburg, A., et al. 2018, AJ, 156, 93